

2017

Investigating RTK using Geostationary Satellites and IRNSS

Bhandari, Vimalkumar

Bhandari, V. (2017). Investigating RTK using Geostationary Satellites and IRNSS (Doctoral thesis, University of Calgary, Calgary, Canada). Retrieved from <https://prism.ucalgary.ca>. doi:10.11575/PRISM/26634
<http://hdl.handle.net/11023/4119>

Downloaded from PRISM Repository, University of Calgary

UNIVERSITY OF CALGARY

Investigating RTK using Geostationary Satellites and IRNSS

by

Vimalkumar Bhandari

A THESIS

SUBMITTED TO THE FACULTY OF GRADUATE STUDIES
IN PARTIAL FULFILMENT OF THE REQUIREMENTS FOR THE
DEGREE OF DOCTOR OF PHILOSOPHY

GRADUATE PROGRAM IN GEOMATICS ENGINEERING

CALGARY, ALBERTA

SEPTEMBER, 2017

© Vimalkumar Bhandari 2017

Abstract

The IRNSS and SBAS constellations have geostationary satellites in the space segment. Geostationary satellites provide additional observations and are always visible to a given user. However, due to their small line-of-sight velocities, geostationary satellites have two unique challenges: Doppler collision and observability, both of which can affect their use in an RTK solution.

The first phase of this research is aimed at understanding Doppler collision. It is a unique phenomenon in GNSS where tracking errors are introduced in the measurements due to cross-correlation between two or more satellites. Doppler collisions affect geostationary satellites for longer durations and the error resembles code multipath. If not mitigated, Doppler collision could have an impact on the ability to use code measurements of geostationary satellites in RTK positioning. This research describes likely conditions for Doppler collision, derives a Doppler collision error envelope for geostationary pseudorange measurements, and then demonstrates the effect using simulated and live signals.

The second phase of this research presents the effect of Doppler collision on an RTK solution using geostationary satellites, with emphasis on ambiguity convergence time. Multiple mitigation techniques such as de-weighting of geostationary observations and use of narrow correlator are proposed to reduce the impact of Doppler collision.

The third phase talks about the observability of a geostationary satellite. The relatively static nature of geostationary satellites leads to poor observability and has a direct impact on the convergence of ambiguities. The poor observability can limit the use of standalone constellations such as IRNSS in an RTK solution.

Finally, an investigation is conducted on both hardware-simulated and live data of IRNSS to understand the impact of Doppler collision and observability. Mitigation methods are applied, and the improvement in the code measurement error and the convergence of ambiguities is presented. Overall, this thesis is aimed at addressing some of the key issues arising from the use of geostationary satellites in an RTK solution so that a multi-constellation RTK solution progresses one step closer to the possibility of an all-constellation RTK solution, including IRNSS.

Preface

This thesis, in part, contains materials from the previously published conference papers, a magazine article and a journal paper that are referenced below.

Bhandari, V., K. O’Keefe, and G. Lachapelle (2013) “Assessment of multi-constellation RTK solutions during differential correction data outages,” *in Proceedings of ION GNSS+ 2013*, 16-20 September, Nashville, TN, pp. 3194-3204, US. The Institute of Navigation, Fairfax VA

Bhandari, V. (2015) “Characterization of Doppler Collision and Its Effect on Indoor Positioning,” *in PhD forum of Proceedings of the International Conference on Indoor Positioning and Indoor Navigation (IPIN 2015)*, Banff, AB, 2 pages

Bhandari, V. and K. O’Keefe (2016) “What is Doppler Collision and is it a problem in GNSS?,” *Inside GNSS*, vol 11, no. 1, Gibbons Media & Research LLC, New Jersey, USA, pages 26-36

Bhandari, V. and K. O’Keefe (2017) “Characterization of Doppler collision and its impact on carrier phase ambiguity resolution using geostationary satellites,” *GPS Solutions*, Springer Berlin Heidelberg, <https://doi.org/10.1007/s10291-017-0648-z>

Acknowledgements

Firstly, I would like to express my sincere gratitude to my supervisor, Professor Kyle O'Keefe, for this exceptional support and guidance throughout my doctoral studies. I was fortunate to have my graduate studies done under his experience. His friendly as well as approachable nature and always motivating words encouraged me to succeed in my research. Personally, I had many challenging situations during the program, however, his constant appreciation of the research progress motivated me to achieve better results and improve the quality of the thesis.

My sincere thanks to former co-supervisor Professor Gérard Lachapelle, Alberta Innovates Technology Futures-Informatics Circle Of Research Excellence (iCORE) Chair in Wireless location, for funding my graduate program. Your vast knowledge and experience in the field of GNSS and RTK were valuable. His curiosity and constant questioning always kept me on toes to find new problems and alternative solutions. I also thank Professor Mark Petovello for his time and patience invested in technical discussions on the RTK software. I thank Dr. Zhe He for his technical help on the software receiver.

I want to specially acknowledge Dr. Shashank Satyanarayana, Accord Software and Systems, India, and Michael Olynik, NovAtel Inc., Calgary for providing live data of IRNSS using commercial receivers. The live data helped to conclude my research in a complete sense. I want to thank Dr. Vyasraj Gururao for guiding and providing multiple thoughts and ideas during the early stage of my research.

Naveen is acknowledged for sharing his knowledge in signal processing and multipath. The technical discussions and question and answer sessions were inspiring moments, which guided me through series of challenges. I thank Srinivas Bhaskar, Ashwitha and Srinivas Tantry; all those overnight discussions were amazing and wonderful. Many thanks to Vijay, Rakesh, Niranjan, Rasika, Bernhard, and Erin, your help at critical moments was exceptional. Special thanks to Anup, Thyagaraja, Ranjeeth, Sashidharan, Ali B, Ali J, Saeed, Tao, Fatemeh, Billy, Jingjing, Sergey, Maryam, Ahmad, Nahal, Adam, Laura, Chandra, Paul, and Sajan. Thank you to Rachael and my Robotics team for constantly providing me motivation to try out new things. Suvarna, Sujay, Shruthi, Aradhya, Simmerdeep, Neha, Narendra, and Raki, thank you for providing me a “home away from home” experience.

I want to thank my parents, my wife and my two little daughters for firmly supporting me in the pursuit of doctoral program. You have made enormous sacrifices in life, and I owe it henceforth. Special thanks to my sisters, Sangeeta and Manjula and family members: my grandmother, Uttamchand, Dineshji, Bharatji, Chetanji and all others who supported me at the time of need.

Finally, many thanks to my childhood teacher Neela Watwe, Deshpande Sir and my mentor Anand Kulkarni. I could achieve this success because of your teaching and guidance.

Dedication

Dedicated to my parents, Madanlalji and Chandrakanta, my wife Aruna and my little daughters, Samata and Riddhi

Table of Contents

Abstract	ii
Preface	iv
Acknowledgements	v
Dedication	vii
Table of Contents	viii
List of Tables	xi
List of Figures and Illustrations	xii
List of Abbreviations	xvii
List of Symbols	xviii
CHAPTER ONE: INTRODUCTION	1
1.1 Problem Statement	1
1.1.1 RTK using GEO Satellites	2
1.1.1.1 Doppler Collision	3
1.1.1.2 Poor Observability	3
1.1.1.3 Stationary Multipath	4
1.1.2 Limitations	5
1.1.3 Motivations	6
1.2 Objectives and Contributions	8
1.3 Thesis Outline	11
CHAPTER TWO: MULTI-CONSTELLATION RTK AND GEOSTATIONARY SATELLITES	13
2.1 RTK Positioning	13
2.1.1 Measurement Differencing and Float Solution	17
2.1.2 Ambiguity Resolution Models	19
2.1.2.1 Geometry-Based Model	19
2.1.2.2 Geometry-Free Model	20
2.1.3 Ambiguity Resolution Methods	20
2.1.3.1 Brute Force and Integer Round-off	21
2.1.3.2 Bootstrapping	22
2.1.3.3 Integer Least-Squares	23
2.1.3.4 LAMBDA	24
2.1.4 Validation of Ambiguity Resolution	25
2.1.4.1 Probability of Correct Fix	25
2.1.4.2 Time To First Fix Ambiguities	26
2.1.4.3 Ratio Test	27
2.1.5 Fixed Solution	28
2.2 Multi-Constellation RTK	29
2.2.1 IRNSS	34
2.2.2 SBAS	37
2.3 RTK with GEO Satellites	38
2.3.1 Doppler Collision	38
2.3.1.1 Relative Doppler	42
2.3.1.2 Cross-Correlation function	43

2.3.1.3 Relative Code Delay	44
2.3.1.4 Relative Power	45
2.3.1.5 Data Message Similitude	46
2.3.1.6 Relative Carrier Phase	46
2.3.2 Observability	47
2.3.2.1 Covariance of Ambiguities	47
2.3.2.2 Standard Kalman Filter	48
2.3.2.3 Modified Kalman Filter	49
CHAPTER THREE: CHARACTERIZATION OF DOPPLER COLLISION	53
3.1 Study of Geostationary Doppler	54
3.1.1 WAAS	54
3.1.2 BeiDou GEO	57
3.1.3 IRNSS GEO	59
3.1.4 GAGAN	59
3.1.5 MSAS	60
3.1.6 EGNOS	61
3.2 GNSS Cross-Correlation Function	62
3.2.1 Spatial Extent of WAAS Doppler Collision	64
3.2.2 Spatial Extent of BeiDou B1I Doppler Collision	67
3.3 Theoretical Error Limits	68
3.4 Doppler Collision using GNSS Simulator	70
3.4.1 Pseudorange Observations during Doppler Collision	74
3.4.2 Nature of Doppler Collision Error	77
3.5 Doppler Collision using Live Data	79
3.5.1 WAAS Live Data	80
3.5.2 IRNSS Live Data	83
3.6 Impact of Doppler collision on Carrier Phase Measurements	85
CHAPTER FOUR: RTK POSITIONING DURING DOPPLER COLLISION	88
4.1 RTK Positioning during Hardware-Simulation of Doppler Collision	89
4.1.1 Test Setup	89
4.1.2 Selection of Satellites	95
4.1.3 TTFFA Analysis	99
4.1.4 De-Weighting Doppler Collision Observations	101
4.2 RTK Positioning during Live Doppler Collision	102
4.2.1 Test Setup	104
4.2.2 Selection of Satellites	105
4.2.3 TTFFA Analysis for Short Baseline	107
4.2.4 TTFFA Analysis for Long Baseline	108
4.3 Doppler Collision mitigation techniques	110
4.3.1 Satellite Doppler	110
4.3.2 Cross-Correlation function	111
4.3.3 Multipath Mitigation Techniques	111
4.3.3.1 Narrow Correlator	111
4.3.4 Delay Lock Loop Bandwidth	113

CHAPTER FIVE: OBSERVABILITY OF GEOSTATIONARY SATELLITES	117
5.1.1 Covariance Computation	117
5.2 Time-correlation of GEO Satellite Errors	119
5.3 Ambiguity Convergence in WAAS	124
5.4 IRNSS and its Observability	130
5.4.1 Ambiguity Convergence in IRNSS	131
5.5 Improvement of IRNSS Observability	133
5.5.1 Augmentation with GAGAN Satellites	133
5.5.2 Introduction of IGSO satellites	135
5.5.3 Augmentation with other GNSS Systems	137
CHAPTER SIX: INVESTIGATION OF DOPPLER COLLISION IN IRNSS	140
6.1 Preliminary Analysis in IRNSS.....	141
6.2 Doppler Collision in Pseudo-IRNSS	144
6.3 RTK Solution using Pseudo-IRNSS.....	147
6.3.1 TTFFA Analysis	150
6.4 Mitigation of Doppler Collision in Pseudo-IRNSS	151
6.4.1 Standard Correlator	151
6.4.2 Narrow Correlator	151
6.5 Doppler Collision using Live IRNSS Signal.....	154
6.6 Single Frequency RTK Solution using Live IRNSS Data	157
6.7 Improvement in IRNSS Observability	161
CHAPTER SEVEN: CONCLUSIONS AND RECOMMENDATIONS	163
7.1 Conclusions	163
7.1.1 Characterization of Doppler Collision.....	163
7.1.2 RTK Positioning during Doppler Collision	164
7.1.3 Observability of Geostationary Satellites	165
7.1.4 Investigation of Doppler Collision in IRNSS	166
7.2 Recommendations for Future Work.....	166
7.2.1 Separation of Doppler collision and multipath.....	167
7.2.2 Cross-Correlation Function	167
7.2.3 Auto-Regressive Modelling of Geostationary Measurement Errors ..	168
7.2.4 Multi-Constellation RTK Solution with Six GNSS and SBAS	168
REFERENCES	169
APPENDIX A: BEIDOU B1I CROSS-CORRELATION DISTRIBUTION.....	181
APPENDIX B: CROSS-CORRELATION MEASUREMENT ERROR.....	183
APPENDIX C: DOPPLER COLLISION ERROR ENVELOPE.....	184
APPENDIX D: SOFTWARE DEVELOPMENT.....	188

List of Tables

Table 2-1 BeiDou-2 constellation and its current status	31
Table 2-2 IRNSS constellation and its current status	36
Table 2-3 SBAS satellites availability	38
Table 3-1 Cross-correlation properties of Gold codes	62
Table 3-2 Cross-correlation properties of truncated Gold codes in BeiDou B1I	63
Table 3-3 Coordinates of WAAS satellites employed in Doppler collision simulation	64
Table 3-4 Maximum Doppler collision errors with different correlator designs and varying signal strength	70
Table 3-5 User location to observe Doppler collision using GNSS simulator	71
Table 3-6 Doppler collision live data setup settings	80
Table 4-1 Doppler collision simulation additional user locations coordinates	90
Table 4-2 Doppler collision live signal user locations coordinates.....	103
Table 5-1 Tabulation of parameters used in the covariance simulation	125
Table 6-1 User locations to collect pseudo-IRNSS observations	145
Table 6-2 Coordinates of base and rover receivers for a single frequency L5 IRNSS – L1 GPS RTK solution	158
Table A-1 Probability of the distribution of the cross-correlation values between BDS PRN1 and PRN2	182
Table D-2 Parameters of modified GSNRx TM	190

List of Figures and Illustrations

Figure 2-1 Flowchart of an RTK solution	29
Figure 2-2 Ground track of IRNSS satellites over the IRNSS service area	35
Figure 2-3 Correlation structure in a GNSS receiver	39
Figure 2-4 Code measurement error due to Doppler collision left side: single cross-correlation peak, blue in-phase and green opposite phase, and right side: successive peaks in transition, magenta in-phase and red opposite phase	45
Figure 3-1 Smoothed observed Doppler variation of PRN 133 and PRN 135	55
Figure 3-2 Smoothed observed Doppler variation of PRN 133 and PRN 138	55
Figure 3-3 Smoothed observed Doppler variation of PRN 135 and PRN 138	56
Figure 3-4 Smoothed observed Doppler variation of PRN 135 and PRN 138 for a week	57
Figure 3-5 Doppler frequencies of BeiDou geostationary satellites, top plot shows variations at mid-latitudes and bottom plot shows variations at lower latitude	58
Figure 3-6 Doppler variation of IRNSS geostationary satellites	59
Figure 3-7 Doppler variation of GAGAN satellites	60
Figure 3-8 Doppler variation of MSAS satellites	60
Figure 3-9 Doppler variation of EGNOS satellites	61
Figure 3-10 Simulation of cross-correlation over a geographical area and its projection	66
Figure 3-11 Cross-section of C/A code cross-correlation function along East-West	67
Figure 3-12 Simulation of truncated Gold codes cross-correlation over a geographical area and its cross-section	69
Figure 3-13 Test setup to observe Doppler collision using GNSS simulator	71
Figure 3-14 Correlation triangle with cross-correlation peak	73
Figure 3-15 Doppler collision effect on pseudorange of PRN 138 when PRN 135 is introduced into the scenario	74
Figure 3-16 PRN 135 measurements during Doppler collision when PRN 138 is moving	76

Figure 3-17 PRN 135 measurements using commercial receiver during Doppler collision	77
Figure 3-18 PRN 135 measurements during first 200 s of Doppler collision when PRN 138 is moving	79
Figure 3-19 Live signal PRN 135 code measurements during Doppler collision	81
Figure 3-20 Live signal code measurements during non-likely Doppler collision conditions because relative Doppler is significant	82
Figure 3-21 Live signal IRNSS 1G measurements during Doppler collision.....	84
Figure 3-22 Live signal IRNSS 1C measurements during Doppler collision.....	85
Figure 4-1 Simulation of Doppler collision at three different locations using GNSS simulator.....	90
Figure 4-2 PRN 135 code-minus-carrier measurements showing effect of Doppler collision simulation at 3 locations along with error envelope in red	91
Figure 4-3 PRN 135 code-minus-carrier measurements and single-differenced pseudorange residuals between two receivers	92
Figure 4-4 Distribution of single-differenced residuals of WAAS satellites during Doppler collision (P1 and P2) and normal conditions (P3) respectively	93
Figure 4-5 RTK solution using Rx2 and Rx3, baseline 900 m. Bottom section indicates ambiguities are fixed for WAAS satellites PRN 135 (blue) and PRN 138 (green).....	94
Figure 4-6 Sky plot observed at Rx1 during Doppler collision simulation. Satellites in blue are common GPS satellites used in RTK solution. The circles indicate the location of the satellite at the end of the test.	95
Figure 4-7 Elevation and C/N ₀ plot of GPS satellites Rx1	96
Figure 4-8 Code-minus-carrier observations of GPS satellites at Rx1	97
Figure 4-9 PDOP plots of various combinations of satellites at Rx1	98
Figure 4-10 Ambiguity convergence during Doppler collision and normal conditions for an RTK solution between Rx2 and Rx3	100
Figure 4-11 TTFFA during Doppler collision and normal conditions.....	102
Figure 4-12 Three user locations for live data collection during Doppler collision	103
Figure 4-13 RTK using live signal at three locations	104

Figure 4-14 Live signals PRN 135 Measurements showing effect of Doppler collision at three different locations	105
Figure 4-15 Live data at base RxA and rover RxB. Top row shows single-differenced ambiguities, middle row shows convergence of single-differenced ambiguities and the number of satellites fixed, and bottom row shows float/fixed solution position error	107
Figure 4-16 TTFFA during Doppler collision with live signals at a short baseline.....	108
Figure 4-17 TTFFA during Doppler collision using live signals at long baseline.....	109
Figure 4-18 Code-minus-carrier measurements obtained using narrow correlator during Doppler collision	112
Figure 4-19 Code-minus-carrier measurements with DLL bandwidth of 1 Hz	114
Figure 4-20 Code-minus-carrier measurements with DLL bandwidth of 0.1 Hz	115
Figure 5-1 Single-differenced code and phase residuals for RTK solution between ...	119
Figure 5-2 Normalized autocorrelation of single-differenced code residuals for simulated Doppler collision data at a baseline of 900 m. Approximation of first order GM Markov model at $\tau = 700$ s	120
Figure 5-3 PSD of single-differenced residuals for simulated Doppler collision data at a baseline of 900 m. The peak corresponding to 3600 s is the variation of single-differenced residuals due to Doppler collision envelope.	121
Figure 5-4 Normalized autocorrelation of single-differenced code residuals for live data at a baseline of 1380 m. The correlation time of first order GM model is 700 s.	122
Figure 5-5 Normalized autocorrelation of single-differenced code residuals for live data at a baseline of 10 m. The correlation time of first order GM model is 500 s.	123
Figure 5-6 Standard deviation of covariance of single-differenced ambiguities using all GPS + 2 WAAS	126
Figure 5-7 Standard deviation of covariance of single-differenced ambiguities using 6 GPS + 2 WAAS	127
Figure 5-8 Standard deviation of covariance of single-differenced ambiguities using 6 GPS	128
Figure 5-9 Standard deviation of covariance of single-differenced ambiguities using 4 GPS + 2 WAAS	129

Figure 5-10 Skyplot of simulated IRNSS constellation	131
Figure 5-11 Convergence of single-differenced ambiguities in IRNSS.....	132
Figure 5-12 Ground Track of IRNSS satellites along with GAGAN satellites located at the longitude of 55.03 ⁰ E and 83.00 ⁰ E respectively.....	134
Figure 5-13 Convergence of single-differenced ambiguities for RTK solution with IRNSS and GAGAN satellites	135
Figure 5-14 Proposed expansion of IRNSS system with two IGSO satellites	136
Figure 5-15 Convergence of single-differenced ambiguities after addition of two IGSO satellites in IRNSS constellation.....	137
Figure 5-16 Convergence of single-differenced ambiguities when IRNSS is augmented with GPS satellites	138
Figure 6-1 Frequency variation of all IRNSS satellites. 1C, 1G, and 1F are geostationary satellites.....	141
Figure 6-2 IRNSS live signal measurements of 1G, middle plot shows code-minus- carrier observations for 1G along error envelope for Doppler collision.....	143
Figure 6-3 Ionospheric error observed in satellites 1G.....	144
Figure 6-4 Code-minus-carrier measurements of pseudo-IRNSS satellite PRN 7 at RxIB	146
Figure 6-5 Code-minus-carrier measurements of pseudo-IRNSS satellite PRN 7 at three different locations.....	147
Figure 6-6 Convergence of single-differenced ambiguities and RTK solution with base RxIB and rover RxIC.....	148
Figure 6-7 Convergence of single-differenced ambiguities and RTK solution with base RxIA and rover RxIB.....	149
Figure 6-8 TTFFA using three combinations of receivers in hardware-simulation of pseudo-IRNSS	150
Figure 6-9 Doppler collision at RxIA and code-minus-carrier measurements: Middle row obtained using standard correlator, bottom row using narrow correlator	152
Figure 6-10 Commercial receiver code-minus-carrier observations for 1G with Doppler collision error envelope obtained using narrow correlator.....	153
Figure 6-11 Periodic variations in code-minus-carrier measurement of 1G, collected using commercial receiver.....	154

Figure 6-12 Doppler collision observed on IRNSS 1G live signal using standard correlator receiver	155
Figure 6-13 Doppler collision observed on IRNSS 1C live signal using a commercial standard correlator receiver	156
Figure 6-14 Doppler collision observed on IRNSS 1G live signal using a commercial narrow correlator receiver	157
Figure 6-15 Code-minus-carrier of 1C observed using commercial receiver at Hyderabad, 12 August 2017.....	159
Figure 6-16 RTK solution using L5 IRNSS – L1 GPS at Hyderabad, 12 August 2017	160
Figure 6-17 RTK solution using L5 IRNSS – L1 GPS with only two GPS satellites.....	161
Figure 6-18 Convergence of IRNSS ambiguities, top plot shows a standalone IRNSS with satellites 1B to 1G, bottom plot shows IRNSS augmented with two GPS satellites: PRN 8 and 17	162
Figure A-1 Plot of cross-correlation values between BDS PRN1 and PRN2 and its distribution.....	181
Figure C-2 Doppler collision error envelope using code phase from pseudorange and geometric range	186
Figure D-3 Development of the modified software defined receiver	188
Figure D-4 Development of the modified software defined receiver	189
Figure D-5 Development of the six constellations + WAAS RTK software	191

List of Abbreviations

Symbol	Definition
BPSK	Binary Phase-Shift Keying
CDMA	Code Division Multiple Access
CDDIS	Crustal Dynamics Data Information System
DD	Double Differencing
DOP	Dilution of Precision
DLL	Delay Lock Loop
DGPS	Differential GPS
ESA	European Space Agency
FLL	Frequency Lock Loop
GEO	Geosynchronous Equatorial Orbit
GLONASS	GLObalnaya NAVigatsionnaya Sputnikovaya Sistema or GLObal NAVigation Satellite System
GNSS	Global Navigation Satellite System
GPS	Global Positioning System
IGS	International GNSS Service
IGSO	Inclined GeoSynchronous Orbit
ILS	Integer Least-Squares
IRNSS	Indian Regional Navigation Satellite System
ISRO	Indian Space Research Organization
JAXA	Japan Aerospace eXploration Agency
LAMBDA	Least-squares AMBiguity Decorrelation Adjustment
MBOC	Multiplexed Binary Offset Carrier
MEDLL	Multipath Estimation Delay-Lock Loop
MEO	Medium Earth Orbit
MLE	Maximum Likelihood Estimator
NCO	Numerically Controlled Oscillator
NavIC	Navigation with Indian Constellation
PCF	Probability of Correct Fix
PLL	Phase Lock Loop
PPP	Precise Point Positioning
QZSS	Quasi-Zenith Satellite System
RTK	Real Time Kinematic
RS	Restricted Service
SBAS	Satellite-Based Augmentation System
SD	Single Differencing
SOS	Sum-Of-Squared
SPP	Single Point Position
SPS	Standard Positioning Service
TTF	Time To First Fix
TTFFA	Time To First Fix Ambiguities
WAAS	Wide Area Augmentation System

List of Symbols

Symbol	Definition
ρ_r^{isf}	Satellite pseudorange, 'r' indicates the receiver under test, 'i' is the observed satellite, 'f' is the symbol for carrier frequency in the GNSS satellite system 'S'
R	Satellite true geometric range
dR	Satellite orbital error
dt	Receiver clock error
dT	Satellite clock error
c	Speed of light
I	Ionospheric error
T	Tropospheric error
$\mu\rho$	Code multipath error
B	Sum of the inter-channel bias and cross-correlation errors
$\varepsilon\rho$	Receiver code noise
Δ	Indicates the differencing of observations between base 'b' and rover 'r' receivers
ϕ	Carrier phase observation
N	Integer ambiguity of carrier phase observation
λ^f	Wavelength for the given carrier frequency f
d	Observed Doppler frequency
D	True Doppler
δt	Receiver clock drift
δT	Satellite clock drift
δI	Ionospheric error
εd	Doppler noise
∇	Indicates the differencing of observations between two satellites
\hat{a}_i	Float ambiguity
$[]$	Ambiguity round-off
\vee	Integer round-off fixed ambiguity
$a_{R,i}$	
$\sigma_{\hat{a}_i}^2$	Covariance of the float ambiguity
$\sigma_{\hat{a}_i \hat{a}_j}$	Covariance of two float ambiguities
$Q_{\hat{a}}$	Covariance matrix of float ambiguities
\vee	Bootstrapping fixed ambiguity
$a_{B,i}$	
χ^2	ILS positive constant

$Q_{\hat{z}}$	Z-transform of covariance matrix of float ambiguities
\hat{z}	Transformed ambiguity
$\Phi(x)$	Mathematical integral for the computation of PCF
\tilde{Q}_i	Sum-Of-Squared (SOS) residuals
K	Ratio test threshold
\mathbf{B}_{pos}	Base coordinates vector
\mathbf{R}_{pos}	Rover coordinates vector
$\mathbf{B}_{\text{b,r}}$	Baseline vector
\mathbf{r}	Position states vector
\mathbf{v}	Velocity states vector
\mathbf{cdt}	Clock bias terms vector
$\dot{c}dt$	clock drift of the receiver
$\Delta N_{b,r}^{iSf}$	Single-differenced ambiguity between base and rover for given system 'S' and frequency band 'f'
$\nabla \Delta N_{b,r}^{jSf,iSf}$	Double-differenced ambiguity
\mathbf{I}_{NXXN}	Identity matrix for size N
C	Input signal power
τ_i	Signal delay
$d(t)$	Navigation data bit
$c(t)$	PRN code bit
f_c	Doppler frequency
θ_c	Carrier phase
$\hat{\tau}$	Locally code phase given
τ	Code phase difference between incoming and locally generated signals
\hat{f}_c	Local carrier frequency
Δf_c^{kn}	Relative Doppler
$\Delta \theta_c$	Phase difference between the incoming signal and the local carrier
T_d	Correlator integration time
T_c	Code chip time
$R(\tau, f)$	Correlator output
\mathbf{x}_k	State vector at a time t_k
\mathbf{H}_k	Design matrix
\mathbf{v}_k	Measurement noise vector
\mathbf{R}_k	Measurement noise covariance vector
Φ_{k-1}	State transition matrix from epoch t_{k-1} to t_k
\mathbf{w}_{k-1}	Process noise vector

\mathbf{P}_k	State covariance matrix
\mathbf{Q}_{k-1}	Covariance matrix of process noise \mathbf{w}_{k-1}
\mathbf{l}_k	Time-correlated observations
\mathbf{A}_k	Design matrix for time-correlated measurements
\mathbf{u}_k	Time-correlated noise
\mathbf{n}_k	White measurement noise
\mathbf{N}_k	Covariance matrix of \mathbf{n}_k
\mathbf{S}_k	Transition matrix for the time-correlated errors
β^{-1}	Correlation time
$\boldsymbol{\varepsilon}_k$	Vector of white noise driving the correlated measurement error process
\mathbf{M}_k	Covariance matrix of $\boldsymbol{\varepsilon}_k$
\mathbf{Q}_k	Process noise for single-differenced ambiguities
qN	Ambiguity random constant power spectral density
qV	Velocity random walk power spectral density
τ_{error}	C/A code error envelope error
α	Ratio of the cross-correlation peak to primary peak
τ_d	Code delay of the cross-correlation peak
τ_{effi}	Observed code phase for the satellite 'i'
$\Delta\tau_{DC}$	Code phase error due to Doppler collision
τ_d^{DC}	Code delay of the cross-correlation peak due to Doppler collision

Chapter One: **Introduction**

The Indian Regional Navigation Satellite System (IRNSS) is an independent regional navigation system developed by the Indian Space Research Organization (ISRO) to provide reliable position, navigation and timing services over the Indian sub-continental region. The IRNSS has the operational name called “NavIC”, an abbreviation of Navigation with Indian Constellation and means “sailor” or “navigator” in Sanskrit. IRNSS provides two types of services – an open service without encryption called Standard Positioning Service (SPS) and an authorized service with encryption called Restricted Service (RS) (Mruthyunjaya and Ganeshan 2014). The SPS service is an open service for civilian applications and is transmitted on the L5-band (centered at 1176.45 MHz) and S-band (centered at 2492.028 MHz).

1.1 Problem Statement

IRNSS is a unique system that, unlike other satellite systems, does not transmit any signals on the L1 band but rather uses the L5 band. The use of L5 band creates a situation where there would be dedicated users only for IRNSS and would be looking for standalone service. While the SPS is intended for single point positioning, similar to the Global Positioning System (GPS) SPS, following positioning services would also be possible with standalone IRNSS:

1. Differential Positioning (Kee et al. 1991; Enge and Van Dierendonck 1996)
2. Real Time Kinematic (RTK) (Remondi 1985; Hwang 1991; Talbot 1993)

3. Precise Point Positioning (PPP) (Kouba and Héroux 2001; Héroux, P. et al. 2004) would also be possible with standalone IRNSS.

IRNSS consists of three geostationary satellites or Geosynchronous Equatorial Orbit (GEO) satellites and four Inclined GeoSynchronous Orbit (IGSO) satellites in contrast to the GPS constellation, which includes only Medium Earth Orbit (MEO) satellites. MEO and IGSO satellites have large Doppler variations and the presence of any Doppler collision effect would last a few seconds (Balaei and Akos 2011). The presence of GEO satellites brings a set of challenges such as Doppler collision (Lestarquit et al. 2009), observability (O’Keefe et al. 2006) and multipath (Braasch 1996) in an RTK solution. Doppler collision and observability are the challenges unique to GEO satellites whereas multipath is observed depending upon the user environment. Doppler collision and observability have an impact on the estimation of the navigation solution. The impact would not be significant on Single Point Positioning (SPP) where the error would be similar to the other errors not accounted for in SPP including code multipath and atmospheric errors whereas the convergence and the accuracy of an RTK or PPP solution would be affected. From this point onwards, the thesis will focus on RTK since the effect of both the factors is similar on an RTK or PPP solution.

1.1.1 RTK using GEO Satellites

Three significant challenges are encountered in an RTK solution using GEO satellites:

1.1.1.1 Doppler Collision

Doppler collision is a physical phenomenon that occurs in Code Division Multiple Access (CDMA) systems where code measurement errors are observed due to cross-correlation effects when the Doppler frequency between measurements from two different satellites is zero or smaller than the code lock loop bandwidth (Lestarquit et al. 2009; Balaei and Akos 2009). During collision periods, Doppler collision introduces error in the code measurements and can affect ambiguity convergence (Teunissen 2001a). Even if the ambiguities are fixed, they could be wrong which can lead to poor accuracy and reliability (Teunissen et al. 1999). The impact of Doppler collision on ambiguity convergence and correct fix requires further study and the effect should be addressed in the RTK solution using GEO satellites of IRNSS.

1.1.1.2 Poor Observability

The observability condition defines our ability to determine the state variables from the given measurements (Gelb et al. 1974). Given that the GEO satellites are relatively static to users on the Earth; the observations at each epoch are highly time correlated with little additional information in subsequent observations (El-Rabbany 1994). The observability of GEO satellites is factored into an estimation solution using time-correlation of measurements. Time-correlated measurements have an adverse impact on the ability to determine the output states and can affect the ambiguity resolution (Olynik et al. 2002; O'Keefe et al. 2006; Petovello et al. 2009). However, in the case of GEO satellites, limited

research has been undertaken to determine the effect of observability on fixing ambiguities, its correctness, and integrity.

1.1.1.3 Stationary Multipath

For a static user in a multipath environment, the multipath error of GEO satellite in the code and carrier phase measurements will change gradually over several hours because relative motion between the user and the satellite is minimal (Landau et al. 2013; Wang et al. 2015). If the error is significant enough to corrupt the double-differenced measurements, false ambiguities will be obtained, and thus efficient multipath mitigation techniques are required to mitigate multipath in GEO satellites. Extensive research has been undertaken on mitigating multipath and well know code multipath mitigation techniques include Narrow Correlator Technology (Van Dierendonck et al. 1992), Multipath Estimation Delay-Lock Loop (MEDLL) (Townsend and Fenton 1994), Strobe Correlator (Garin and Rousseau 1997), and Vision Correlator (Fenton and Jones 2005). Carrier multipath mitigation techniques include the use of antenna array (Ray et al. 1999). Multipath mitigation is a broad area of research, and this work will cover topics based on the requirements to mitigate Doppler collision.

These issues associated with GEO satellites are not limited to IRNSS as they can be observed in BeiDou and Satellite-Based Augmentation System (SBAS) GEO satellites that provide ranging information. One such segment of SBAS is the Wide Area

Augmentation System (WAAS), which transmits ranging information (Schempp et al. 2008). If an RTK solution incorporates WAAS satellites, the issues with GEO satellites discussed about will come into effect.

1.1.2 Limitations

Despite a decade of research work in the area of assessing GEO satellites for navigation solutions, limited research addresses issues related to GEO satellites in an RTK solution. Boriskin et al. (2007) have shown improvement in the satellite availability of WAAS satellites in an RTK solution. Odolinski et al. (2015) and Odolinski et al. (2014) investigated the use of BeiDou's GEO satellites in an RTK solution but do not discuss the issues unique to GEO satellites.

Doppler collision is an important aspect of GEO satellites that has only been studied using WAAS satellites. Lestarquit and Nouvel (2012) found code measurement errors introduced due to Doppler collision. Using the standard correlator, the error varies about +/- 9 m for a single cross-correlation peak and lasts up to two hours. Considering the magnitude of code error and its duration, use of WAAS satellites in RTK solution during Doppler collision is challenging. Similarly, IRNSS uses Binary Phase-Shift Keying (BPSK) modulated C/A codes (Mruthyunjaya and Ganeshan 2014) and hence the same effects of Doppler collision are possible in GEO satellites of IRNSS. Given the lack of research towards the Doppler collision on GEO satellites in IRNSS, it is important to analyze its

effects and limitations in the use of GEO satellites in an RTK solution because GEO satellites form a significant part of the entire IRNSS system. Extensive study is required to understand whether Doppler collision can limit the use of IRNSS system for an RTK solution and if so, effective mitigations techniques are needed to overcome the effect and realize the RTK solution.

The observability was not a primary concern in the case of MEO satellites because of continuously changing satellite geometry, and thus there was limited focus on observability. However, with the deployment of GEO satellites in IRNSS, there are temporal effects on the observations (Olynik et al. 2002; El-Rabbany and Kleusberg 2003; Miller et al. 2010) and the poor observability of GEO satellites needs to be studied. If the time correlation of observations is severe, it can significantly affect the convergence time of ambiguities. A detailed analysis incorporating the covariance analysis of GEO satellites can resolve this issue. If the IRNSS constellation were to be expanded in the future, any changes required in the space segment to improve observability could be recommended.

1.1.3 Motivations

In the area of multi-constellation RTK, much of the research work has been accomplished in parts. GPS and GLObal NAVigation Satellite System (GLONASS) constellations have been widely used in RTK (Dai 2000; Rossbach 2000; Ong et al. 2009) while RTK using GPS and Galileo have been analyzed in detail (Alves 2001; Tiberius et al. 2002; O'Keefe

et al. 2009). The combination of BeiDou and Quasi-Zenith Satellite System (QZSS) in an RTK solution has been extensively researched (Nadarajah and Teunissen 2014; Odolinski et al. 2015). Limited research is available on the integration of all six constellations (including IRNSS) along with SBAS satellites for an RTK solution. An attempt was made to create a multi-constellation RTK solution consisting of GPS, GLONASS, Galileo, and BeiDou (Bhandari et al. 2013). The next step would be to integrate the RTK solution using standalone IRNSS and later SBAS and QZSS. However, an all constellation RTK solution is possible only if the issues related to GEO satellites are resolved. The primary motivation behind this research is to address the issues of Doppler collision and observability and realize RTK solution using IRNSS and other GEO satellites.

Another emerging field of carrier phase positioning is low-cost high accuracy positioning. Bhaskar et al. (2015) demonstrated the use of carrier phase positioning in handheld devices despite g-sensitivity challenges with oscillators whereas Pesyan et al. (2017) obtained centimeter-accurate GNSS positioning using low-cost antennas. Odolinski and Teunissen (2017) successfully demonstrated the application of RTK using an inexpensive device. All these applications are constrained by the bandwidth of the GNSS signal and would be more effective using larger correlator spacing that can provide less noise in the code and carrier phase measurements. However, due to hardware constraints on front-end bandwidth, if the correlator uses a wide chip spacing, it is important to analyze the

effect of Doppler collision because its impact is severe with large chip spacing. Although the multipath and the antenna bias are significant challenges in handheld devices, once resolved, the focus would shift towards Doppler collision errors.

1.2 Objectives and Contributions

The primary aim of the research is to investigate the RTK solution using GEO satellites. The investigation will help to incorporate observations of GEO satellites from IRNSS and SBAS in an RTK solution that can accept observations from all six constellations and provide an accurate, reliable, and robust RTK solution for static as well as dynamic applications. The research has the following objectives:

1. The first objective is to assess the likely conditions of Doppler collision and its impact on code measurements by observing Doppler across geostationary satellites, finding Doppler crossing windows, deriving possible combinations of code for Doppler collision and then obtaining code measurement errors. The process includes the use of simulated data in controlled conditions as well as live data from WAAS and other GEO satellites.
2. The second objective is to obtain and assess the RTK solution using GEO satellites during Doppler collision through the development of an RTK software that can accept WAAS observations and provide metrics that signify the effect of Doppler collision. Once the impact is observed, possible solutions to mitigate

Doppler collision are discussed. A comparison is provided between improvement in the RTK solution with and without reducing Doppler collision errors.

3. The third objective is to assess observability of GEO satellites in IRNSS. First, the poor observability is presented using WAAS satellites, and then the same method is extended to IRNSS. A complete theoretical analysis is undertaken to determine the limitations of existing IRNSS constellation for RTK. Multiple solutions are developed to address poor observability and are presented using post processing estimation techniques. A new IRNSS constellation is proposed to overcome the shortcomings of the poor observability.
4. Lastly, the Doppler collision mitigation techniques and the possible solutions for improved observability are applied to IRNSS constellation. The improvement in an RTK solution is demonstrated using simulated as well as live data from IRNSS satellites. This assessment will help realize an integrated RTK solution for all constellations.

The objective of assessing Doppler collision is achieved in stages and published as follows. Bhandari (2015) presents preliminary results of the Doppler collision and its effect on the correlation triangle. The Doppler variations of GEO satellites and occurrence of Doppler collision over a geographical region are discussed in a magazine article (Bhandari and O'Keefe 2016). Bhandari and O'Keefe (2017) provide a complete analysis of the first two objectives. The magnitude of Doppler collision error, its duration, and its

behavior are discussed in great detail. An RTK solution using WAAS satellites is obtained and the impact of Doppler collision on convergence time is analyzed. The last two objectives are under development for publication and will discuss the impact of observability on IRNSS and geostationary satellites. It will present the limitations of IRNSS constellation in achieving desired results of convergence time in RTK and possible solutions to overcome the issues.

The major contributions of this thesis are summarized as follows:

1. The thesis provides the description of parameters affecting the Doppler collision due to geostationary satellites in SBAS, BeiDou, and IRNSS. It establishes systematic methods to repeatedly observe Doppler collision using hardware simulation and live data. This is a key contribution for any future research on Doppler collision. The measurement error is observed using geostationary satellites and the nature of Doppler collision is described.
2. Secondly, the thesis established the effect of Doppler collision on an RTK solution, especially when the number of geostationary satellites employed in the RTK solution is significant. The Doppler collision affects the float solution and convergence of ambiguities which in turn lead to larger time to fix ambiguities. Mitigation techniques are proposed at the navigation solution and measurement level.

3. The third major contribution is establishing the effect of poor observability of geostationary satellites in an RTK solution using WAAS satellites and later standalone IRNSS satellites. Several mitigation techniques are obtained and recommendations are provided for the expansion of IRNSS constellation.
4. Lastly, the effect of Doppler collision is observed in IRNSS using hardware simulated data and live data and an RTK solution using IRNSS is demonstrated.

1.3 Thesis Outline

The structure of the thesis is as follows:

Chapter 2 presents background information about the carrier phase positioning and RTK solution using multi-constellation observations. An overview of IRNSS and other constellations using geostationary satellites is provided. Further, a brief explanation of the Doppler collision and its impact on code measurements is presented. The chapter ends with a theoretical discussion about the observability of GEO satellites.

Chapter 3 describes Doppler collision in detail. Initial sections discuss the parameters affecting Doppler collision event and its likely conditions. A series of experiments are conducted to observe Doppler collision using simulated conditions and live data collection. The impact of Doppler collision on code measurements is presented with extensive analysis on code and Doppler measurements.

Chapter 4 describes an RTK solution using GEO satellites during Doppler collision. The RTK solution provides a set of metrics and highlights the impact of Doppler collision. Further, mitigation methods for Doppler collision are discussed. Multiple experiments are conducted to demonstrate the improvement in the RTK solution due to mitigation techniques.

Chapter 5 provides an exhaustive analysis of the observability of GEO satellites and IRNSS constellations. The current IRNSS constellation has limitations on observability, and hence various modifications in IRNSS constellation are presented. A recommendation for the expansion of IRNSS is provided and the improvement in observability is validated using software simulations.

Chapter 6 presents an RTK solution using IRNSS. The subsections provide in-depth analysis of the Doppler collision and observability on the IRNSS constellation. Finally, the reduction in the code measurement errors in IRNSS during Doppler collision conditions is discussed.

Chapter 7 summarizes the conclusions along with suggestions for future work.

Chapter Two: **Multi-Constellation RTK and Geostationary Satellites**

This chapter begins with the theoretical background of RTK positioning with emphasis on ambiguity resolution and convergence time involving all six constellations. Further, an overview of the current state of IRNSS and other GEO segments is presented. A literature review is conducted on an RTK solution using GEO satellites, and limitations of current research are described. Lastly, a theoretical discussion on the Doppler collision and the observability is provided.

2.1 RTK Positioning

In satellite navigation, the distance measured between the user and a satellite is called pseudorange (Parkinson et al. 1996a). The term “range” is prefixed with “pseudo” because observation includes user clock bias. A receiver measures pseudorange given as

$$\rho_r^{iSf} = R_r^{iSf} + dR^{iS} + c(dt_r - dT^{iS}) + I^{iSf} + T^{iS} + \mu\rho_r^{iSf} + B_r^{iSf} + \varepsilon\rho_r^{iSf} \quad 2.1$$

where ρ is the pseudorange (m), ‘ r ’ indicates the receiver under test, ‘ i ’ is the observed satellite, ‘ f ’ is the symbol for carrier frequency in the GNSS satellite system ‘ S ’, R is the true geometric range (m), dR is the satellite orbital error (m), dt and dT are the receiver and satellite clock errors respectively (s), c is the speed of light (m/s), I is the ionospheric error (m), T is the tropospheric error (m), $\mu\rho$ is the code multipath error (m), B is the sum of inter-channel hardware bias, inter-frequency bias, and cross-correlation errors (m), and $\varepsilon\rho$ is the receiver code noise (m).

The code measurements consist of errors that can be divided into three categories. Firstly, the distance-specific errors consist of satellite orbital error, satellite clock error and user clock error (Lachapelle 1991). Secondly, spatial errors include ionospheric and tropospheric delays, multipath, interference, and jamming (interference and jamming effects are beyond the scope of this research). Lastly, receiver-specific errors consist of inter-channel bias, cross-correlation error and receiver noise. Even though receiver noise is independent of the satellite system, it is dependent on the receiver make and the signal tracking strategies used in the receiver. If only code measurements are used to compute a navigation solution, the positioning method is called “Single Point Solution” (SPS) (Parkinson et al. 1996a). The user has to employ various techniques to get rid of all the measurement errors including atmospheric errors and multipath, which form a significant portion of the code error.

Differencing code observations from a reference station to the user receiver minimizes atmospheric errors along with satellites orbital error and satellite clock error. The reference station and user receiver are also called “base” and “rover” respectively. The distance between base and rover is named “baseline” and typically varies from a few metres to hundreds of kilometres (Kee et al. 1991; Parkinson et al. 1996b). This technique is called Differential GPS (DGPS), and marine navigation uses it widely. The differencing between base and rover observations can be modelled as

$$\Delta\rho_{b,r}^{iSf} = \Delta R_{b,r}^{iSf} + \Delta dR^{iS} + c(\Delta dt_{b,r}) + \Delta I^{iSf} + \Delta T^{iS} + \Delta\mu\rho_{b,r}^{iSf} + \Delta B_{b,r}^{iSf} + \Delta\varepsilon\rho_{b,r}^{iSf} \quad 2.2$$

where Δ stands for the differencing observations between base 'b' and rover 'r' receivers.

Differencing observations between a base and the rover statistically add receiver noise since base and rover observations are independent. The multipath is not eliminated because the multipath environment is different for given base and rover. A minimum multipath environment for base and rover can reduce this effect.

GNSS receivers may collect the second set of observations called carrier phase measurements (Remondi 1985; Parkinson et al. 1996a). A carrier phase measurement is the number of carrier cycles present between satellite phase center and receiver phase center. Carrier phase measurements are generated by integrating the count of Numerically Controlled Oscillator (NCO), which represent the Doppler readings (O'Driscoll 2010). Since the exact number of cycles is not known to the receiver, the NCO is initialized with a pre-defined value and integrated over the time. The initialization leads to a situation where carrier phase measurements are ambiguous in nature. The carrier phase measurement is represented as

$$\phi_r^{iSf} = R_r^{iSf} + dR^{iS} + c(dt_r - dT^{iS}) + \lambda^f N - I^{iSf} + T^{iS} + \mu\phi_r^{iSf} + \varepsilon\phi_r^{iSf} \quad 2.3$$

where ϕ is the carrier phase observation, N is the integer ambiguity, and λ^f is the wavelength for the given carrier frequency f .

The carrier phase measurement noise is a tiny fraction of carrier wavelength and very small in comparison to code measurement noise (Misra and Enge 2006). However, due to ambiguous nature of carrier phase measurement, SPS cannot use carrier phase measurements directly in a solution. Fortunately, code and carrier phase measurements can be combined to form carrier smoothed code measurements and offer a modest improvement in solution accuracy (Misra and Enge 2006).

The third set of observations in GNSS receivers consists of Doppler measurements. A Doppler measurement is the satellite Doppler frequency observed by the user. It is affected by satellite motion, user dynamics and includes the satellite and user clock drifts and can be denoted as

$$d_r^{iSf} = D_r^{iSf} + f(\delta t_r - \delta T^{iS}) - \delta I^{iSf} / \lambda^f + \varepsilon d_r^{iSf} \quad 2.4$$

where d is the observed Doppler (Hz), D is the true Doppler (Hz), δt and δT are the receiver and satellite clock drifts respectively (seconds per second), δI is the drift in ionospheric error (m/s), and εd is the Doppler noise (Hz).

2.1.1 Measurement Differencing and Float Solution

Differencing code and carrier measurements of a base with the rover observations reduces atmospheric errors. With this operation, satellite errors such as orbital error and satellite clock error, and spatial errors such as ionospheric errors and tropospheric errors, are reduced or eliminated. This step is called Single Differencing (SD) (Misra and Enge 2006) given as

$$\Delta\phi_{b,r}^{iSf} = \Delta R_{b,r}^{iSf} + \Delta dR^{iS} + c(\Delta dt_{b,r}) + \lambda^f \Delta N - \Delta I^{iSf} + \Delta T^{iS} + \Delta\mu\phi_{b,r}^{iSf} + \Delta\varepsilon\phi_{b,r}^{iSf} \quad 2.5$$

The underlying assumption in the between-receiver differencing is that the errors mentioned above are same in rover and base receivers. If the errors vary, then effective methods are incorporated to reduce or eliminate the errors. For example, the tropospheric error over an extended baseline varies a few metres and is removed using tropospheric modelling (Hopfield 1969; Saastamoinen 1972). The resultant solution is called “float solution” (Talbot 1993), which consists of position states and single-differenced ambiguities. If the ambiguous factor of differenced carrier phase measurements is determined, then the ambiguities are called fixed ambiguities. The solution obtained using fixed ambiguities is a precise solution with an accuracy of a few centimetres.

By performing between-receiver differencing, the receiver clock is not eliminated and is present as single-differenced clock bias. If the clock bias is stable, one can resolve ambiguities; however, in general, the oscillators in base and rover have clock drift, and

this puts limitations on fixing ambiguities. Fortunately, single-differenced measurements reduce errors of large magnitude (ionospheric and tropospheric errors), and it is possible to get an improved solution called “single-differenced float solution” without fixing ambiguities.

After SD, the second level of differencing, called Double Differencing (DD), is performed. Here the single-differenced measurements between two satellites are subtracted (Hwang 1991; Misra and Enge 2006). DD removes single-differenced clock bias and provides an option to fix ambiguities. The measurements consist of double-differenced geometric range and double-differenced ambiguities plus the noise terms shown as

$$\nabla\Delta\phi_{b,r}^{iSf,jSf} = \underbrace{\nabla\Delta R_{b,r}^{iSf,jSf}}_{DD\ True\ Range} + \underbrace{\lambda^f \nabla\Delta N}_{DD\ Ambiguities} + \nabla\Delta\mu\phi_{b,r}^{iSf,jSf} + \nabla\Delta\varepsilon\phi_{b,r}^{iSf,jSf} \quad 2.6$$

DD cannot eliminate the statistically independent random error, which is receiver noise. In fact, the receiver noise gets added up, and the measurements are more prone to receiver noise of base or rover. Also, the DD cannot eliminate multipath, receiver cross-correlation errors and inter-channel bias. If any or all of the receiver noise, multipath, receiver cross-correlation error and inter-channel bias are of large magnitude, mitigation methods are required before performing using the base and rover observations.

Between-receiver differencing and between-satellite differencing can be completed in any sequence. However, the advantage of performing between-receiver differencing at first step is the availability of float solution using single-differenced measurements without the need of the fixing the ambiguities. If between-satellite differencing is carried out at the first step, the majority of large errors are present, and float solution offers no significant improvement in comparison to an SPS.

2.1.2 Ambiguity Resolution Models

The important step in an RTK solution is the ambiguity resolution, which is computationally intensive and introduces an integrity risk since the accuracy of a fixed solution depends on correct ambiguity resolution. This process may or may not include the simultaneous estimation of the position solution using geometry-based model or the satellite-to-receiver range using geometry-free model (Odijk 2002).

2.1.2.1 Geometry-Based Model

The geometry-based model linearizes code and phase observations. The linearization step requires true base position, and the estimation process includes the relative position of rover, which is known as “baseline components” in output states. The geometry-based model has better redundancy because the baseline components are coupled to pseudorange measurements. The major disadvantage of this model is the linearization step. In geometry-based model, the ambiguity resolution can also be achieved using only

carrier phase measurements. However, the estimation step requires carrier phase measurements at two epochs (Odijk 2008).

2.1.2.2 Geometry-Free Model

In the geometry-free model, the primary goal is to fix ambiguities. The state estimates include receiver-satellites ranges, and no baseline components are estimated. Since no baseline components are present in the estimation process, this model adds one more step of finding the user position after ambiguity resolution. In the geometry-free Model, code measurements are required in the estimation otherwise the design matrix rank will be deficient.

2.1.3 Ambiguity Resolution Methods

Irrespective of the model used in the ambiguity resolution, the mathematics for the resolution process is the same. There are many ambiguity resolution methods as listed below:

1. Least-Squares Ambiguity Search Technique – LSAST (Hatch 1991)
2. Fast Ambiguity Resolution Approach – FARA (Frei and Beutler 1990)
3. Modified Cholesky Decomposition (Euler and Landau 1992)
4. Least-squares Ambiguity Decorrelation Adjustment – LAMBDA (Teunissen 1995)
5. Fast Ambiguity Search Filter – FASF (Chen and Lachapelle 1995)
6. Three Carrier Ambiguity Resolution – TCAR (Harris 1997)

7. Integrated TCAR by (Vollath et al. 1999)
8. Optimal Method for Estimating GPS Ambiguities – OMEGA (Kim and Langley 1999)
9. Cascaded Integer Resolution – CIR (Jung et al. 2000)

The LAMBDA is widely accepted method because it is computationally efficient and hence the discussion here is limited from the evolution of the simplest method to LAMBDA.

2.1.3.1 Brute Force and Integer Round-off

This method rounds the float ambiguities to the nearest integer ambiguity. The ambiguity search space is defined based on the variance of ambiguity states, and the correct integer ambiguities are obtained by examining the search space on each ambiguity. The major disadvantage of this method is the large computational load and wider search space that makes ambiguity resolution practically impossible on the fly. The mathematical representation of Integer Round-off is (Odijk 2002)

$$\underset{\vee}{\mathbf{a}}_R = \begin{bmatrix} \underset{\vee}{a}_{R,1} \\ \underset{\vee}{a}_{R,2} \\ \vdots \\ \underset{\vee}{a}_{R,q} \end{bmatrix} = \begin{bmatrix} \hat{[a_1]} \\ \hat{[a_2]} \\ \vdots \\ \hat{[a_q]} \end{bmatrix} \quad 2.7$$

where the float ambiguity vector and its corresponding correlation matrix respectively are

$$\hat{a}_R = \begin{bmatrix} \hat{[a_1]} \\ \hat{[a_2]} \\ \vdots \\ \hat{[a_q]} \end{bmatrix}; Q_a = \begin{bmatrix} \sigma_{a_1}^2 & \sigma_{a_1 a_2} & \cdots & \sigma_{a_1 a_q} \\ \sigma_{a_2 a_1} & \sigma_{a_2}^2 & \cdots & \sigma_{a_2 a_q} \\ \vdots & \vdots & \ddots & \vdots \\ \sigma_{a_q a_1} & \sigma_{a_q a_2} & \cdots & \sigma_{a_q}^2 \end{bmatrix} \quad 2.8$$

where $\hat{[a]}$ is the nearest integer rounding operation, and $[a_1 \ a_2 \ \dots \ a_q]$ is the vector of single-differenced or double-differenced float ambiguities.

2.1.3.2 Bootstrapping

The double-differenced ambiguities are highly correlated, and if the correlation between the double-differenced ambiguities is taken into consideration, the search space can be reduced moderately. This method is defined as Bootstrapping and represented as

$$\check{a}_R = \begin{bmatrix} \check{a}_{B,1} \\ \check{a}_{B,2} \\ \vdots \\ \check{a}_{B,q} \end{bmatrix} = \begin{bmatrix} \hat{[a_1]} \\ [a_2 - \sigma_{a_2 a_1} \sigma_{a_1}^{-2} (\hat{a_1} - \check{a}_{B,1})] \\ \vdots \\ [a_q - \sum_{i=1}^{q-1} \sigma_{a_q a_{i|I}} \sigma_{a_{i|I}}^{-2} (\hat{a_{i|I}} - \check{a}_{B,i})] \end{bmatrix} \quad 2.9$$

2.1.3.3 Integer Least-Squares

Integer Least-Squares (ILS) method is based on the Maximum Likelihood Estimator (MLE). The estimation of ambiguity states provides minimal residuals between float and fixed ambiguities. The minimization criteria is

$$\min_{a \in Z^q} (\hat{a} - a)^T Q_a^{-1} (\hat{a} - a) \quad 2.10$$

The ambiguity search space is a hyper-ellipsoid centered at \hat{a} of which the shape is governed by Q_a and the search space bound is given by

$$(\hat{a} - a)^T Q_a^{-1} (\hat{a} - a) \leq \chi^2 \quad 2.11$$

where the factor χ^2 is a positive constant and chosen sufficiently large, such that search space still contains the ILS ambiguities. The upper limit for χ^2 is obtained using the integer bootstrapped solution as follows

$$\chi^2 = (\hat{a} - \check{a}_B)^T Q_a^{-1} (\hat{a} - \check{a}_B) \quad 2.12$$

Using this ILS space search concept (Teunissen 1995), the integer ambiguities are bounded as

$$\begin{aligned}
(\hat{a}_1 - a_1)^2 &\leq \sigma_{a_1}^2 \chi^2 \\
(\hat{a}_{2|1} - a_1) &\leq \sigma_{a_{2|1}}^2 [\chi^2 - (\hat{a}_1 - a_1)^2 / \sigma_{a_1}^2] \\
&\vdots \\
(\hat{a}_{q|Q} - a_q)^2 &\leq \sigma_{a_{q|Q}}^2 [\chi^2 - \sum_{i=1}^{q-1} (\hat{a}_{i|I} - a_i)^2 / \sigma_{a_{i|I}}^2]
\end{aligned} \tag{2.13}$$

ILS has been proven to be the optimal integer ambiguity resolution method in terms of theoretical success rate when compared with other methods including Integer Ambiguity Rounding and Bootstrapping (Teunissen 1998, 1999). Teunissen et al. (1999) have also discussed the reliability of ambiguity resolution based on the integer bootstrapping success rate and have described the effect of optimality of ILS using an approximate ambiguity Variance-Covariance (VC) matrix (Teunissen 2000).

2.1.3.4 LAMBDA

In the case of double-differenced ambiguities, the correlation matrix is non-diagonal that leads to large search space and computationally inefficient ILS. The search space can be reduced by decorrelating the original float ambiguities, and the correlation matrix becomes a diagonal matrix. The process is called Z-transformation (Teunissen 1993, 1995) and is given as

$$\hat{z} = Z^T \hat{a}; \quad Q_{\hat{z}} = Z^T Q_{\hat{a}} Z \tag{2.14}$$

where Z is the transformation matrix consisting of only integers elements. Once the ambiguities are transformed, the search operation is performed using the ILS criterion:

$$\min_{z \in Z^q} (\hat{z} - z)^T Q_z^{-1} (\hat{z} - z) \quad 2.15$$

The solution of this minimization problem, denoted by \check{z} , can be back-transformed to the original ambiguity domain using inverse Z -transformation given as

$$a = Z^{-T} \check{z} \quad 2.16$$

The entire process is called the LAMBDA method and is a well-proven method for ambiguity resolution method (de Jonge and Tiberius 1996). The statistical aspects of carrier phase ambiguity resolution using LAMBDA have been extensively studied (Teunissen 2001b; Verhagen 2005a).

2.1.4 Validation of Ambiguity Resolution

The performance of ambiguity resolution is validated using one or more of the following metrics:

2.1.4.1 Probability of Correct Fix

The Probability of Correct Fix (PCF), also known as Probability of Success, is a theoretical criterion defined to quantify the correctness of the ambiguity fix (Teunissen 1998;

Verhagen 2005a). If PCF is close to one, the ambiguity is deemed as fixed correctly. There is another term called Probability of Incorrect Fix (PIF), which is equal to one minus the PCF. The calculation of PCF is theoretically and computationally difficult. Hence PCF is usually approximated by a lower bound of the probability of correct ILS estimation (Teunissen 1999). The PCF can be computed as

$$PCF = \prod_{i=1}^n \left(2\Phi\left(\frac{1}{2\sigma_{\hat{a}_{i|I}}}\right) - 1 \right) \quad 2.17$$

where

$$\Phi(x) = \int_{-\infty}^x \frac{1}{\sqrt{2\pi}} \exp\left(-\frac{1}{2}y^2\right) dy \quad 2.18$$

n is the number ambiguities, and $\sigma_{\hat{a}_{i|I}}$ is the covariance of $\hat{a}_{i|I}$, which stands for the i th Least-Squares ambiguity obtained through a conditioning on the previous $I = \{1, \dots, (i-1)\}$ sequentially rounded ambiguities.

2.1.4.2 Time To First Fix Ambiguities

Time To First Fix Ambiguities (TTFFA) is calculated by averaging the time required to fix all ambiguities in each attempt throughout a given dataset. The less the TTFFA, the shorter time in which ambiguities are resolved. If fixed ambiguities are obtained in one epoch, then it is called instantaneous ambiguity resolution. The term TTFFA is not uniformly defined in the literature on ambiguity resolution and its variants include Mean Time To First Fix ambiguities (MTFF) (Zhang et al. 2003), Mean Time To First Fix

Ambiguities (MTTFFA) (Cao 2009), and Time To Fix Ambiguities (TTFA) (Odijk et al. 2010). This thesis uses the term TTFFA.

2.1.4.3 Ratio Test

In ILS, the “most likely” integer estimate is determined and validated using a Discrimination Test (Verhagen 2005b) or also called the F-test (Ong 2010). The standard form of ratio test is

$$\frac{\check{\Omega}_2}{\check{\Omega}_1} > K \quad 2.19$$

where $\check{\Omega}_1$ is the Sum-Of-Squared (SOS) residuals computed from the most likely integer estimates, $\check{\Omega}_2$ is the SOS residuals computed from the second most likely integer estimates, and K is the ratio threshold. The likelihood of the correctly fixed solution is always larger than any other integer estimate, provided there are no systematic errors in phase measurements (zero bias in residual errors). In case the likelihood of fixed solution is not sufficiently larger than the likelihood of the second solution, the ratio test cannot discriminate two solutions. The test is valid under the assumption that measurements have normally distributed errors and when passed through an ILS estimator results in normally distributed parameter errors.

2.1.5 Fixed Solution

After ambiguity resolution, the final step in an RTK solution is to obtain a fixed solution. The resolved ambiguities, either single-differenced or double-differenced ambiguities, are put back into corresponding phase observations, and the baseline vector between two receivers is obtained. For example, if the ambiguity resolution method provides double-differenced ambiguities, the state estimation process can use phase observation model in equation-2.6 and compute baseline components. Finally, the baseline vector is added to the base position, and the rover position is computed as

$$\mathbf{R}_{\text{pos}} = \mathbf{B}_{\text{pos}} + \mathbf{B}_{\text{b,r}} \quad 2.20$$

where \mathbf{B}_{pos} and \mathbf{R}_{pos} are the base and rover coordinates respectively, and $\mathbf{B}_{\text{b,r}}$ is the baseline vector. The ambiguities of a satellite will remain fixed and not affect fixed solution as long as no cycle slip is observed in the carrier phase measurement (Kim and Langley 2001). Once a cycle slip is observed, the entire process of ambiguity resolution and validation is repeated.

In summary, an RTK solution involves four steps: float solution, ambiguity resolution, ambiguity validation and compute fixed solution. Figure 2-1 shows a simple flowchart of an RTK solution. An RTK solution can employ one of the ambiguity resolution methods discussed above.

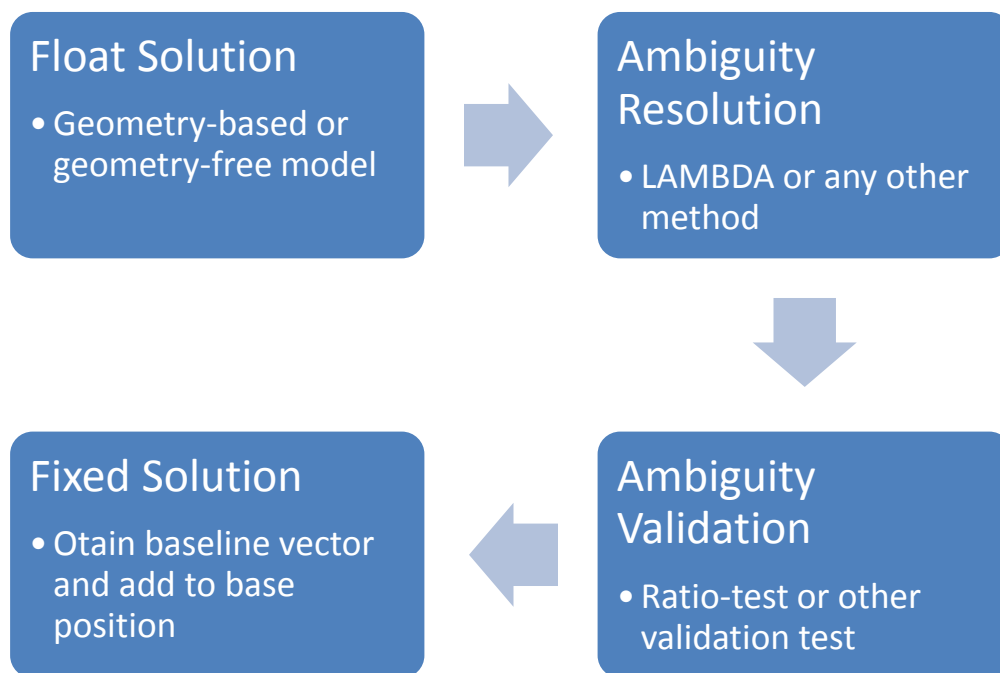


Figure 2-1 Flowchart of an RTK solution

2.2 Multi-Constellation RTK

GPS and GLONASS constellations have been extensively studied and widely used in an RTK (Dai 2000; Rossbach 2000; Ong et al. 2009). One of the biggest challenges in using GLONASS signals in an RTK solution is that the system uses Frequency Division Multiple Access (FDMA) and thus each satellite signal has a different carrier frequency (Takac 2009; Reussner and Wanninger 2011). The difference in carrier frequency between satellites leads to inter-channel bias that the receiver design must address. Furthermore, ambiguity resolution is complicated by the fact that the double-differenced ambiguities

formed using multiple frequencies cannot be easily converted back to units of distance without first resolving or assuming a single-differenced ambiguity on the base satellite (Leick et al. 1998; Habrich et al. 1999). RTK using GPS and GLONASS is assessed in various operational conditions (Ong et al. 2009) and obstructed environments (Kleiner 2010). Both these implementations use the LAMBDA method to resolve ambiguities and compute the RTK solution using GPS and GLONASS.

Galileo is a newly deployed GNSS, which is a quadruple frequency constellation, designed and maintained by the European Union (EU) and the European Space Agency (ESA). It consists of 24 operational satellites and up to 6 active spares, positioned in three MEO planes (Galileo ICD 2016). As of June 2017, four (In-Orbit Validation) IOV and 14 Full Operational Capabilities (FOC) satellites have been launched with 10 FOC satellites in operations (Montenbruck et al. 2014, 2017). RTK using Galileo is possible using the same approach as GPS. Tiberius et al. (2002) provide a theoretical analysis, which shows that GPS and Galileo can provide 0.99999999 of confidence in ambiguity resolution for RTK solutions over short baselines when dual frequency observations are available from both systems. Verhagen et al. (2010) have demonstrated successful instantaneous single frequency resolution using GPS and Galileo, albeit only on short baselines and only in simulation. Recently, more results using E1 live signals has been presented (Nadarajah and Teunissen 2014; Teunissen et al. 2014).

BeiDou is a triple frequency GNSS system being developed by China (BeiDou ICD 2016). BeiDou-2 is already deployed and consists of 13 satellites in operation (Montenbruck et al. 2014, 2017) among which five satellites are GEOs, six satellites are IGSOs and remaining MEO satellites. In 2015, China started building of the 3rd generation BeiDou (BeiDou-3), which will offer fully global navigation service by 2020. Table 2-1 provides the current status of the BeiDou-2 constellation.

Table 2-1 BeiDou-2 constellation and its current status

Carrier	Frequency	Operational Satellites
B1/B1-2	1561.098 MHz / 1589.742 MHz	GEOs – C01, C02, C03, C04, C05 IGSOs – C06, C07, C08, C09, C10, C13
B2	1207.14 MHz	MEOs – C11, C12, C14

Single-epoch ambiguity resolution is explored using GPS and BeiDou over the Asia Pacific region (Odolinski et al. 2013; Teunissen et al. 2014). Shi et al. (2013) have shown that an RTK solution is possible using GSO and IGSO satellites in Asia whereas Dou and O’Keefe (2013) have presented a float RTK solution using GPS with augmentation from two BeiDou MEO satellites in North America. Fairhurst et al. (2013) and Odolinski et al. (2015) have shown an integrated solution using GPS and BeiDou; however, the analysis

with live data does not explain issues such as observability and multipath related to use of GEO satellites in the RTK solution.

Bhandari et al. (2013) took a step forward and realized a combined four constellation RTK solution. First, the observations from base and rover are differenced (between-receiver SD). If it were a single constellation, one of the satellites could act as a base satellite and DD could be performed easily. However, in the case of DD using four constellations, a satellite from each constellation is selected as a base satellite. An example for DD operator matrix in multi-constellation RTK using four GPS satellites and three satellites each from GLONASS, Galileo, and BeiDou is shown in equation 2.21.

$$\underbrace{\begin{bmatrix} \mathbf{r} \\ \mathbf{v} \\ \nabla \Delta N_{b,r}^{2GL1,1GL1} \\ \nabla \Delta N_{b,r}^{3GL1,1GL1} \\ \nabla \Delta N_{b,r}^{4GL1,1GL1} \\ \nabla \Delta N_{b,r}^{2KL1,1KL1} \\ \nabla \Delta N_{b,r}^{3KL1,1KL1} \\ \nabla \Delta N_{b,r}^{2EL1,1EL1} \\ \nabla \Delta N_{b,r}^{3EL1,1EL1} \\ \nabla \Delta N_{b,r}^{2BL1,1BL1} \\ \nabla \Delta N_{b,r}^{3BL1,1BL1} \end{bmatrix}}_{x^{DD} \text{ State Vector}} = \underbrace{\begin{bmatrix} \mathbf{I}_{3 \times 3} & 0 & 0 & 0 & 0 & 0 & 0 & 0 & 0 & 0 & 0 & 0 & 0 & 0 & 0 & 0 \\ 0 & \mathbf{I}_{3 \times 3} & 0 & 0 & 0 & 0 & 0 & 0 & 0 & 0 & 0 & 0 & 0 & 0 & 0 & 0 \\ 0 & 0 & 0 & 0 & -1 & 1 & 0 & 0 & 0 & 0 & 0 & 0 & 0 & 0 & 0 & 0 \\ 0 & 0 & 0 & 0 & -1 & 0 & 1 & 0 & 0 & 0 & 0 & 0 & 0 & 0 & 0 & 0 \\ 0 & 0 & 0 & 0 & -1 & 0 & 0 & 1 & 0 & 0 & 0 & 0 & 0 & 0 & 0 & 0 \\ 0 & 0 & 0 & 0 & 0 & 0 & 0 & 0 & -1 & 1 & 0 & 0 & 0 & 0 & 0 & 0 \\ 0 & 0 & 0 & 0 & 0 & 0 & 0 & 0 & -1 & 0 & 1 & 0 & 0 & 0 & 0 & 0 \\ 0 & 0 & 0 & 0 & 0 & 0 & 0 & 0 & 0 & 0 & -1 & 0 & 1 & 0 & 0 & 0 \\ 0 & 0 & 0 & 0 & 0 & 0 & 0 & 0 & 0 & 0 & 0 & 0 & 0 & -1 & 1 & 0 \\ 0 & 0 & 0 & 0 & 0 & 0 & 0 & 0 & 0 & 0 & 0 & 0 & 0 & -1 & 0 & 1 \end{bmatrix}}_{DD \text{ Transformation matrix}} \underbrace{\begin{bmatrix} \mathbf{r} \\ \mathbf{v} \\ \mathbf{cdt} \\ \dot{c}dt \\ \Delta N_{b,r}^{1GL1} \\ \Delta N_{b,r}^{2GL1} \\ \Delta N_{b,r}^{3GL1} \\ \Delta N_{b,r}^{4GL1} \\ \Delta N_{b,r}^{1KL1} \\ \Delta N_{b,r}^{2KL1} \\ \Delta N_{b,r}^{3KL1} \\ \Delta N_{b,r}^{1EL1} \\ \Delta N_{b,r}^{2EL1} \\ \Delta N_{b,r}^{3EL1} \\ \Delta N_{b,r}^{1BL1} \\ \Delta N_{b,r}^{2BL1} \\ \Delta N_{b,r}^{3BL1} \end{bmatrix}}_{x^{SD} \text{ State Vector}}$$

2.21

where \mathbf{r} is the vector of position states, \mathbf{v} is the vector of velocity states, \mathbf{cdt} is the vector of clock bias terms that contains the sum of receiver clock bias and inter-system clock biases corresponding to each constellation, and $\dot{c}dt$ is the clock drift of the receiver. G, K, E, and B denotes GPS, GLONASS, Galileo, and BeiDou systems respectively, L1 indicates frequency in use.

The emergence of newly developed navigation satellites systems is not limited to global systems, and two more regional systems are being developed. The first is the Quasi-Zenith Satellite System (QZSS), which is under development by the Japan Aerospace Exploration Agency (JAXA) (QZSS ICD 2016). QZSS is a quadruple frequency system. Currently, it has one operational satellite (Montenbruck et al. 2014, 2017) whereas the entire constellation will consists of three IGSO satellites and will provide coverage over Japan, Philippines, Indonesia and Australia. Nadarajah and Teunissen (2014) and Odolinski et al. (2015) have shown that RTK positioning is possible using QZSS observation.

The second regional system is IRNSS which is an important system for a multi-constellation RTK solution.

2.2.1 IRNSS

The IRNSS, operationally named as NavIC, has seven satellites with PRN ranging from 1A to 1G. All seven satellites provide continuous coverage over the Indian sub-continent

(Majithiya et al. 2011; Thaelert et al. 2014; Mruthyunjaya and Ganeshan 2014). Figure 2-2 shows the ground tracks of IRNSS satellites.

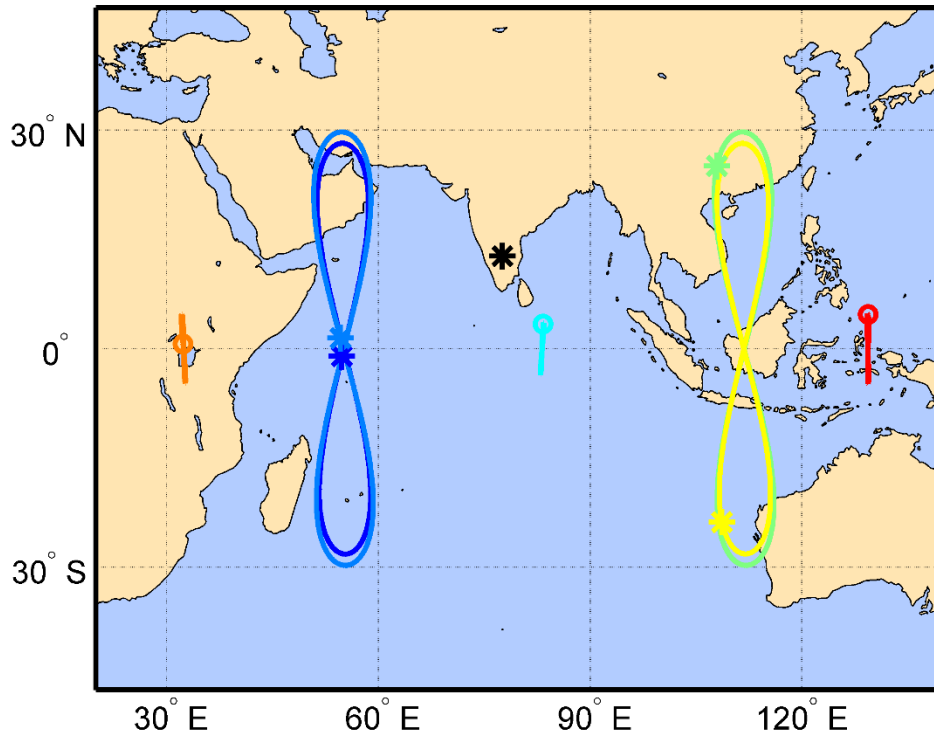


Figure 2-2 Ground track of IRNSS satellites over the IRNSS service area

Among seven satellites, three are GEOs and four are IGSOs. The three GEOs: 1C, 1F, and 1G are located at 83°E , 32.5°E , and 131.5°E respectively. The IGSOs have their longitude crossings at 55°E and 111.75°E with two satellites in each plane.

Table 2-2 describes the signal structure of IRNSS. IRNSS transmits on two bands: L5 and S bands with no transmission on L1 band. IRNSS offers two services: SPS and RS. SPS is a BPSK (1) modulated signal and uses C/A Gold codes with chip length of 1023.

The navigation data rate is 50 symbols per seconds with $\frac{1}{2}$ rate of FEC encoder. The RS signal consists of data and pilot channels with BOC (5, 2) signal modulation. Recent reports state that the onboard clock of IRNSS-1A has failed (GPS World Staff 2017).

Table 2-2 IRNSS constellation and its current status

Carrier	Carrier Frequency	Bandwidth	Service Type	Modulation
L5	1191.795 MHz	24 MHz (1164.45 - 1188.45 MHz)	SPS	BPSK (1), data rate 50 Hz
			RS	BOC (5, 2), data rate 50 Hz
S	2492.08 MHz	16.5 MHz (2483.50 - 2500.00 MHz)	SPS	BPSK (1), data rate 50 Hz
			RS	BOC (5, 2), data rate 50 Hz

Much of the research work related to IRNSS is accomplished on its onboard atomic clock (Babu et al. 2012; Thoelert et al. 2014) and improving its Time To First Fix (TTFF) (Rao 2013). Recent works have assessed IRNSS L5 signal (Nadarajah et al. 2016) and obtained SPS using IRNSS (Zaminpardaz et al. 2016a, b) with a few results on RTK using IRNSS (Li et al. 2017). A significant scope is available in developing a robust and reliable RTK solution with IRNSS.

2.2.2 SBAS

Another important aspect of building a multi-constellation RTK solution is to incorporate GEO satellites from the SBAS augmentation systems. Boriskin et al. (2007) demonstrated use of SBAS satellites in an RTK solution with benefits of an increased number of observations at a minimal cost of generating carrier phase measurements for SBAS satellites. As of June 2017, WAAS PRN 135 and PRN 138 provide ranging information (Montenbruck et al. 2014, 2017). Limited research is undertaken on issues unique to GEO satellites. If more SBAS satellites were to transmit ranging information in future, use of SBAS satellites in RTK solutions would be imminent. Table 2-3 shows the availability of SBAS satellites.

Table 2-3 SBAS satellites availability

SBAS System	Region	SV PRN	Signals	Ranging Information Available
Wide Area Augmentation System (WAAS)	USA and parts of Canada	133, 135, 138	L1/L5	Yes
European Geostationary Navigation Overlay Service (EGNOS)	European Continent	120, 123, 136	L1/L5, PRN 120 only L1	No
GPS-Aided Geo-Augmented Navigation (GAGAN)	Indian Sub-continent	127, 128	L1/L5	No
Multi-functional Satellite Augmentation System (MSAS)	Japanese region	129, 137	L1	No
System for Differential Corrections and Monitoring (SDCM)	Russian region	125, 140	L1	No

2.3 RTK with GEO Satellites

As discussed above, GEOs are a significant segment of IRNSS as well as BeiDou and are the only satellites in SBAS. An RTK solution with GEOs is possible if issues unique to geostationary satellites: Doppler collision and observability, are addressed. The following section provides a complete theoretical background of Doppler collision and observability of a GNSS satellite.

2.3.1 Doppler Collision

Consider a simple correlation structure in a GNSS receiver (Kaplan and Hegarty 2005) as given in Figure 2-3.

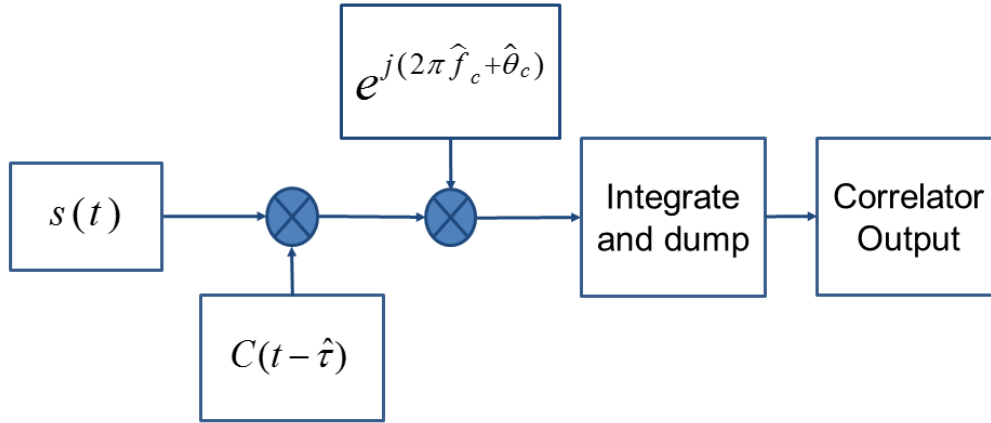


Figure 2-3 Correlation structure in a GNSS receiver

A simplified model of the received GNSS signal, ignoring the noise term is given as (Nouvel et al. 2007; Balaei and Akos 2011)

$$s(t) = \sqrt{2C}d(t - \tau_i)c(t - \tau_i)e^{j(2\pi f_c t + \theta_c)} \quad 2.22$$

where C is the input signal power, τ_i is the signal delay, $d(t)$ is the data modulation, $c(t)$ is the PRN code, f_c is the Doppler frequency, and θ_c is the carrier phase. The incoming signal is multiplied by locally generated code $c(t - \hat{\tau})$, where $\hat{\tau}$ is the code phase given as $\hat{\tau} = \tau_i + \tau$, and τ is the code phase difference between incoming and locally generated signals. Then it is multiplied with locally generated carrier resulting as

$$\hat{s}(t) = \sqrt{2C}d(t - \tau_i)c(t - \tau_i)c(t - \hat{\tau})e^{j(2\pi\Delta f_c t + \Delta\theta_c)} \quad 2.23$$

where $\Delta f_c = f_c - \hat{f}_c$, \hat{f}_c is the local carrier frequency, and $\Delta\theta_c$ is the phase difference between the incoming signal and the local carrier. Consider the Fourier series expansion of $c(t)$, where T_c is the period of the code length.

$$c(t) = \sum_{i=-\infty}^{\infty} A_i e^{-j\left(2\pi\frac{i}{T_c}t\right)} \quad 2.24$$

The expansion of code terms is

$$c(t - \tau_i)c(t - \hat{\tau}) = \sum_{l=-\infty}^{\infty} \sum_{i=-\infty}^{\infty} A_i A_l e^{j\left(2\pi\left[\frac{(i+l)}{T_c} + \Delta f_c\right]t + \Delta\theta_c\right)} e^{-j\left(2\pi\frac{l}{T_c}\tau\right)} \quad 2.25$$

where $\Delta f_c = f_c - \hat{f}_c$, \hat{f}_c is the local carrier frequency, and $\Delta\theta_c$ is the phase difference between the incoming signal and the local carrier. Let $m = i + l$ and

$$R_m(\tau) = \sum_{l=-\infty}^{\infty} A_{m-l} A_l e^{-j\left(2\pi\frac{l}{T_c}\tau\right)} \quad 2.26$$

Equation 2.21 is re-written as

$$\hat{s}(t) = \sqrt{2C}d(t - \tau_i) \sum_{m=-\infty}^{\infty} R_m(\tau) e^{j\left(2\pi\left[\frac{m}{T_c} + \Delta f_c\right]t + \Delta\theta_c\right)} \quad 2.27$$

Consider the correlator integration time T_d . For GPS L1 C/A code, T_d is nT_c , where $n = \{1, 2, 4, 5, 10 \text{ or } 20\}$. If data aiding is used, the value of n can exceed 20. Integrating equation 2.25 between $-T_d/2$ and $T_d/2$, the resultant correlator output is (Balaei and Akos 2011)

$$R(\tau, f) = \sum_{m=-\infty}^{\infty} \sqrt{2CT_d}d(t - \tau_i) \text{sinc}\left[\left(\Delta f_c + \frac{m}{T_c}\right)T_d\right] \times R_m(\tau) e^{j\Delta\theta_c} \quad 2.28$$

For $\Delta f_c \ll 1/T_c$, where acquisition or tracking is within the main lobe of the integrate and dump frequency response, and $m \neq 0$, the term $\text{sinc}\left[\left(\Delta f_c^k + \frac{m}{T_c}\right)T_d\right]$ is negligible (Balaei and Akos 2011). Hence the only remaining term will be the case in which $m = 0$. Thus,

$$R(\tau, f) \cong \sqrt{2CT_d}d(t - \tau_i)\text{sinc}[(\Delta f_c)T_d]R_0(\tau)e^{j\Delta\theta_c} \quad 2.29$$

If the signal is acquired and tracked, then the term Δf_c is zero, and a perfect correlation triangle is observed.

Similarly, if there are more than one satellites in line-of-sight (PRN ranging from $n = 1$ to N), then the cross-correlation formulation is given by (Balaei and Akos 2011)

$$R_N(\tau, f) \cong \sum_{n=1}^N \sqrt{2C_n}d_n(t - \tau_i)T_d R_m^{kn}(\tau) \times \text{sinc}\left[\left(\Delta f_c^{kn} + \frac{m}{T_c}\right)T_d\right]e^{(j\Delta\theta_{kn})} \quad 2.30$$

where C_n is the n^{th} signal power, $d_n(t)$ is data modulation, R_m^{kn} is cross-correlation function as defined Eq. 5, and $\Delta\theta_{kn}$ is the carrier phase difference between the k^{th} and n^{th} satellites. $\Delta f_c^{kn} = f_c^n - \hat{f}_c^k$, where \hat{f}_c^k is the receiver estimation of the desired k^{th} satellite Doppler frequency, f_c^n is the received Doppler frequency of the n^{th} satellite signal. The value of Δf_c^{kn} can reach zero or a few kHz depending on user dynamics and satellite motion.

Consider an integer M such that $\Delta f_c^{kn} \mp \frac{M}{T_c} \ll \frac{1}{T_d}$ and $m \neq M$, the term $\text{sinc} \left[\left(\Delta f_c^{kn} + \frac{m}{T_c} \right) T_d \right]$ is negligible. For example, consider GPS C/A code with code length duration $T_c = 1$ ms, given integration time $T_d = 2$ ms, and relative Doppler between two satellites $\Delta f_c^{kn} = 1$ kHz. The inequality condition is satisfied at $M = 1$. If $m \neq 1$, the *Sinc* term will reduce to zero. Thus the only remaining term is

$$R_N(\tau, f) \cong \sum_{n=1}^N \sqrt{2C_n} d_n(t - \tau_i) T_d R_D^{kn}(\tau) \times \text{sinc} \left[\left(\Delta f_c^{kn} + \frac{M}{T_c} \right) T_d \right] e^{(j\Delta\theta_{kn})} \quad 2.31$$

Based on the available number of interfering satellites, the correlation output is determined by equations 2.28 and 2.29. The resultant correlator output is a combination of cross-correlation peaks of other satellites and the primary peak of desired GEO, which is similar to multipath effect. The introduced error is a function of multiple factors (Nouvel et al. 2007) and discussed below in detail.

- Relative Doppler $\left(\Delta f_c^{kn} \right)$
- Cross-correlation function $\left(R_D^{kn}(\tau) \right)$
- Relative code delay (τ)
- Relative power (C_n)
- Message data $(d_n(t))$
- Relative carrier phase $\left(\theta_{kn} \right)$

2.3.1.1 Relative Doppler

In GNSS, although there are many instances on a given day where relative Doppler between two MEO satellites is small, the duration is insignificant because the satellites'

Doppler is changing rapidly. However, consider geostationary satellites where relative Doppler remains small for a good amount of time because of little relative motion. Nouvel et al. (2007) have shown that Doppler collision between two WAAS satellites occurs twice a day and each duration lasts for more than an hour. Such significant durations of small relative Doppler may lead to Doppler collision effect lasting for long durations. The relative Doppler is an important factor in the occurrence of Doppler collision. If the relative Doppler is greater than the receiver code lock loop bandwidth, the relative phase moves too much during the code lock loop integration period and the cross-correlation peak is filtered out.

In the next chapter, the analysis of Doppler collision will begin by observing Doppler crossing and finding a window of small relative Doppler.

2.3.1.2 Cross-Correlation function

During Doppler collision, the primary peak and a cross-correlation peak formed between two satellites can interfere creating a distorted correlation triangle (Lestarquit and Nouvel 2012). The error introduced by Doppler collision appears similar to code multipath, however, in this case, the measurement error is due to the between-satellite cross-correlation peak rather than a delayed copy of the main peak. Unlike multipath, the cross-correlation peak of Doppler collision may be present on either side of a primary peak resulting in a delay or an advance. The cross-correlation peak will contribute to the correlation function and cause an offset of the zero-crossing of the discrimination functions that will result in a tracking error. For example in WAAS C/A codes, which are Gold codes like the GPS C/A codes, the normalized cross-correlation peak values are

63/1023 or -65/1023 (Braasch 1997). Figure 2-4 shows that Doppler collision can induce errors up to 9 m in a standard correlator, when two signals have same signal strength. The computed error peak is sharp because it is derived based on ideal receiver conditions such as infinite receiver bandwidth, no receiver noise or multipath error. If the cross-correlation peak is in transition, where cross-correlation peaks of opposite values are present successive to each other, the error goes up to 18 m. This amount of pseudorange measurement error is large to perform carrier phase positioning.

2.3.1.3 Relative Code Delay

In C/A code, the relative code delay leads to an interference between the primary peak and a cross-correlation peak from another satellite with a probability of 25% (Van Dierendonck et al. 1999). The possibility of Doppler collision events over a given geographical region increases strongly with more GEO satellites in view. Given “N” GEO satellites in view, the occurrence of Doppler collision increases by the number of combinations of 2 elements (${}^N C_2$). Unfortunately, the situation is not going to improve in the future as GNSS deploy more GEO satellites with overlapping inter-operative regions. The service areas of IRNSS and BeiDou-2 are potential areas of Doppler collision with scores of GEO satellites in view. If these systems are used in high accuracy applications, it is important to understand the impact of Doppler collision on ambiguity convergence and the RTK solution for IRNSS and BeiDou-2 users.

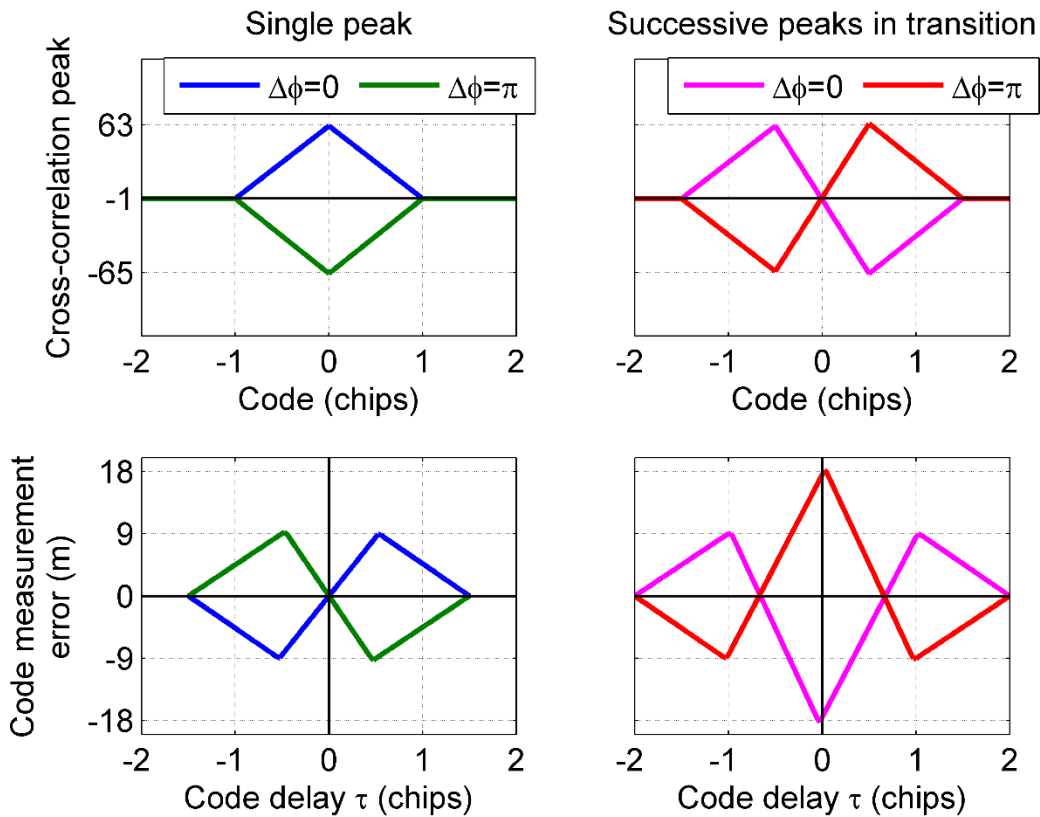


Figure 2-4 Code measurement error due to Doppler collision left side: single cross-correlation peak, blue in-phase and green opposite phase, and right side: successive peaks in transition, magenta in-phase and red opposite phase

2.3.1.4 Relative Power

C/A code cross-correlation properties show that cross-correlation margin between two satellites with equal signal strength is 24 dB (Van Dierendonck et al. 1999). In the case of GEOs, satellites with equal signal strength are a more likely condition, and this will lead to code measurement error that would be similar to a multipath with Signal to Multipath Ratio (SMR) of 20 dB, and approximately zero mean (Ray 2000). If the relative power is

not zero, the impact of Doppler collision would be more severe. Limited research is available to show the magnitude of errors due to different levels of signal strength.

2.3.1.5 Data Message Similitude

Data message similitude is a condition where navigation bits from two GEO satellites are correlated. In WAAS, navigation data is transmitted with the same sign for 90% of data symbols between two WAAS satellites (Nouvel et al. 2008). Data messages similitude will lead to a situation where the sign of error will remain constant for most the significant portion of the Doppler collision window.

2.3.1.6 Relative Carrier Phase

In multipath, the error varies as a function of relative phase delay between the Line Of Sight (LOS) and the Non-LOS signal (Braasch 1996). The sign of the error can be positive or negative depending on the relative carrier phase and is not zero-mean (Nievinski and Larson 2014; Gowdayyanadoddi et al. 2015). If the relative magnitude of the cross-correlation peak is small, the error varies sinusoidally with zero-mean. However, if the relative magnitude is large, the error signal is not sinusoidal, and the error might not average out to zero. Similar effects are possible during Doppler collision, and a detailed analysis is required to assess its impact on ambiguity convergence.

The Doppler collision error between two satellites is determined by the first three parameters whereas the magnitude is affected by the relative power, the data message similitude, and the relative carrier phase. Chapter-3 discusses the impact of Doppler

collision on code measurements of geostationary satellites using simulated and live data in detail. Chapter-4 analyzes and describes the effect of Doppler collision on an RTK solution.

2.3.2 Observability

Observability is an ability to determine state variables from the given measurements (Gelb et al. 1974). In the case of GEOs, the satellites are relatively static to the user on earth's surface, and thus no additional information is added over time due to the motion of the satellite. This condition increases the time-correlation of differential errors (El-Rabbany 1994) as well as non-differential errors and deteriorates observability, which in turn increases convergence time of ambiguities (O'Keefe et al. 2006). To determine the convergence of the state vector, one needs to obtain the correlation time of geostationary satellite's measurement errors. El-Rabbany (1994) had outlined the method for GPS satellites where poor observability is captured in the covariance of ambiguities. If covariance of ambiguities is affected by the time-correlation of measurements, it will further affect the PCF (Teunissen 2000). The following section describes the effect of poor observability on the estimation of covariance of ambiguities.

2.3.2.1 Covariance of Ambiguities

An RTK solution output state consists of position, velocity and ambiguities, and its variance. If the estimation process uses single-differenced observations, the output state also has clock bias and clock drift. Initially, the covariance of ambiguities (diagonal elements of the state covariance matrix) is significant, however, over a period, it

converges to a small value. To isolate the impact of time-correlation on GEO measurement errors, the convergence of single-differenced ambiguities is analyzed using covariance values. Instead of double-differenced ambiguities, the analysis considers only single-differenced ambiguities because SD treat each satellite independently and ambiguities do not depend on a base satellite. Petovello et al. (2009) provide a Modified Kalman Filter (MKF) that factors in the time-correlation. The derivation of MKF starts from a Standard Kalman Filter (SKF) and incorporates terms to reflect time-correlation of output states.

2.3.2.2 Standard Kalman Filter

Consider a measurement model given as

$$\mathbf{z}_k = \mathbf{H}_k \mathbf{x}_k + \mathbf{v}_k \quad 2.32$$

where \mathbf{x}_k is the state vector at a time t_k , \mathbf{H}_k is the design matrix, and \mathbf{v}_k is the measurement noise vector with covariance \mathbf{R}_k , assumed to be white. The prediction step is given by

$$\begin{aligned} \mathbf{x}_k &= \mathbf{\Phi}_{k-1} \mathbf{x}_{k-1} + \mathbf{w}_{k-1} \\ \mathbf{P}_k &= \mathbf{\Phi}_{k-1} \mathbf{P}_{k-1} \mathbf{\Phi}_{k-1}^T + \mathbf{Q}_{k-1} \end{aligned} \quad 2.33$$

where $\mathbf{\Phi}_{k-1}$ is the state transition matrix from epoch t_{k-1} to t_k , \mathbf{w}_{k-1} is the process noise vector, assumed to be white, \mathbf{P}_k is the state covariance matrix, and \mathbf{Q}_{k-1} is the covariance matrix of process noise \mathbf{w}_{k-1} . The updated state and covariance is given by

$$\begin{aligned}
\hat{\mathbf{x}}_k^+ &= \hat{\mathbf{x}}_k^- + \mathbf{K}_k (\mathbf{z}_k - \mathbf{H}_k \hat{\mathbf{x}}_k^-) \\
\mathbf{P}_k^+ &= (\mathbf{I} - \mathbf{K}_k \mathbf{H}_k) \mathbf{P}_k^- \\
\mathbf{K} &= \mathbf{P}_k^- \mathbf{H}_k^T (\mathbf{H}_k \mathbf{P}_k^- \mathbf{H}_k^T + \mathbf{R}_k)^{-1}
\end{aligned}
\tag{2.34}$$

where (-) and (+) superscripts denote a value before and after measurement update respectively.

The process noise \mathbf{w}_k and measurement noise \mathbf{v}_k are both assumed to be white and uncorrelated with each other, as well as uncorrelated with the state vector.

2.3.2.3 Modified Kalman Filter

The single-differenced measurements consist of residual ionospheric and tropospheric errors, quasi-periodic errors such as receiver multipath and Doppler collision, and receiver noise. The SKF does not consider the time-correlation between measurement errors, and thus the estimated state variance is optimistic (Petovello et al. 2005). A Modified Kalman Filter (MKF) is required which can account for the time-correlation of measurements and reflects the effect in the state estimates. Brown and Hwang (1997) provides a Kalman Filter that incorporates time-correlated errors in the estimation process. The time-correlated observations is represented by vector \mathbf{l}_k where

$$\mathbf{l}_k = \mathbf{A}_k \mathbf{x}_k + \mathbf{u}_k + \mathbf{n}_k
\tag{2.35}$$

where \mathbf{A}_k is the design matrix and the error has been decomposed into two parts: time-correlated noise \mathbf{u}_k and a white measurement noise \mathbf{n}_k . The time-correlated errors are given by

$$\mathbf{u}_{k+1} = \mathbf{S}_{k+1,k} \mathbf{u}_k + \boldsymbol{\varepsilon}_k \quad 2.36$$

where \mathbf{S}_k is the transition matrix for the time-correlated errors. For a first order Gauss-Markov (GM) process, the transition matrix is given by (O'Keefe et al. 2006)

$$\mathbf{S}_{k+1,k} = \text{diag}(e^{-\beta \Delta t}) \quad 2.37$$

where β^{-1} is the correlation time and $\Delta t = t_{k+1} - t_k$. $\boldsymbol{\varepsilon}_k$ is a vector of white noise driving the correlated measurement error process and is assumed to be uncorrelated with both measurement noise \mathbf{n}_k and the process noise \mathbf{w}_k . Applying the time-differencing approach yields a new measurement \mathbf{z}_k as (O'Keefe et al. 2006)

$$\mathbf{z}_k = (\mathbf{A}_k - \mathbf{S}_k \mathbf{A}_{k-1} \boldsymbol{\Phi}_{k-1,k}^{-1}) \mathbf{x}_k + \mathbf{S}_k \mathbf{A}_{k-1} \boldsymbol{\Phi}_{k-1,k}^{-1} \mathbf{w}_{k-1} + \boldsymbol{\varepsilon}_{k-1} + \mathbf{n}_k - \mathbf{S}_k \mathbf{n}_{k-1} \quad 2.38$$

The above equation is equivalent to equation 2.32 where \mathbf{H}_k and \mathbf{v}_k are

$$\begin{aligned} \mathbf{H}_k &= \mathbf{A}_k - \mathbf{S}_k \mathbf{A}_{k-1} \boldsymbol{\Phi}_{k-1,k}^{-1} \\ \mathbf{v}_k &= \mathbf{S}_k \mathbf{A}_{k-1} \boldsymbol{\Phi}_{k-1,k}^{-1} \mathbf{w}_{k-1} + \boldsymbol{\varepsilon}_{k-1} + \mathbf{n}_k - \mathbf{S}_k \mathbf{n}_{k-1} \end{aligned} \quad 2.39$$

The terms $\boldsymbol{\varepsilon}_{k-1}$, \mathbf{n}_k , and \mathbf{n}_{k-1} are all assumed to be white and mutually uncorrelated whereas the new measurement error vector \mathbf{v}_k is also white and thus uncorrelated over

time. However, the measurement vector is now a function of \mathbf{w}_{k-1} . Thus the measurement and process noise are correlated as

$$\mathbf{C}_k = \mathbf{E}\{\mathbf{w}_{k-1} \mathbf{v}_{k-1}^T\} = \mathbf{Q}_{k-1} (\mathbf{\Phi}_{k-1}^T)^{-1} \mathbf{A}_{k-1}^T \mathbf{S}_k^T \quad 2.40$$

The updated Kalman Filter equations in the alternative form are (Brown and Hwang 1997)

$$\begin{aligned} \mathbf{K}_k &= (\mathbf{P}_k^* \mathbf{H}_k^T + \mathbf{C}_k) (\mathbf{H}_k \mathbf{P}_k^* \mathbf{H}_k^T + \mathbf{R}_k + \mathbf{H}_k \mathbf{C}_k + \mathbf{C}_k^T \mathbf{H}_k^T)^{-1} \\ \mathbf{P}_k^+ &= \mathbf{P}_k^* - \mathbf{K}_k (\mathbf{H}_k \mathbf{P}_k^* \mathbf{H}_k^T + \mathbf{R}_k + \mathbf{H}_k \mathbf{C}_k + \mathbf{C}_k^T \mathbf{H}_k^T) \mathbf{K}_k^T \end{aligned} \quad 2.41$$

The covariance matrix of measurement noise is now given by

$$\mathbf{R}_k = \mathbf{M}_{k-1} + \mathbf{N}_k + \mathbf{S}_k \mathbf{N}_{k-1} \mathbf{S}_k^T + \mathbf{S}_k \mathbf{A}_{k-1} \mathbf{\Phi}_{k-1,k}^{-1} \mathbf{A}_{k-1}^T \mathbf{S}_k^T \quad 2.42$$

where \mathbf{M}_k is the covariance matrix of $\boldsymbol{\varepsilon}_k$ and \mathbf{N}_k is the covariance matrix of \mathbf{n}_k .

Both the SKF and MKF provide covariance of ambiguities as part of the estimated state covariance matrix that can be used to assess the observability of the ambiguities. This approach differs from the classical observability calculation (Gelb et al. 1974; Brown and Hwang 1997) where the rank of an observability matrix composed of the design and transition matrices is assessed over multiple epochs to determine if sufficient observations have been taken to observe the unknown states. For example, the classical method can demonstrate that a user with sufficient range measurements from two epochs can observe user position and velocity while a user with only range-rate measurements cannot observe position. The current approach of determining observability using the P-matrix offers the advantage that it can determine not only the observability in the sense

that sufficient observations exist to estimate the states, but also the time convergence of the covariance of the states. Chapter-5 discusses multiple cases of GEO in an RTK solution and provides a comparison of convergence of ambiguities using SKF and MKF to distinguish the effect of time-correlation.”

Chapter Three: **Characterization of Doppler Collision**

The previous chapter discussed theoretical aspects of the Doppler collision. The objective of this chapter is to demonstrate Doppler collision and analyze its impact on the code measurements. The outline is as follows: The Doppler variation of geostationary satellites is obtained and analyzed for the potential collision events. The cross-correlation function is discussed and analyzed in detail to obtain the theoretical limits of Doppler collision error. The relative code phase is presented to show the spatial extent of Doppler collision using WAAS and BeiDou. Further, a Doppler collision event is simulated using GNSS simulator with WAAS satellites to observe the impact on code measurements in a receiver. The Doppler collision measurement error and its variation are discussed to understand its behavior over the time. Finally, multiple live data collections are performed to observe pseudorange measurement error associated with the Doppler collision.

Section 2.3.1 shows that the following parameters determine the effect of Doppler collision:

- Relative Doppler (Δf_c^{kn})
- Cross-correlation function ($R_D^{kn}(\tau)$)
- Relative code delay (τ)
- Relative power (C_n)
- Message data ($d_n(t)$)
- Relative carrier phase (θ_{kn})

The following section analyzes the effects of each parameter with observations (simulated or live data) in order to develop the ability to observe Doppler collision in code measurements.

3.1 Study of Geostationary Doppler

To observe Doppler collision, the first step is to understand the satellite Doppler variations and identify the Doppler crossing for likely Doppler collision conditions. All geostationary satellites across constellations: WAAS, BeiDou GEOs, IRNSS GEOs, and SBAS such as GAGAN, MSAS, and EGNOS, are considered.

3.1.1 WAAS

Figure 3-1 shows a variation of Doppler of WAAS PRN 133 and PRN 135 as observed from a location in Calgary, Alberta, in July 2014. The Doppler variation is smooth because it is computed using the change in geometric range and resembles true Doppler observed using a WAAS receiver. PRN 133 varies between ± 100 Hz while PRN 135 exhibits less motion. There are only limited periods where the relative Doppler between two satellites is smaller than 1 Hz, which is a typical code lock loop bandwidth (Lestarquit and Nouvel 2012). Similarly, Figure 3-2 shows the variation of PRN 133 and PRN 138. Here too, the duration of small relative Doppler is not significant. However, PRN 135 and PRN 138 have little variation and could form a potent combination for small relative Doppler.

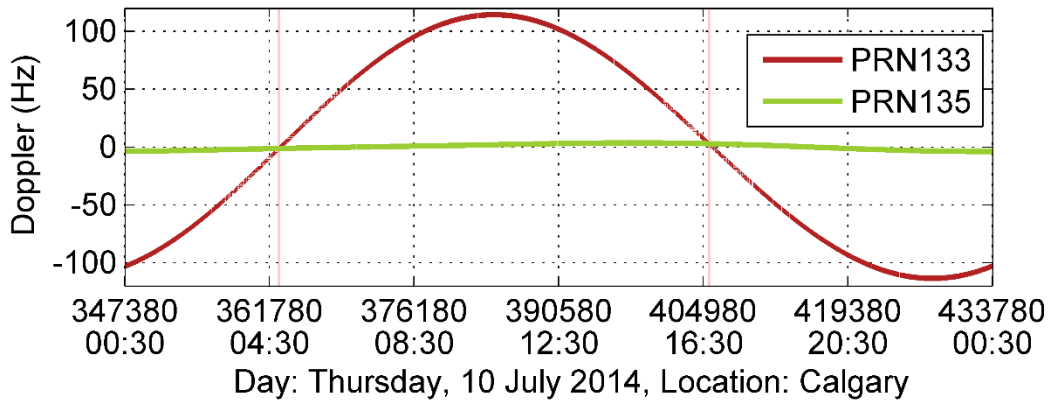


Figure 3-1 Smoothed observed Doppler variation of PRN 133 and PRN 135

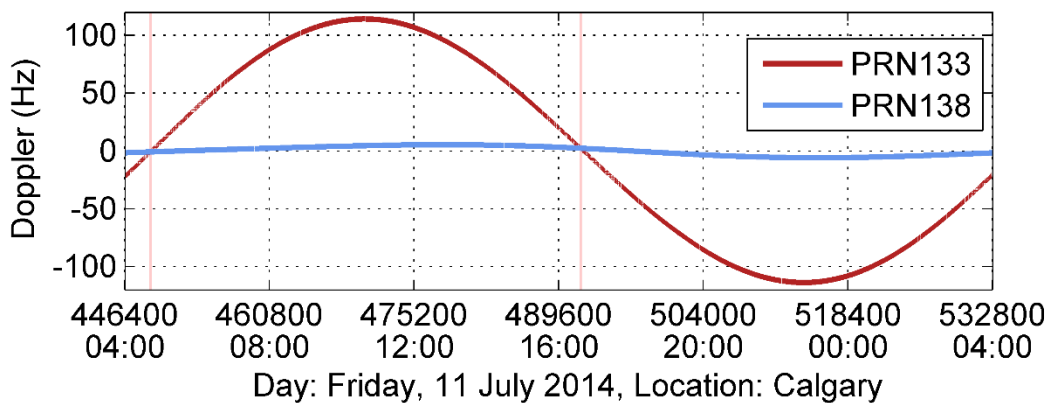


Figure 3-2 Smoothed observed Doppler variation of PRN 133 and PRN 138

Figure 3-3 shows the Doppler frequencies of PRN 135 and PRN 138 on two different days roughly one year apart. On both days, the relative Doppler is smaller than 1 Hz for many hours, as indicated by the shaded region, and provides likely conditions for Doppler collision. The time of the event and the overall duration might change based on the satellite Doppler variations at given time of the year.

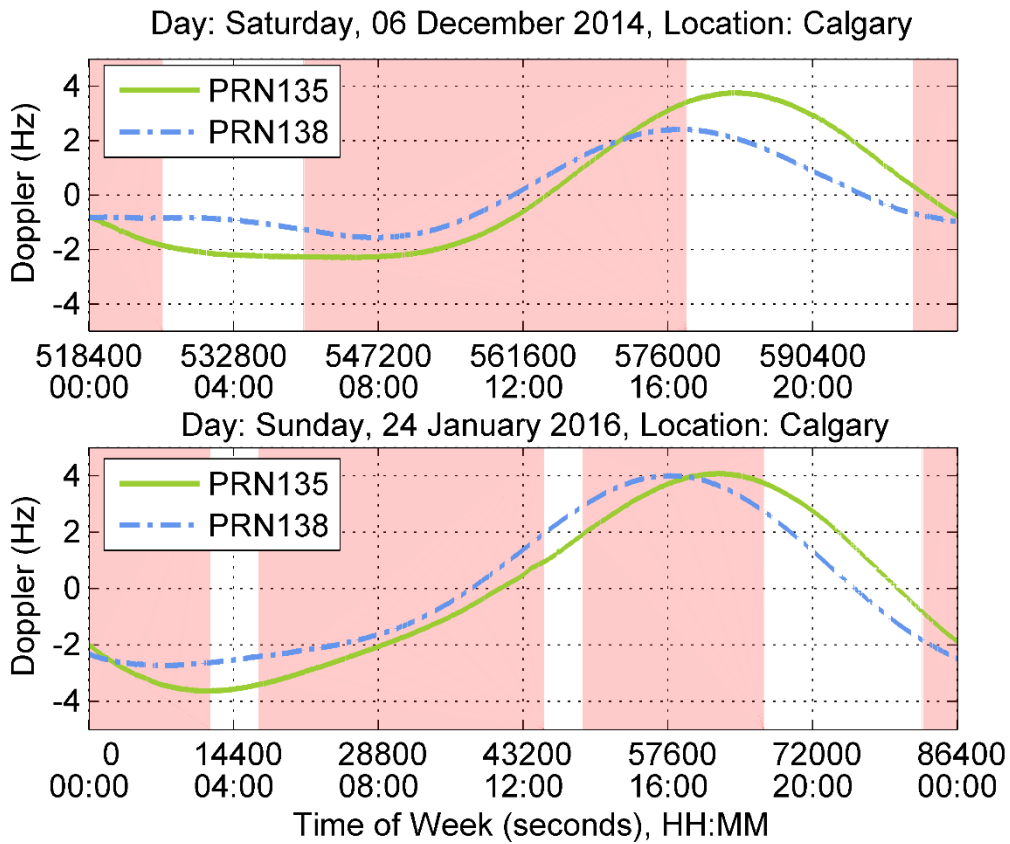


Figure 3-3 Smoothed observed Doppler variation of PRN 135 and PRN 138

Figure 3-4 shows an example where the duration of small relative Doppler varies over five days. The change in duration is due to WAAS satellites' maneuvers for house-keeping operations (Aaron 2006). The Doppler variations conclude that PRN 135 and PRN 138 provide long duration of small relative Doppler over successive days and also vary with the time of the year.

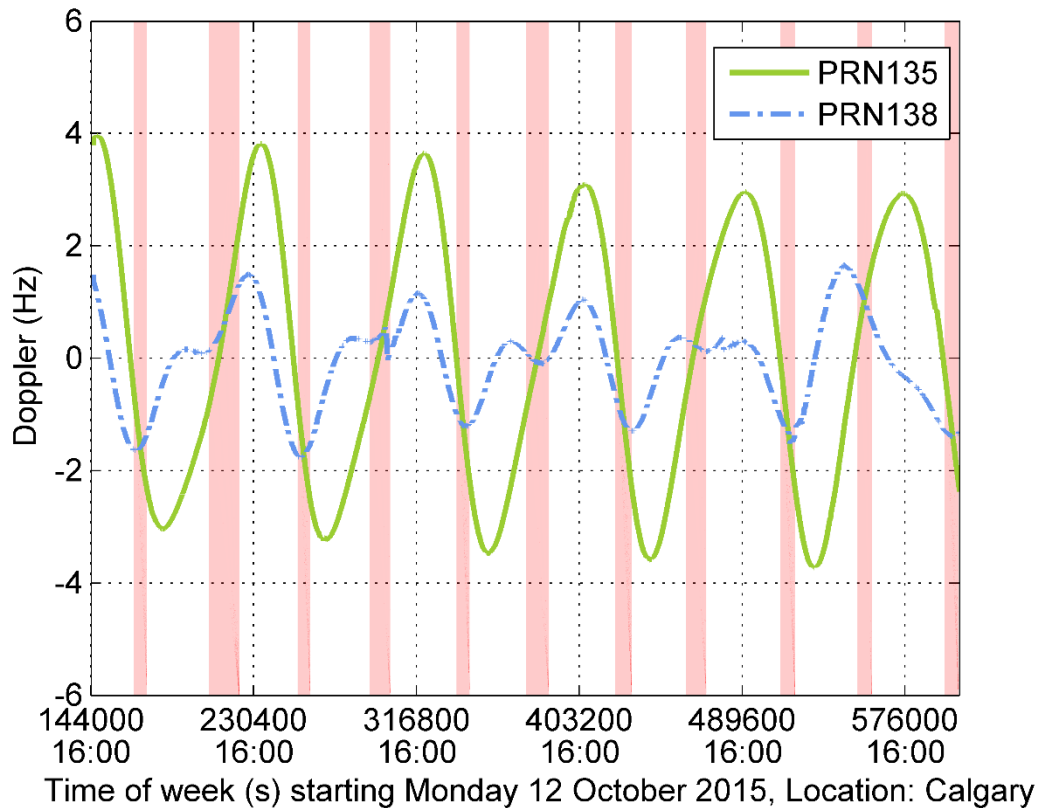


Figure 3-4 Smoothed observed Doppler variation of PRN 135 and PRN 138 for a week

3.1.2 BeiDou GEO

The top section of Figure 3-5 shows Doppler variation of BeiDou Phase-II geostationary satellites at mid-latitudes. The change of Doppler is significant between the satellites. However, satellite C03 and C04 have many close variations and small relative Doppler for long durations as highlighted. Also, C02 and C05 have close variations, and over a period in a given year, it is highly likely that both satellites may have small relative Doppler for longer durations.

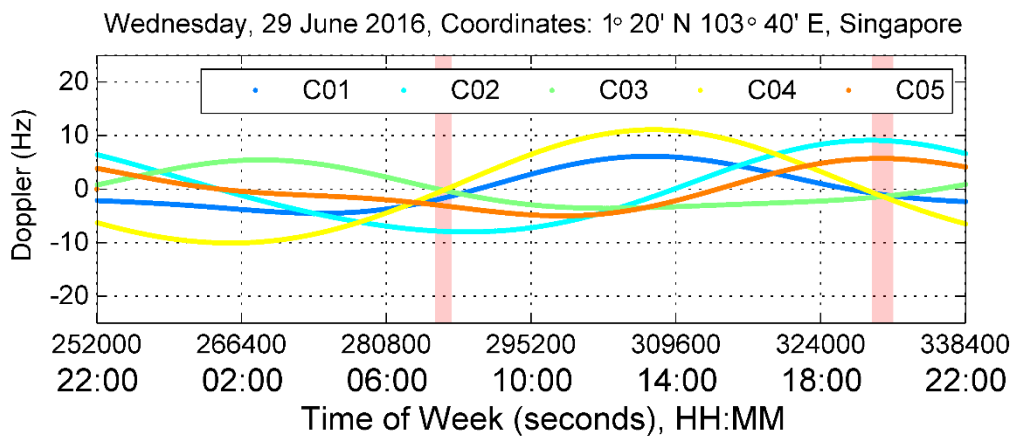
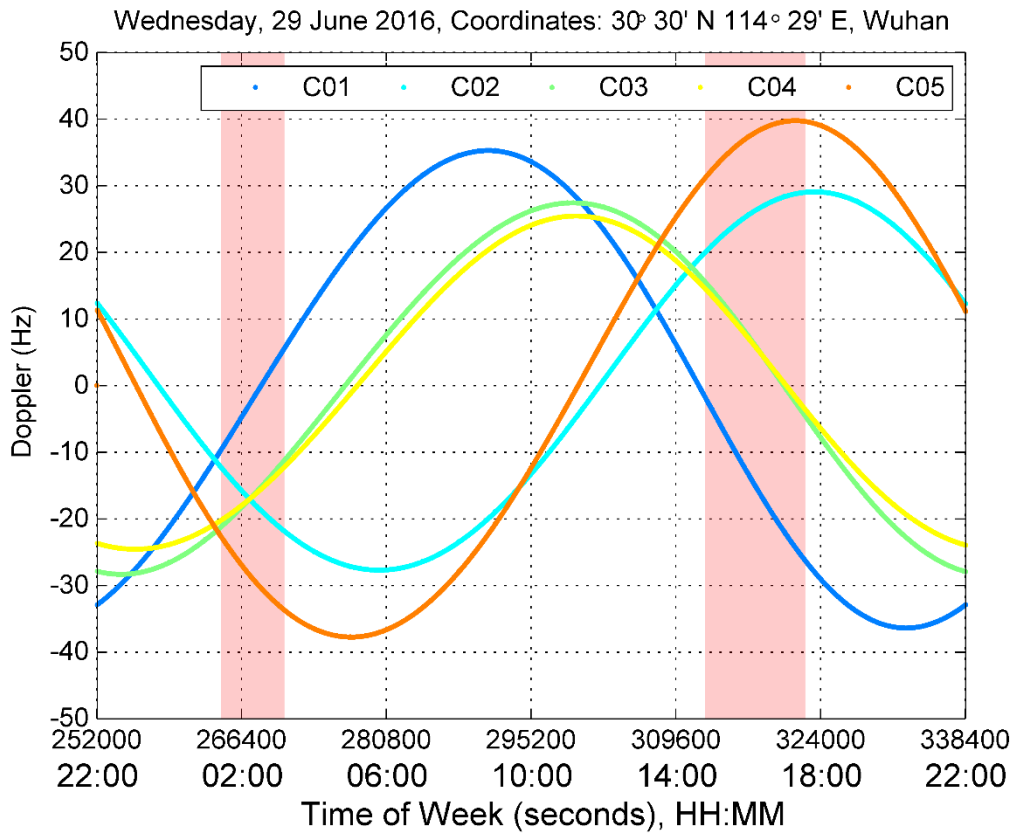


Figure 3-5 Doppler frequencies of BeiDou geostationary satellites, top plot shows variations at mid-latitudes and bottom plot shows variations at lower latitude

On the same day, the Doppler variation is quite different at a location near the equator, as shown in the bottom plot of Figure 3-5. Although the duration of small relative Doppler is small, the variation range of Doppler is ± 10 Hz, and this could lead to possible longer durations of small relative Doppler.

3.1.3 IRNSS GEO

Figure 3-6 shows the Doppler variation of IRNSS geostationary satellites over a day. Here too, the Doppler variations of 1C and 1G are close and relative Doppler is small for tens of minutes suggesting that Doppler collision may be an issue for IRNSS.

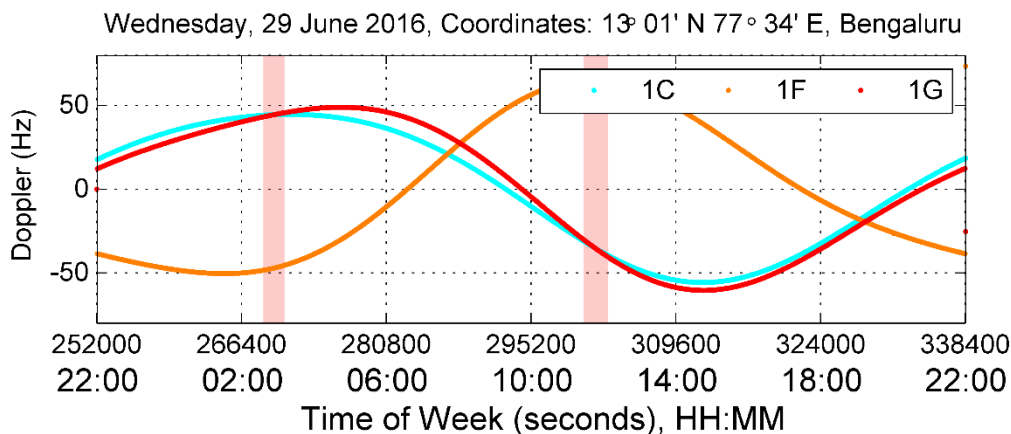


Figure 3-6 Doppler variation of IRNSS geostationary satellites

3.1.4 GAGAN

Figure 3-7 shows Doppler plots of GAGAN satellites. The variation range of Doppler is small in comparison to IRNSS satellites. The relative Doppler is again small for a couple of hours on a given day.

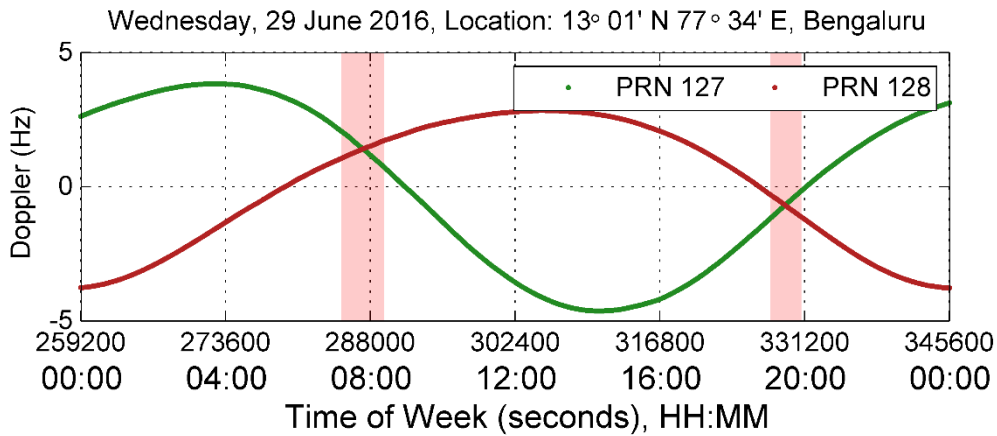


Figure 3-7 Doppler variation of GAGAN satellites

3.1.5 MSAS

Figure 3-8 shows Doppler variation of MSAS satellites. Even though the two satellites are located at two different latitudes, that is 140°E and 145°E, the Doppler variation is much same and thus provides likely conditions throughout the day.

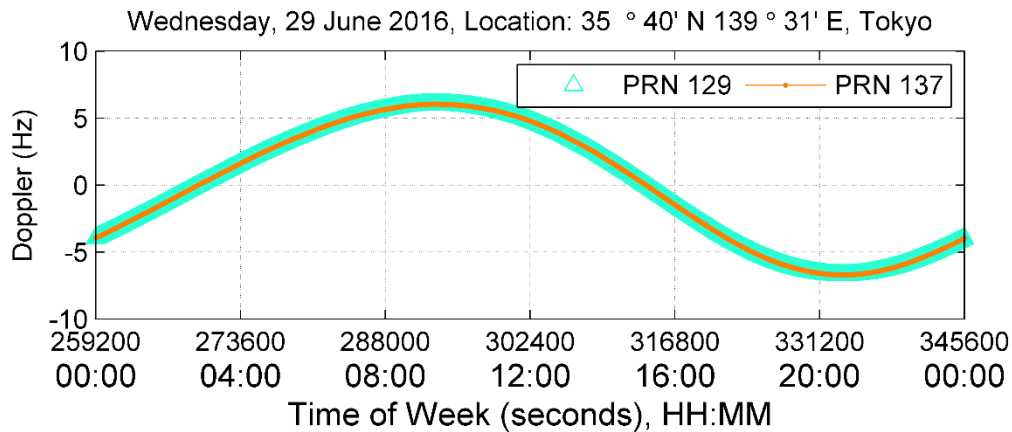


Figure 3-8 Doppler variation of MSAS satellites

3.1.6 EGNOS

Figure 3-9 shows Doppler frequencies of EGNOS satellites observed at Toulouse, France. Since EGNOS ephemeris parameters are not available in Broadcast Ephemeris, the Doppler frequencies are obtained from a receiver located at Toulouse, France, which tracks all three EGNOS satellites. This receiver is a part of the International GNSS Service (IGS) and the data was accessed from the Crustal Dynamics Data Information System (CDDIS) repository (Noll 2010). PRN 120 has considerable variation and is not an ideal candidate for Doppler collision. PRN 123 and PRN 136 have small Doppler variations, and the relative Doppler is less than 1 Hz for a significant number of hours. Thus EGNOS is also a potential candidate for Doppler collision.

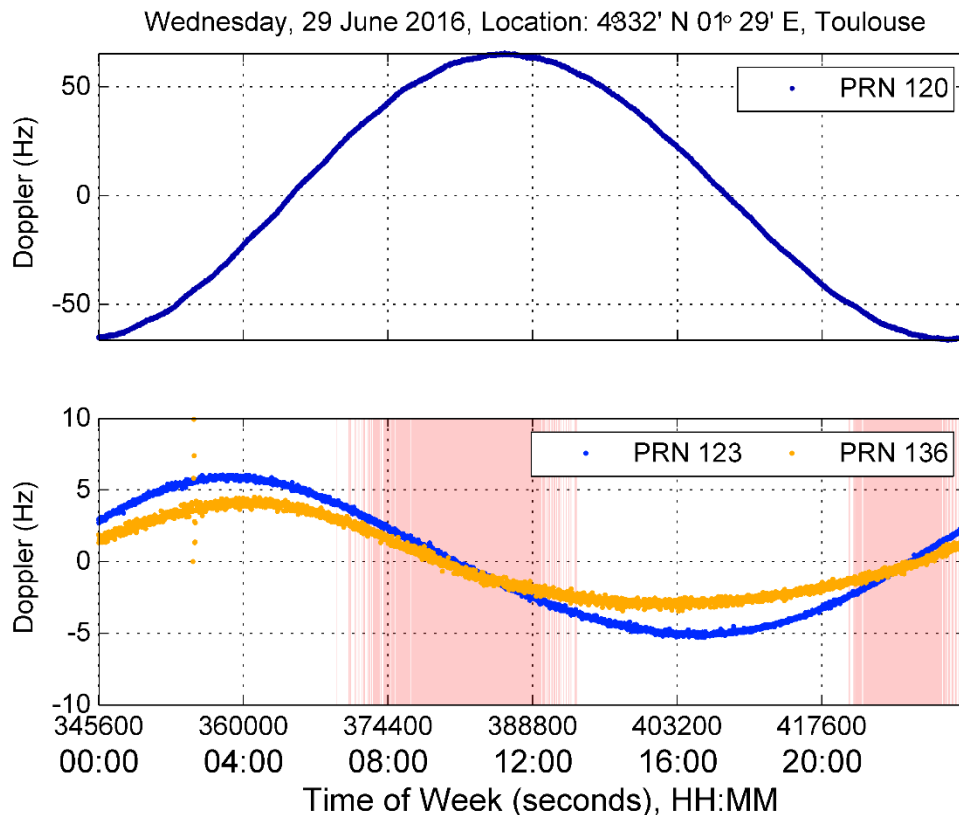


Figure 3-9 Doppler variation of EGNOS satellites

The analysis of relative Doppler concludes that geostationary satellites across SBAS, BeiDou, and IRNSS might experience Doppler collision for longer durations.

3.2 GNSS Cross-Correlation Function

The overlapping of the cross-correlation peak determines the magnitude and the variation of a Doppler collision error. The type of cross-correlation peak and the probability of its occurrence is dependent on the class of codes used in the signal modulation. Table 3-1 lists an example of the cross-correlation properties of the Gold codes (Spilker Jr. 1996).

Table 3-1 Cross-correlation properties of Gold codes

Code Length	N = length of shift register	Normalized cross-correlation level	Probability of level
$P = 2^N - 1$	N – odd	$-[2^{(N+1)/2} + 1]/P$	0.25
		$-1/P$	0.5
		$-[2^{(N+1)/2} - 1]/P$	0.25
$P = 2^N - 1$	N – even and $N \neq 4i$	$-[2^{(N+2)/2} + 1]/P$	0.125
		$-1/P$	0.75
		$-[2^{(N+2)/2} - 1]/P$	0.125

The SBAS and IRNSS L5 open service uses even C/A code of length 1023, where $n = 10$ (Spilker Jr. 1996; Mruthyunjaya and Ganeshan 2014). The possible cross-correlation levels in IRNSS are $-65/1023$, $-1/1023$, and $63/1023$ with a probability of 0.125, 0.75 and

0.125 respectively. The cross-correlation levels are equivalent to GPS where maximum (-65 or +63) cross-correlation occurs for one-quarter of the possible delays.

The cross-correlation properties of BeiDou B1I are not similar to C/A codes because B1I use truncated even Gold codes with chip length of 2046 chips (BeiDou ICD 2016). Because of the truncated nature, the cross-correlation properties do not follow the cross-correlation levels in Table 3-1 and have varying cross-correlation peaks. Table 3-2 lists the probability distribution of cross-correlation peaks found in B1I using code chips of all 5 BeiDou GEOs. Appendix A demonstrates the probability of distribution of Truncated Gold codes for a pair of BeiDou satellites.

Table 3-2 Cross-correlation properties of truncated Gold codes in BeiDou B1I

Code Length	Normalized cross-correlation level	Cross-correlation level magnitude	Distribution of levels	Probability of distribution
P = 2^{N-2} , where N = 11	$[2^{(N+1)/2} + 2^{(N-1)/2}] / P$	96	Level > 96	1.02 %
	$[2^{(N+1)/2}] / P$	64	Level > 64	8.20 %
	$[2^{(N-1)/2}] / P$	32	Level > 32	23.83 %
	$-[2^{(N-1)/2}] / P$	-32	Level < -32	25.41 %
	$-[2^{(N+1)/2}] / P$	-64	Level < -64	8.20 %
	$-[2^{(N+1)/2} + 2^{(N-1)/2}] / P$	-96	Level < -96	1.29 %

In comparison to C/A codes where the maximum cross-correlation is 63 or -65 with a probability of 12.5%, in B1I significant cross-correlation values (higher than +64 and less than -64) have a probability of 8.20 %. However, the cross-correlation magnitude of 64 will have half the impact in comparison to a C/A code because the code length is 2046. The probability of cross-correlation peaks other than -1 is higher, however, the likelihood of maximum cross-correlation peaks with levels > 96 and <-96 is small. The following section describes the effect of cross-correlation function using spatial extent.

3.2.1 Spatial Extent of WAAS Doppler Collision

A simulation is conducted over a small geographical area in Calgary to determine areas under cross-correlation for PRN 135 and PRN 138. Table 3-3 provides the coordinates of the WAAS satellites used in the simulations which are close to the true coordinates of WAAS satellites.

Table 3-3 Coordinates of WAAS satellites employed in Doppler collision simulation

Details	Latitude	Longitude	Height
PRN 135	0°N	133° W	35,786.037 km
PRN 138	0°N	108° 18' W	35,786.037 km
User location Rx1	51° 04' 47.8320'' N	114° 07' 38.2472'' W	1118.51 m

The cross-correlation values and their projection on a geographical area (Google Maps 2017) are shown in Figure 3-10. The cross-correlation values are computed on an assumption of infinite receiver bandwidth, which provides ideal cross-correlation values.

Appendix B explains the computation of cross-correlation values. The cross-correlation peaks run as stripes along the North-South direction as WAAS satellites are located in the equatorial plane. Since the geographical area under consideration is at higher latitudes and not equidistant from each WAAS satellite, the North-South stripes are not perpendicular to latitude. Figure 3-11 shows the cross-section of the correlation value at the user location. A cross-correlation peak is present at the user location.

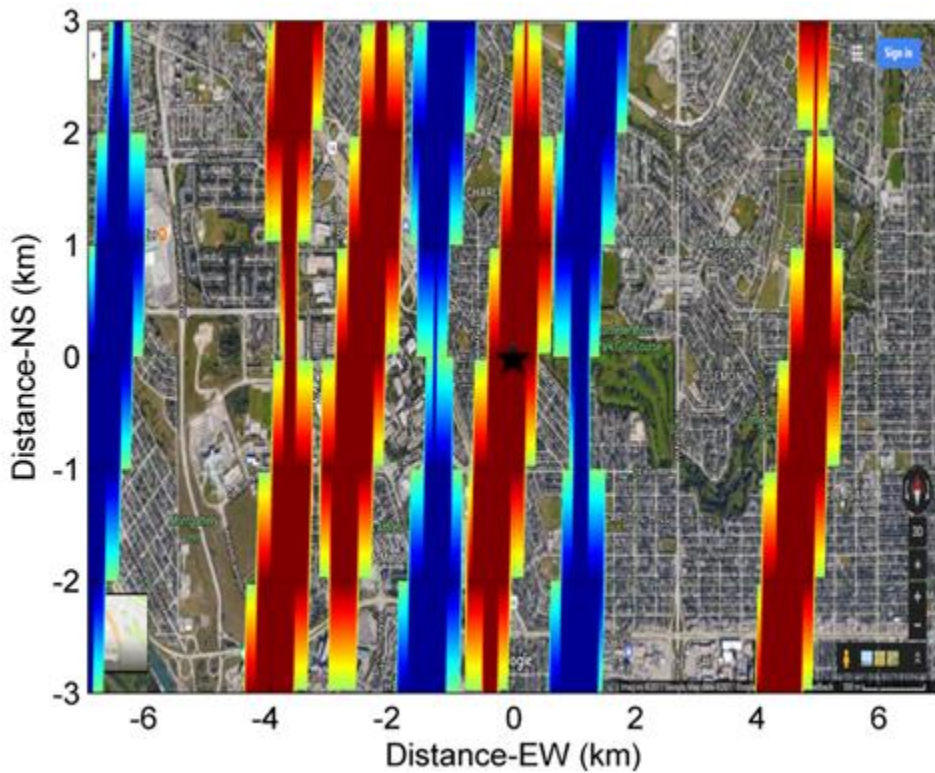
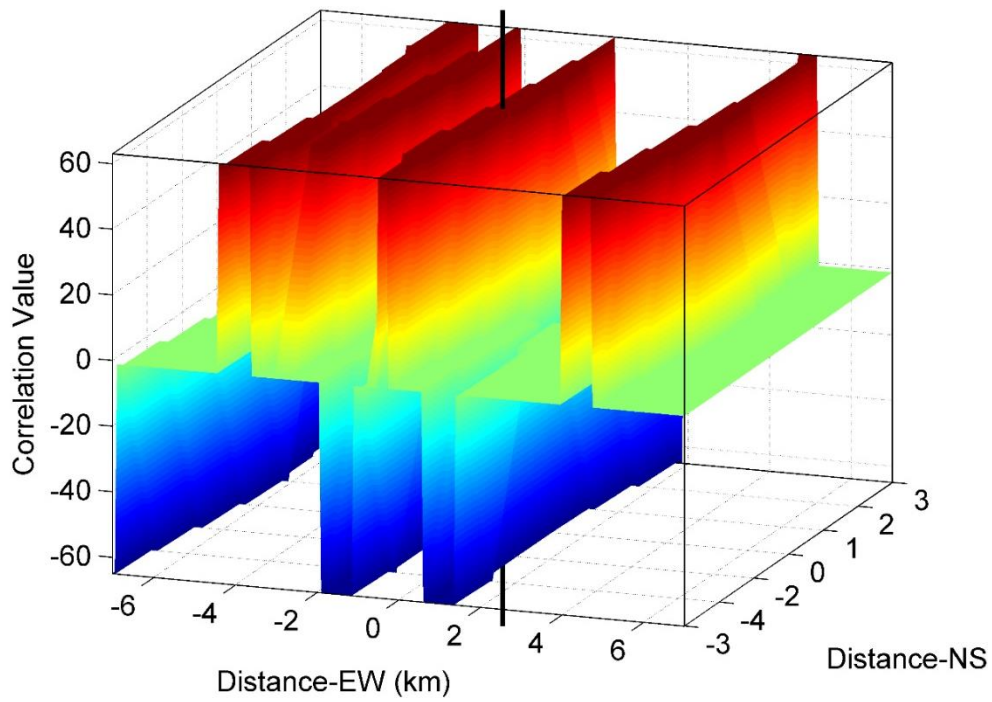


Figure 3-10 Simulation of cross-correlation over a geographical area and its projection

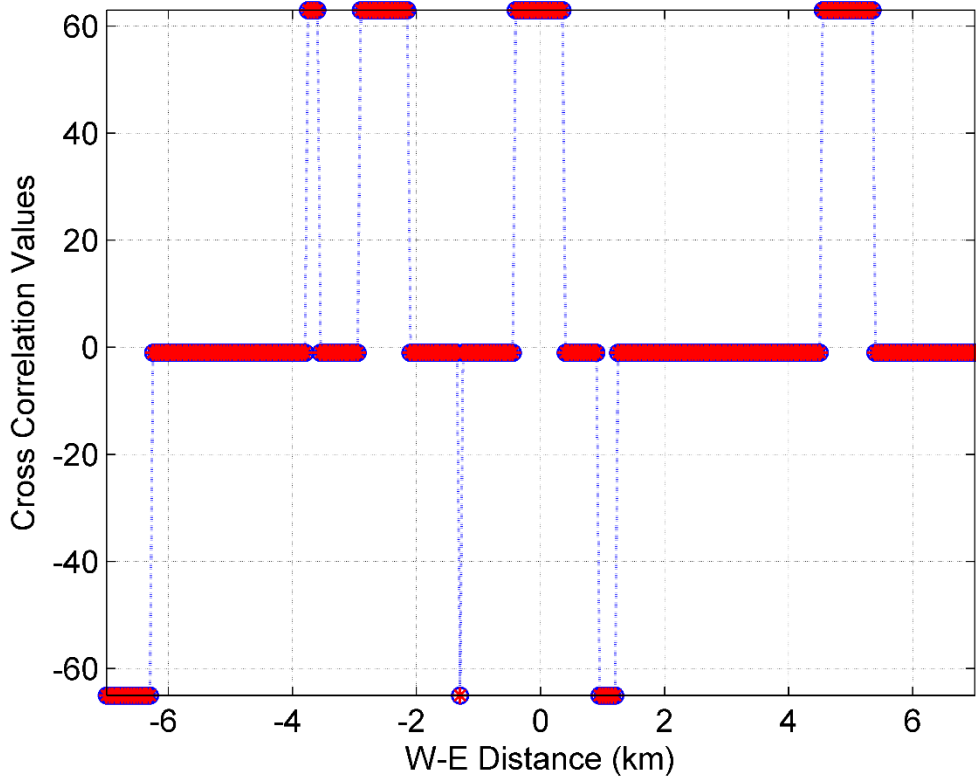


Figure 3-11 Cross-section of C/A code cross-correlation function along East-West

3.2.2 Spatial Extent of BeiDou B1I Doppler Collision

Similar to WAAS satellites, a simulation of spatial extent for BeiDou geostationary satellites is conducted to understand the impact of the cross-correlation function. Figure 3-5 shows GEO C03 and C04 have similar Doppler variations. A cross-correlation function is projected over a geographical area around Wuhan at the time of Doppler crossing for GEO C03 and C04. Figure 3-12 shows the cross-correlation values over the geographical area and its cross-section along East-West. As described in Table 3-2, the cross-correlation peaks have varying levels. The multi-level cross-correlation peaks are in sharp contrast to WAAS satellites where a user location can only experience large

cross-correlation values (63 or -65) or -1. The magnitude of the cross-correlation peak varies as the user moves East-West. Since it is hard to find maximum cross-correlation peaks in BeiDou B1I, the further analysis of Doppler collision is conducted using only the Gold codes in the WAAS and IRNSS constellations.

3.3 Theoretical Error Limits

Unlike multipath, the occurrence of cross-correlation peaks in Doppler collision is possible on either side of the desired peak. The magnitude of a Doppler collision error is dependent on the code and modulation used. It is also reliant on the chip spacing and the type of correlators used in the receiver design. Ideally, a minimal chip spacing can reduce the Doppler collision error significantly. Unfortunately, the effectiveness of reducing chip spacing is limited by the frequency content of the sampled signal, which is a function of both signal bandwidth and sampling frequency at the front end. For example, if GPS C/A code is sampled at 20 MHz, I and Q separately, the minimum effective E-L chip spacing is 0.1 chip. The 0.1 E-L chip spacing is also known as the narrow correlator design, shown to reduce multipath (Van Dierendonck et al. 1992). The range of measurement errors at various signal strengths, assuming a 20 MHz bandwidth, using standard and narrow correlators are computed and shown in Table 3-4. Even after using a narrow correlator, the magnitude of the Doppler collision error is significant to be ignored in an RTK solution. The third chip spacing, known as the ideal correlator, is one where the magnitude of the code error is less than a quarter of L1 wavelength at equal signal strength. Ideally, the error is well within acceptable range for an RTK solution, however, the bandwidth required is 400 MHz and very large for practical implementation.

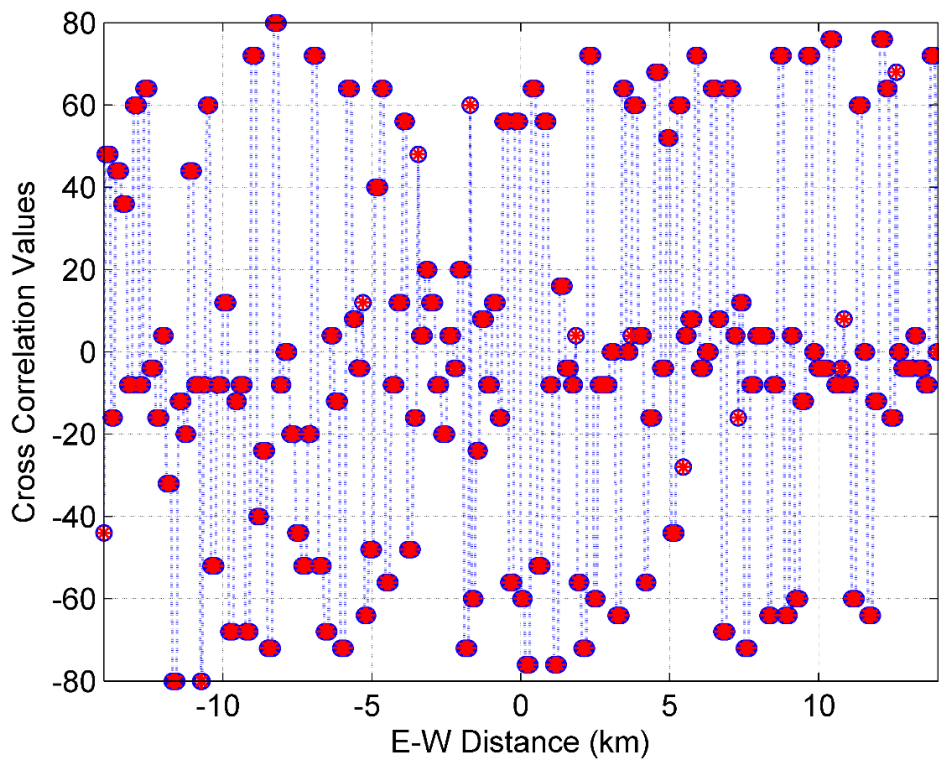
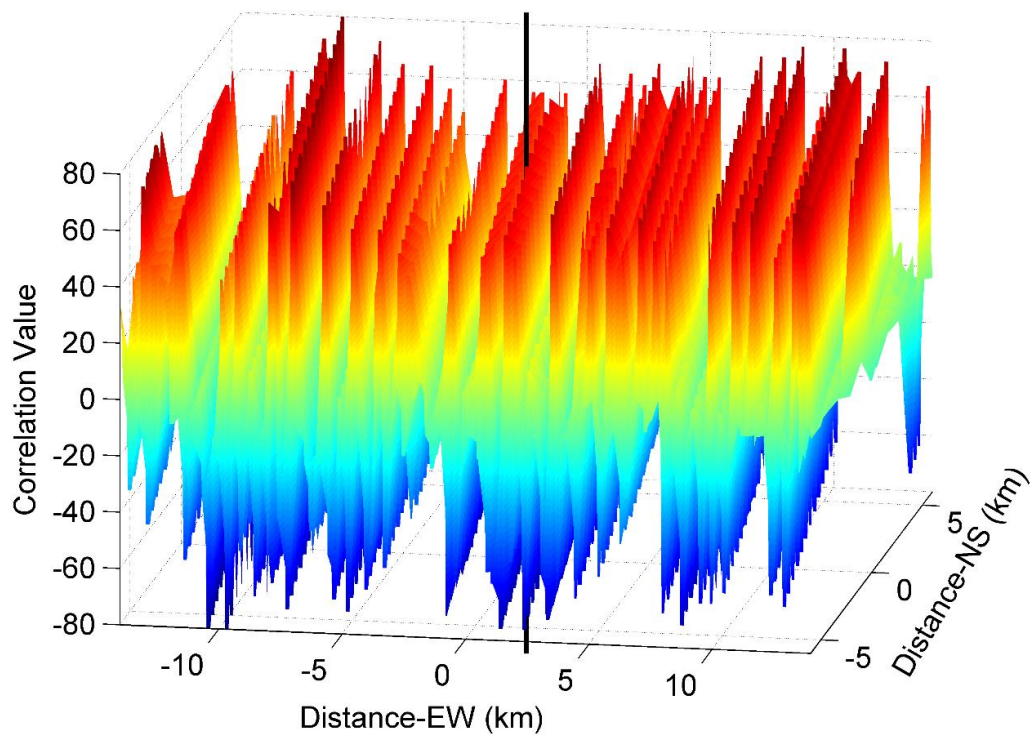


Figure 3-12 Simulation of truncated Gold codes cross-correlation over a geographical area and its cross-section

Because of the similarity to multipath, other multipath resistant correlator designs may be useful. The strobe correlator, using two early and two late correlators to estimate the slope of the triangle is one example (Garin and Rousseau 1997; Braasch 2001). Here too, the maximum error is close to the narrow correlator as shown in Table 3-4. For IRNSS, which uses Gold codes and has a bandwidth of 24 MHz (Mruthyunjaya and Ganeshan 2014), the Doppler collision error would be close to that observed with the L1 C/A code.

Table 3-4 Maximum Doppler collision errors with different correlator designs and varying signal strength

Signal strength	Correlators			
	Early-Late correlator			Strobe correlator
	Standard correlator - 1 chip	Narrow correlator - 0.1 chip	Ideal correlator - 0.005 chip	Chip spacing: 0.1, 0.2
0 dB	8.91 m	0.93 m	0.046 m	1.09 m
6 dB	17.70 m	1.85 m	0.093 m	2.10 m
12 dB	35.78 m	3.70 m	0.185 m	4.43 m

3.4 Doppler Collision using GNSS Simulator

It is easier to observe Doppler collisions in a controlled environment where the relative Doppler between two geostationary satellites can be set to zero. Figure 3-13 shows the Doppler collision test setup. A Spirent GSS7700 simulator was configured to generate

measurements for two WAAS satellites (PRN 135 and PRN 138), located at actual coordinates as given in Table 3-3. The dynamic parameters for the WAAS satellites were defined such that both PRN 135 and PRN 138 were completely stationary as observed by a static user. The simulator introduced no multipath effects, and the user location was selected such that the relative code phase would result in a Doppler collision. Table 3-5 provides the user coordinates.

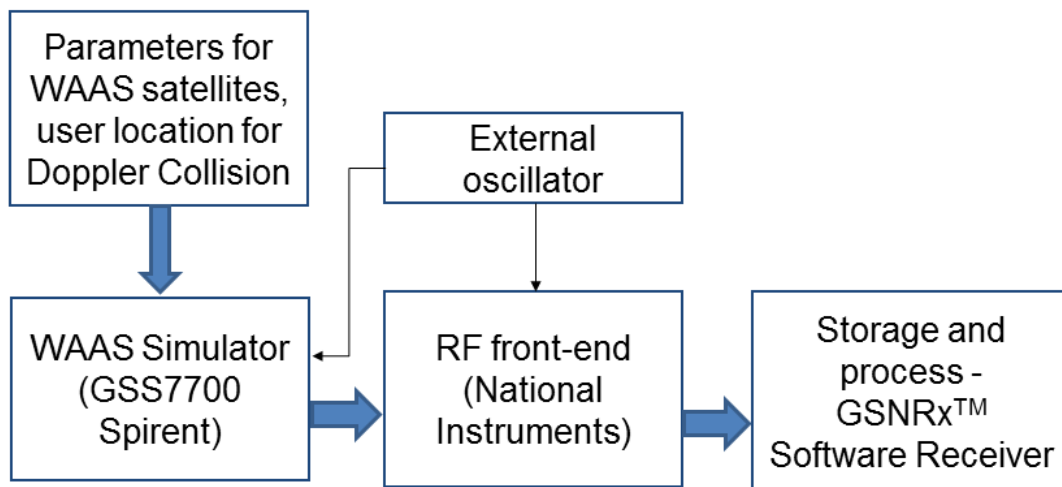


Figure 3-13 Test setup to observe Doppler collision using GNSS simulator

Table 3-5 User location to observe Doppler collision using GNSS simulator

Details	Latitude	Longitude	Height
User location at E1	51° 04' 47.8327' N	114° 08' 01.3606'' W	1118.50 m

Intermediate Frequency (IF) samples of the simulated Radio Frequency (RF) signal, consisting of in-phase and quadrature components, were collected at 20 MHz using 16 bit National Instrument front-end. The simulator and the front-end were driven using a common external oscillator resulting in zero Doppler for both the stationary WAAS satellites. A common oscillator is not required to observe Doppler collision, however, in this case, the common oscillator makes it simple to observe Doppler around 0 Hz on both simulated satellites. The IF data were processed using a modified and extended version of GSNRx™, a highly configurable software defined GNSS receiver developed at the University of Calgary (Petovello et al. 2008). The modified GSNRx™ has the capability to acquire and track WAAS satellites and generates code, carrier, and Doppler measurements with the external aid of RINEX ephemeris obtained from the IGS (Dow et al. 2009). Refer Appendix D for more details. Figure 3-14 shows a plot of a correlation triangle generated by a combination of I and Q values after phase lock.

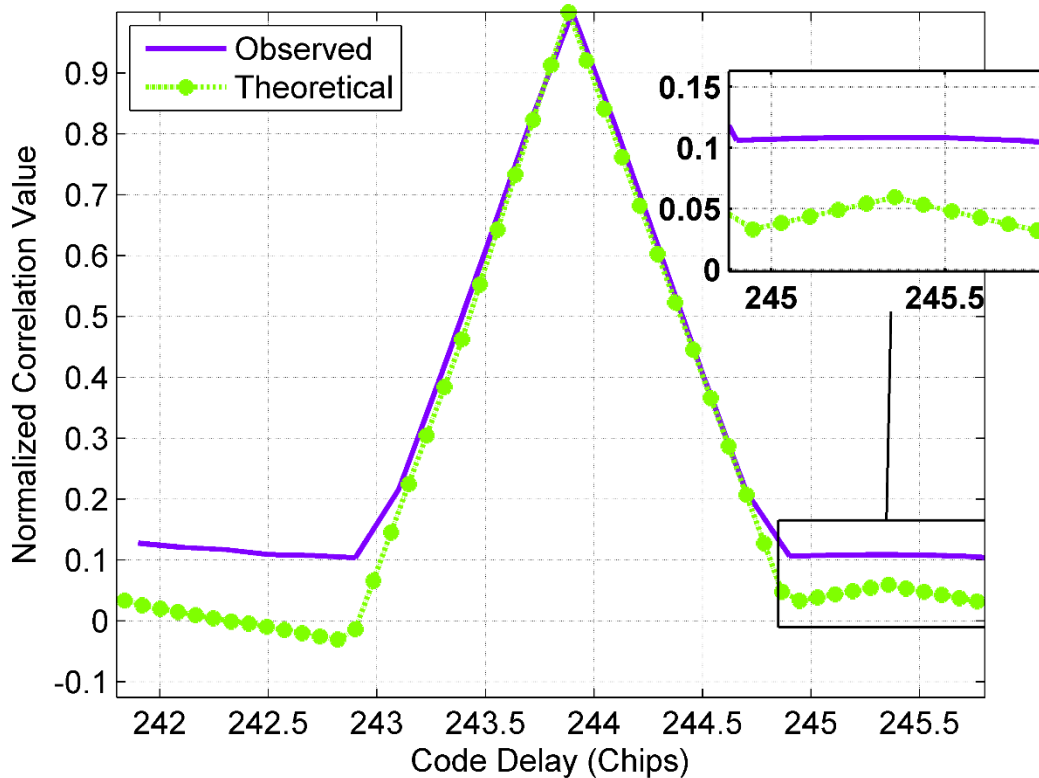


Figure 3-14 Correlation triangle with cross-correlation peak

The cross-correlation triangle of PRN 135 is visible next to the primary peak of PRN 138. In this example, the cross-correlation peak is more than half a chip from the primary peak, and thus no error will be introduced in the measurement when using standard correlator spacing. The user location is re-defined in the simulator, as shown in Table 3-3, to move the cross-correlation peak closer to the main peak and observe the impact on code measurements. The simulation was then re-run turning on the second satellite after 100 seconds. Figure 3-15 shows the code-minus-carrier phase combination (PR-CP) at the moment when the second satellite is introduced. Code-minus-carrier is plotted to highlight changes in the pseudorange due to Doppler collision (similarly to how the combination is commonly used to estimate code multipath). In this case, the effect of Doppler collision is

a bias in the code-minus-carrier combination because both WAAS satellites are static in the simulator settings.

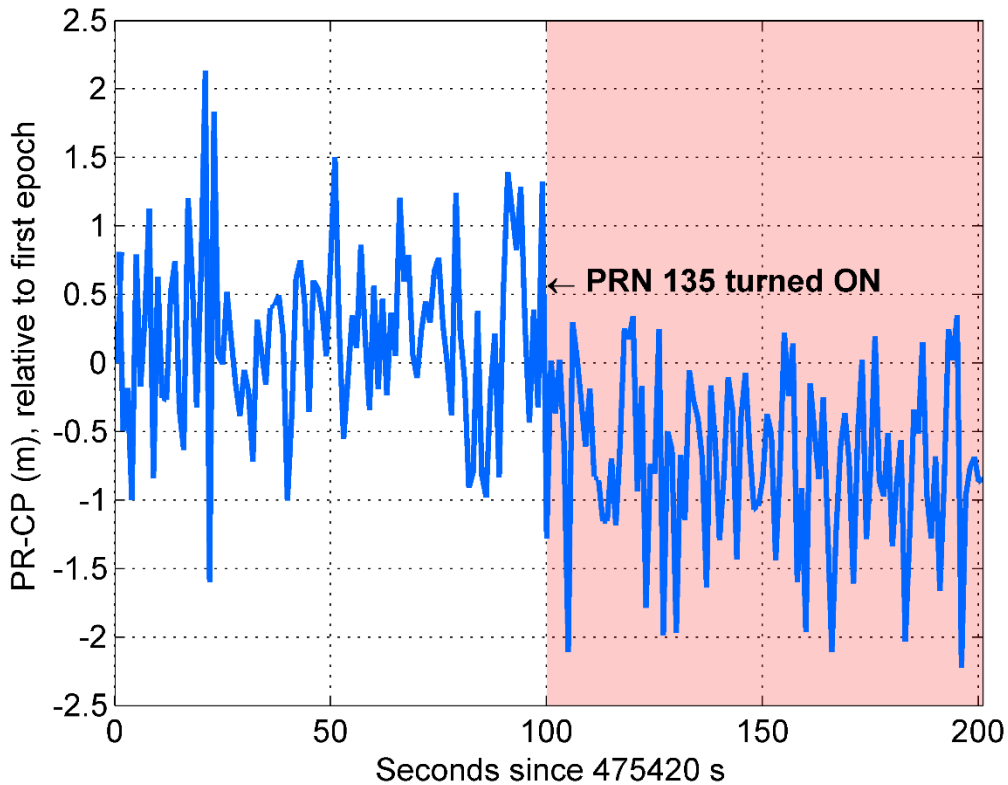


Figure 3-15 Doppler collision effect on pseudorange of PRN 138 when PRN 135 is introduced into the scenario

3.4.1 Pseudorange Observations during Doppler Collision

The next step is to observe a longer set of measurements when Doppler collision is in effect. The sampling frequency was reduced to 2 MHz to observe the worst case error. While all WAAS satellites currently have a 41 MHz bandwidth, some SBAS continue to use 2.2 MHz transponders (Wanninger 2008; Schempp et al. 2008). The simulator setup

was modified such that PRN 138 was moving slowly relative to the user with a Doppler close to 1 Hz. Samples were collected for 2 hours shown in Figure 3-16. The Doppler frequencies observed for PRN 135 and PRN 138, plotted after applying a 120 s moving average, differ by less than 1 Hz. The code-minus-carrier phase plot, relative to the first epoch, is also shown along with the estimated error bounds of the code variation due to Doppler collision. The observed error envelope does not match the theoretical error envelope exactly because the theoretical error envelope is derived based on ideal assumptions such as infinite receiver bandwidth, no receiver noise or multipath error. The DLL bandwidth used in the software defined receiver is 0.5 Hz, which is less than 0.85 Hz of relative Doppler and hence the maximum observed error is less than the theoretical bound. Furthermore, the theoretical error envelope always has an inherent error margin that is larger during the rise and fall of the error envelope. Appendix C describes the theoretical error and derives the estimated envelope using code phase observations. The third subplot shows the ratio of cross-correlation peak to primary peak (obtained using the I and Q values of the correlators), based on the given code phase of satellites. The code-minus-carrier phase plot indicates variation on code phase due to Doppler collision.

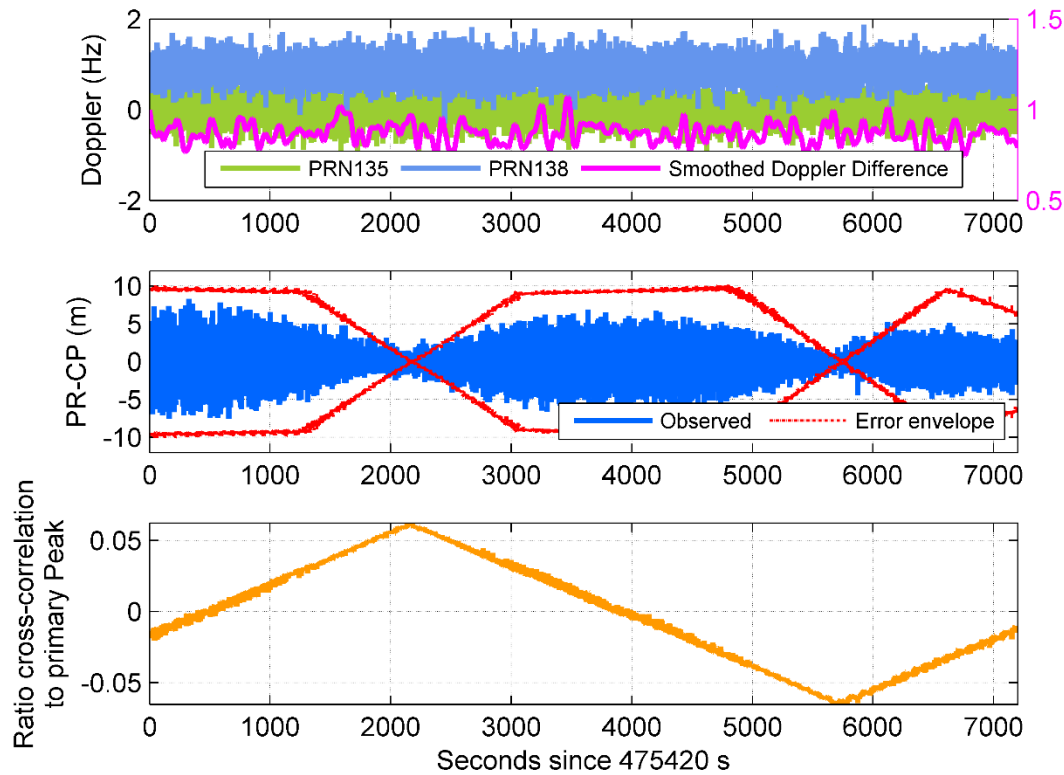


Figure 3-16 PRN 135 measurements during Doppler collision when PRN 138 is moving

Figure 3-17 shows the code-minus-carrier plot of measurements collected using Novatel ProPakV3, a commercial survey grade receiver under the same hardware-simulation conditions. ProPakV3 uses correlator type with a combination of the standard correlator, narrow correlator, and Pulse Aperture Correlator (PAC) (Novatel OEMV® Reference Manual 2010) and may have smaller code lock loop bandwidth. However, the Doppler collision variation is still significant and follows the error envelope over the entire test duration.

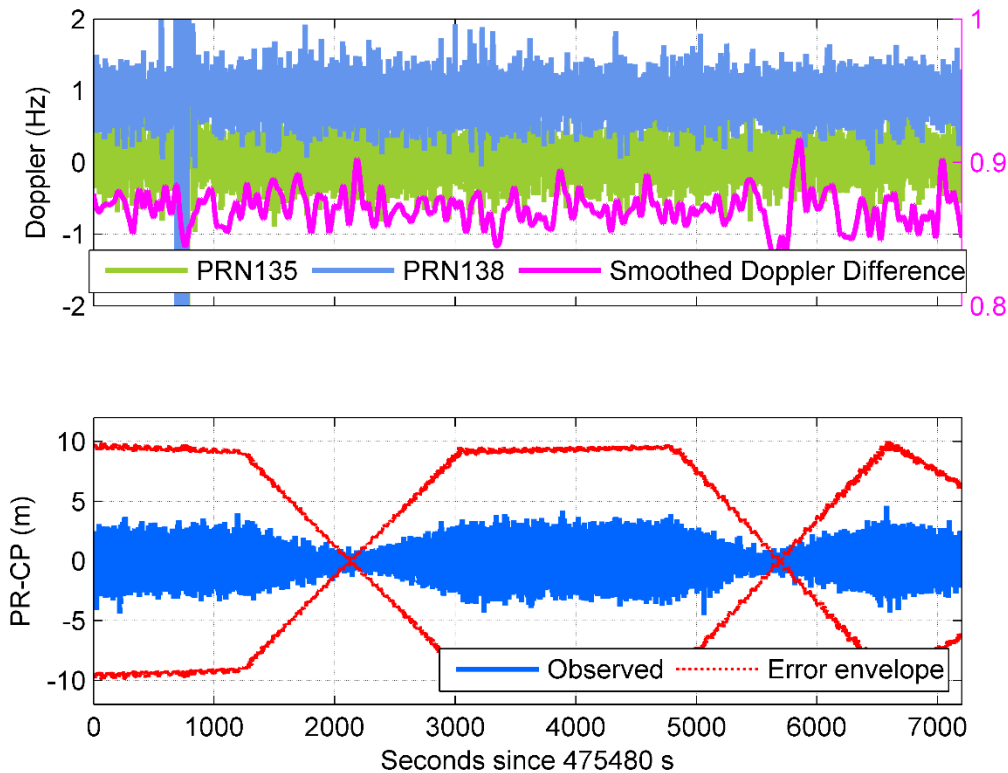


Figure 3-17 PRN 135 measurements using commercial receiver during Doppler collision

3.4.2 Nature of Doppler Collision Error

As seen in Figure 3-16, the cross-correlation peak introduces errors in code measurements that are not biases but instead follow an envelope. The cross-correlation error varies as a function of relative phase delay (Spilker Jr. 1996). If the relative magnitude of the cross-correlation peak is small, the error variation is sinusoidal with zero mean. However, if the relative magnitude of the cross-correlation peak is large, the error signal is not sinusoidal, and the error might not average out to zero. Given the same signal strength for two GEO satellites, the relative power of the cross-correlation peak is

24 dB, and the error due to the cross-correlation peak would be similar to a multipath with Signal to Multipath Ratio (SMR) of 20 dB (Ray 2000). Most recently Nievinski and Larson (2014) applied this effect to a multipath simulation. Multipath varies because the carrier phase between the Line Of Sight (LOS) and the Non-LOS signal varies with time. The sign of the error can be positive or negative depending on the relative carrier phase and is not generally zero-mean (Ray 2000; Gowdayyanadoddi et al. 2015). Similarly, in Doppler collision, the error in the code measurements follows a quasi-random variation. Figure 3-18 shows an enlarged window of first 200 s in Figure 3-16. Over the period, the mean value of relative Doppler is 0.87 Hz with a carrier phase difference of 0.13 cycle every second. The value of 0.13 cycle every second corresponds to 13 oscillations of the code error every 100 s. The error mean value is close to zero because the cross-correlation peak is typically more than 20 dB lower than the main peak. Although the error mean value is close to zero, the oscillating behavior can still affect RTK performance.

Lestarquit et al. (2003) shows that carrier smoothing gives good results to mitigate Doppler collision error during non-zero relative Doppler mainly because the mean value of a quasi-random measurement error is close to zero. If the relative Doppler is zero, the quasi-random variation of measurement error manifests as a constant bias and no amount of carrier smoothing can remove the measurement error. The effect of carrier smoothing is equivalent to code-carrier combination through Kalman filtering (Hatch 1991). If the relative Doppler is non-zero, the quasi-random variations will lead to smoothing of state estimates, albeit with a higher time of convergence. However, if the

relative Doppler is zero, the code-carrier combination through Kalman Filter will provide incorrect state estimates and can lead to wrong ambiguity fix.

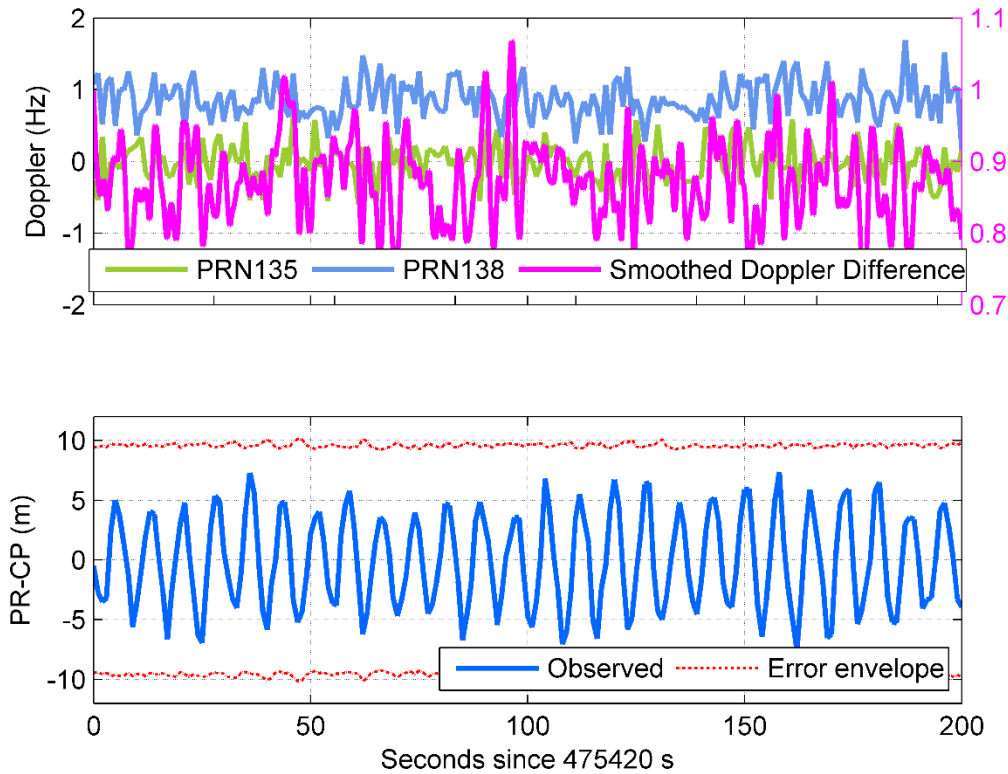


Figure 3-18 PRN 135 measurements during first 200 s of Doppler collision when PRN 138 is moving

3.5 Doppler Collision using Live Data

Until this point, Doppler collision has been observed using simulated signals. Figure 3-3 shows that significant time duration is available to observe Doppler collision using live data. The section below describes an attempt to observe Doppler collision using live data.

3.5.1 WAAS Live Data

The test setup as described in Figure 3-13 was modified to collect live signals of GPS and WAAS using a geodetic grade antenna. Table 3-6 provides the details. Doppler variations of PRN 135 and PRN 138 were observed for successive days to determine periods where small relative Doppler occurred. On Thursday, 25 February 2016, a period beginning at 00 hours 40 minutes was identified and IF data was collected at a sampling rate of 2 MHz for I/Q samples. The data was processed using modified GSNRx™ software receiver to obtain receiver measurements. Figure 3-19 shows one such window where Doppler collision was observed. The variations in measurement errors correspond to the estimated error envelope.

Table 3-6 Doppler collision live data setup settings

Date	26 February 2016		
Details	Latitude	Longitude	Height
PRN 135 at start time	0° 2' 0.0844'' N	132° 59' 3.4927'' W	35,778.959 km
PRN 138 at start time	0° 1' 4.1902'' W	107° 16' 48.0152'' W	35,777.283 km
User location RxA	51° 04' 47.9162'' N	114° 08' 01.8533'' W	1118.8315 m

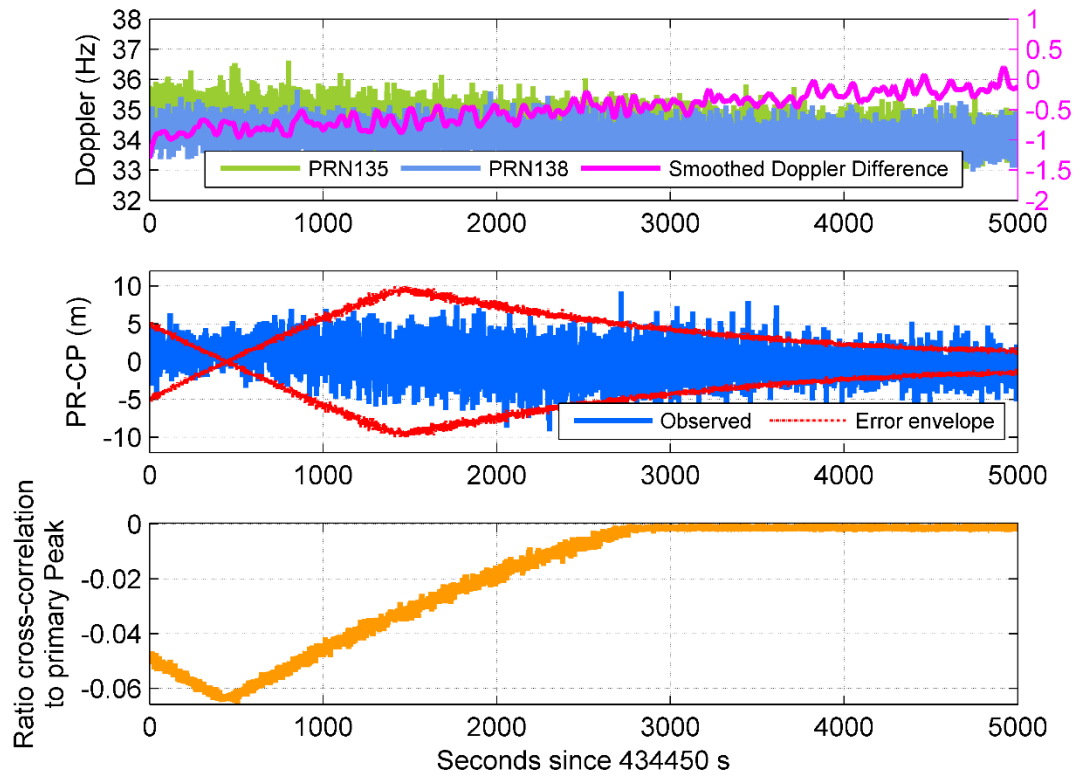


Figure 3-19 Live signal PRN 135 code measurements during Doppler collision

Figure 3-20 shows an example of code-minus-carrier collected at RxA, in the same time window on a different day when no Doppler collision was observed. The combination of code phases should result in Doppler collision. However, the Doppler difference is around 2 Hz in this case, and hence no Doppler collision is observed. The test duration has no quasi-periodic pattern in the code-minus-carrier combination.

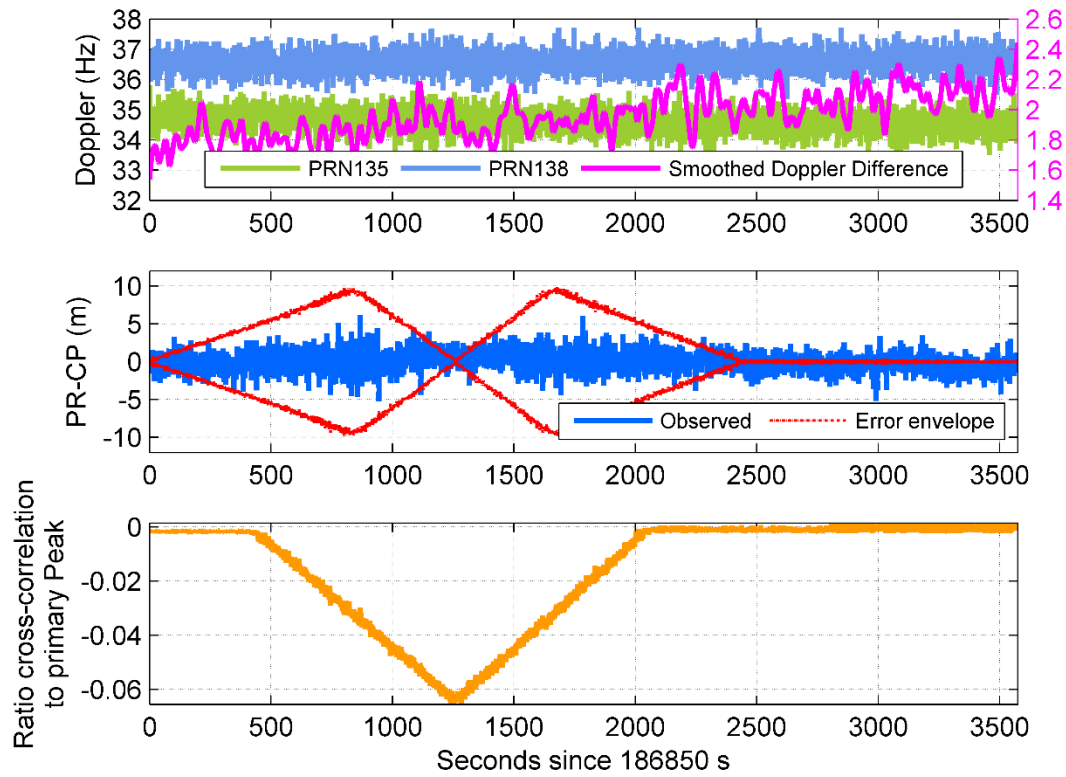


Figure 3-20 Live signal code measurements during non-likely Doppler collision conditions because relative Doppler is significant

3.5.2 IRNSS Live Data

An effort was then made to observe Doppler collision using live IRNSS signals. A commercial grade receiver with standard correlator chip spacing was used to collect live data of IRNSS at Bengaluru. After collecting data for multiple days, a window of Doppler collision event was identified on Sunday, 28 May 2017. Figure 3-6 shows that satellites 1C and 1G have small relative Doppler for a long duration. The code-minus-carrier combination for satellite 1G is plotted in Figure 3-21 along with the variation of Doppler frequencies and the relative Doppler between two satellites 1G and 1C, which is between ± 2 Hz throughout. Superimposed on the code-minus-carrier is the estimated error envelope obtained using the observed code phase values. The significant variation in code-minus-carrier measurement is in sync with error envelope. The bottom plot shows the ratio of the cross-correlation peak to primary peak.

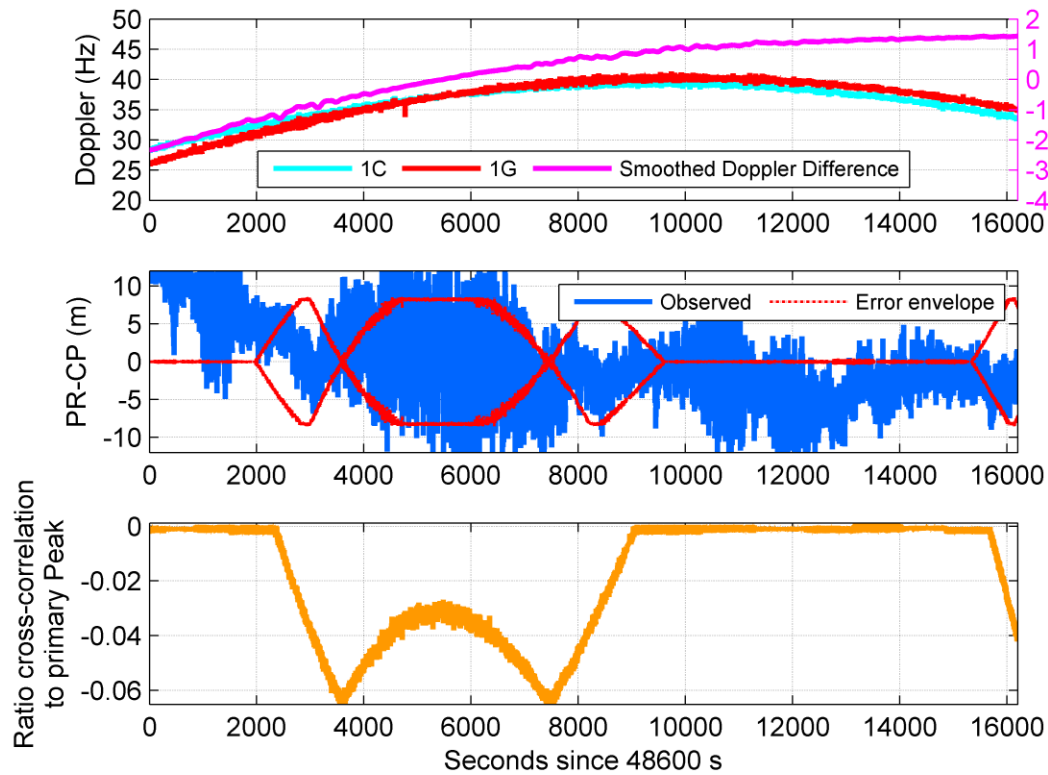


Figure 3-21 Live signal IRNSS 1G measurements during Doppler collision

Figure 3-22 shows code-minus-carrier measurement of 1C during the same window. Similar to 1G, there is an envelope in code-minus-carrier measurement. However, the magnitude of code-minus-carrier variation is small in comparison to 1G. During the test period, 1C is at an elevation of about 75° with 5 dB higher signal strength as compared to 1G, which is at an elevation of 28.66° . Thus the effect of Doppler collision is large on 1G.

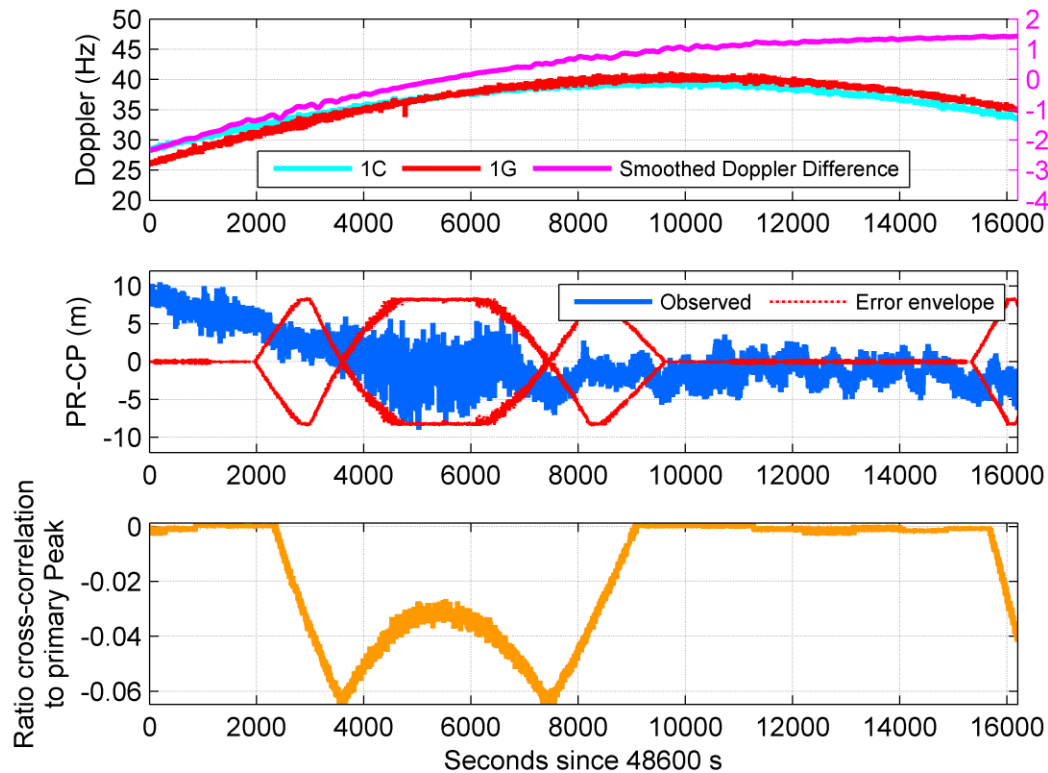


Figure 3-22 Live signal IRNSS 1C measurements during Doppler collision

3.6 Impact of Doppler collision on Carrier Phase Measurements

Until this point, the entire analysis of Doppler collision has focused on code measurement error. Doppler collision is similar to multipath effect and like multipath, it may impact carrier the phase measurement as well. Carrier phase multipath is widely studied and multiple mitigations methods are available (Braasch 1996; Ray 2000). This would act as a starting point to derive the impact of Doppler collision on carrier phase measurements.

Based on Ray et al. (1999), the phase error model for two geostationary satellites, considering all static conditions, is given as

$$\tan(\theta_0 - \hat{\theta}_0) = \frac{\alpha_1 R_c(\tau_0 + \Delta\tau_1 - \hat{\tau}_0) \cdot \sin(\Delta\theta_1)}{R_c(\tau_0 - \hat{\tau}_0) + \alpha_1 \cos(\Delta\theta_1) R_c(\tau_0 + \Delta\tau_1 - \hat{\tau}_0)} \quad 3.1$$

where $\tan(\theta_0 - \hat{\theta}_0)$ is the error due to Doppler collision in carrier phase, α_1 is the desired and secondary signal coefficient, $\Delta\theta_1$ is the relative phase, $R_c(\tau_0 - \hat{\tau}_0)$ is the correlation function, $\Delta\tau_1$ is the relative time delay. Dividing the numerator and denominator by

$R_c(\tau_0 - \hat{\tau}_0)$ and assigning $K_c = \frac{R_c(\tau_0 + \Delta\tau_1 - \hat{\tau}_0)}{R_c(\tau_0 - \hat{\tau}_0)}$, equations 3.1 is written as

$$\tan(\theta_0 - \hat{\theta}_0) = \frac{\alpha_1 K_c \cdot \sin(\Delta\theta_1)}{1 + \alpha_1 K_c \cdot \cos(\Delta\theta_1)} \quad 3.2$$

Appendix C shows that the maximum value of $\alpha_1 = 0.0616$. If the relative phase is zero, the term in equation 3.2 is zero. If the relative phase is out of phase, the maximum value of equation 3.2 is 0.0616, which approximates to 3 degrees. This amount of carrier phase error is below the typical carrier phase noise of 5 degrees (Kaplan and Hegarty 2005) and hence the effect of Doppler collision on a carrier phase measurement is not significant.

In summary, Doppler collision is a possible event if parameters that determine Doppler collision are in a certain range. The primary factor is the relative Doppler which defines the window of Doppler collision. The cross-correlation function, relative code, and signal strength difference determine the magnitude and spatial extent of the Doppler collision.

Other parameters such as navigation message and carrier phase define the sign of the Doppler collision error. Doppler collision is observed using multiple experiments using simulated signals and later with live signals of WAAS and IRNSS. Lastly, the impact of Doppler collision on carrier phase measurements is studied and analysis shows that the effect is negligible. The next chapter presents the impact of Doppler collision on an RTK solution.

Chapter Four: **RTK Positioning during Doppler Collision**

The previous chapter demonstrates Doppler collision and its impact on code measurements. This chapter performs single-frequency RTK positioning using measurements affected by Doppler collision. The chapter is organized as follows: An RTK solution using hardware-simulated data is obtained. The RTK solution is further analyzed by reducing the number of satellites to observe the impact of Doppler collision when using a limited constellation that includes geostationary satellites. The behavior of ambiguity convergence is discussed to understand the effect on TTFFA. A similar analysis is conducted on live data collected over two baselines in Calgary. Finally, mitigation techniques are shown to reduce the impact of Doppler collision.

Section 2.1 reviewed the theoretical background of RTK positioning. RTK positioning uses code and carrier phase measurements to compute a differential position solution. Between-receiver SD removes atmospheric and satellite clock errors. The float solution is first obtained using the between-receiver single-differenced observations that includes an estimated receiver clock offset and single-differenced ambiguities. The single-differenced observations are then subtracted between-satellites to eliminate the receiver clock to form double-differenced ambiguities and as a consequence decouples the estimated ambiguities from the receiver clock offset. The double-differenced ambiguities are then fixed using the LAMBDA algorithm (Teunissen 1993; de Jonge and Tiberius 1996). The differencing steps and ambiguity resolution method are realized in the modified and extended version of PLANSoft™, a C++ based RTK solution software developed by the PLAN Group (Ong et al. 2009). The extended version can accept

observations from geostationary satellites such as WAAS and compute a combined GPS-WAAS RTK solution. Appendix D provides details about of the software and its implementation. The software processes both simulated and live data during Doppler collision and normal conditions as described in the following sections.

4.1 RTK Positioning during Hardware-Simulation of Doppler Collision

Section 3.4 demonstrated a hardware-simulation of Doppler collision and the variation of code measurements errors. In order to study the impact of Doppler collision on an RTK solution, data is collected at two or more locations during the Doppler collision event.

4.1.1 Test Setup

The simulation of Doppler collision obtained using the GNSS simulator is expanded to collect data at two additional locations. Figure 4-1 shows the complete test setup. The rover locations are selected at 900 m and 1800 m east of the reference position (Rx1) and are marked as Rx2 and Rx3 respectively. The baseline lengths are reasonable for single-frequency (L1) RTK. East-West baselines have been chosen because the cross-correlation that leads to Doppler collision is a function of relative range and for an observer on the surface of the earth, the relative range between two GEO satellites varies most rapidly when moving East-West. Table 4-1 provides coordinates of all three locations.

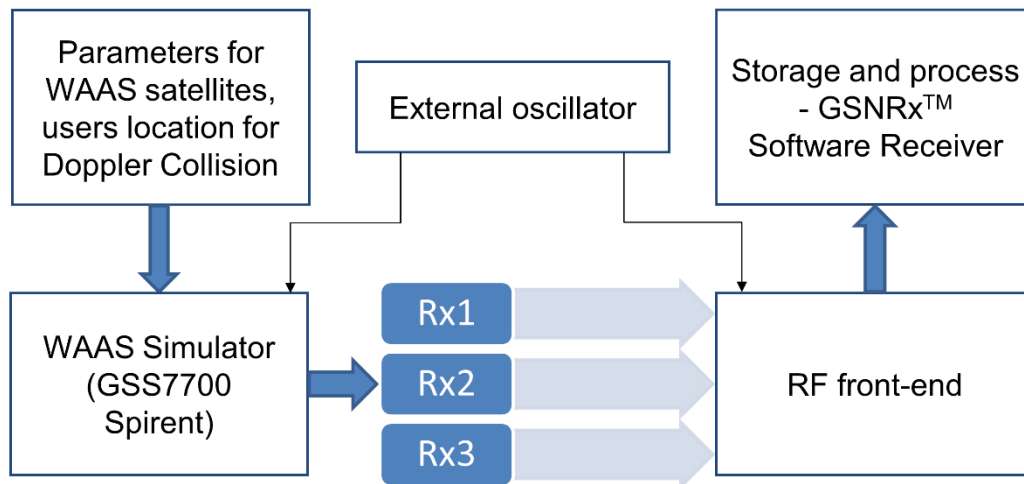


Figure 4-1 Simulation of Doppler collision at three different locations using GNSS simulator

Table 4-1 Doppler collision simulation additional user locations coordinates

User location	Latitude	Longitude	Height
Rx1	51 ⁰ 04' 47.8320'' N	114 ⁰ 07' 38.2472'' W	1118.51 m
Rx2	51 ⁰ 04' 47.8295'' N	114 ⁰ 06' 52.0204'' W	1118.58 m
Rx3	51 ⁰ 04' 47.8219'' N	114 ⁰ 06' 5.7936'' W	1118.77 m

Figure 4-2 shows the effect of Doppler collision on the code measurements of PRN 135 at the three locations. Rx1 experiences Doppler collision for entire test duration whereas Rx2 and Rx3 have periods of Doppler collision mixed with periods of no collision. For further analysis, the test duration is divided into three periods:

P1: Doppler collision observed on all three receivers – start time 475420 s

P2: Doppler collision on two receivers – start time 478600 s

P3: Doppler collision observed only on one receiver – start time 481180 s and end time 482620 s

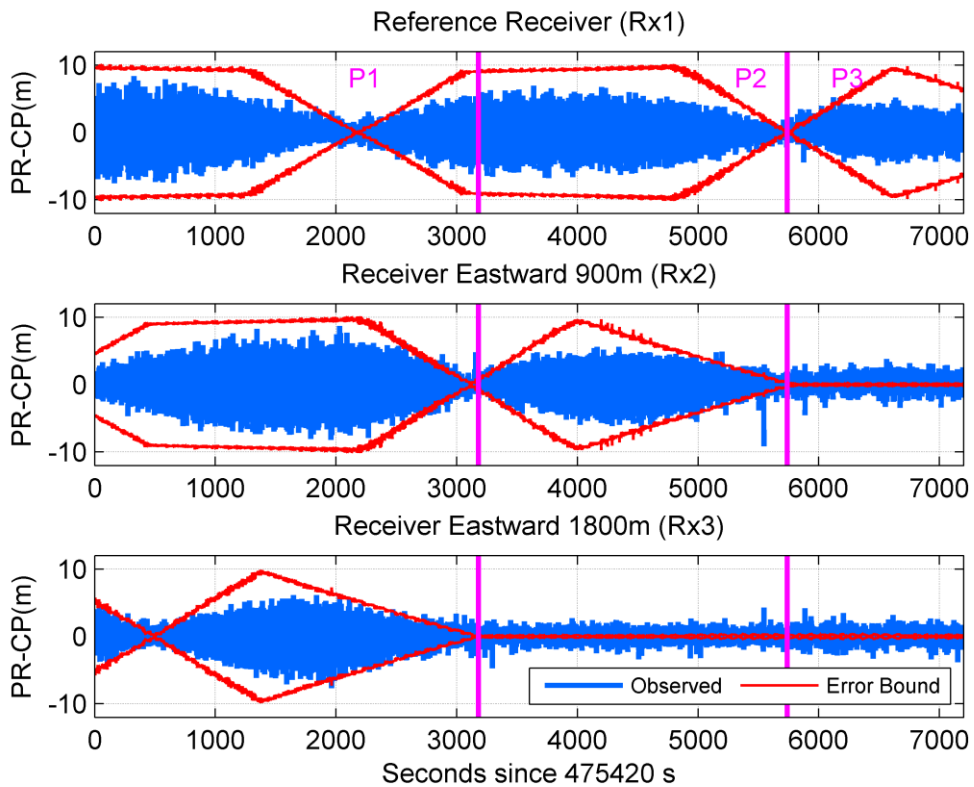


Figure 4-2 PRN 135 code-minus-carrier measurements showing effect of Doppler collision simulation at 3 locations along with error envelope in red

An RTK solution is obtained using receiver Rx2 and Rx3 because the combination of Rx2 and Rx3 provides time periods where all three conditions are observed: Doppler collision on both receivers, Doppler collision on a single receiver and no Doppler collision. Figure

4-3 shows the float solution between-receiver single-differenced residuals. During period P3, there is no Doppler collision, and the single-differenced residuals are uniformly distributed without any pattern. During period P2, when Doppler collision is observed on Rx2, a pattern corresponding to Doppler collision is seen in the single-differenced residuals. During period P1, a woven pattern corresponding to Doppler collisions on both Rx2 and Rx3 is seen in the single-differenced pseudorange residuals.

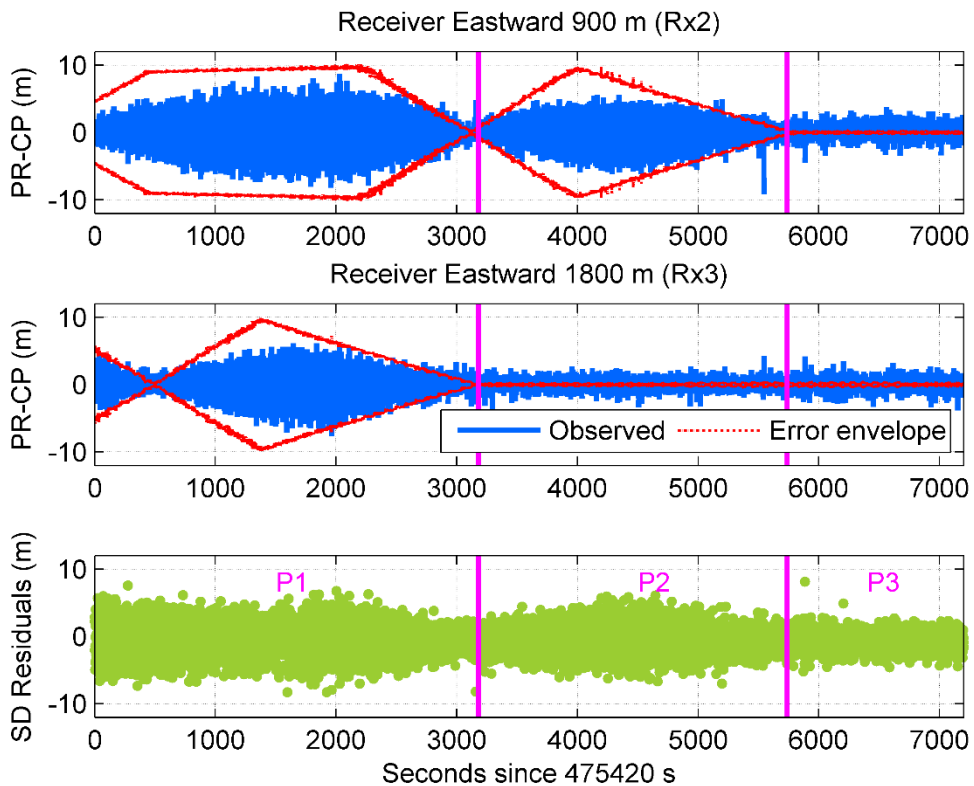


Figure 4-3 PRN 135 code-minus-carrier measurements and single-differenced pseudorange residuals between two receivers

Figure 4-4 shows the distribution of single-differenced pseudorange residuals for both PRN 135 and 138 during the test periods. For PRN 135, the standard deviations during

P1 and P2 are 2 and 1.7 times larger than during P3, respectively. Similarly, for PRN 138, the standard deviations during P1 and P2 are 1.7 and 1.35 times larger than during P3, respectively. There is an increase in standard deviation of single-differenced pseudorange residuals when Doppler collision is observed only on one receiver and observed on both the receivers. The larger variation in single-differenced residuals will have an impact on the convergence of float ambiguities and affect TTFFA.

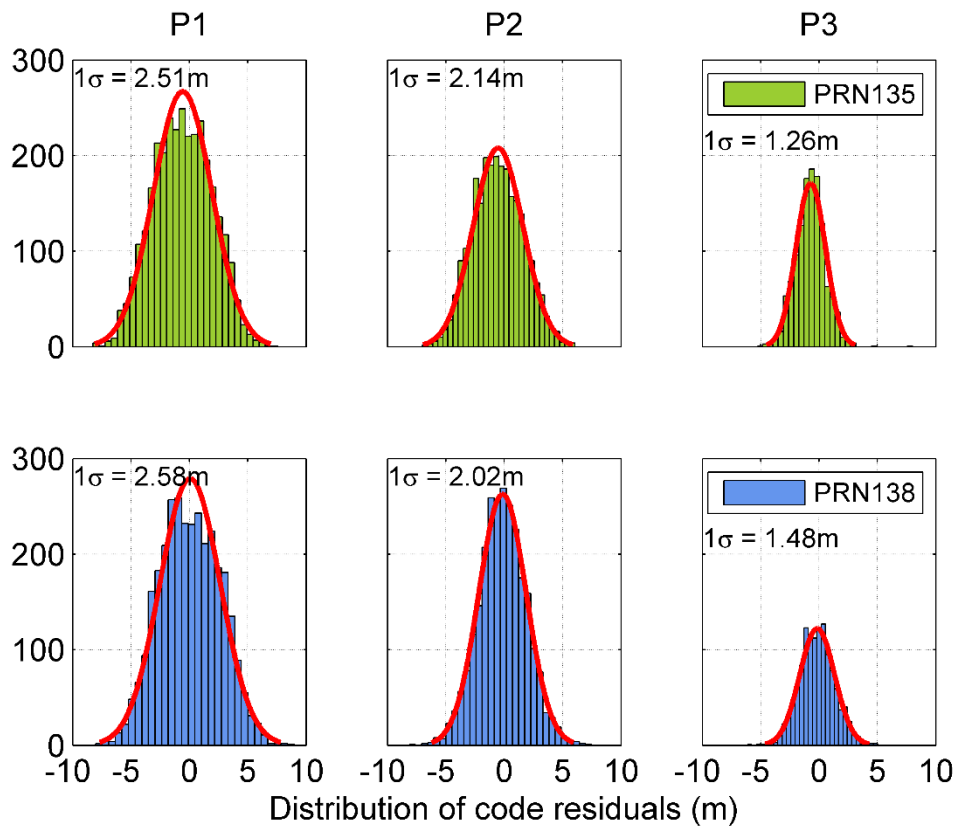


Figure 4-4 Distribution of single-differenced residuals of WAAS satellites during Doppler collision (P1 and P2) and normal conditions (P3) respectively

Using all satellites in view, a fixed solution is obtained over the 900 m baseline (using Rx2 and Rx3) for periods P1, P2, and P3. Figure 4-5 shows that the ambiguities, including PRN 135 and PRN 138, can be fixed even if a Doppler collision is occurring. The difference in TTFFA across the periods is small because of a large number of observations in the RTK solution. The following section describes the purpose behind reducing the number of satellites and demonstrates the effect of Doppler collision on the RTK solution.

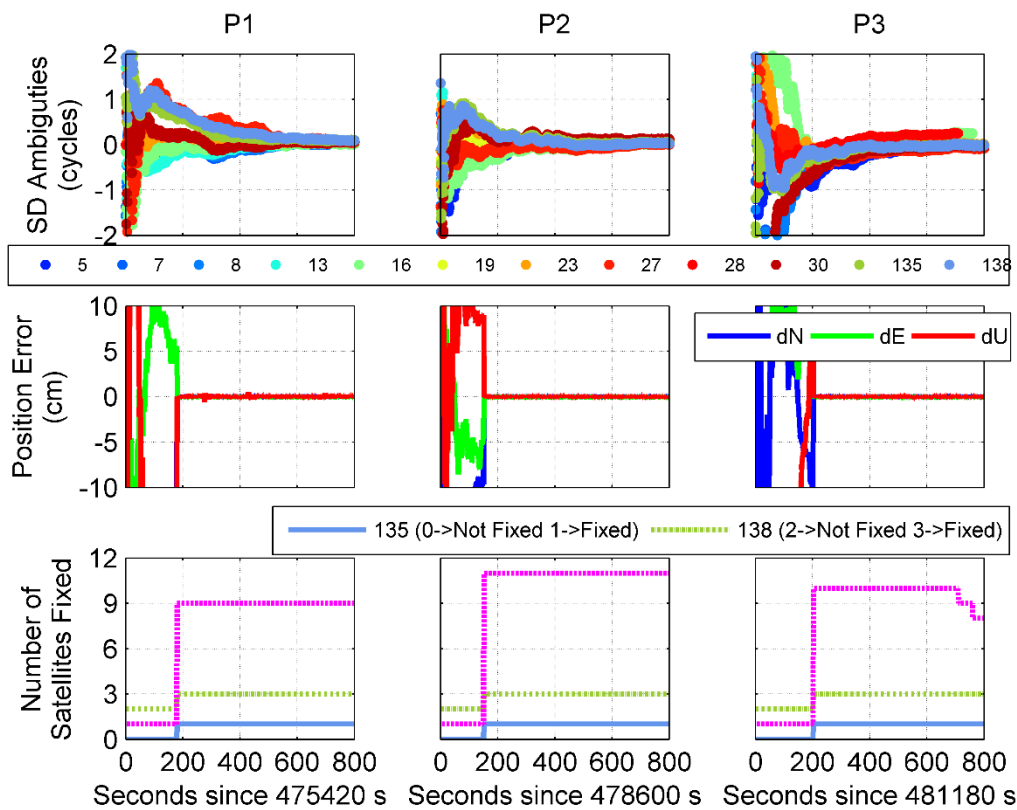


Figure 4-5 RTK solution using Rx2 and Rx3, baseline 900 m. Bottom section indicates ambiguities are fixed for WAAS satellites PRN 135 (blue) and PRN 138 (green)

4.1.2 Selection of Satellites

Figure 4-6 shows a sky plot during the test duration at Rx1. The satellite visibility is equivalent at the remaining two receivers since the baselines are 900 m and 1800 m respectively. The WAAS satellites PRN 135 and PRN 138 are available at an elevation of 30° in the southern sky.

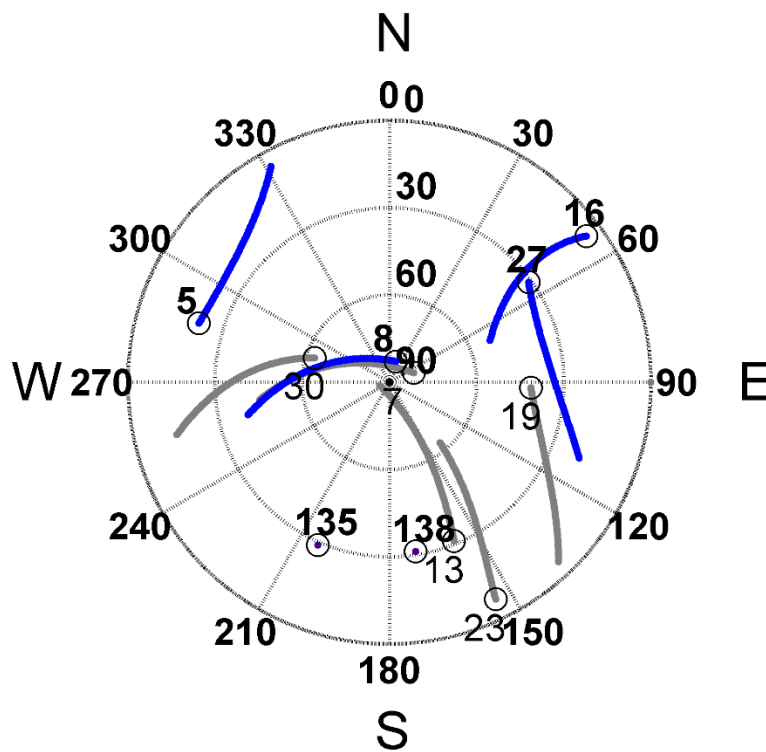


Figure 4-6 Sky plot observed at Rx1 during Doppler collision simulation. Satellites in blue are common GPS satellites used in RTK solution. The circles indicate the location of the satellite at the end of the test.

GPS satellites have varying elevation as shown in Figure 4-7. There are additional GPS satellites available during the test duration. However, they are not considered in the sky plot because of the limited length of availability. The GNSS simulator is configured to have the same signal strength for all satellites during the entire test duration. A few GPS satellites such as 13, 19 and 30 are tracked and then lost during the test duration as shown by the drop in C/N_0 value in Figure 4-7.

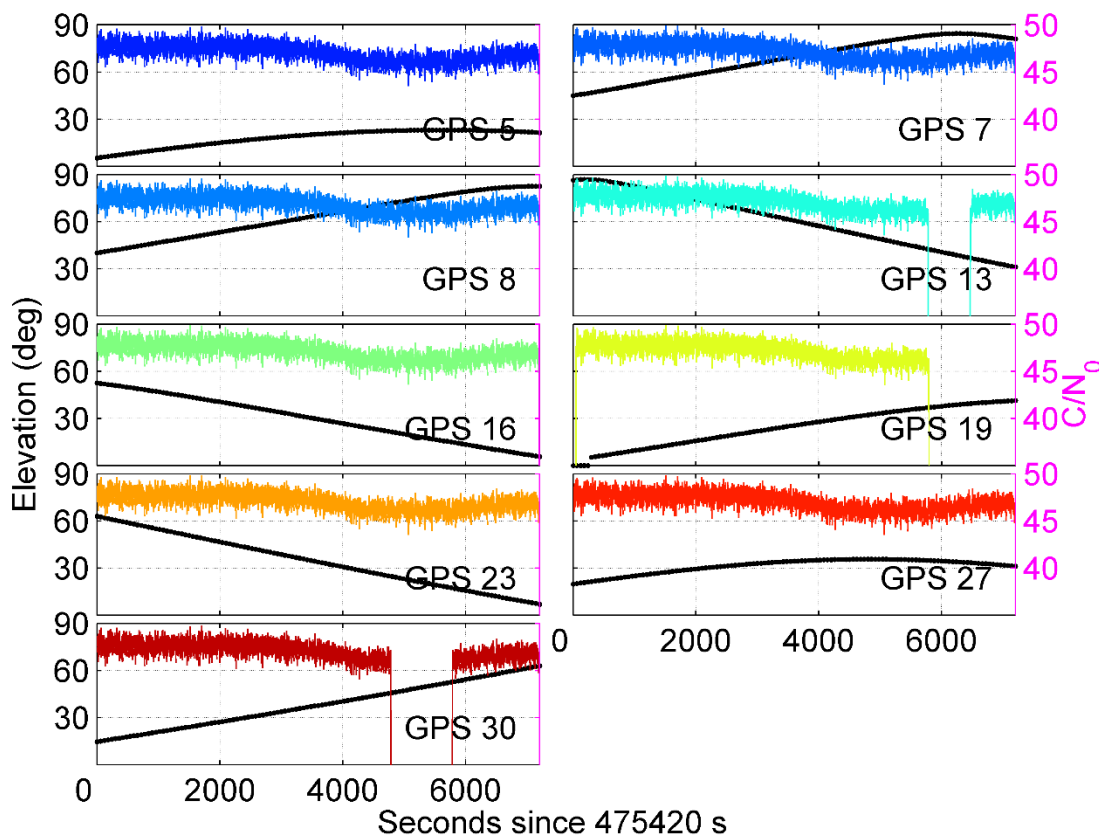


Figure 4-7 Elevation and C/N_0 plot of GPS satellites Rx1

Figure 4-8 provides the code-minus-carrier measurements for all GPS satellites. Based on the geometry of satellites and their availability, GPS satellites 5, 8, 16 and 27 are

selected as common satellites across combinations. Between 4000 s and 6000 s, there is an envelope in code-minus-carrier of PRN 5 and 27. However, the relative Doppler between two satellites is varying over hundreds of Hz, and there is no Doppler collision between these two GPS satellites. Also, code phase combinations do not provide likely conditions for Doppler collision. As shown in Figure 4-7, after 4000s seconds into the test, signal strengths across all satellites decrease, and this is one of the reasons for large spikes in code-minus-carrier measurements across all satellites, the small envelope in the case of satellites 5 and 27 and loss of lock for 13, 19 and 30.

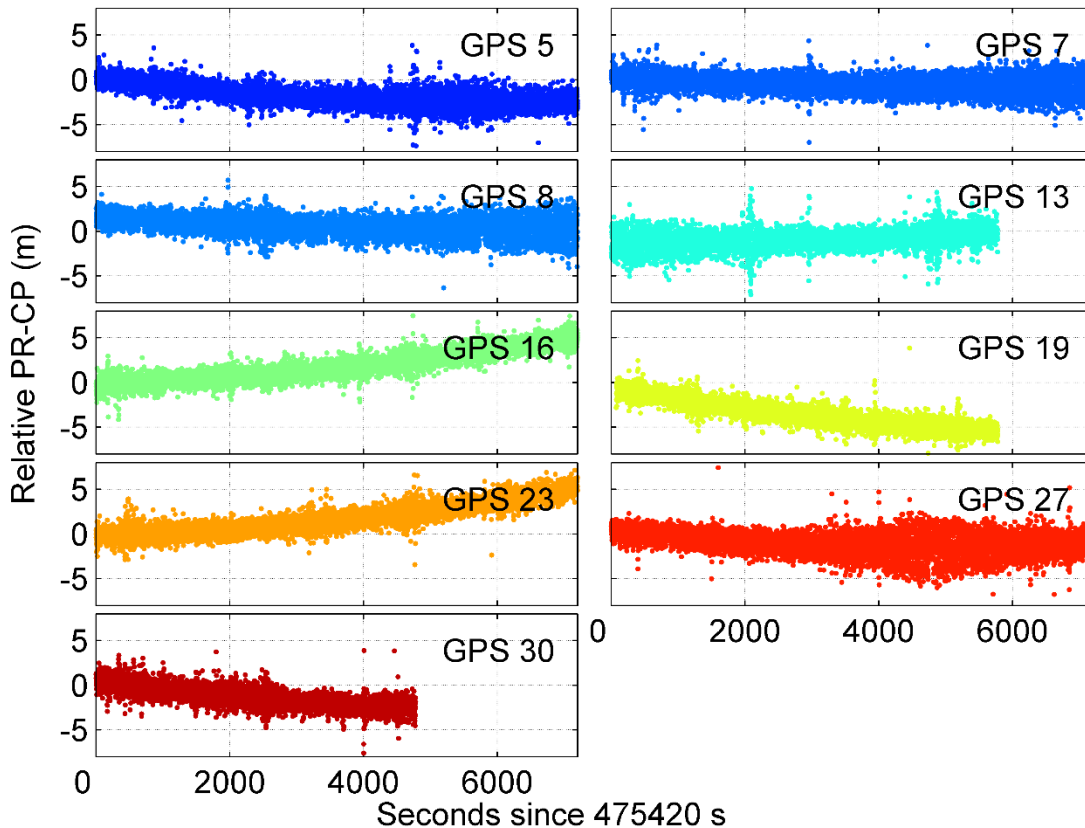


Figure 4-8 Code-minus-carrier observations of GPS satellites at Rx1

To observe the impact of the WAAS observations, a combination of 4 GPS + 2 WAAS satellites (PRNs 5, 8, 16, 27, 135, and 138) was selected and then compared to a set of 6 GPS satellites (PRNs 5, 8, 16, 27, and additional two GPS satellites: 7 and 23, 13 and 19, and 23 and 30 during P1, P2 and P3 respectively). This combination of 4 GPS + 2 WAAS satellites is similar to IRNSS which has 4 IGSO and 3 GEO satellites. The two additional GPS satellites that replace the WAAS satellites were chosen to obtain similar Position Dilution of Precision (PDOP) for both combinations over the duration of the test as shown in Figure 4-9. Figure 4-9 also shows PDOP value when all 6 GPS + 2 WAAS satellites are selected.

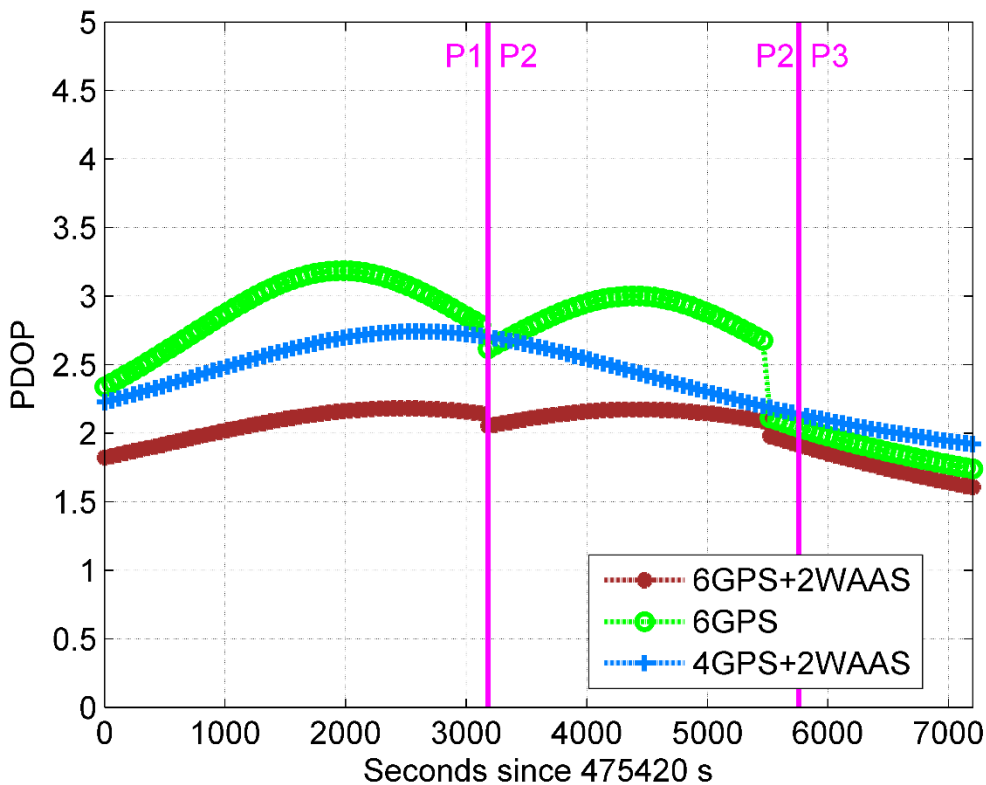


Figure 4-9 PDOP plots of various combinations of satellites at Rx1

4.1.3 TTFFA Analysis

Figure 4-10 shows the ambiguity convergence time of an RTK solution between Rx2 and Rx3 using the combination of 4 GPS + 2 WAAS against the solution using only 6 GPS satellites, which are not affected by Doppler collision. When two of the six satellites are replaced by GEO satellites, the convergence time in comparison to 6 GPS solution increases significantly during P1, when Doppler collision is occurring on both receivers. The estimated standard deviation (σ) of the single-differenced ambiguities also converges at a slower rate. However, during P2, when Rx3 is not in Doppler collision, the impact is smaller than during P1. During P3, the convergence of the ambiguity states closely follows the pattern of GPS satellites. To further observe the effect, the data was reprocessed resetting the estimation process every minute to obtain a series of TTFFA estimates. Figure 4-11 shows the TTFFA using 4 GPS + 2 WAAS satellites as well as the results obtained using 6 GPS and 6 GPS + 2 WAAS satellites.

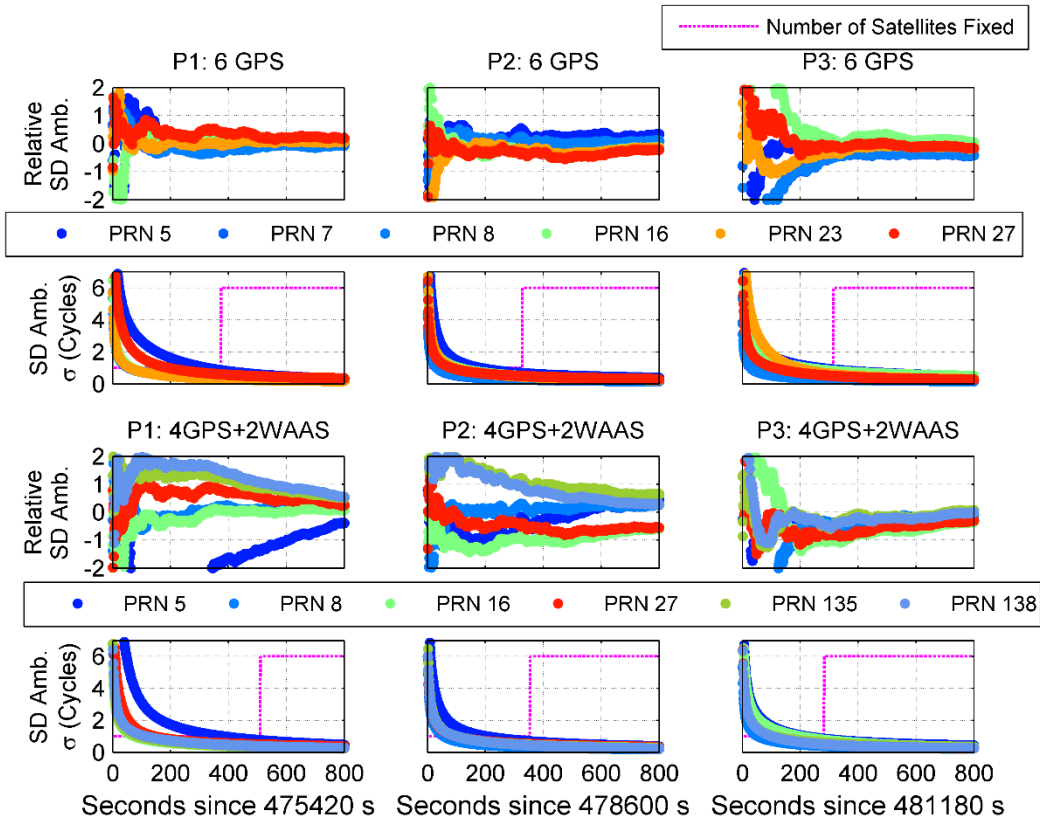


Figure 4-10 Ambiguity convergence during Doppler collision and normal conditions for an RTK solution between Rx2 and Rx3

Figure 4-11 also provides TFFFA using 6 GPS + 2 WAAS satellites which acts as a baseline to assess the impact of reducing the number of satellites to six and the effect of two satellites experiencing Doppler collision. During P1, the impact of Doppler collision is severe, and thus a substantial increase in TFFFA is observed using 4 GPS + 2 WAAS against a combination of 6 GPS satellites. During P2, the impact of Doppler collision is present only on one receiver and the difference in TFFFA is smaller than P1. The jumps in TFFFA using 6 GPS + 2 WAAS satellites or 6 GPS satellites correspond to the changes in GPS satellite combinations over the test duration.

4.1.4 De-Weighting Doppler Collision Observations

One possible approach to mitigate the effect of Doppler collision is to de-weight the affected observations. As shown in Figure 4-3, the code errors on the WAAS satellites increase during P1 and P2. The RTK solutions were re-calculated with the affected observations de-weighted by a factor of 4 (the squared value of the ratio of the code residuals standard deviation between P1 and P3). The TTFFA for the 4 GPS + 2 de-weighted WAAS satellite combination is also included in Figure 4-11. At the peak of Doppler collision during period P1, the TTFFA using de-weighting WAAS observations is similar to the equal weight solution with a difference of less than 5 %. As the effect of Doppler collision recedes in P2, the TTFFA using the de-weighted solution increases and the largest during P3 (when no Doppler collision is occurring and is thus an incorrect observation weight). Thus de-weighting the observations during Doppler collision and applying normal weights when there is no Doppler collision could be an efficient solution to mitigate the effect of Doppler collision in an RTK solution, particularly when there are many signals available.

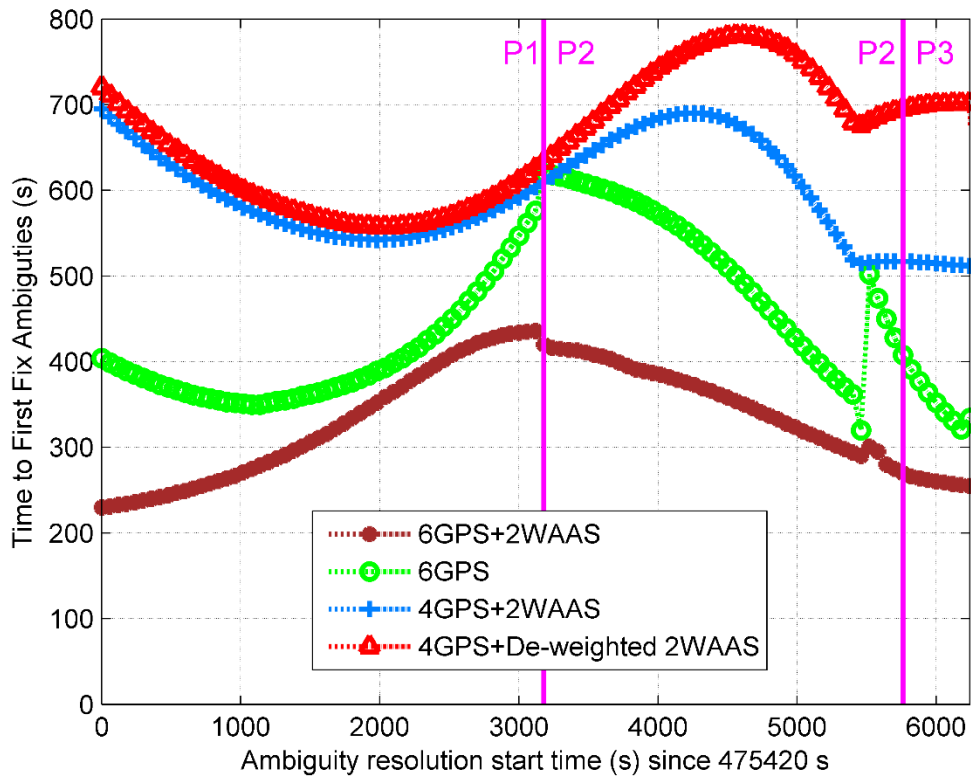


Figure 4-11 TFFFA during Doppler collision and normal conditions

4.2 RTK Positioning during Live Doppler Collision

This section describes RTK positioning during Doppler collision observed using live signals. The Doppler crossing window was selected after recording Doppler variations of WAAS satellites over successive days. Along with the user location RxA, as defined in section 3.5.1, two more locations, RxB and RxC, were selected. Similar to the simulation setup in section 4.1.1, the locations were selected in an East-West direction. Each location is an open sky environment with minimum possible multipath. Table 4-2 provides all three user coordinates. Figure 4-12 shows the location of all three receivers over a geographical region in Calgary, Canada.

Table 4-2 Doppler collision live signal user locations coordinates

User location	Latitude	Longitude	Height
RxA	51° 04' 47.9162'' N	114° 08' 01.8533'' W	1118.831 m
RxB	51° 04' 47.9168'' N	114° 08' 01.3605' W	1118.504 m
RxC	51° 04' 13.8212'' N	114° 08' 46.0586' W	1089.304 m



Figure 4-12 Three user locations for live data collection during Doppler collision

4.2.1 Test Setup

A test setup similar to Figure 4-1 is formed, except that the RF port is connected to geodetic grade antenna rather than a hardware simulator. Figure 4-13 shows the complete test setup at all three locations. RxA and RxB collected I/Q samples at 2MHz whereas RxC collected real samples at 10 MHz.

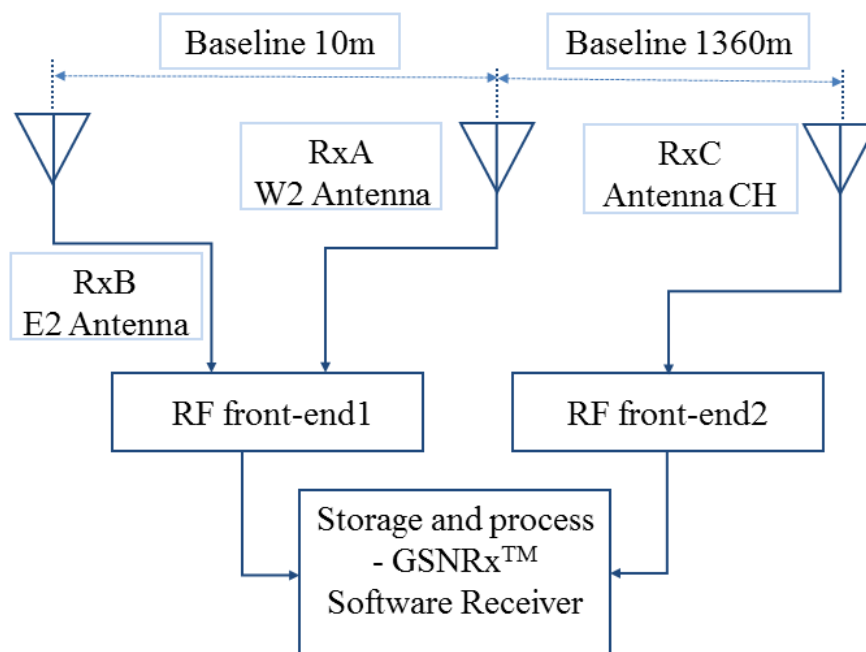


Figure 4-13 RTK using live signal at three locations

Figure 4-14 shows the code-minus-carrier observations for all three receivers. During this period, Doppler collision is observed on receivers RxA and RxB whereas no Doppler collision is observed in rover RxC. This combination is a similar case to the period P2 in Figure 4-2.

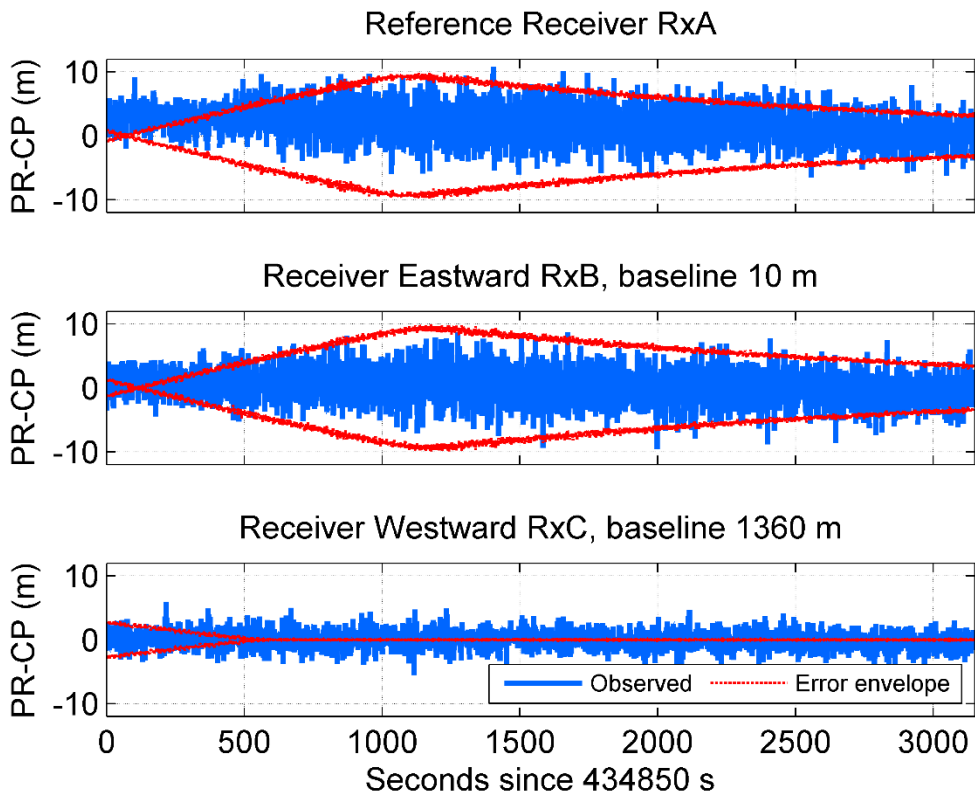


Figure 4-14 Live signals PRN 135 Measurements showing effect of Doppler collision at three different locations

4.2.2 Selection of Satellites

Consider receivers RxA and RxB. Since the baseline is very short (10 m), the Doppler collision envelopes resemble each other. Similar to the analysis in the hardware-simulation of Doppler collision, the number of satellites used in the RTK solution is reduced to a combination of 6 GPS and 4 GPS + 2 WAAS satellites. Figure 4-15 shows the RTK solution using the combinations. The solution is obtained at epoch 600 s from the start time when the effect of Doppler collision is present of on both receivers RxA and RxB. The top row shows single-differenced float ambiguities relative to the last epoch

rounded value. The middle row shows estimated standard deviation of float single-differenced ambiguities and number of satellites for which ambiguities are fixed. In both the cases, the variation in estimated standard deviation is same, however, for the GPS-alone combination, the convergence of single-differenced ambiguities is faster and hence the fixed solution is obtained much earlier. For 4 GPS + 2 WAAS, convergence is much slower because of large code-minus-carrier values on the observations and hence large TTFFA. The bottom row shows the estimated solution. With 2 WAAS satellites in the RTK solution, the convergence of ambiguities is slower and hence float solution is available for a considerable duration from the start.

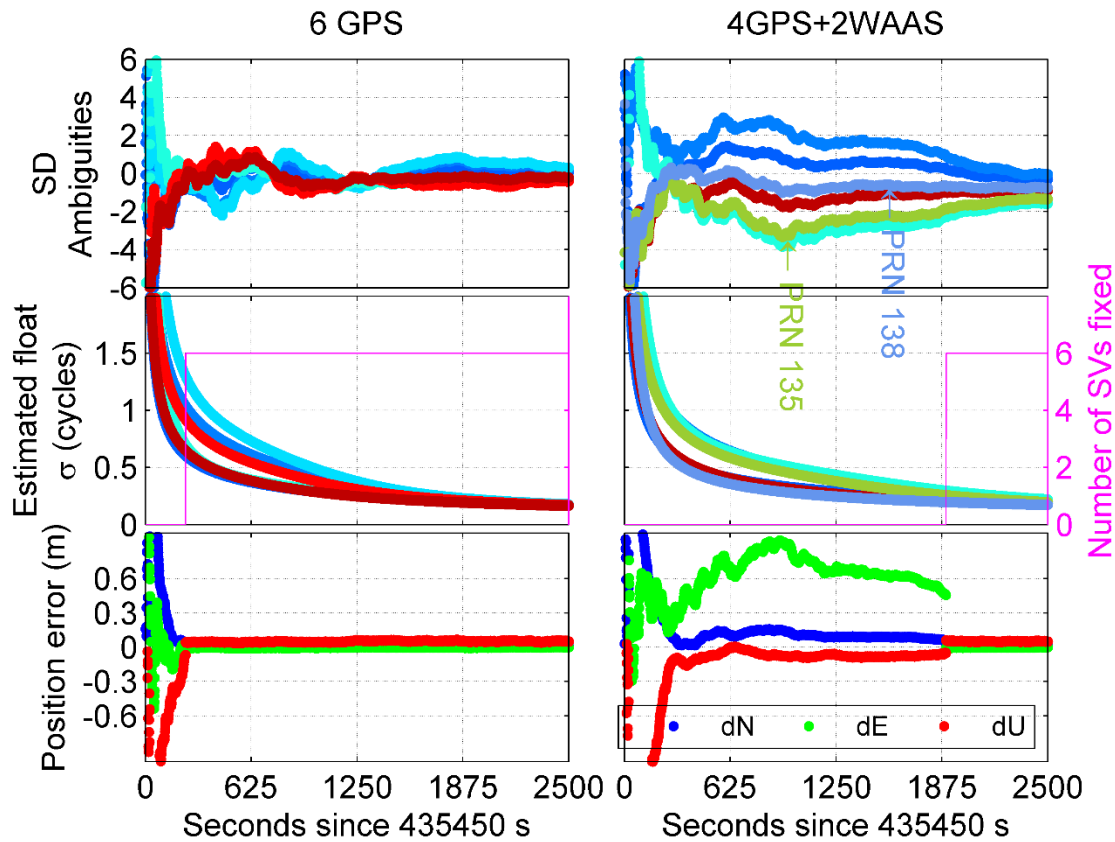


Figure 4-15 Live data at base RxA and rover RxB. Top row shows single-differenced ambiguities, middle row shows convergence of single-differenced ambiguities and the number of satellites fixed, and bottom row shows float/fixed solution position error

4.2.3 TTFFA Analysis for Short Baseline

TTFFA is obtained using all - combinations of satellites: 6 GPS and 4 GPS + 2 WAAS against the baseline of 6 GPS + 2 WAAS, as shown in Figure 4-16. TTFFA is small for a solution using 6 GPS satellites and close to baseline values. The WAAS observations have minimum effect on TTFFA when a good number of GPS satellites are present in the solution. For a solution using 4 GPS + 2 WAAS, the TTFFA is large, especially during the

peak of Doppler collision effect on both receivers RxA and RxB. Figure 4-16 also shows the plot of TTFFA using de-weighting of WAAS observations as analyzed in hardware-simulation of Doppler collision. By de-weighting the affected observations as explained in section 4.1.4, there is a small improvement in the TTFFA during the peak of Doppler collision.

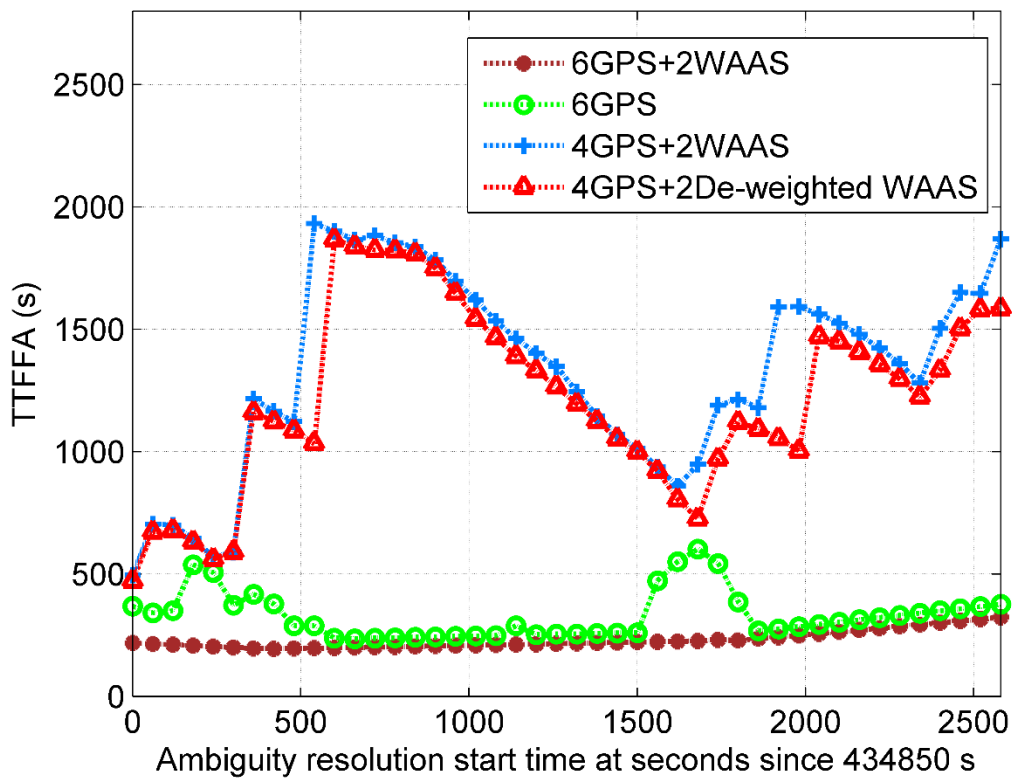


Figure 4-16 TTFFA during Doppler collision with live signals at a short baseline

4.2.4 TTFFA Analysis for Long Baseline

Similarly, using receivers RxA and RxC, an RTK solution is obtained for a long baseline. TTFFA is obtained using all four combinations of satellites as shown in Figure 4-17. Here too, an improvement is observed by de-weighting the WAAS observations during the

Doppler collision event. Overall, de-weighting of GEO observations results in maintained or improved TTFFA during Doppler collision across varying baselines. Appendix C shows that the pseudorange code phase observations can be used to determine the occurrence of Doppler collision and thus de-weighting can be an efficient method where the GEO observations can be de-weighted real-time during likely conditions of Doppler collision.

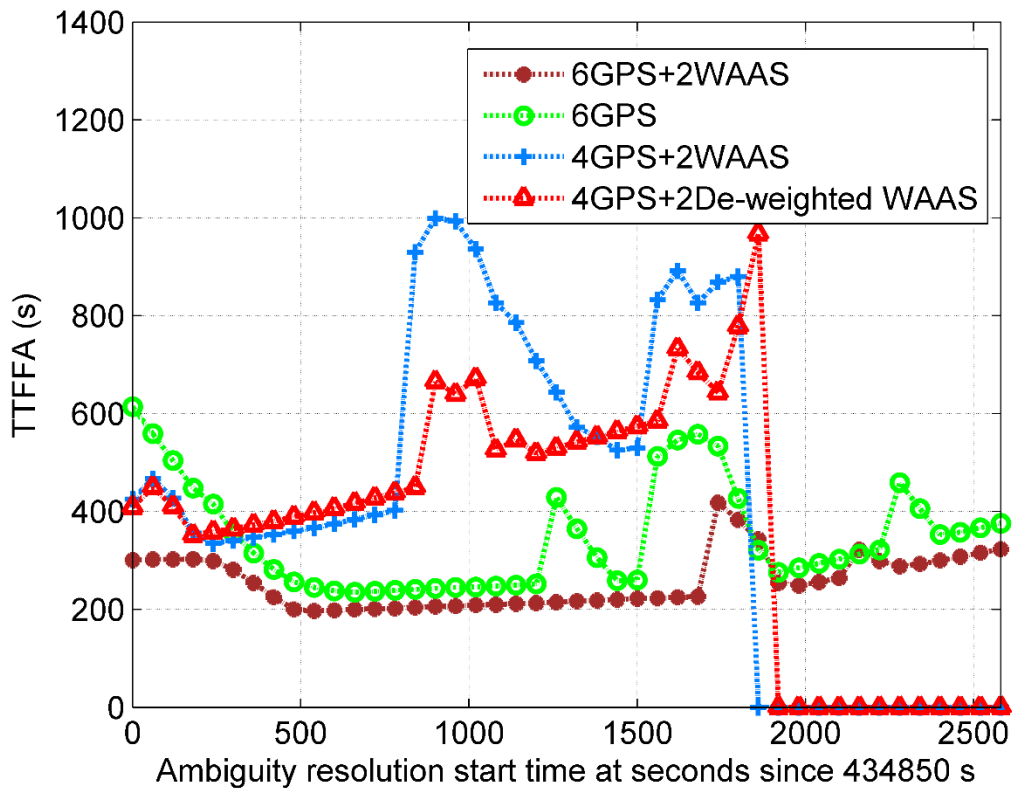


Figure 4-17 TTFFA during Doppler collision using live signals at long baseline

4.3 Doppler Collision mitigation techniques

This section lists several mitigation techniques for Doppler collision.

4.3.1 Satellite Doppler

The primary factor for the occurrence of Doppler collision is the magnitude of relative Doppler between two satellites. If it is zero or less than code lock loop bandwidth, there is a likely condition for Doppler collision. In the case of MEO satellites such as GPS, the duration is minimal, and its effect is minuscule. Regarding geostationary satellites, the range of Doppler variation is limited. Consider the Doppler variation of BeiDou satellites in Figure 3-5. Satellites C03 and C04 have similar variations, and thus a long duration of small relative Doppler is present. However, the change in Doppler frequencies of C01 and C05 is such that a short length of small relative Doppler is present. Thus, Doppler collision can be avoided if there is a significant variation in the Doppler frequency of the geostationary satellites. Doppler collision can also be prevented if the variations of Doppler frequencies are such that a tiny duration of small relative Doppler is present. As shown in Figure 3-8, MSAS presents the exact opposite of the required conditions to avoid Doppler collision. The Doppler variations are very similar and lead to a situation where likely conditions for Doppler collision are present throughout the day.

Controlling satellite Doppler is an effective method. However, it is not an easy solution if the satellite is already deployed. There will be limitations on maneuvering geostationary satellites, and not all geostationary satellites can orbit for the significant variation in

Doppler frequencies. Alternatively, a small magnitude of satellite clock drift parameter (af1) can be defined to induce Doppler due to the satellite clock.

4.3.2 Cross-Correlation function

Table 3-2 shows the distribution of cross-correlation values for B1I in comparison to GPS or WAAS C/A codes. Selection of codes could be an important step to avoid likely conditions for Doppler collision. Figure 3-12 shows the spatial extent of the cross-correlation function of the B1I codes where the probability of maximum cross-correlation peaks is minimal. The even length of Gold Codes in B1I are a better option than regular C/A codes to avoid the severe impact of Doppler collision on the code measurements. This solution is effective if the system is in the planning phase. However, if the system is designed and deployed, there are no mechanisms to change the signal and code structure to avoid Doppler collision.

4.3.3 Multipath Mitigation Techniques

In section 3.3, theoretical limits obtained using narrow correlator showed a significant drop in the magnitude of the Doppler collision error. The narrow correlator is a widely accepted design to mitigate the effects of multipath, and since Doppler collision is multipath-like effect, it is important to consider its application during Doppler collision.

4.3.3.1 Narrow Correlator

Figure 4-18 shows a plot of code-minus-carrier measurements obtained using narrow correlator. The IF data is collected at 20 MHz (I and Q samples separately) using test

setup described in Figure 4-1 at location Rx1. The data is collected for 4000 s to limit the size of IF data file and processed using narrow correlator with E-L chip spacing of 0.1 chips. In comparison to the top plot of Figure 4-2, the code-minus-carrier variation is significantly reduced. There is a dip in the code-minus-carrier measurements when cross-correlation peak is transitioning over the primary peak indicating that the magnitude of Doppler collision is greatly reduced but not eliminated.

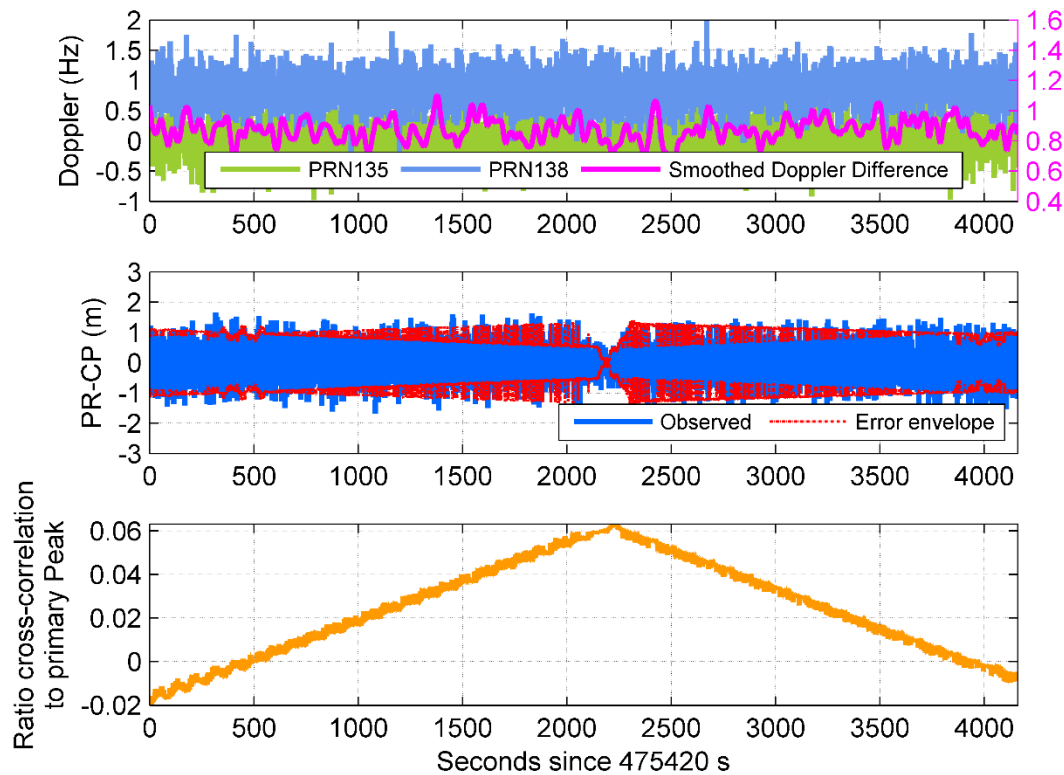


Figure 4-18 Code-minus-carrier measurements obtained using narrow correlator during Doppler collision

The narrow correlator is widely used in high accuracy receivers and can form an effective method of mitigating Doppler collision effects. However, the use of narrow correlator is limited in low-cost receivers where signal bandwidth is small.

4.3.4 Delay Lock Loop Bandwidth

Section 2.3.1 explains that the key factor to determine Doppler collision is the magnitude of the relative Doppler compared to code lock loop bandwidth, also called Delay Lock Loop (DLL) bandwidth (Kaplan and Hegarty 2005). If the relative Doppler is greater than the DLL bandwidth, the relative phase moves too much during the integration period and the correlation peak will be filtered out. Thus decreasing DLL bandwidth can provide an effective method to reduce the effect Doppler collision

Figure 3-16 shows the effect of Doppler collision when the software defined receiver is configured with $DLL = 0.5$ Hz. Although the DLL bandwidth is less than relative Doppler, the effect is still significant and closely follows the theoretical error envelope. Figure 4-19 shows the plot of code-minus-carrier measurements for the same data processed using DLL bandwidth of 1 Hz. Compared to Figure 3-16, there is a substantial increase in the variation of code-minus-carrier measurement with maximum error reaching edges of the error envelope.

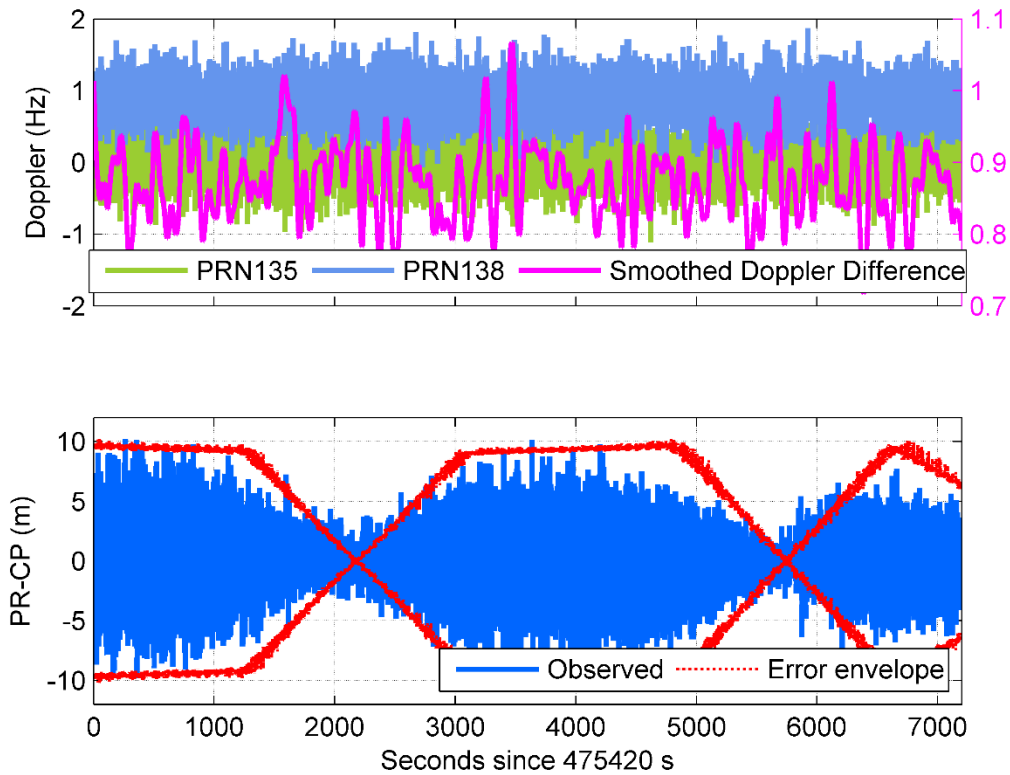


Figure 4-19 Code-minus-carrier measurements with DLL bandwidth of 1 Hz

Figure 4-20 shows the code-minus-carrier measurement for the same data with the DLL bandwidth set to 0.1 Hz. Here, the variation of code-minus-carrier measurement has reduced significantly in comparison to the processing using a DLL bandwidth of 0.5 Hz and 1 Hz.

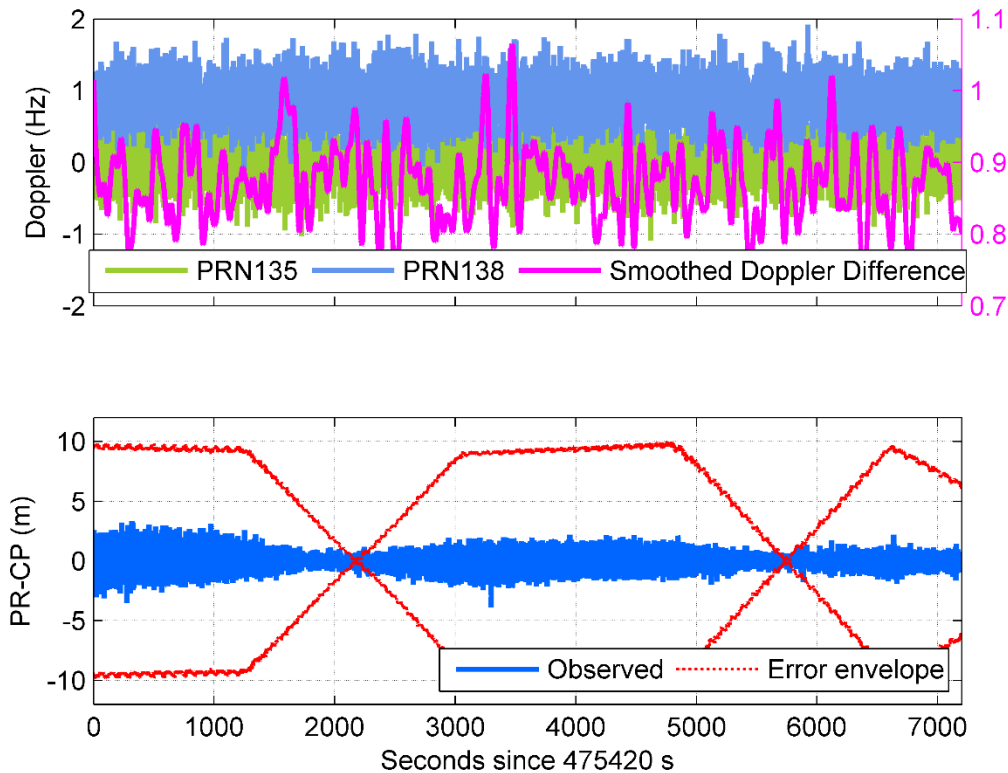


Figure 4-20 Code-minus-carrier measurements with DLL bandwidth of 0.1 Hz

If the effect of Doppler collision can be controlled using DLL bandwidth, it will provide a lot of flexibility to a user because once the signal is tracked by the phase lock loop, the user can dynamically reduce the DLL bandwidth and get better measurements. The flip side of reducing the DLL bandwidth is the limitation on the user dynamics. If user dynamics are large, there will be a constraint on the reduction of DLL bandwidth (Kaplan and Hegarty 2005).

To summarize, Doppler collision has an impact on the RTK solution where the convergence of ambiguities is affected, and this leads to increase in TTFFA. The effect

is severe especially in the case of a limited number of MEO satellites along with geostationary satellites. This observation implies that Doppler collision will affect standalone IRNSS RTK. The increase in TFFFA is presented using hardware-simulated data and live data. The simplest solution to overcome Doppler collision is to decrease the observation weight of GEOs during Doppler collision. Alternative solutions include modifications in the design of the satellite systems. At measurement level, the effective solution is the narrow correlator which shows a significant reduction in the Doppler collision error. However, the use of narrow correlator is limited in the case of low-cost receivers. The effect of Doppler collision can also be reduced by decreasing DLL bandwidth and provides alternative solution to mitigate Doppler collision. In the next chapter, the observability of geostationary satellites is discussed, and Chapter-6 will continue the discussion on mitigation of Doppler collision effect in IRNSS.

Chapter Five: **Observability of Geostationary Satellites**

The previous two chapters covered Doppler collision and demonstrated its impact on an RTK solution using WAAS satellites. This chapter covers observability issue of geostationary satellites, specifically GEOs in IRNSS. The outline of this chapter is as follows: the computation of covariance of ambiguities using MKF is presented to demonstrate the effect of time-correlation of geostationary satellite errors. The time-correlation of observation errors affect convergence of ambiguities and is analyzed using the combinations of GPS and WAAS satellites. After identifying the impact of time-correlation on the observability of geostationary satellite, the analysis is extended to an RTK solution using standalone IRNSS. A list of possible solutions is presented to overcome the effect of time-correlation of satellite errors in the IRNSS.

5.1.1 Covariance Computation

Section 2.3.2 provides a complete theory of an SKF and MKF. This section continues with the same definition of the measurement model and the Kalman Filter equations (Petovello et al. 2009) and then presents a computation of the covariance of the ambiguities using both filter models.

In the prediction step of Kalman Filters, a random constant model is considered for the ambiguities since single-differenced ambiguities have unknown initial value, and the rate of single-differenced ambiguities is zero unless a cycle slip is encountered. The process noise for single-differenced ambiguities is given by

$$\mathbf{Q}_k = \mathbf{diag}(qN \times \Delta t) \quad 5.1$$

where $qN = 1e^{-10}$ cycles/s/ \sqrt{Hz} is considered. For position, a velocity random walk model is considered with $qV = 10e^{-3}$ m/s²/ \sqrt{Hz} .

The term \mathbf{n}_k corresponds uncorrelated measurement noise of single-differenced code or phase measurements for given pair of receivers, under the assumption that the rover and the base have equivalent receiver noise. The covariance of uncorrelated measurement noise is

$$\mathbf{N}_k = 2 \times \mathbf{diag}(\sigma^2) \quad 5.2$$

where σ is the standard deviation of code or carrier phase noise.

The next section demonstrates the time-correlation of single-differenced measurement errors. The analysis indicates that the time-correlated part can be modeled as a first order Gauss-Markov (GM) model. The continuous time format of first order GM is $\dot{s} = -\beta s + w$.

In discrete terms, it modifies as

$$\mathbf{u}_{k+1} = \mathbf{e}^{-\beta \Delta t} \mathbf{u}_k + \boldsymbol{\varepsilon}_k \quad 5.3$$

The covariance matrix of $\boldsymbol{\varepsilon}_k$ is given by

$$\mathbf{M}_k = \mathbf{E}\{\boldsymbol{\varepsilon}_k \boldsymbol{\varepsilon}_k^T\} = \mathbf{diag}[\sigma^2 (1 - e^{-2\beta \Delta t})] \quad 5.4$$

In the covariance analysis, the covariance of double-differenced ambiguities is not considered because between-satellites differencing makes it difficult to isolate whether the base satellite or remaining satellites have increased the variance. Since the goal is to

observe the convergence of ambiguities and impact of the GEO satellites, the analysis of single-differenced ambiguities can provide a clear picture of the effect of GEO satellites.

5.2 Time-correlation of GEO Satellite Errors

Consider the case of hardware-simulation of Doppler collision using three receivers in section 4.1. Figure 5-1 shows the plot of single-differenced residuals obtained using Rx1 and Rx2. The phase residuals are uniformly distributed with no definite pattern whereas code residuals show an envelope, which is formed by the combination of code error envelope of the two receivers. The envelope has a period of approximately 1800 s with a different magnitude of code residuals in each interval.

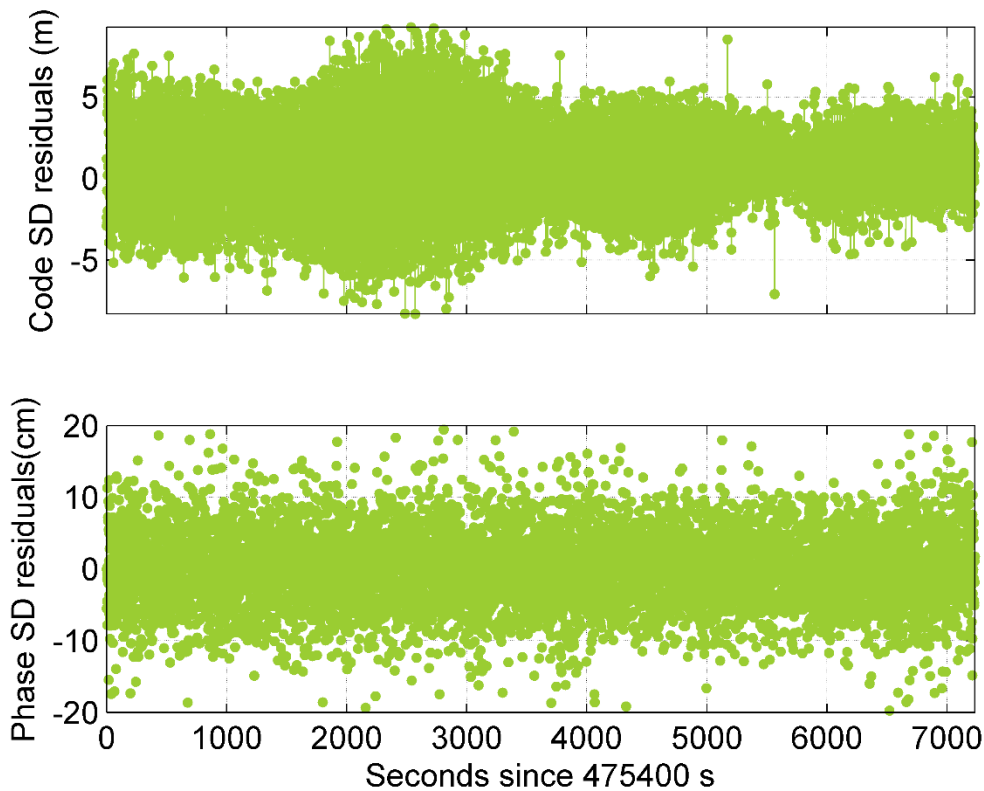


Figure 5-1 Single-differenced code and phase residuals for RTK solution between

Figure 5-2 shows an autocorrelation plot of single-differenced code residuals. As shown, the autocorrelation plot can be approximated to a first order Gauss-Markov (GM) model.

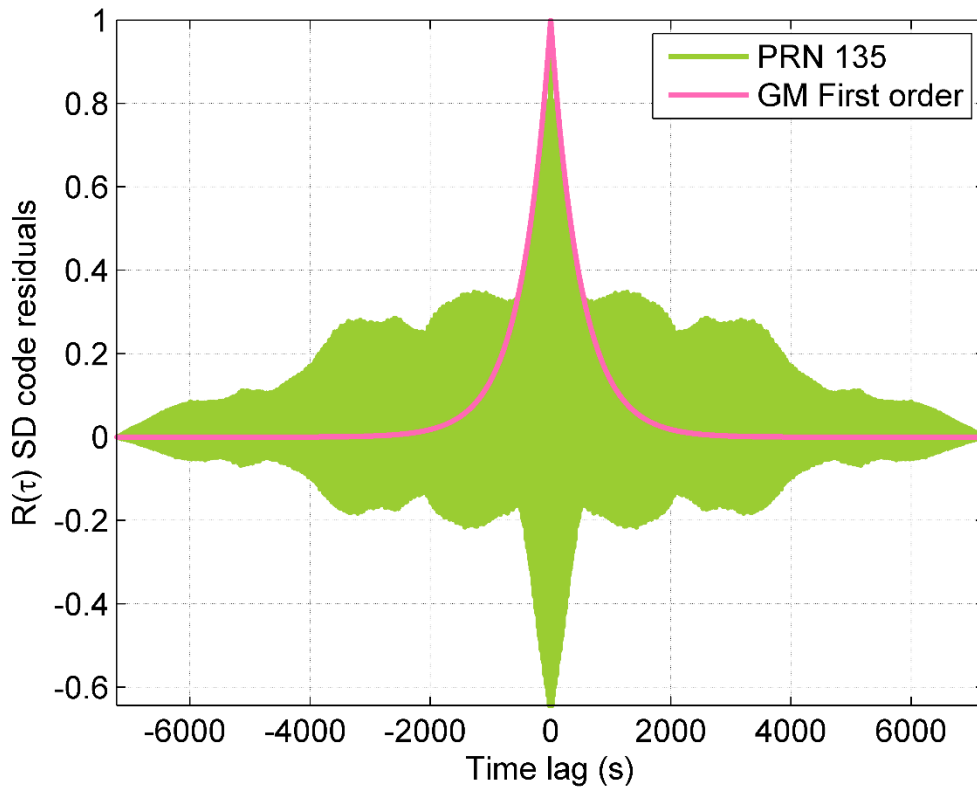


Figure 5-2 Normalized autocorrelation of single-differenced code residuals for simulated Doppler collision data at a baseline of 900 m. Approximation of first order GM Markov model at $\tau = 700$ s

To identify peaks, Figure 5-3 shows a frequency plot of the single-differenced residuals. A peak of a period 7.6 s is observed which corresponds to 0.13 Hz which is the relative difference of carrier cycle every second between two Doppler frequencies. The first positive and negative peaks in the autocorrelation plot point to the presence of this

component. The first order GM model for measurement error approximates to a correlation time of 700 s. In addition to the first peak, there are secondary peaks at an interval of about 1800 s which corresponds the period of single-differenced code residuals envelope as shown in Figure 5-1.

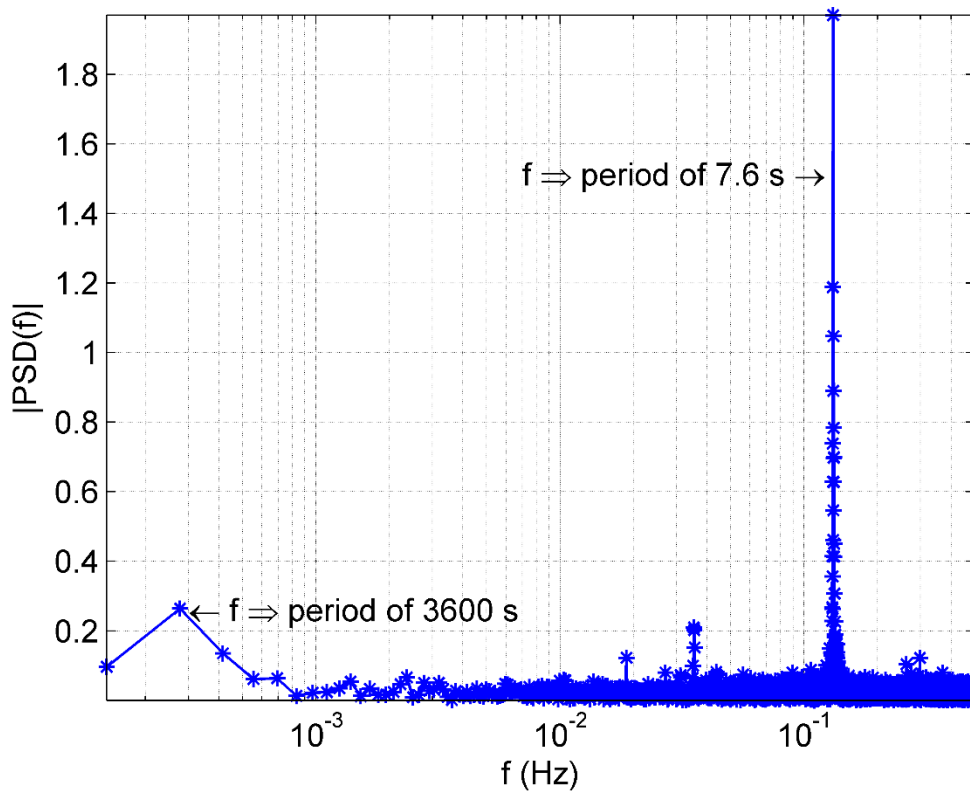


Figure 5-3 PSD of single-differenced residuals for simulated Doppler collision data at a baseline of 900 m. The peak corresponding to 3600 s is the variation of single-differenced residuals due to Doppler collision envelope.

A similar analysis is extended to live signal RTK solution using WAAS satellites discussed in section 4.2. Figure 5-4 shows autocorrelation of single-differenced code residuals for long baseline when there is no Doppler collision. The autocorrelation can be

approximated to first order GM model. It could be argued that first order GM model is not sufficient and higher order GM model or Auto-regressive models (Nassar et al. 2004) could be considered. However, the primary goal of this section to understand time-correlation of measurement errors. If the study using first order GM proves the impact on ambiguity resolution time, it could be extended using a higher order of GM models or Auto-regressive models.

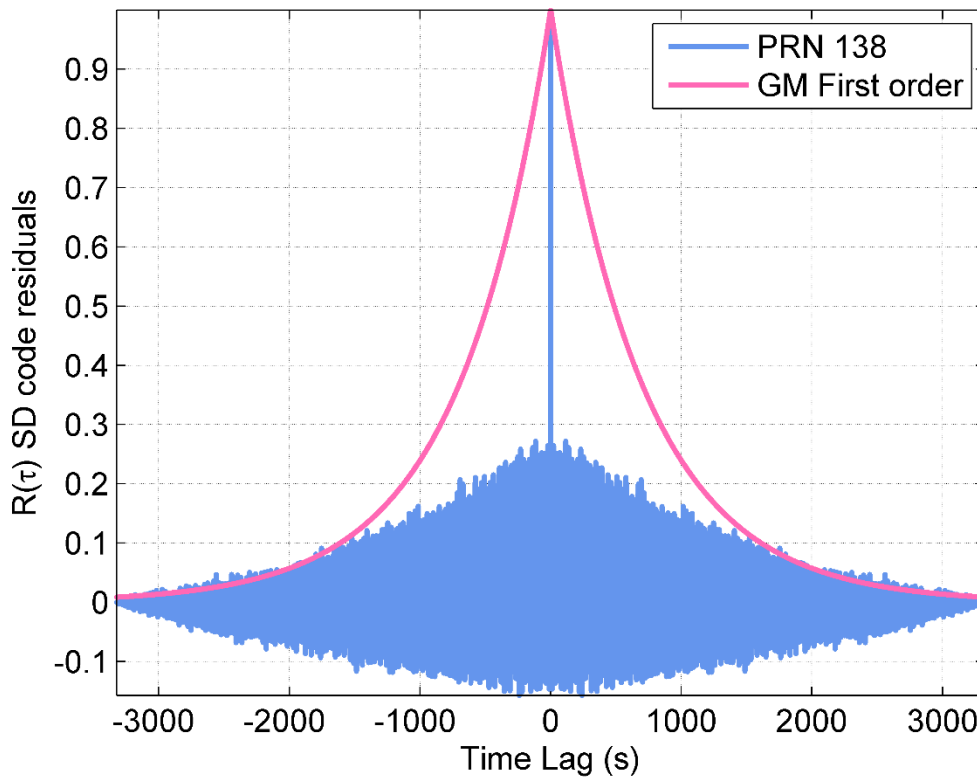


Figure 5-4 Normalized autocorrelation of single-differenced code residuals for live data at a baseline of 1380 m. The correlation time of first order GM model is 700 s.

Figure 5-5 shows autocorrelation of single-differenced code residuals for a short baseline when there is no Doppler collision. Here too, the variation can be approximated to first order GM model. Therefore, if there is a Doppler collision event or not, time-correlation on the single-differenced code residuals of WAAS satellites is always present.

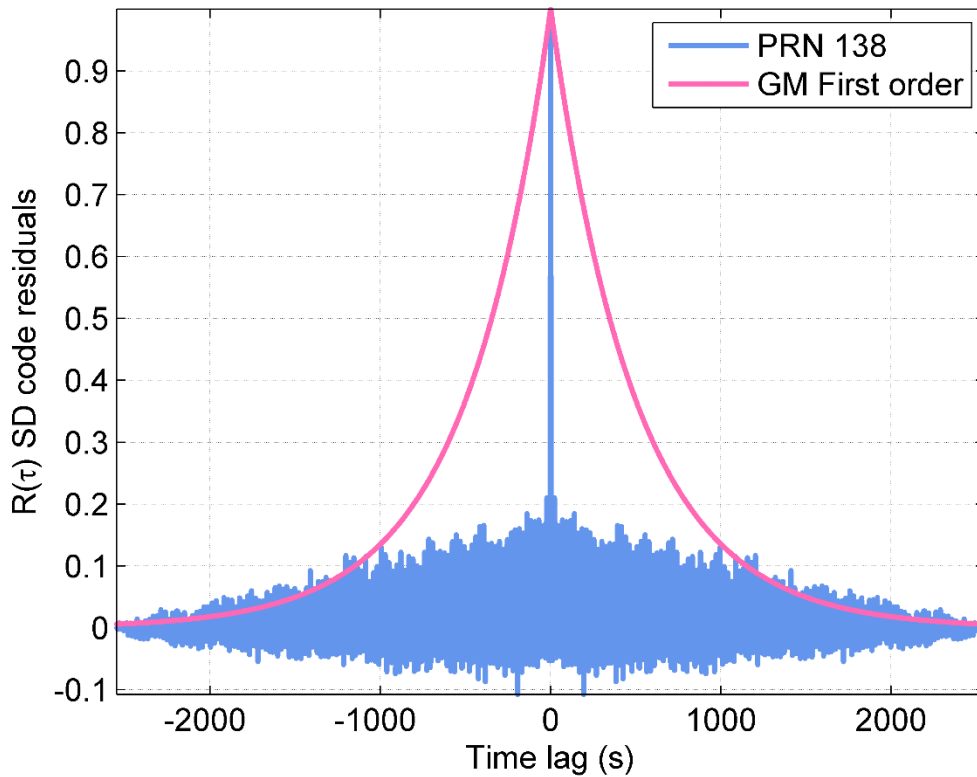


Figure 5-5 Normalized autocorrelation of single-differenced code residuals for live data at a baseline of 10 m. The correlation time of first order GM model is 500 s.

5.3 Ambiguity Convergence in WAAS

Based on the analysis in the last section, a correlation time β^{-1} of 700 s is factored for WAAS satellites. For GPS satellites, a correlation time β^{-1} of 40 s is taken from previous research (O'Keefe et al. 2006; Petovello et al. 2009). As considered in the last chapter, the following four combinations are analyzed:

1. All GPS and WAAS satellites in view
2. 6 GPS + 4 WAAS satellites in view
3. Only 6 GPS in view
4. 4 GPS + 2 WAAS satellites in view

The covariance of ambiguities and corresponding standard deviation (σ) is computed using SKF and MKF. A short baseline of 10 m is defined between the base and rover, and the convergence of covariance is obtained over a duration of 3000 s. It is the same test setup of RTK positioning using live data during Doppler collision, as discussed in section 4.2.3. Table 5-1 lists parameters used in the covariance simulation.

Table 5-1 Tabulation of parameters used in the covariance simulation

Parameters	Value	Comments
Processing rate	1 Hz	
Satellite elevation cut-off	5°	
Time constant β^{-1} for MEO	40 s	Same value is extended to IGSO
Time constant β^{-1} for GEO	700 s	Based on multiple tests
Code input σ	2 m	Based on successive measurement analysis of GPS/WAAS measurements collected using front-end under test
Carrier phase input σ	0.02 cycle	
Doppler input σ	0.1 Hz	
Spectral density for ambiguities random constant qN	1e-10 <i>cycles / s / \sqrt{Hz}</i>	For a static user
Spectral density for velocity random walk qV	1e-3 <i>m / s / \sqrt{Hz}</i>	

Figure 5-6 shows the convergence of ambiguities when all GPS and WAAS satellites are present. The convergence time using MKF is higher in comparison to SKF due to the introduction of correlation time for GPS satellites. The number of satellites is then reduced to isolate the impact of WAAS satellites.

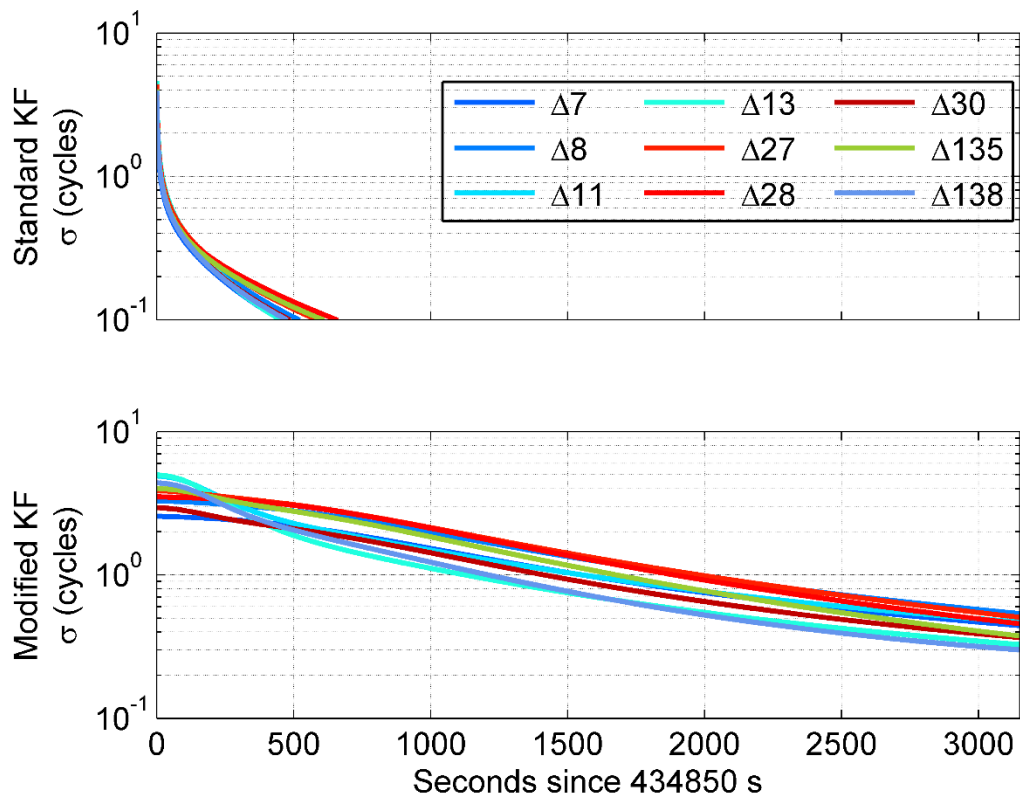


Figure 5-6 Standard deviation of covariance of single-differenced ambiguities using all GPS + 2 WAAS

Figure 5-7 shows a baseline result with 6 GPS + 2 WAAS satellites. Using SKF, there is no difference in ambiguity convergence time compared to the all satellite combination. Similarly, in MKF, the standard deviation of single-differenced ambiguities reaches values of 1 cycles in about 1000 s.

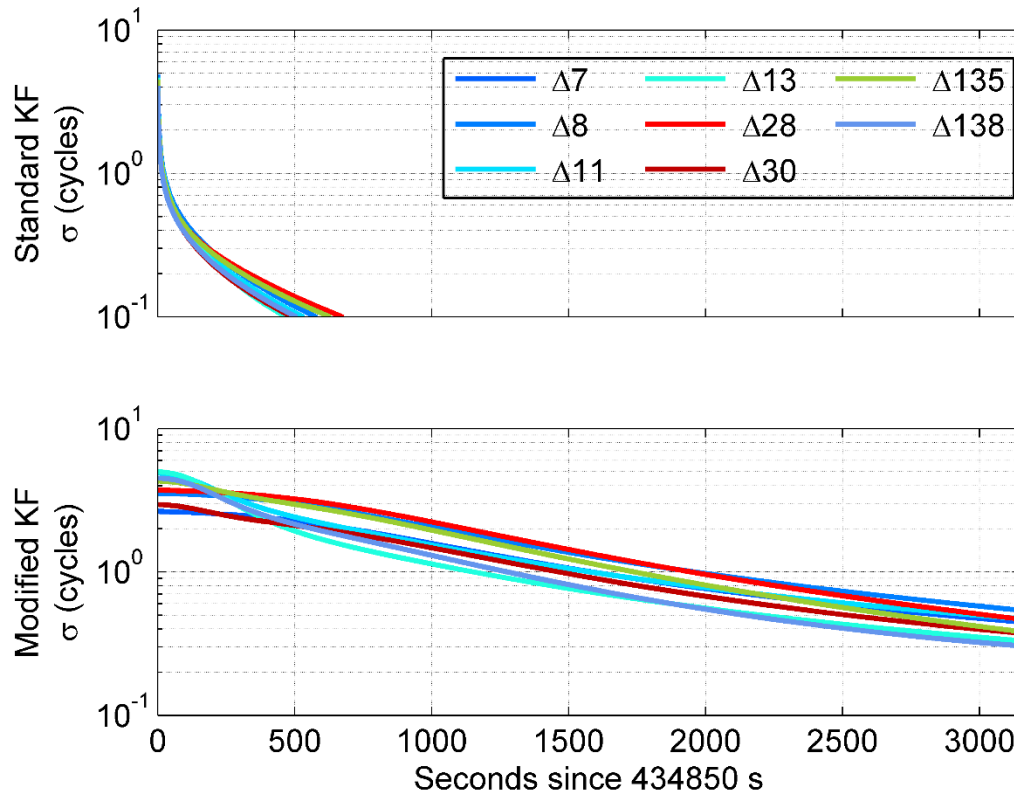


Figure 5-7 Standard deviation of covariance of single-differenced ambiguities using 6 GPS + 2 WAAS

Figure 5-8 shows ambiguity convergence using only 6 GPS satellites. Again, there is no significant variation in the ambiguity convergence in comparison to 6 GPS + 2 WAAS solution. With a good number of MEO satellites in the estimation process, there is little or no impact on ambiguity convergence.

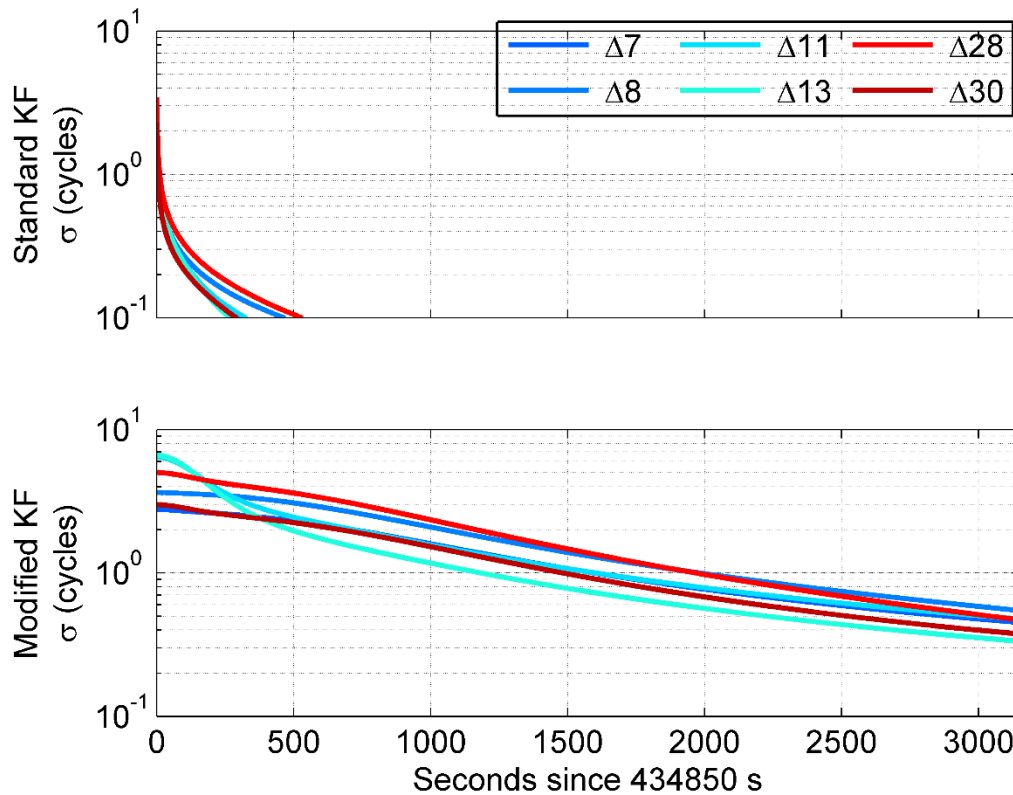


Figure 5-8 Standard deviation of covariance of single-differenced ambiguities using 6 GPS

Figure 5-9 shows the convergence of ambiguities when two GPS satellites are replaced with 2 WAAS satellites while maintaining similar PDOP values. There is a drastic change in ambiguity convergence behavior, and standard deviation reaches a value of 1 cycle close to the end of test duration. The delay in convergence implies that if the correlation time of code measurement errors of GEO stationary satellites is factored into the estimation process, there is a significant impact on the ambiguity convergence and in turn, will affect TFFFA.

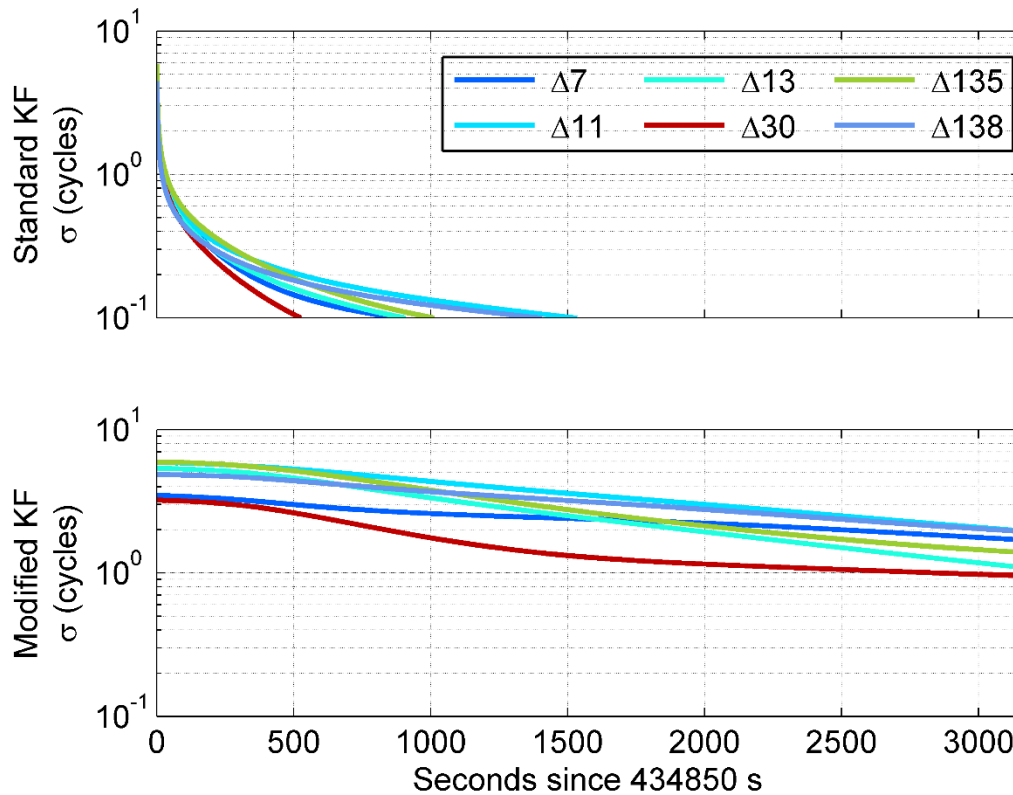


Figure 5-9 Standard deviation of covariance of single-differenced ambiguities using 4 GPS + 2 WAAS

Teunissen (1999) shows that success rate of ambiguity fix using bootstrapping is less than or equal to Integer-Least Squares (ILS) and forms the lower bound. If the bootstrapping ambiguity fix method is used, the first ambiguity is rounded off when its standard deviation is less than a cycle, and further ambiguities are decorrelated and fixed. The success rate using ILS must be on the higher side and leads to higher PCF. The LAMBDA method, which is built on the principle of ILS, will also have higher PCF and will provide smaller TFFFA. Thus the covariance analysis focuses on the convergence of

standard deviation of single-differenced ambiguities to determine if TTFFA would be small in regular cases or large when there are more time-correlated measurement errors.

5.4 IRNSS and its Observability

IRNSS consists of three GEO satellites and four IGSO satellites in contrast to the GPS constellation that includes only MEO satellites. Figure 2-2 shows the ground tracks of IRNSS satellites. The four IGSO satellites trace a ground track of figure-eight whereas GEO satellites move slightly above and below equatorial plane. The focus of this section is to understand whether the IRNSS is capable of providing a standalone RTK solution. An RTK solution using standalone IRNSS would be necessary for a user in Indian sub-continent if the user wants to avoid the use of other constellations.

For a user located in Bengaluru, India (Coordinates: $+13^{\circ} 01' 16.1971''$ N, $77^{\circ} 34' 13.3534'$ E, height 843.71 m), the sky plot is as shown in Figure 5-10. For a standalone IRNSS system, HDOP is large in comparison to GPS constellation due to the poor geometry where all satellites are available at high elevation angles (Rao et al. 2011). The poor HDOP will have an impact on the observability of standalone IRNSS system as discussed below.

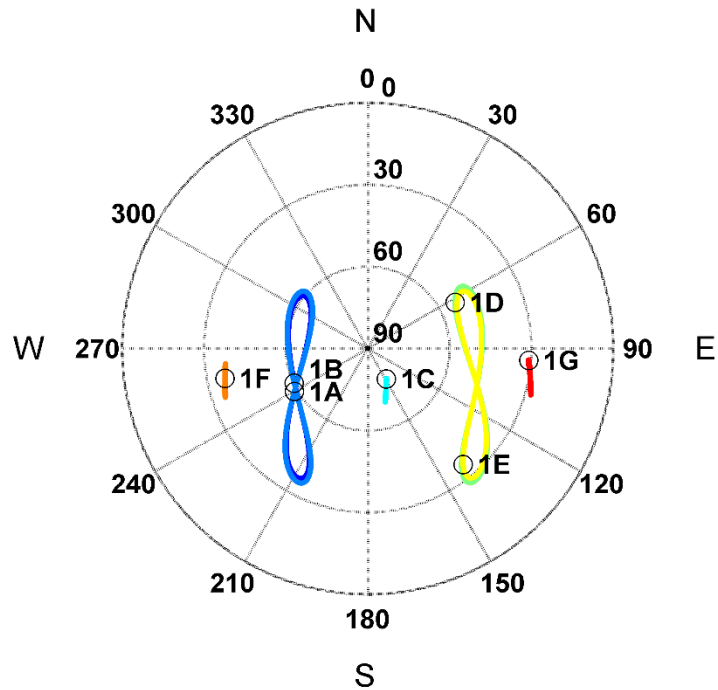


Figure 5-10 Skyplot of simulated IRNSS constellation

5.4.1 Ambiguity Convergence in IRNSS

The autocorrelation analysis of single-differenced code residuals of WAAS satellites provided a correlation time constant of 700 s for GEO satellites, and this value is significant in comparison to the correlation time constant of 40 s for MEO satellites. Using time constant of 700 s for GEO satellites and time constant of 40 s for IGSOs in IRNSS, an attempt is made to simulate the convergence of single-differenced ambiguities for standalone IRNSS system. There is limited research available on correlation time of IGSO satellites, hence the correlation time equal to MEO is considered for IGSO satellites, which is still an optimistic value. Figure 5-11 shows the convergence of single-differenced ambiguities for IRNSS constellation using SKF and MKF. The simulation is processed at

1 Hz and the baseline between base and rover is 10 m, which is similar to the analysis of WAAS satellites in Figure 5-6. The convergence time of single-differenced ambiguities is small using SKF whereas using MKF, the convergence of single-differenced ambiguities is slow and reaches a value of 1 cycle at more than 2000 s. Overall, the observability of standalone IRNSS constellation is poor, similar to a combination of 4 WAAS and 2 GPS satellites as shown in Figure 5-9 and it would be challenging to quickly fix the ambiguities in an RTK solution using standalone IRNSS.

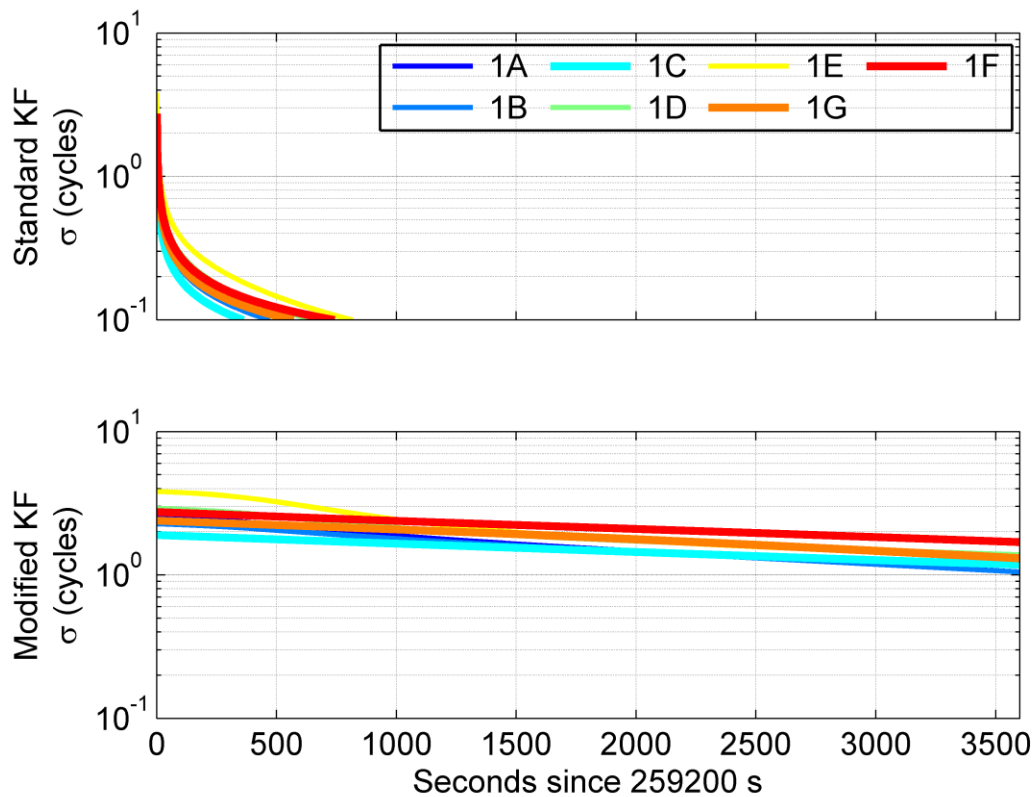


Figure 5-11 Convergence of single-differenced ambiguities in IRNSS

5.5 Improvement of IRNSS Observability

This section describes a list of solutions to improve the observability of standalone IRNSS constellation for an RTK solution. The solutions are defined considering the current satellites in other GNSS segments and certain assumptions on the expansion of the IRNSS system in future.

5.5.1 Augmentation with GAGAN Satellites

The GAGAN is an SBAS augmentation system built by ISRO to provide satellite based augmentation services to GPS users over the Indian sub-continent. The primary role of GAGAN satellites is to provide augmentation services, however, if the same satellites can be modified to provide ranging information (Rao 2013), it will increase the number of observations in the IRNSS. Figure 5-12 shows the ground track of IRNSS satellites along with GAGAN satellites located at the longitude of 55.03° E and 83.00° E respectively. The orbital information of GAGAN satellites is obtained using Broadcast Ephemeris (Montenbruck et al. 2014, 2017).

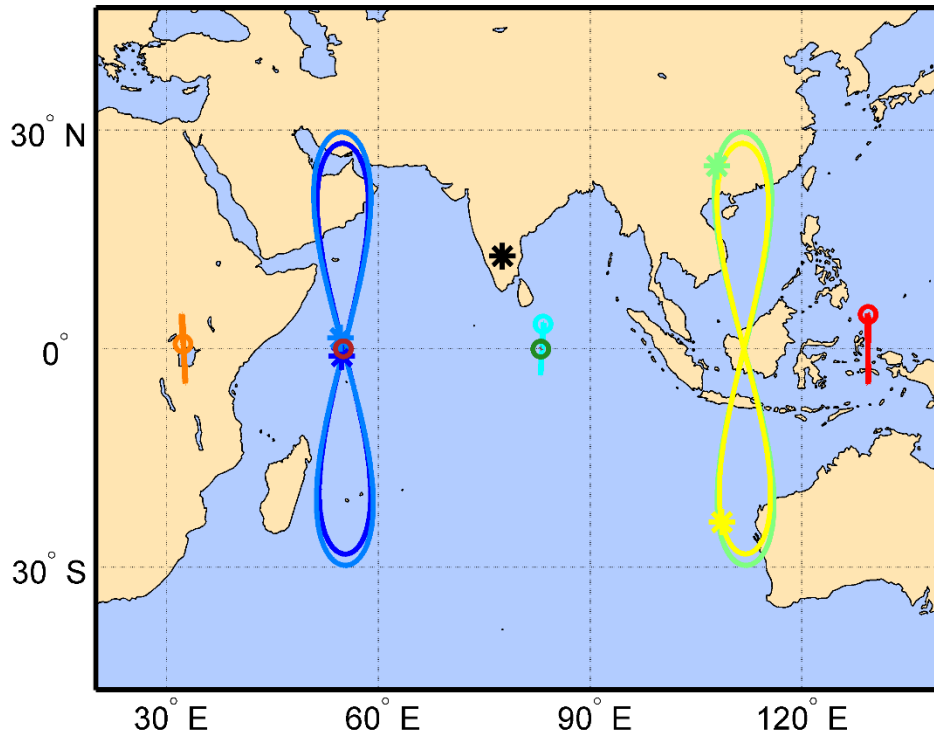


Figure 5-12 Ground Track of IRNSS satellites along with GAGAN satellites located at the longitude of 55.03° E and 83.00° E respectively

Figure 5-13 provides convergence of single-differenced ambiguities when GAGAN observations are added in the estimation process. The correlation time of WAAS satellites is used for GAGAN in MKF. One of the GAGAN satellites is located at the longitude of one of the IRNSS GEO satellites and the second one is located at the longitude of an IRNSS IGSO equatorial crossing. Since GAGAN satellites are geostationary in nature, the ambiguity convergence is poor when time-correlation is factored in the filtering process. Consequently, there is no significant improvement in the observability using MKF in comparison to Figure 5-11.

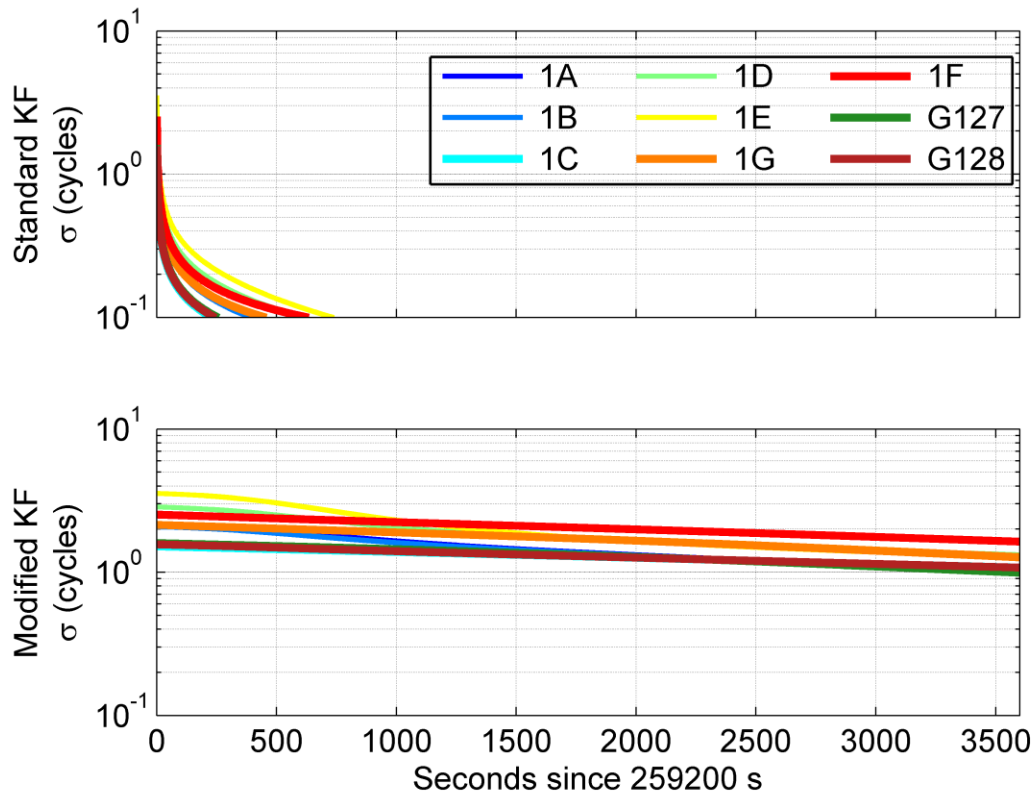


Figure 5-13 Convergence of single-differenced ambiguities for RTK solution with IRNSS and GAGAN satellites

5.5.2 Introduction of IGSO satellites

Recently, the IRNSS-1A satellite lost its clocks and is no longer used for navigation solutions (Montenbruck et al. 2017). In future, if the IRNSS constellation were to expand and add two IGSO satellites, it would be good to add the new satellites away from the existing IGSOs. A simple solution would be to add an IGSO at the same longitude of the geostationary satellites present at the end of the equatorial plane. Figure 5-14 shows the ground track of the proposed constellation. The orbital parameters of two IGSOs have an

orbital inclination of 30° and the argument of perigee is proposed in such a way that it would remain out of phase in orbit with respect to the existing IGSO satellites. Figure 5-15 shows the convergence of ambiguities using SKF and MKF. There is a small improvement in the convergence time using MKF compared to Figure 5-11, and it is on par with the convergence time of MKF using 6 GPS + 2 WAAS satellites as shown in Figure 5-7.

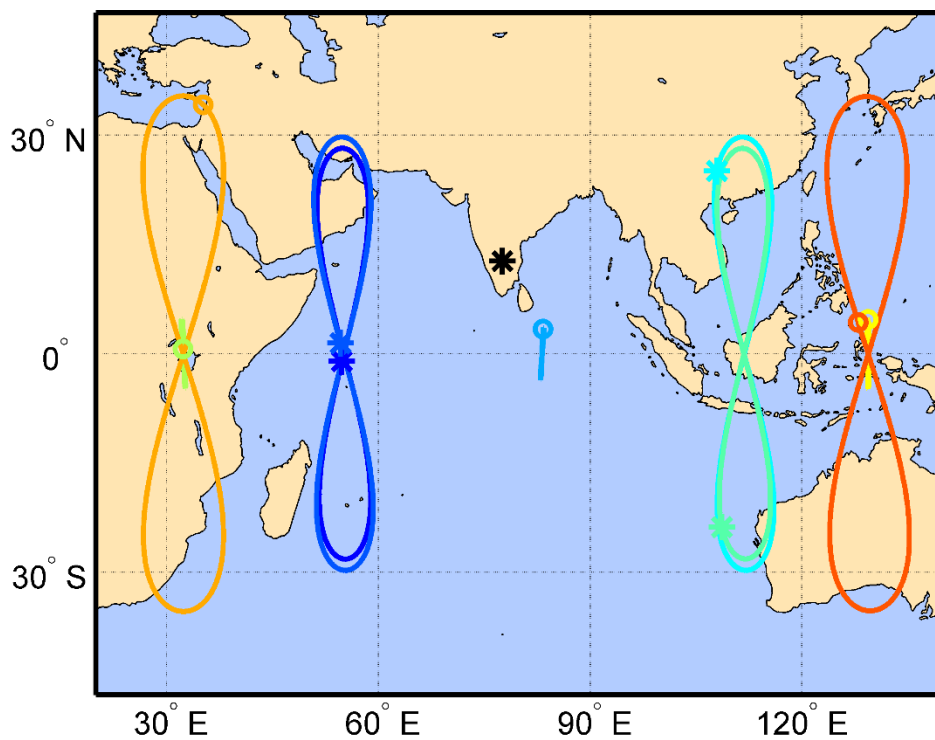


Figure 5-14 Proposed expansion of IRNSS system with two IGSO satellites

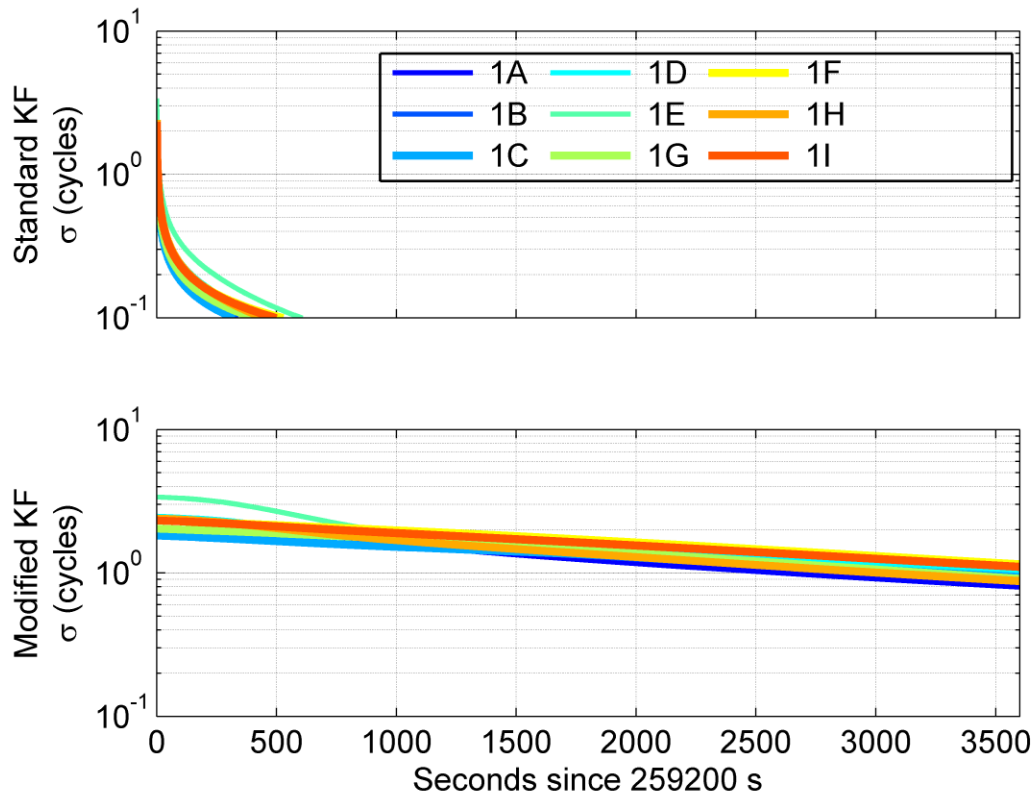


Figure 5-15 Convergence of single-differenced ambiguities after addition of two IGSO satellites in IRNSS constellation.

5.5.3 Augmentation with other GNSS Systems

Satellites from other GNSS systems can help to improve the observability of IRNSS when incorporated into the ambiguity resolution. Figure 5-16 shows an example of single-differenced ambiguity convergence when IRNSS is complemented with two GPS satellites in view. GPS PRN 1 and PRN 3 are considered in the solution because the satellites provide improved HDOP in comparison to the standalone IRNSS. A time constant of 40 s is considered for GPS satellites based on the previous studies (El-Rabbany and Kleusberg 2003; O’Keefe et al. 2006) The convergence of single-

differenced ambiguities using MKF improves significantly in comparison to Figure 5-11. After fixing ambiguities, the GPS measurements can be ignored to achieve an RTK solution with standalone IRNSS. With this method, there is no need to launch additional IRNSS satellites. On the flip side, it will compromise the goal of achieving an RTK solution using standalone IRNSS at the start of ambiguity resolution process.

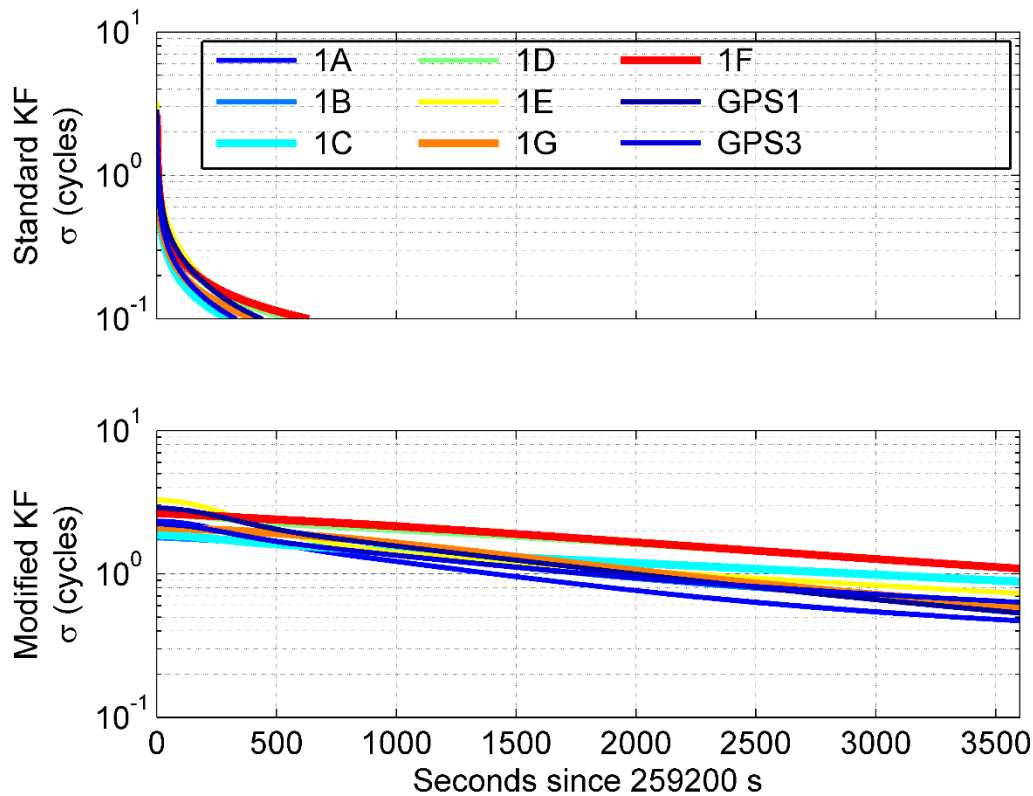


Figure 5-16 Convergence of single-differenced ambiguities when IRNSS is augmented with GPS satellites

To summarize, this chapter shows that there is a time-correlation in the code measurement errors of geostationary satellites. The time-correlated measurements lead

to poor observability and affect convergence of ambiguities as investigated using MKF. The slow convergence of ambiguities will lead to higher TTFFA when a large number of observations are from geostationary satellites. Use of satellites from other constellations has a major implication especially if a user wants to do RTK positioning using standalone IRNSS. Multiple solutions and their simulations results show that convergence time can be improved. More analysis is presented in the next chapter where a live data from IRNSS and GPS demonstrates improvement in TTFFA.

Chapter Six: **Investigation of Doppler Collision in IRNSS**

The Doppler collision and its impact on pseudorange observations are discussed in Chapter-3 using WAAS satellites whereas Chapter-4 discusses its implications on the RTK solution and options to mitigate the effect of Doppler collision. Chapter-5 presents the analysis of the observability of geostationary satellites and the implications of using geostationary satellites in RTK position and ambiguity solutions. In this chapter, the effect of Doppler collision is investigated using hardware-simulated and real IRNSS observations, including several of the previously discussed mitigation methods.

The chapter is organized as follows: First, the occurrence of Doppler collision in IRNSS is discussed. It begins with a Doppler variation analysis IRNSS followed by derivation of the IRNSS Doppler collision error envelope based on code phase. Preliminary observations with a commercial receiver show no effect of Doppler collision. Hence a hardware-simulation of the IRNSS constellation is implemented to observe Doppler collision. After identifying the Doppler collision window, code measurements are obtained, and the impact of the Doppler collision on the RTK solution is analyzed. Further, the application of narrow correlator demonstrates a significant reduction in Doppler collision error. To observe Doppler collision using live IRNSS signal, two commercial receivers with both standard and narrow correlators are used. The data from two receivers show that the narrow correlator is an effective mitigation method for Doppler collision in IRNSS signals. An IRNSS-GPS RTK is attempted using live signal and finally, the improvement in observability using GPS satellites is presented.

6.1 Preliminary Analysis in IRNSS

To study the occurrence of Doppler collision in the IRNSS constellation, the Doppler frequency variation of all IRNSS satellites is plotted over a 24 hour period and Doppler crossings are identified. A commercial receiver was used to collect IRNSS data at Bengaluru, India on 05 June 2016, before the clock on satellite 1A failed (GPS World Staff 2017). Figure 6-1 shows the variation of Doppler frequency of all seven satellites. Satellite 1C, 1F, and 1G are geostationary satellites, and among these three satellites, 1C and 1G have similar variations of Doppler frequencies.

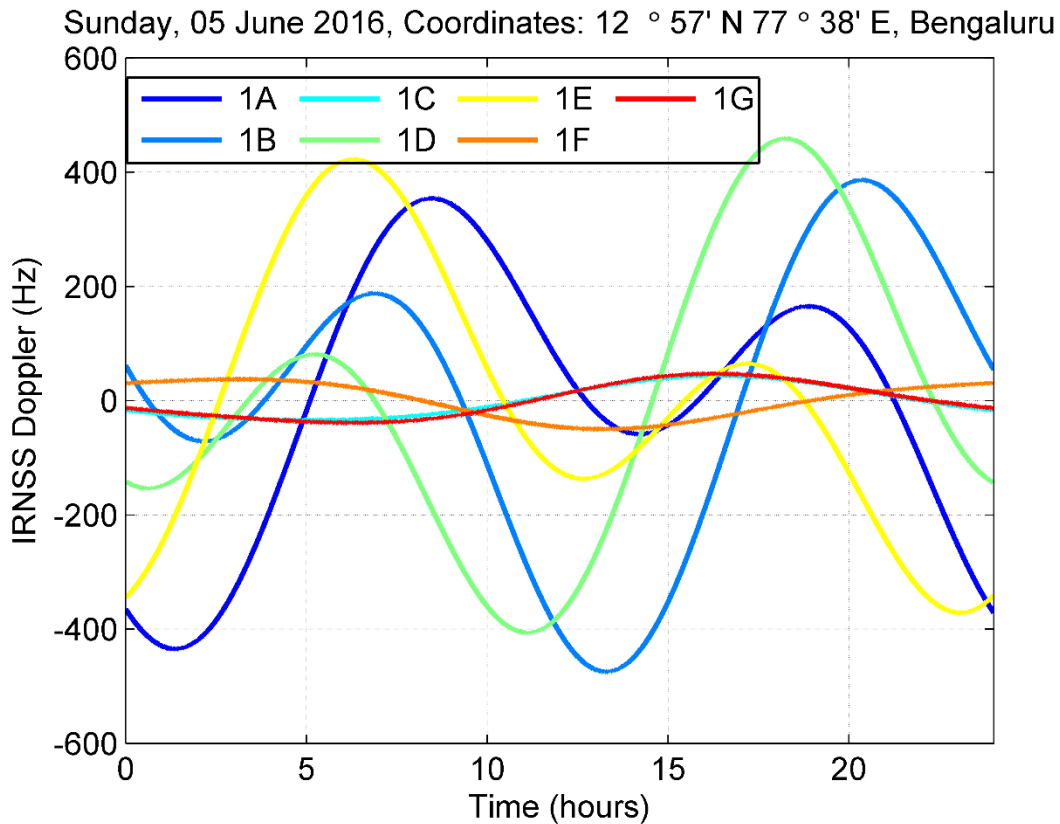


Figure 6-1 Frequency variation of all IRNSS satellites. 1C, 1G, and 1F are geostationary satellites

Further, a data collection was conducted on 10 April 2017 to log pseudorange and carrier phase observations of IRNSS satellites over a window when the Doppler crossing is expected. Figure 6-2 shows the Doppler variation of satellites 1C and 1G, its difference, and code-minus-carrier measurements on 10 April 2017. A predicted error envelope of Doppler collision, similar to that observed with WAAS satellites in Figure 3-16, was expected. For more details on the expected error envelope calculation, refer to Appendix C. However, unlike with the WAAS satellites, no envelope was observed in the corresponding code-minus-carrier observations corresponding. Unfortunately, since this data set was collected by a former colleague in India using a commercial equipment, limited information is available, specifically the type of correlator and chip spacing were unknown. With this limited real data, it is difficult to conclude much about the impact of Doppler collision on IRNSS.

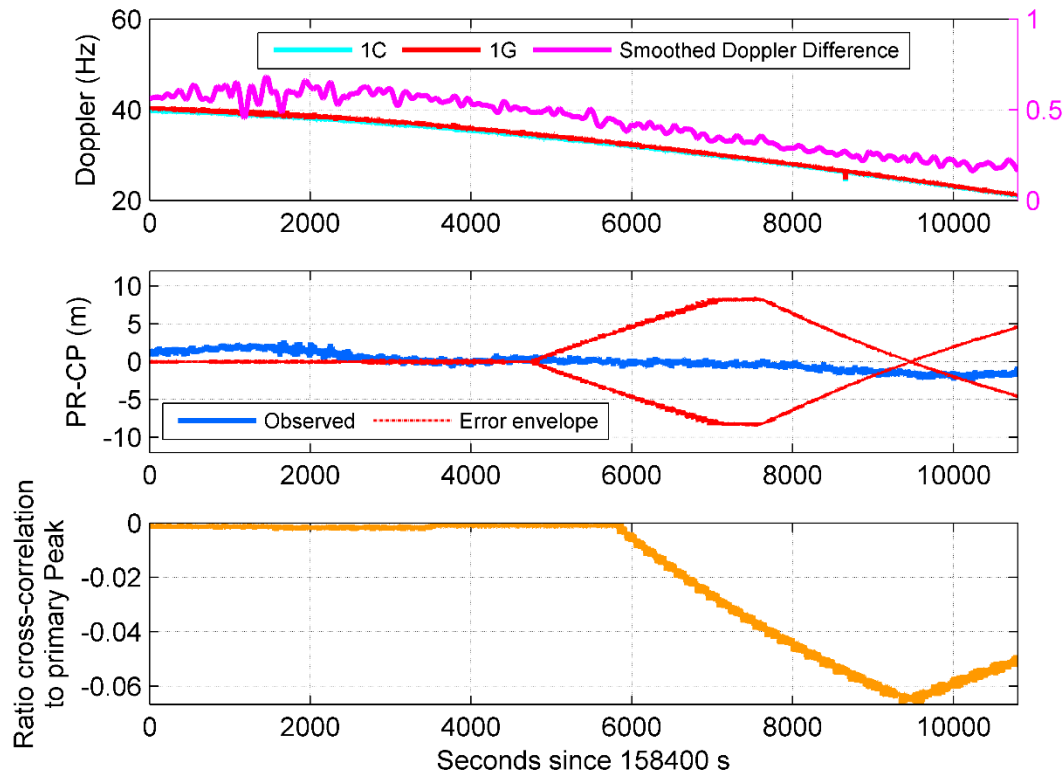


Figure 6-2 IRNSS live signal measurements of 1G, middle plot shows code-minus-carrier observations for 1G along error envelope for Doppler collision

The variation of a few metres in code-minus-carrier measurements over the entire data set corresponds to ionospheric error as shown in Figure 6-3 and does not demonstrate Doppler collision. While an additional data collection was being planned, a hardware-simulation of the IRNSS constellation in a GNSS simulator was conducted to collect and analyse pseudorange and phase observations with complete control over the receiver design.

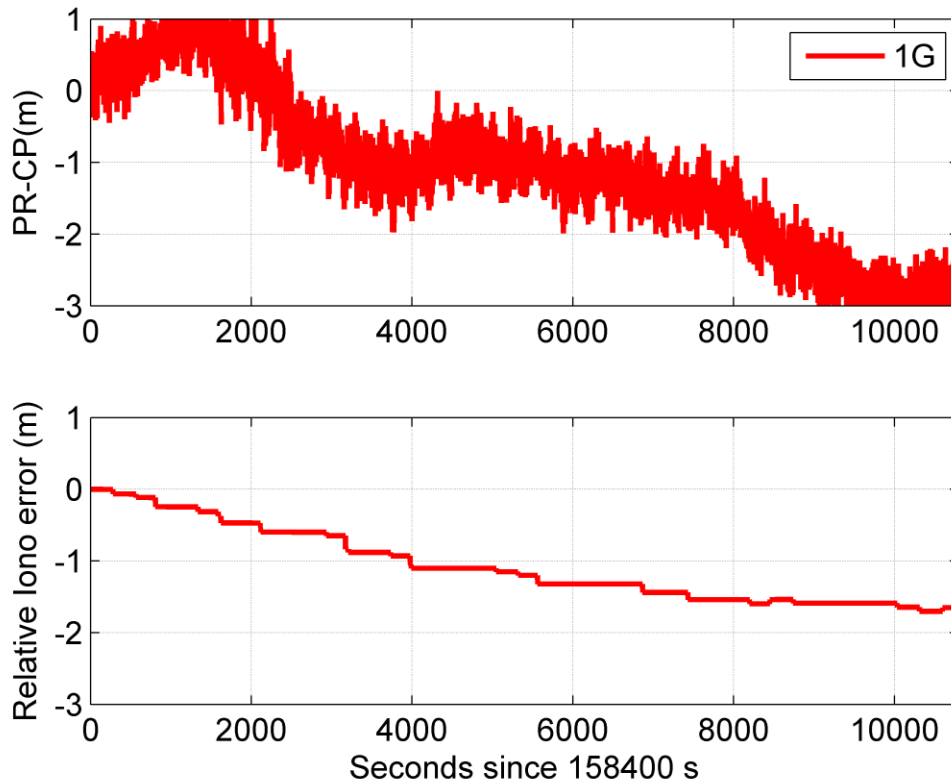


Figure 6-3 Ionospheric error observed in satellites 1G

6.2 Doppler Collision in Pseudo-IRNSS

A scenario was created in the Spirent Simulator GSS7700 in which the first seven GPS satellites were programmed as IRNSS satellites using the ephemeris information on 10 April 2017 from the IRNSS Broadcast Ephemeris (Montenbruck et al. 2017). This simulated constellation will be referred to as the pseudo-IRNSS constellation. The pseudo-IRNSS satellites have orbital parameters of IRNSS constellation but the carrier frequency and PRN codes of GPS L1 C/A. The change in carrier frequency does not affect Doppler collision events as long as the relative Doppler is zero and the IRNSS BPSK(1) codes are C/A codes with a different PRN. Table 6-1 provides the coordinates

of three different locations. RxIB is at the same location as the previous commercial receiver data collection.

Table 6-1 User locations to collect pseudo-IRNSS observations

User location	Latitude	Longitude	Height
RxIA	12 57' 20.166399"	77 38' 12.835145"	824.458 m
RxIB	12 57' 20.166281"	77 38' 27.763540"	824.474 m
RxIC	12 57' 20.165924"	77 38' 42.691934"	824.521 m

IF data was collected using a National Instrument front-end with I and Q sampled at 2 MHz. After processing the IF data using the GSNRx™ software receiver with a standard correlator spacing, the observed code-minus-carrier plot is shown in Figure 6-4. The variation in code-minus-carrier measurement follows Doppler collision error envelope and indicates the occurrence of Doppler collision in the pseudo-IRNSS satellites.

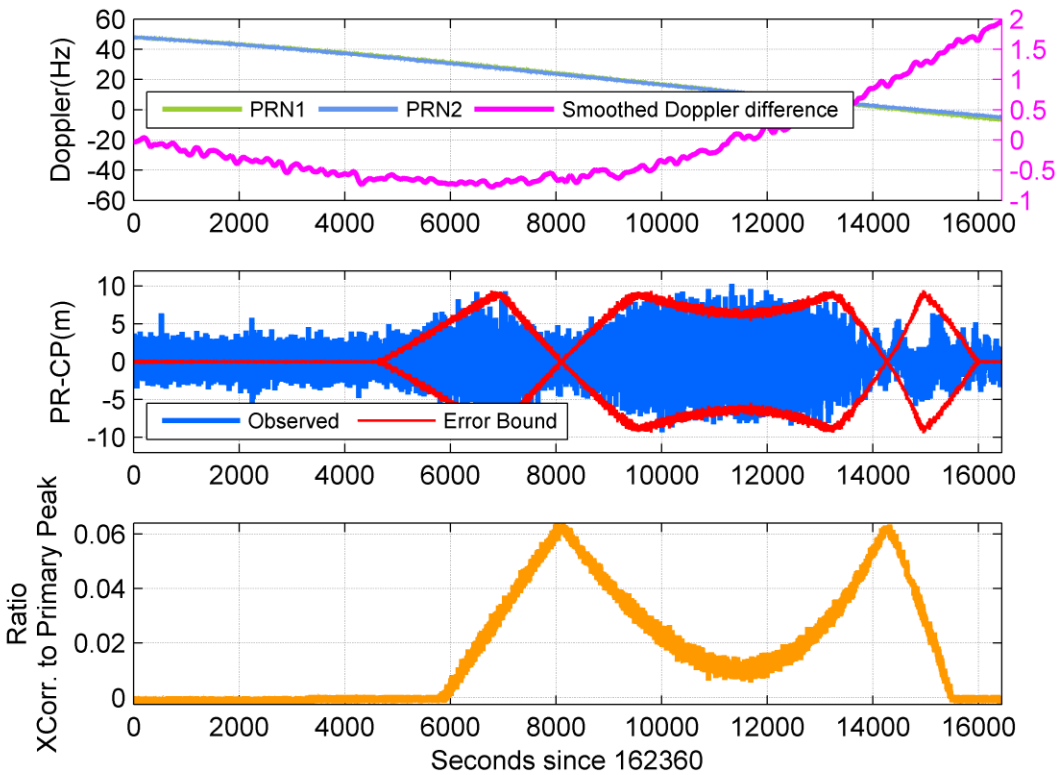


Figure 6-4 Code-minus-carrier measurements of pseudo-IRNSS satellite PRN 7 at RxIB

The same experiment was repeated at two more locations: RxIA, westward 450 m of RxIB and RxIC, eastward 450 m of RxIB. Table 6-1 provides the coordinates of the two additional locations. Figure 6-5 shows the code-minus-carrier measurements for all three receivers. The Doppler collision effect, observed at RxIA, begins at Rx1B after a duration whereas, at RxIC, there is a small tail of Doppler collision effect at the start and no Doppler collision for the rest of test duration. The effect of Doppler collision may be stretched or sharp, depending upon the relative Doppler between two satellites PRN 3 and PRN 7.

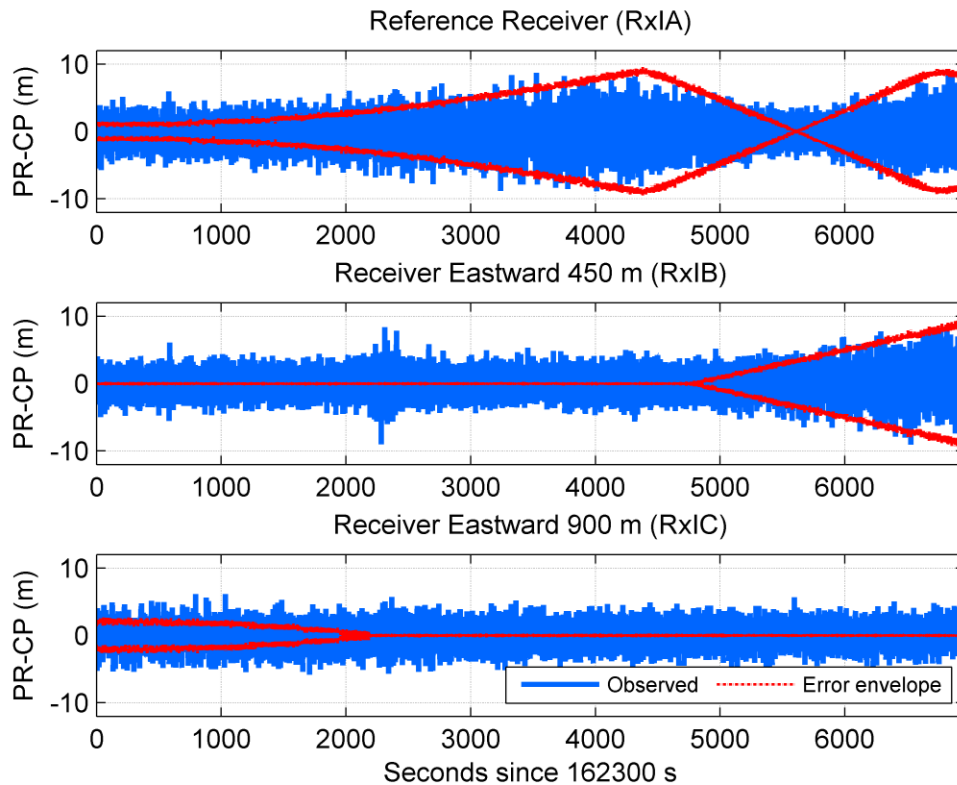


Figure 6-5 Code-minus-carrier measurements of pseudo-IRNSS satellite PRN 7 at three different locations

6.3 RTK Solution using Pseudo-IRNSS

Consider epoch 3000 s from the start time. Rx1B and Rx1C have no effect of Doppler collision where as Rx1A is experincing large variations in the code-minus-carrier measurement. Now at epoch 6000 s from start time, Rx1C has no collision effects whereas both receivers Rx1A and Rx1B are encountering Doppler collision. RTK solution is obtained at both epochs using following receiver combinations. Equal measurement weightage is given to all satellites.

1. RxIB and RxIC – no Doppler collision on both receivers at 3000 s and Doppler collision on RxIB at 6000 s
2. RxIA and RxIB – Doppler collision on RxIB at 3000 s and on both receivers at 6000 s.

Figure 6-6 shows the convergence of ambiguities and the float solution using the first combination of receivers. At 6000 s, when RxIB is experiencing Doppler collision, the float ambiguities have larger variations and are converging at slower rate. The float solution variation is also large and the fix time is slightly high.

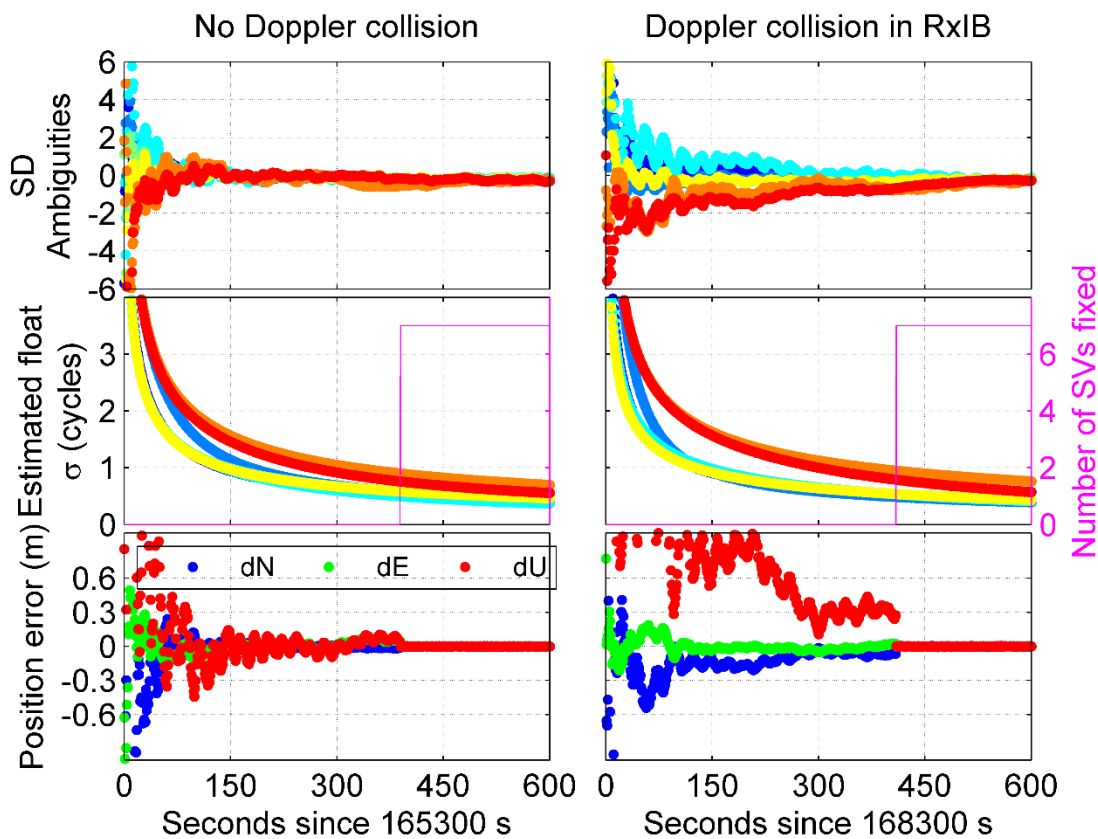


Figure 6-6 Convergence of single-differenced ambiguities and RTK solution with base RxIB and rover RxIC

An RTK solution using the second combination of receivers behaves similarly to the previous example. Figure 6-7 shows the convergence of ambiguities and the RTK solution at both epochs. At 6000 s, the convergence is poorer than the one at 4000 s when only the base receiver is experiencing Doppler collision.

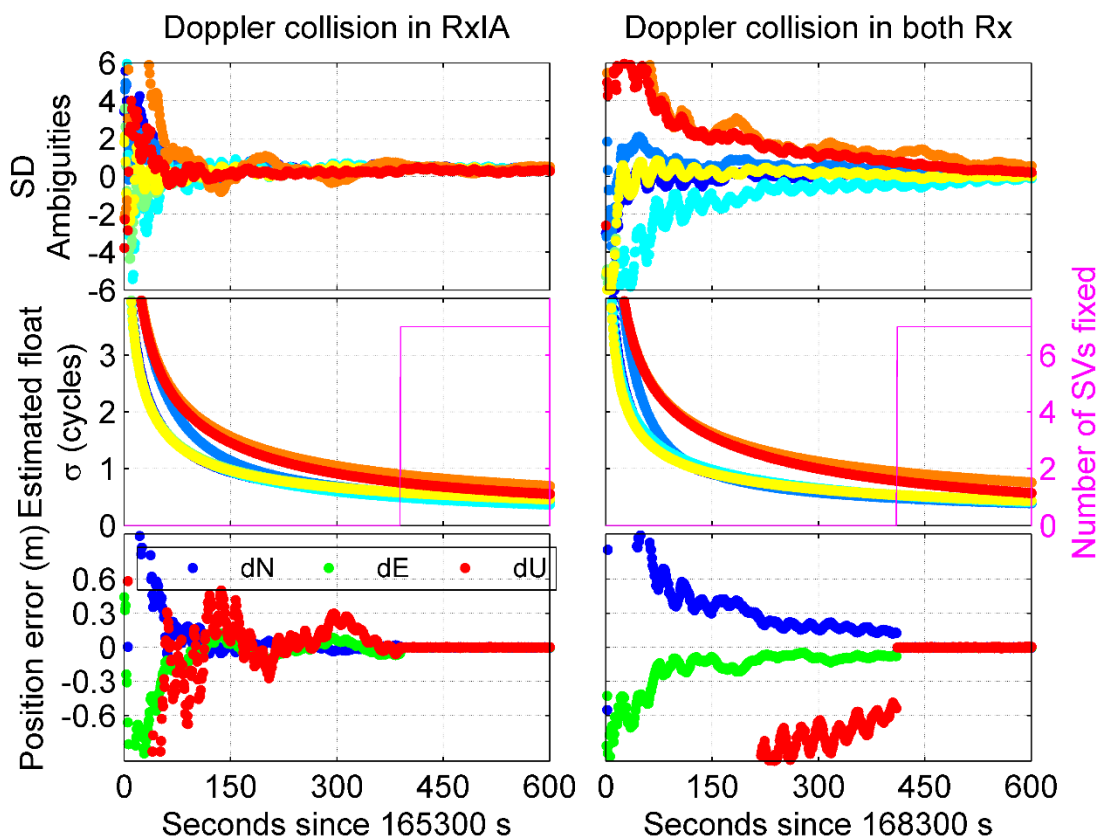


Figure 6-7 Convergence of single-differenced ambiguities and RTK solution with base RxIA and rover RxIB

6.3.1 TTFFA Analysis

To understand the complete impact of Doppler collision on pseudo-IRNSS, an analysis of TTFFA is conducted. Figure 6-8 shows the TTFFA obtained at an interval of every 60 s during the test period. All three receiver combinations are considered and the test period is divided into two segments. In the second segment, Doppler collision is observed on one or both receivers in the RTK solution. The plot shows that there is a small rise in the TTFFA during Doppler collision event. During the first segment, when only RxIA is experiencing Doppler collision, there is not much difference in TTFFA. The reason might be a small increase in code variation in comparison to the overall code measurement variance, which is not significant enough to affect TTFFA. However, the impact is observed on the float solution that has large position error before ambiguities are fixed.

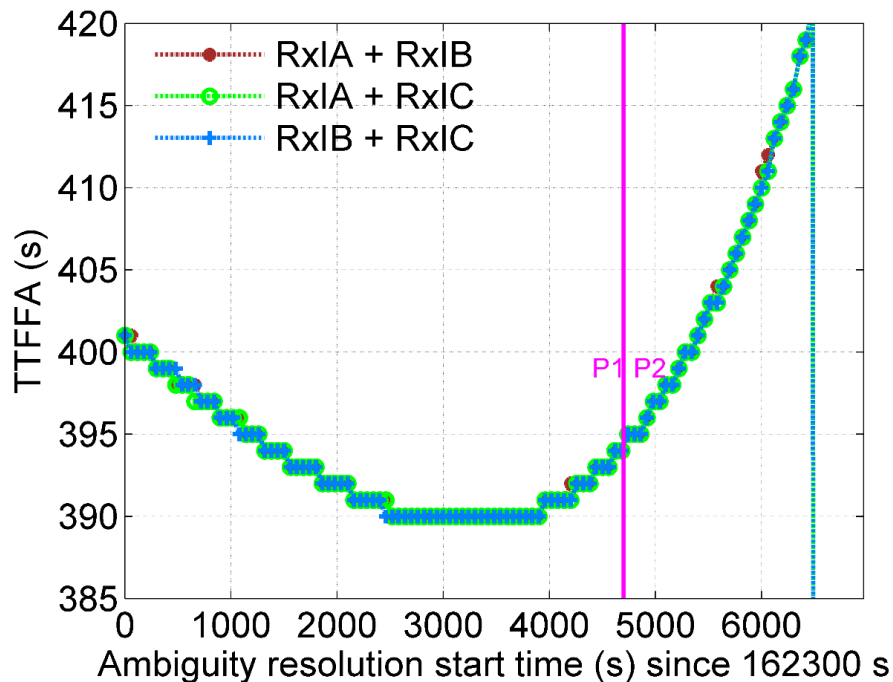


Figure 6-8 TTFFA using three combinations of receivers in hardware-simulation of pseudo-IRNSS

6.4 Mitigation of Doppler Collision in Pseudo-IRNSS

Section 4.3.3 shows that the effect of Doppler collision can be mitigated using narrow correlator. However, in the case of pseudo-IRNSS, all three data collections were performed using 2 MHz sampling rate which limits re-processing using narrow correlator. Therefore, the simulation was repeated at location Rx1A using a sampling rate of 20 MHz and measurements were obtained using two different chip spacing values as discussed below.

6.4.1 Standard Correlator

Figure 6-9 shows the Doppler variation and code-minus-carrier measurement of the data collected at Rx1A. It corresponds to first 25 minutes of the top row in Figure 6-5. The duration was limited due to the size of the data file which is large at the 20 MHz sampling rate. The plot shows that Doppler collision error is setting in and the code error is increasing with time.

6.4.2 Narrow Correlator

The bottom row in Figure 6-9 shows code-minus-carrier measurement for the same data that is processed using narrow correlator. The observed value and the error envelope indicates a minimal effect of Doppler collision. The use of narrow correlator could be one of the reasons not to observe Doppler collision in code-minus-carrier measurement in Figure 6-2, where a commercial grade receiver might be using effective multipath mitigation techniques in the receiver correlator.

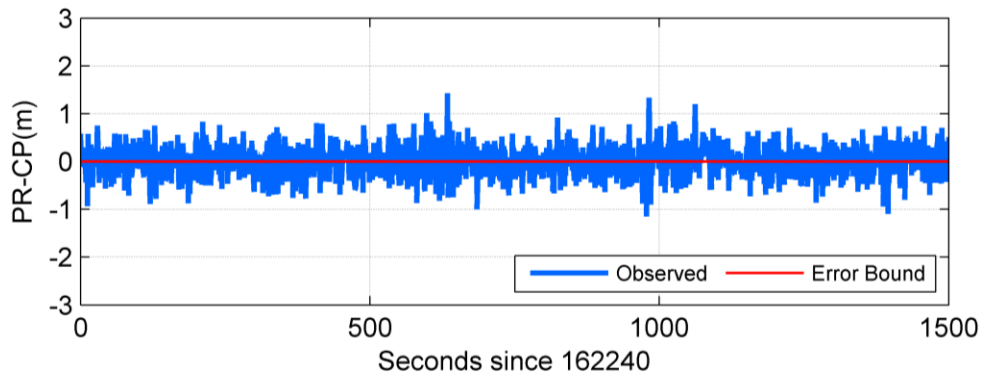
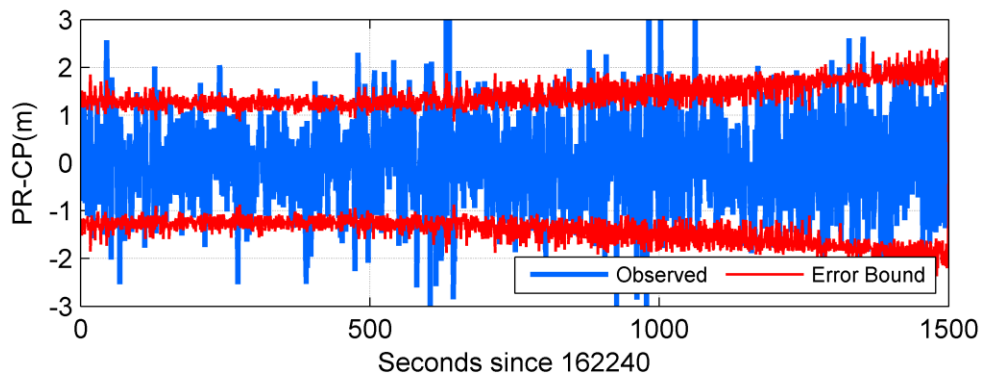
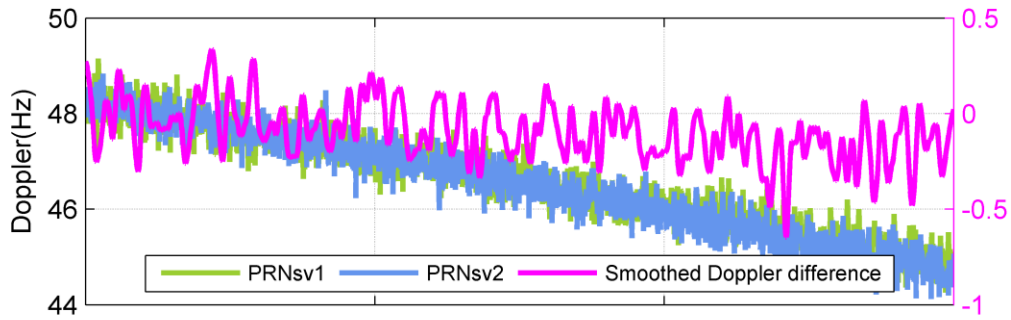


Figure 6-9 Doppler collision at RxIA and code-minus-carrier measurements: Middle row obtained using standard correlator, bottom row using narrow correlator

Returning to the live data plotted in Figure 6-2, if the same code-minus-carrier measurement is plotted with the error envelope computed using narrow correlator, the Doppler collision error envelope would resemble that shown in Figure 6-10. The measurement variation is well within the error envelope, and thus it is difficult to detect the Doppler collision effect in the observations.

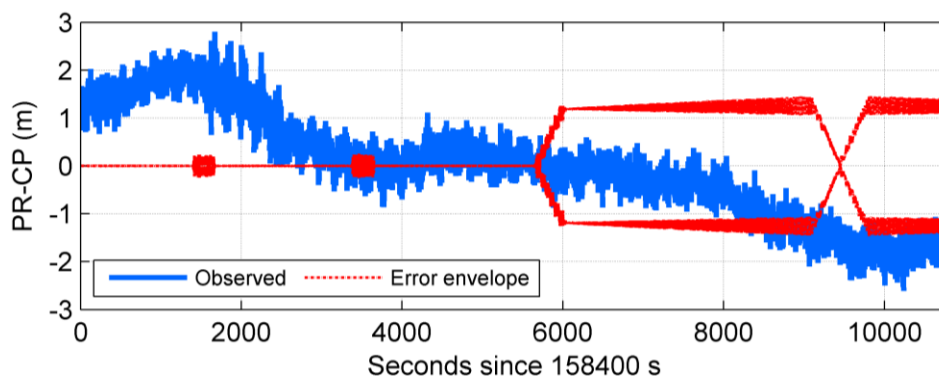


Figure 6-10 Commercial receiver code-minus-carrier observations for 1G with Doppler collision error envelope obtained using narrow correlator

Figure 6-10 shows that the code-minus-carrier measurement has periodic variation. Figure 6-11 shows an enlarged section of the plot. The periodic variation corresponds to approximately 300 s which is equivalent to 3.33 milli-Hz. This amount of Doppler corresponds to a multipath signal (Nievinski and Larson 2014; Gowdayyanadoddi et al. 2015), and the magnitude of variation shows that it cannot be carrier phase multipath (Ray et al. 1999). Thus it can be attributed only to code multipath. Multipath is a likely

scenario as the data collection was performed in a semi-open urban environment. The variation is not due to Doppler collision because similar variation is present in code-minus-carrier measurements even when Doppler collision error envelope is not present.

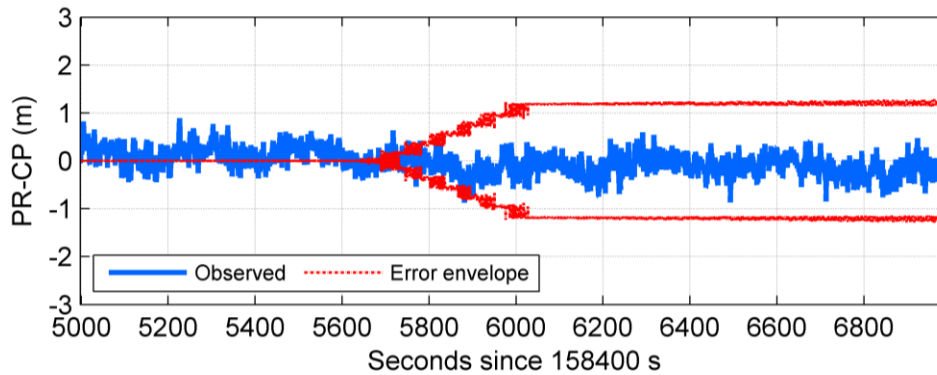


Figure 6-11 Periodic variations in code-minus-carrier measurement of 1G, collected using commercial receiver

6.5 Doppler Collision using Live IRNSS Signal

Section 3.5.2 shows an example of Doppler collision using live IRNSS signal, which was the first example of real data collected using standard correlator. In the previous section the second attempt to collect live IRNSS data with a Doppler collision was unsuccessful because receiver correlator chip spacing was not known. In the third attempt, two commercial receivers, one programmed with standard correlator and second programmed with narrow correlator, are used to collect IRNSS data simultaneously during likely conditions of Doppler collision. The baseline between two receivers is small, and hence the effect of Doppler collision would be similar. Figure 6-12 shows Doppler collision effect on standard correlator receiver. The top plot shows Doppler variation, the middle

plot is code-minus-carrier with error envelope, and the bottom plot is ratio of cross-correlation peak to primary peak. The variation in the code-minus-carrier in sync with the error envelope.

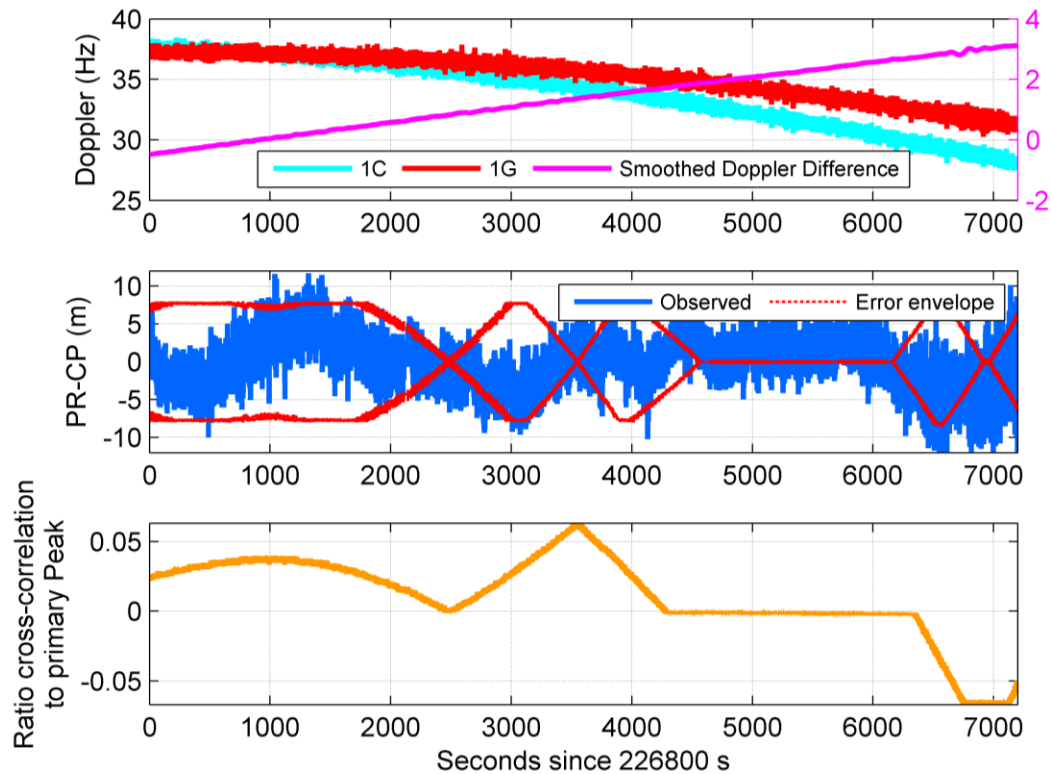


Figure 6-12 Doppler collision observed on IRNSS 1G live signal using standard correlator receiver

Figure 6-13 shows the effect of Doppler collision on measurements of 1C collected using same standard correlator receiver. The magnitude of code-minus-carrier variation is small in comparison to 1G. During the test period, 1C is at an elevation of about 75° with C/N_0 varying between 46 to 48 dB-Hz and is 5 dB higher than 1G, which is at an elevation of

30°. Kaplan and Hegarty (2005) shows that at C/N_0 greater than 40 dB-Hz, a drop of 5 dB leads to an increase of 0.5 m in the measurement standard deviation. Thus the effect of Doppler collision is large on 1G.

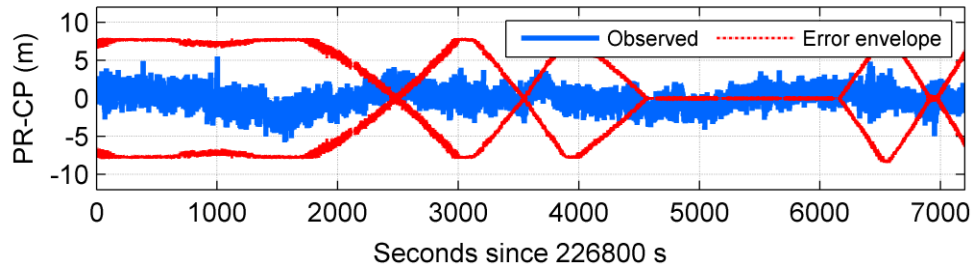


Figure 6-13 Doppler collision observed on IRNSS 1C live signal using a commercial standard correlator receiver

Figure 6-14 shows a plot of code-minus-carrier of 1G observed during Doppler collision using narrow correlator receiver. In comparison to standard correlator, the error envelope is significantly reduced. The plot demonstrates that the use of narrow correlator can mitigate the effect of Doppler collision on live IRNSS signal.

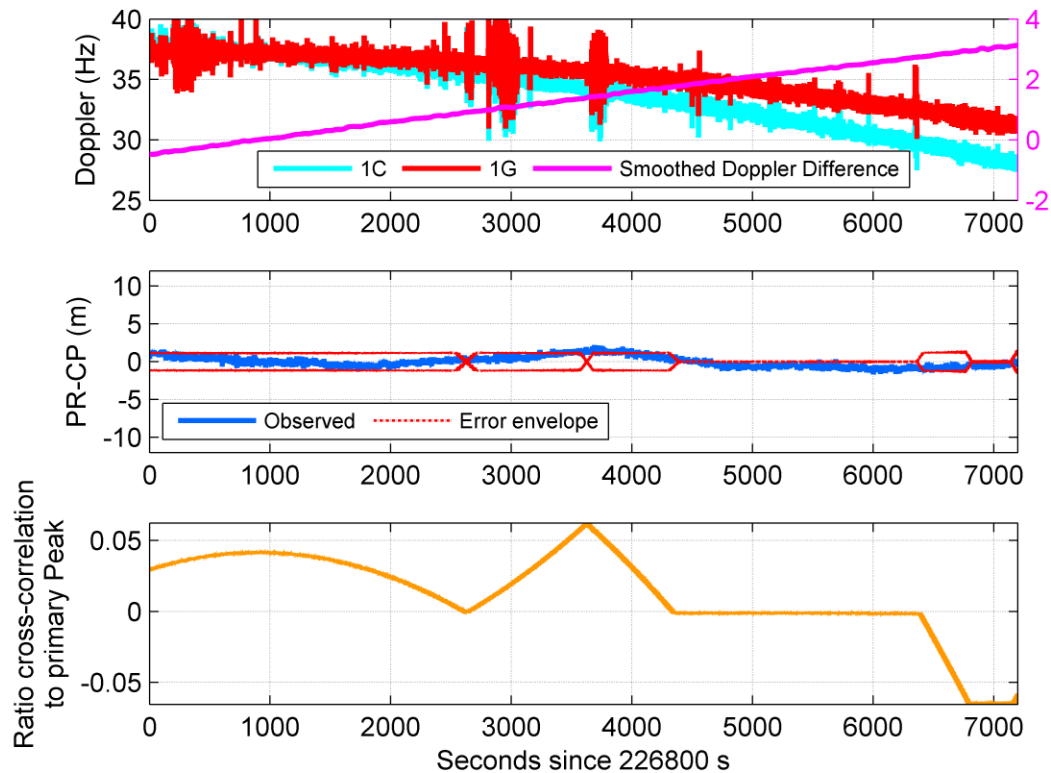


Figure 6-14 Doppler collision observed on IRNSS 1G live signal using a commercial narrow correlator receiver

6.6 Single Frequency RTK Solution using Live IRNSS Data

In the final phase of the research, an attempt is made realize a single frequency L5 IRNSS – L1 GPS RTK solution. Appendix D provides more information about the software development and requirements implemented in PLANSoft™ to realize an IRNSS-GPS RTK solution. IRNSS-GPS live data was collected on Saturday, 12 August 2017 using two survey grade commercial receivers at Hyderabad, India. Since, the data was collected by Novatel Inc., limited information is available about receivers' configuration.

Table 6-2 provides the user coordinates for base and rover receivers. The baseline between base and rover is about 5 m.

**Table 6-2 Coordinates of base and rover receivers for a single frequency L5
IRNSS – L1 GPS RTK solution**

User location	Latitude	Longitude	Height
Base	17 ⁰ 26' 34.8646'' N	78 ⁰ 22' 26.8056'' W	651.08 m
Rover	17 ⁰ 26' 35.0366'' N	78 ⁰ 22' 26.8302'' W	651.06 m

Figure 6-15 shows the variation of Doppler frequencies of 1C and 1G along with code-minus-carrier measurement of 1C at the base location. The error envelope is computed assuming the receiver is using narrow correlator. Between 500 s and 1000 s, Doppler crossing is observed and the relative Doppler varies around 0 Hz. However, the code phase combination does not lead to Doppler collision as seen in ratio of cross-correlation peak to primary peak. Also, the code-minus-carrier variation is very small and is smooth throughout the test duration. Given, the variation of code-minus-carrier variation, the effect of Doppler collision, even if present, would be very small and can be ignored.

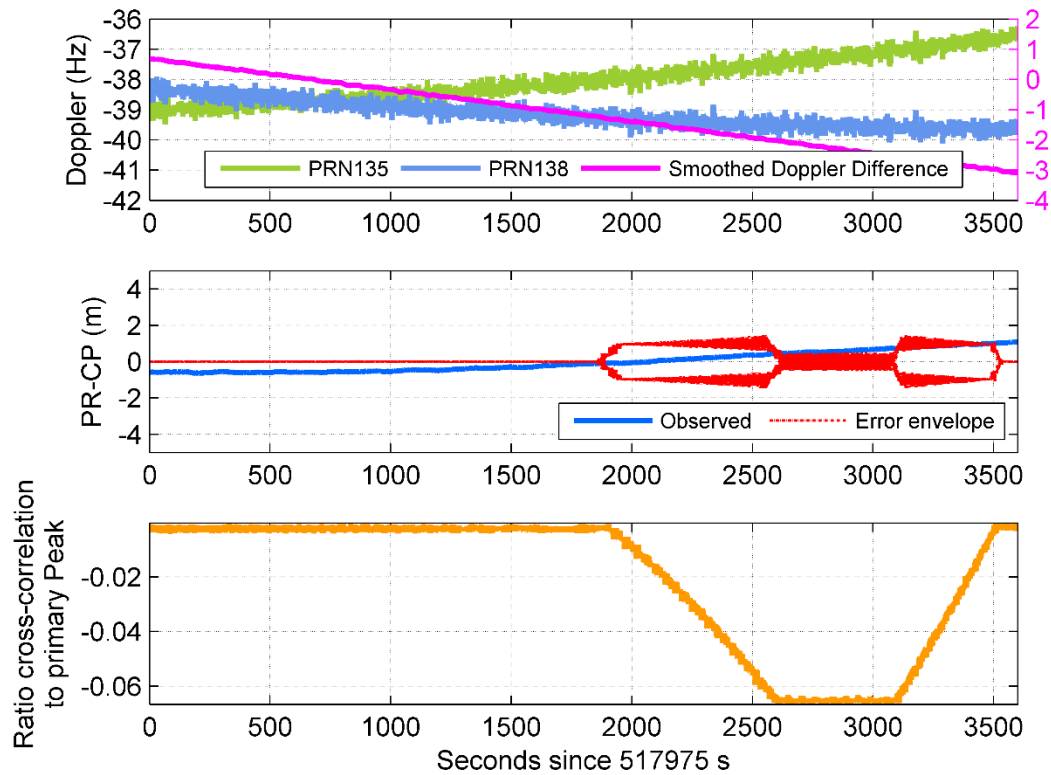


Figure 6-15 Code-minus-carrier of 1C observed using commercial receiver at Hyderabad, 12 August 2017

Figure 6-16 shows the RTK solution using L5 IRNSS – L1 GPS. Since all visible GPS satellites and six IRNSS satellites are used in solution fix, the convergence of SD ambiguities is quick and solution fix is obtained in a minute.

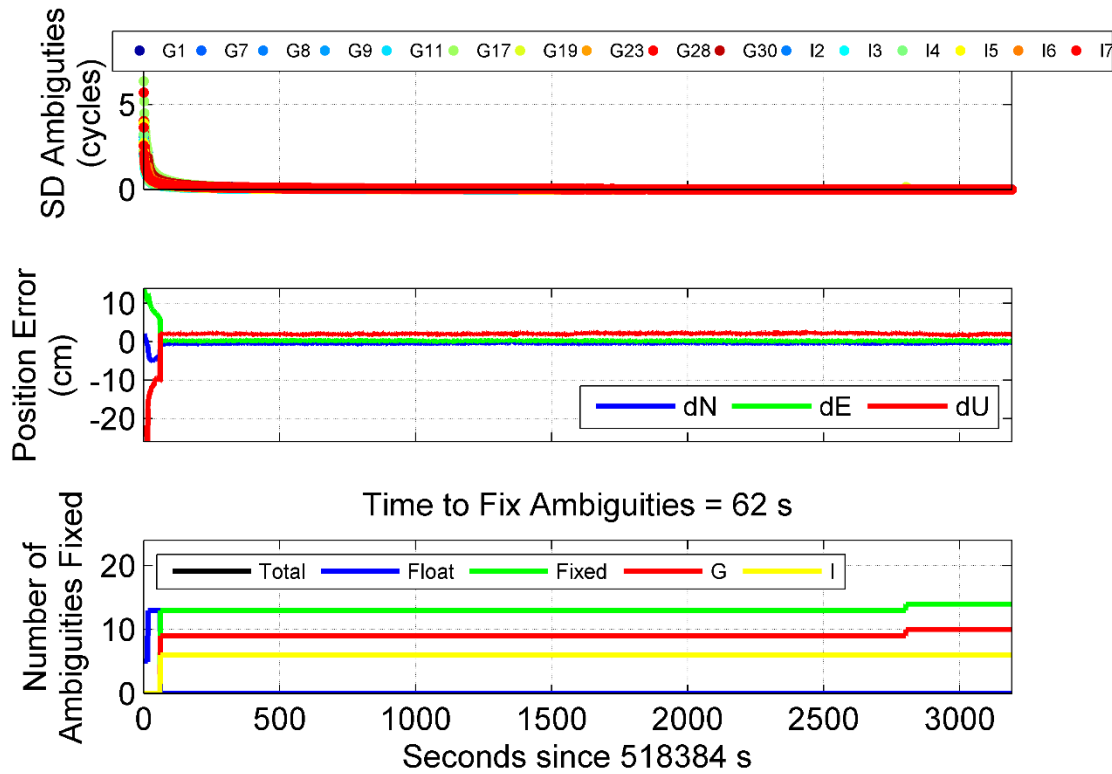


Figure 6-16 RTK solution using L5 IRNSS – L1 GPS at Hyderabad, 12 August 2017

Figure 6-17 shows an RTK solution with all IRNSS satellites and only 2 GPS satellites (PRN 8 and 17). There is an increase in the TTFFA because of the reduced number of satellites. Given the quality of measurements of a survey grade commercial receiver, even if the effect of Doppler collision is present, the impact on the convergence of ambiguities would be negligible.

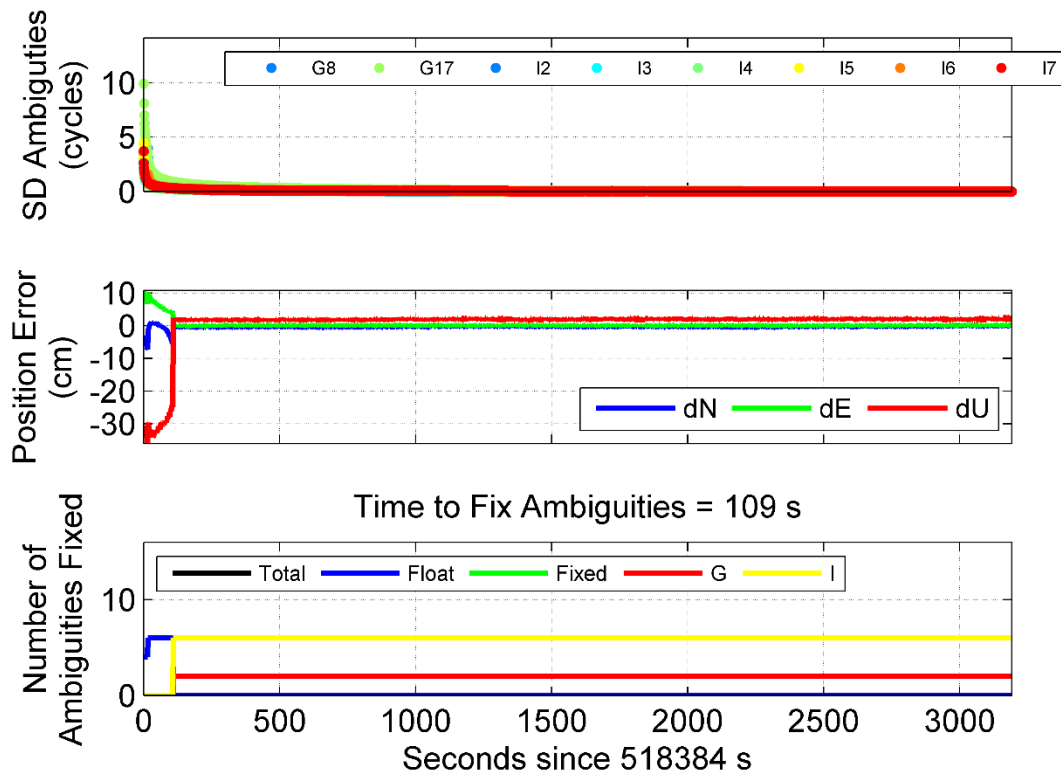


Figure 6-17 RTK solution using L5 IRNSS – L1 GPS with only two GPS satellites

6.7 Improvement in IRNSS Observability

An observability analysis is conducted on the previous IRNSS-GPS data and the convergence of ambiguities is obtained. Figure 6-18 shows the convergence of single-differenced IRNSS ambiguities obtained using MKF. The top row shows the convergence of a standalone IRNSS and the bottom row shows the convergence of IRNSS augmented with two GPS satellites. The time-correlation of measurements error is factored in the convergence of ambiguities using MKF, which is discussed in section 5.2. Using GPS as an augmentation system, there is a significant improvement in the ambiguity convergence in comparison to the standalone IRNSS system.

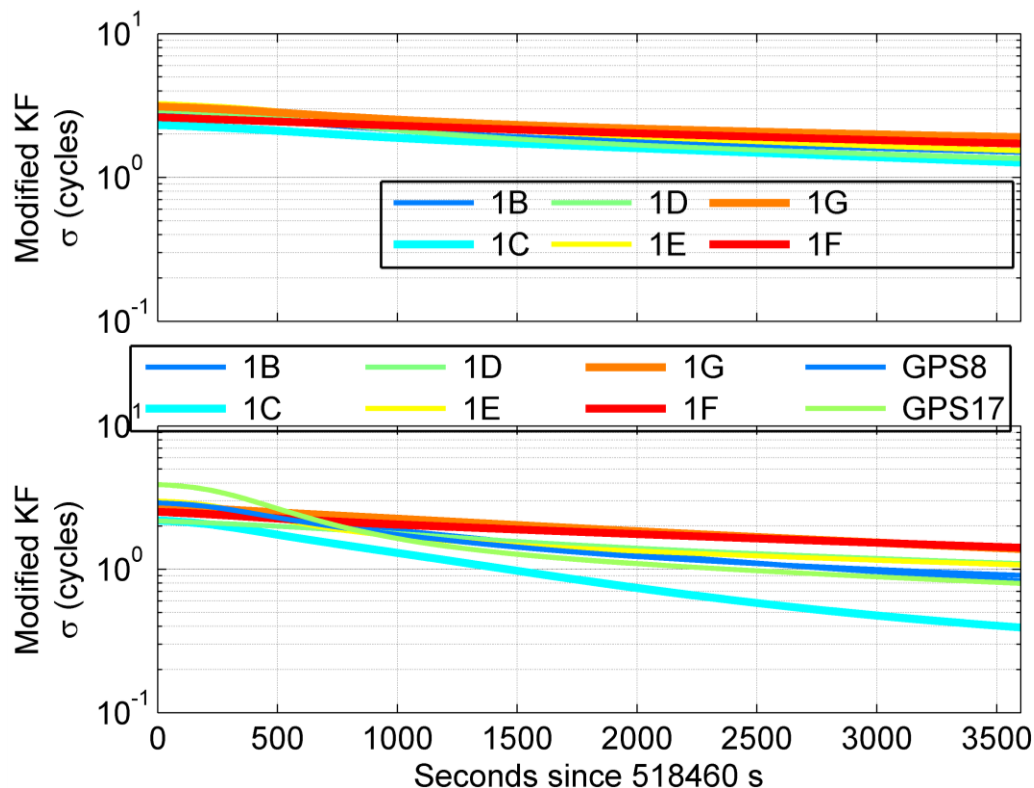


Figure 6-18 Convergence of IRNSS ambiguities, top plot shows a standalone IRNSS with satellites 1B to 1G, bottom plot shows IRNSS augmented with two GPS satellites: PRN 8 and 17

In summary, Doppler collision has an impact on live IRNSS signal. An attempt was made to measure the impact on an IRNSS-like pseudo-IRNSS system. The Doppler collision affects the convergence of ambiguities and in turn increase the TTFFA. The Doppler collision effect on live signal is significantly reduced with the use of narrow correlator. Also, the convergence of ambiguities as observed using MKF is improved with the augmentation of GPS satellites. Due to the geographical constraints and limited access to IRNSS receivers, the impact of Doppler collision on an RTK solution is not assessed using live signal.

Chapter Seven: **Conclusions and Recommendations**

In a multi-constellation RTK solution, all constellations including IRNSS and SBAS may be used. Geostationary satellites form a major segment of IRNSS and BeiDou and all satellites in SBAS. In addition to multipath that is prevalent for a significant time of the day, GEOs encounter two major challenges: Doppler collision and poor observability. Doppler collision affect code measurements and has impact on an RTK solution whereas the poor observability is a challenge in realising a standalone IRNSS RTK solution. This chapter concludes the thesis with a summary of conclusions and a discussion on recommended future work.

7.1 Conclusions

The following conclusions can be drawn from the findings of the research:

7.1.1 Characterization of Doppler Collision

Doppler collision is a phenomenon in GNSS signals. Doppler collision between two satellites is determined by six factors: relative Doppler, cross-correlation function, relative code delay, relative power, data message similitude, and relative carrier phase. The examination of relative Doppler showed that while short lived in MEO GNSS satellites, extended periods of Doppler collision are possible in SBAS and the geostationary satellites of IRNSS and BeiDou. Cross-correlation function analysis proved that Doppler collision is possible in SBAS and IRNSS, whereas the occurrence of large cross-correlation peaks in BeiDou is small because of its use of truncated even Gold codes. The spatial analysis shows the occurrence of Doppler collision based on relative code

delay. The magnitude of Doppler collision error is determined by the relative signal strength whereas the sign is determined by data message similitude and the relative carrier phase. Multiple hardware-simulations demonstrated Doppler collision events and their impact on code measurements. An experimental method to provide a systematic methodology to observe Doppler collision repeatedly was developed. Furthermore, live SBAS data were collected to observe Doppler collision.

7.1.2 RTK Positioning during Doppler Collision

Doppler collision primarily affects code measurements and complicated the use of geostationary satellites in an RTK solution. Hardware-simulated SBAS observations were generated and used in an RTK solution. Single-differenced code residuals increased significantly when one or both of the receivers in the RTK solution were experiencing Doppler collision. The ambiguity convergence was delayed, and there was an increase in TTFFA. De-weighting the affected observations was demonstrated as a simple mitigation method.

When using live data, de-weighting of GEO observations shows an improvement in TTFFA when the impact of Doppler collision is severe. The theoretical analysis shows that the occurrence of Doppler collision can be identified using code phase and the magnitude of the Doppler collision can be computed. Therefore in a real-time solution, a user can de-weight the GEO observations experiencing Doppler collision and achieve improvement in TTFFA.

Also, multiple solutions are discussed to address Doppler collisions. The system level changes include an increase in Doppler variation of satellites as well as the out-of-phase overlap of Doppler variation. The second solution includes changes in transmission codes which can reduce the occurrence of Doppler collision. Finally, the application of multipath mitigation techniques such as narrow correlator shows promising results with a significant decrease in code variance. The reduction in variance brings the code variation to a level where Doppler collision variation is buried under the code noise.

7.1.3 Observability of Geostationary Satellites

Geostationary satellites also experience poor ambiguity observability due to the inability of geostationary satellites to add information in an RTK solution as a result of their relatively static position in the sky. GEO pseudorange observation error is highly correlated and was evaluated using autocorrelation analysis. If the time-correlation is factored into the estimation of ambiguities, the convergence of covariance of ambiguities is very poor and in turns affects the TTFFA.

Multiple solutions are presented to improve the observability of the IRNSS constellation. First, a user can include observations from GAGAN satellites. Simulation results show no significant improvement is observed because both GAGAN satellites are geostationary. The second solution includes expansion of the IRNSS constellation with two additional IGSO satellites. There is a small improvement in observability. The addition of IGSO would be a possible solution if IRNSS were to expand in the near future. Finally, a user can use other GNSS systems such as GPS to initiate ambiguity resolution. This solution

is possible without any changes or expansion of IRNSS. However, it would compromise the goal of achieving an RTK solution exclusively with IRNSS.

7.1.4 Investigation of Doppler Collision in IRNSS

After observing Doppler collision in hardware-simulated and live data, the impact of Doppler collision on the IRNSS constellation was assessed. The Doppler variations of all IRNSS satellites were analyzed, and Doppler crossing windows were identified. Real data and hardware-simulated data were collected. RTK results using the simulated data show the impact of Doppler collision on the convergence of ambiguities. The Doppler collision is mitigated using a narrow correlator receiver design while tracking the live IRNSS signal. Finally, the improvement in observability is demonstrated by augmenting the RTK solution using GPS satellites.

7.2 Recommendations for Future Work

Although this thesis covers the effect of Doppler collision and observability in geostationary satellites and IRNSS, the actual impact of Doppler collision in an IRNSS-GPS RTK solution using a live signal was not observed. The immediate step would be to collect more live IRNSS data and establish the relevance of Doppler collision on the IRNSS-GPS RTK solution. Furthermore, some interesting questions relevant to Doppler collision, modelling of measurement errors and six GNSS + SBAS RTK remain unanswered. Some of these are listed below.

7.2.1 Separation of Doppler collision and multipath

In this thesis, all live data collection is performed with utmost care to avoid multipath. Even in the case of hardware simulation, no multipath was introduced. However, a large number of practical cases will encounter multipath in addition to Doppler collision. Since Doppler collision is similar to multipath effect, it would be challenging to isolate the effects of Doppler collision and multipath. The major contribution of this research is the real-time determination of Doppler collision effect based on the code phase of geostationary satellites. It is possible to estimate the effect of Doppler collision and separate from multipath. The next step would be to observe both effects simultaneously and mitigate the errors based on the estimated effect of Doppler collision.

7.2.2 Cross-Correlation Function

In this thesis, analysis to determine cross-correlation peaks was limited to BPSK(1) modulation using C/A code and, to a certain extent, BeiDou's B1I truncated even Gold codes. Galileo, for example, uses random codes and has MBOC (Multiplexed Binary Offset Carrier) modulation. It would be interesting to know what the occurrence and the magnitude of Doppler collision would be, if similar codes are used in geostationary satellites. An extensive analysis of all codes under geostationary satellite conditions could provide insights into which codes are better suited for geostationary satellites to avoid Doppler collision.

7.2.3 Auto-Regressive Modelling of Geostationary Measurement Errors

The modeling of geostationary code measurement errors used a first order GM model to approximate time-correlation. Although it was a good fit, there is scope to model the time-correlation using auto-regressive models and derive the coefficients of shaping filter. Higher order auto-regressive models will have a direct consequence on the MKF and will alter the estimate states. At this stage, it is hard to predict the overall improvement on the covariance of the ambiguities; higher order models will add more computational steps in the filter.

7.2.4 Multi-Constellation RTK Solution with Six GNSS and SBAS

The primary motivation behind this research was the realization of an RTK solution with all six constellations and SBAS satellites. Nadarajah and Teunissen (2014) and Odolinski et al. (2014) have undertaken instantaneous ambiguity resolution with multiple constellations whereas Nadarajah et al. (2016) and Zaminpardaz et al. (2016b) have attempted positioning using IRNSS. The next step would be to combine all constellation in a single RTK solution, especially geostationary satellites, after addressing Doppler collision and factoring in the time-correlation of observations.

References

- Aaron, B. S. (2006) *Geosynchronous satellite maneuver detection and orbit recovery using ground based optical tracking*. MSc Thesis, Department of Aeronautics and Astronautics, Massachusetts Institute of Technology, USA, 116 pages (Available at <https://dspace.mit.edu/handle/1721.1/36175>)
- Alves, P. (2001) "The effect of Galileo on carrier phase ambiguity resolution," in *Proceedings of ION GPS*, 11-14 September, Salt Lake city, UT, pp. 11–14, U.S Institute of Navigation, Fairfax VA
- Babu, R., T. Rethika, and S. C. Rathnakara (2012) "Onboard Atomic Clock Frequency Offset for Indian Regional Navigation Satellite System" *International Journal of Applied Physics and Mathematics*, vol 2, no 4, July, pp.270-272
- Balaei, A. T. and D. M. Akos (2009) "Doppler collision and cross correlation interference in GPS receivers," in *Proceedings of the IGSS Symposium 2009*, Holiday Inn Surfers Paradise, Qld, Australia, 13 pages, International Global Navigation Satellite Systems Society
- Balaei, A. T. and D. M. Akos (2011) "Cross Correlation Impacts and Observations in GNSS Receivers," *Navigation, Journal of the Institute of Navigation*, vol 58 no 4, December, John Wiley & Sons Inc., New York, NY, pp. 323-33
- BeiDou ICD (2013) *BeiDou Navigation Satellite System Signal in Space Interface Control Document Open Service Signal Version 2.0*
- Bhandari, V. (2015) "Characterization of Doppler Collision and Its Effect on Indoor Positioning," in *PhD forum of Proceedings of the International Conference on Indoor Positioning and Indoor Navigation (IPIN 2015)*, Banff, AB, 2 pages
- Bhandari, V. and K. O’Keefe (2016) "What is Doppler Collision and is it a problem in GNSS?," *Inside GNSS*, vol 11, no. 1, Gibbons Media & Research LLC, New Jersey, USA, pages 26-36
- Bhandari, V. and K. O’Keefe (2017) "Characterization of Doppler collision and its impact on carrier phase ambiguity resolution using geostationary satellites," *GPS Solutions*, Springer Berlin Heidelberg, <https://doi.org/10.1007/s10291-017-0648-z>
- Bhandari, V., K. O’Keefe, and G. Lachapelle (2013) "Assessment of multi-constellation RTK solutions during differential correction data outages," in *Proceedings of ION GNSS+ 2013*, 16-20 September, Nashville, TN, pp. 3194-3204, US. The Institute of Navigation, Fairfax VA
- Bhaskar, S., J. T. Curran, and G. Lachapelle (2015) "Improving GNSS carrier-phase tracking via oscillator g-sensitivity compensation," *IEEE Transactions on Aerospace and*

Electronic Systems, vol 51 no 4, December, pp. 2641-2654 doi: 10.1109/TAES.2015.130197

Boriskin, A., D. Kozlov, and G. Zyryanov (2007) "L1 RTK system with fixed ambiguity: what SBAS ranging brings," In *Proceedings of ION GNSS 2007*, 25-28 September, Fort Worth, Texas, pp 2196–2201, U.S Institute of Navigation, Fairfax VA

Braasch M. S. (1996) "Multipath Effects," [Chapter-14] in *Global Positioning System: Theory and Applications Volume I*, American Institute of Aeronautics and Astronautics, Washington, DC, pp. 547-568

Braasch, M. S. (1997) "Autocorrelation sidelobe considerations in the characterization of multipath errors," *IEEE Transactions on Aerospace and Electronic Systems* vol 33 no 1, January, pp. 290–295 doi: 10.1109/7.570787

Braasch, M. S. (2001) "Performance comparison of multipath mitigating receiver architectures," In *IEEE Proceedings Aerospace Conference*, Big Sky, MT, pp 1309–1315 doi: 10.1109/AERO.2001.931361

Brown, R. G. and P. Y. C. Hwang (1997) "Linearization and Additional Intermediate-Level Topics on Applied Kalman Filtering," [Chapter 9] in *Introduction to Random Signals and Applied Kalman Filtering*, 3^{ed} Ed, John Wiley & Sons, Inc., New York, NY, pp 335–391

Cao, W. (2009) *Multi-frequency GPS and Galileo kinematic positioning with partial ambiguity fixing*, MSc. Thesis, Department of Geomatics Engineering, University of Calgary, Canada, 180 pages, (Available at <http://www.geomatics.ucalgary.ca/research/publications>)

Chen, D. and G. Lachapelle (1995) "A Comparison of the FASF and Least-Squares Search Algorithms for on-the-Fly Ambiguity Resolution," *Navigation, Journal of the Institute of Navigation*, vol 42 no 2, June, John Wiley & Sons Inc., New York, NY, pp. 371–390

Cox, D. T., K. W. Shallberg, and A. Manz (1999) "Definition and analysis of WAAS receiver multipath error envelopes," *Navigation, Journal of the Institute of Navigation*, vol 46 no 4, June, John Wiley & Sons Inc., New York, NY, pp. 271–282

Dai, L., (2000) "Dual-frequency GPS/GLONASS real-time ambiguity resolution for medium-range kinematic positioning," In *Proceedings of ION GPS*, 19-22 September, Salt Lake City, UT, pp. 1071-1080, U.S Institute of Navigation, Fairfax VA

de Jonge, P. and C. Tiberius (1996) *The LAMBDA method for integer ambiguity estimation: implementation aspects* Publications of Delft Computing Centre LGR-Series 47 pages

Dou, J. and K. O’Keefe (2013) "Augmenting GPS RTK with Regional BeiDou in North America," In *Proceedings of ION GNSS+ 2013*, 16-20 September, Nashville, TN, pp 3205–3213, U.S Institute of Navigation, Fairfax VA

Dow, J. M., R. E. Neilan, and C. Rizos (2009) "The International GNSS Service in a changing landscape of Global Navigation Satellite Systems," *Journal of Geodesy*, vol 3, no. 83, February, pp. 191–198, doi: 10.1007/s00190-008-0300-3

El-Rabbany, A. and A. Kleusberg (2003) "Effect of Temporal Physical Correlation on Accuracy Estimation in GPS Relative Positioning," *Journal of Surveying Engineering*, vol 129, no 1, October, pp. 28–32, doi: 10.1061/(ASCE)0733-9453(2003)129:1(28)

El-Rabbany, A. E. (1994) *The effect of physical correlations on the ambiguity resolution and accuracy estimation in GPS differential positioning*, Ph.D. Thesis, Department of Geodesy and Geomatics Engineering, University of New Brunswick, Canada, 177 pages

Enge, P. K. and A. J. Van Dierendonck (1996) "Wide Area Augmentation System," [Chapter-4] in *Global Positioning System: Theory and Applications, Volume II*, American Institute of Aeronautics and Astronautics, Washington, DC pp. 117-142

Euler, H. J. and H. Landau (1992) "Fast GPS ambiguity resolution on-the-fly for real-time applications," In *Proceedings of 6th International Geodesy Symposium on satellite Positioning*, Columbus, Ohio. pp 17–20

Fairhurst, P., X. Luo X and A. Aponte A (2013) "New Systems, New Signals, New Positions – Providing BeiDou Integration," in *Proceedings of ION GNSS+ 2013*, 16-20 September, Nashville, TN, pp. 3214–3220, US. The Institute of Navigation, FairFax VA

Fenton, P. C. and J. Jones (2005) "The theory and performance of NovAtel Inc.’s vision correlator," in *Proceedings of the ION GNSS*, 13-16 September, Long Beach, CA, pp 2178–2186, US. The Institute of Navigation, FairFax VA

Frei, E. and G. Beutler (1990) "Rapid Static Positioning Based on the Fast Ambiguity Resolution Approach “FARA”: Theory and First Results," *Manuscripta Geodaetica*, vol 15 no 4, pp. 325–356

Galileo ICD (2016) *European GNSS (Galileo) Open Service Signal-In-Space Interface Control Document (OS SIS ICD) Issue 1.3*

Garin, L. and J-M Rousseau (1997) "Enhanced strobe correlator multipath rejection for code & carrier," in *Proceedings of ION GPS 1997*, 16-19 September, Kansas City, MO, pp 559–568, US. The Institute of Navigation, FairFax VA

Gelb, A., J. F. Kasper Jr., R. A. Nash, Jr., C. F. Price, and A. A. Suther;and Jr. (1974) *Applied optimal estimation*, The M.I.T. Press Massachusetts Institute of Technology, Cambridge, Massachusetts, and London, England, 374 pages

Google Maps (2017) *Google Maps. In: NW Calgary* <https://www.google.ca/maps/@51.0767118,-114.1046905,3967m/data=!3m1!1e3>, last accessed February 28 2017

Gowdayyanadoddi, N. S., J. T. Curran, A. Broumandan, and G. Lachapelle (2015) "A Ray-Tracing Technique to Characterize GPS Multipath in the Frequency Domain," *International Journal of Navigation and Observation*, 16 pages, doi: <http://dx.doi.org/10.1155/2015/983124>

GPS World Staff (2017) *3 atomic clocks fail on 1 Indian satellite, replacement prepped.* *GPS World*, <http://gpsworld.com/3-atomic-clocks-fail-on-1-indian-satellite-replacement-prepped/>, last accessed June 21, 2017

Habrigh, H., G. Beutler, W. Gurtner, M. Rothacher (1999) "Double difference ambiguity resolution for GLONASS/GPS carrier phase," in *Proceedings of ION GPS 1999*, 14-17 September, Nashville, TN, pp 1609–1618, U.S. The Institute of Navigation, Fairfax VA

Harris, R. A. (1997) *Direct resolution of carrier phase ambiguity by "bridging the wavelength gap"*, ESA, ESA Pub. TST/60, 107 pages

Hatch, R. (1990) "Instantaneous ambiguity resolution," in *Proceedings of Kinematic systems in geodesy, surveying, and remote sensing*, 10-13 September, Symposium No. 107 Banff, Alberta, Canada, pp 299–308

Héroux, P., Y. Gao, J. Kouba, F. Lahaye, Y. Mireault, P. Collins, K. Macleod, P. Tétreault, and K. Chen (2004) "Products and Applications for Precise Point Positioning - Moving Towards Real-Time," in *Proceedings of ION GNSS 2004*, 21-24 September, Long Beach, CA, pp.1832–1843, U.S. The Institute of Navigation, Fairfax VA

Hopfield, H. S. (1969) "Two-quartic tropospheric refractivity profile for correcting satellite data," *Journal of Geophysics Research*, vol 74 no 18, August, pp. 4487–4499, doi: 10.1029/JC074i018p04487

Hwang, P. Y. C. (1991) "Kinematic GPS for Differential Positioning: Resolving Integer Ambiguities on the Fly," *Navigation, Journal of the Institute of Navigation*, vol 38 no 1, March, John Wiley & Sons Inc., New York, NY, pp. 1-15, doi: 10.1002/j.2161-4296.1991.tb01711.x

Jung, J., P. Enge, and B. Pervan (2000) "Optimization of cascade integer resolution with three civil GPS frequencies," in *Proceedings of ION GPS 2000*, 19-22 September, Salt Lake City, UT, pp. 2191 - 2200, U.S. The Institute of Navigation, Fairfax VA

Kaplan, E. D. and C. J. Hegarty (2005) "Satellite Signal Acquisition, Tracking, and Data Demodulation," [Chapter 5] in *Understanding GPS: Principles and Applications*, 2nd Ed, Artech House Inc., Norwood, MA, pp 153–239

Kee, C., B. W. Parkinson, and P. Axelrad (1991) "Wide Area Differential GPS," *Navigation, Journal of the Institute of Navigation*, vol 38 no 2, June, John Wiley & Sons Inc., New York, NY, pp. 123–145, doi: 10.1002/j.2161-4296.1991.tb01720.x

Kim, D. and R. B. Langley (1999) "An optimized least-squares technique for improving ambiguity resolution and computational efficiency," in *Proceedings of ION GPS 1999*, 14-17 September, Nashville, TN, pp. 1579-1588, U.S. The Institute of Navigation, Fairfax VA

Kim, D., R. B. Langley (2001) "Instantaneous real-time cycle-slip correction of dual frequency GPS data," in *Proceedings of the international symposium on kinematic systems in geodesy, geomatics and navigation*, 5-8 June, Banff, Alberta, Canada, pp 255–264

Kleiner, L. (2010) *Ambiguity Resolution with GPS and GLONASS measurements in obstructed environment*, MSc Thesis, École polytechnique fédérale de Lausanne, Switzerland, 98 pages (Available at http://plan.geomatics.ucalgary.ca/papers/l%20kleiner_master_epfl_june2010.pdf)

Kouba, J. and P. Héroux (2001) "Precise Point Positioning Using IGS Orbit and Clock Products," *GPS Solutions* vol 5 no 2, pp. 12–28, doi: 10.1007/PL00012883

Lachapelle, G. (1991) "GPS observables and error sources for kinematic positioning," in *Kinematic Systems in Geodesy, Surveying, and Remote Sensing*, 10-13 September, Symposium No. 107 Banff, Alberta, Canada, pp. 17–26

Landau, H., M. Brandl, X. Chen, R. Drescher, M. Glocker, A. Nardo, M. Nitschke, D. Salazar, U. Weinbach, F. Zhang (2013) "Towards the inclusion of Galileo and BeiDou/compass satellites in trimble centerpoint RTX," in *Proceedings of the ION GNSS 2013+*, 16-20 September, Nashville, TN, pp. 1215–1223, U.S. The Institute of Navigation, Fairfax VA

Leick, A., J. Beser, P. Rosenboom, and B. Wiley B (1998) "Assessing GLONASS observation," in *Proceedings of ION GPS*, 15-18 September, Nashville, TN, pp 1605–1612, U.S. The Institute of Navigation, Fairfax VA

Lestarquit, L., J-L Issler, O. Nouvel, M. Sihrener, G. Lamontagne, J. C. Guay, R. Landry, O. Julien, C. Macabiau, and M. Nouvel-Malicorne (2009) "Worst-case scenario SBAS Interference," *GPS World*, vol 20 no 4, A Questex Publication, NewTon, MA, pp. 37–42

Lestarquit, L., O. Nouvel (2012) "Determining and measuring the true impact of C/A code cross-correlation on tracking," in *Proceedings of IEEE/ION PLANS*, 24-26 April, Myrtle Beach, SC, pp. 1134–1140, U.S. The Institute of Navigation, Fairfax VA

Li, W., N. Nadarajah, P. J. G. Teunissen, and A. Khodabandeh (2017) "Array-Aided Single-Frequency State-Space RTK with Combined GPS, Galileo, IRNSS, and QZSS

L5/E5a Observations," *Journal of Surveying Engineering*, vol 143, no 4, 10 pages, doi: 10.1061/(ASCE)SU.1943-5428.0000227

Majithiya, P., K. Khatri K, and J. K. Hota (2011) "Indian regional navigation satellite system: correction parameters for timing group delays," *Inside GNSS*, vol 6, no 1, January/February, Gibbons Media & Research LLC, Red Bank, NJ, pp. 40-46

Miller, C., K. O'Keefe, Y. Gao (2010) "Operational performance of RTK positioning when accounting for the time correlated nature of GNSS phase errors," in *Proceedings of the ION GNSS*, 21-24 September, Portland, OR, pp. 1513 - 1524, U.S. The Institute of Navigation, Fairfax VA

Misra, P. and P. Enge (2006) "GPS measurements and error sources," [Chapter 5] in *Global Positioning System: Signals, Measurements, and Performance*, 2nd Ed, Ganga-Jamuna Press, Lincoln, MA, pp. 147–193

Montenbruck, O., P. Steigenberger, R. Khachikyan, G. Weber, R. Langley, L. Mervart and U. Hugentobler (2014) "IGS-MGEX: preparing the ground for multi-constellation GNSS science," *Inside GNSS*, vol 9, no 1, January/February, Gibbons Media & Research LLC, Red Bank, NJ, pp. 42–49

Montenbruck, O., P. Steigenberger, L. Prange, Z. Deng, F. Perosanz, I. Romero, C. Noll, A. Stürze, G. Weber, and R. Schmid (2017) "The Multi-GNSS Experiment (MGEX) of the International GNSS Service (IGS)—Achievements, prospects and challenges," *Advances in Space Research*, vol 59 no 7, January, pp. 1671–1697

Mruthyunjaya, L. and A. S. Ganeshan (2014) *Indian Regional Navigation Satellite System Standard Positioning Service Signal in Space Interface Control Document (IRNSS SPS SIS ICD)*, Version 1.0

Nadarajah, N., A. Khodabandeh, and P. J. G Teunissen (2016) "Assessing the IRNSS L5-signal in combination with GPS, Galileo, and QZSS L5/E5a-signals for positioning and navigation," *GPS Solutions*, vol 20, no 2, pp. 289–297, doi: 10.1007/s10291-015-0450-8

Nadarajah, N. and P. J. G. Teunissen (2014) "Instantaneous GPS/Galileo/QZSS/SBAS Attitude Determination: A Single-Frequency (L1/E1) Robustness Analysis under Constrained Environments," *Navigation, Journal of the Institute of Navigation*, vol 61 no 1, March, John Wiley & Sons Inc., New York, NY, pp. 65-75, doi:10.1002/navi.51

Nassar, S., K-P Schwarz, N. El-Sheimy, and A. Noureldin (2004) "Modeling inertial sensor errors using autoregressive (AR) models," *Navigation, Journal of the Institute of Navigation*, vol 51 no 4, December, John Wiley & Sons Inc., New York, NY, pp. 259–268

Nievinski, F. G. and K. M. Larson (2014) "An open source GPS multipath simulator in Matlab/Octave," *GPS Solutions*, vol 18, no 3, pp. 473–481, doi: 10.1007/s10291-014-0370-z

Noll, C. E. (2010) "The crustal dynamics data information system: A resource to support scientific analysis using space geodesy," *Advances in Space Research*, vol 45, no 12, pp. 1421–1440, doi: 10.1016/j.asr.2010.01.018

Nouvel, O., M. Sihrener, J-L Issler, L. Lestarquit, C. Macabiau and O. Julien (2008) "SBAS C/A code interference characterization and mitigation," in ENC-GNSS 2008, Conférence Européenne de la Navigation, 23 April, Toulouse, France, 9 pages

Nouvel, O., M. Sihrener, J-L. Issler, L. Lestarquit, C. Macabiau, and O. Julien (2007) "SBAS C/A code interferences: observations and induced tracking errors," in *Proceedings of ION GNSS*, Fort Worth, Texas, pp 950–959, U.S. The Institute of Navigation, Fairfax VA

Novatel OEMV® Reference Manual (2010) *OEMV Family Firmware Version 3.800 Reference Manual Rev 8*, NovAtel Inc. Canada, 650 pages

Odijk, D. (2002) *Fast precise GPS positioning in the presence of ionospheric delays*, Ph.D. Thesis, Department of Mathematical Geodesy and Positioning, Delft University of Technology, Delft, Netherlands, 264 pages (Available at [uuid:40d49779-2ef4-4641-9ae4-f591871063fa](https://doi.org/10.1002/978111871063fa))

Odijk, D. (2008) "Mathematical Models and GNSS Interference," *Inside GNSS*, vol 3, no 2, March/April, Gibbons Media & Research LLC, Red Bank, NJ, pp. 25–27

Odijk, D., S. Verhagen, P. J. G. Teunissen, M. Hernandez-Pajares, J. M. Juan, J. Sanz, J. Samson, and M. Tossaint (2010) "LAMBDA-based ambiguity resolution for next-generation GNSS wide area RTK," in *Proceedings of the 2010 International Technical Meeting of the Institute of Navigation*, 25-27 January, San Diego, CA, pp. 566-576

Odolinski, R., D. Odijk, P. J. G. Teunissen (2014) "Combined GPS and BeiDou Instantaneous RTK Positioning," *Navigation, Journal of the Institute of Navigation*, vol 61 no 2, December, John Wiley & Sons Inc., New York, NY, pp. 135–148. doi: 10.1002/navi.61

Odolinski, R., P. J. G. Teunissen (2017) "Low-cost, high-precision, single-frequency GPS–BDS RTK positioning," *GPS Solutions*, vol 21 no 3, March, pp. 1315-1330, doi: 10.1007/s10291-017-0613-x

Odolinski, R., P. J. G. Teunissen, D. Odijk (2015) "Combined BDS, Galileo, QZSS and GPS single-frequency RTK," *GPS Solutions*, vol 19 no 1, April, pp. 151–163 doi: 10.1007/s10291-014-0376-6

Odolinski, R., P. J. G. Teunissen, D. Odijk (2013) "Quality analysis of a combined COMPASS/BeiDou-2 and GPS RTK positioning model," in *Proceedings of the IGNSS Symposium 2013*, 16-18 July, Outrigger Gold Coast, Qld Australia, 15 pages, International Global Navigation Satellite Systems Society

O'Driscoll, C. (2010) "Generating Carrier Phase Measurements," *Inside GNSS*, vol 5, no 5, July/August, Gibbons Media & Research LLC, Red Bank, NJ, pp. 18–22

O'Keefe, K., M. Petovello, W. Cao, G. Lachapelle, and E. Guyader (2009) "Comparing multicarrier ambiguity resolution methods for geometry-based GPS and Galileo relative positioning and their application to low earth orbiting satellite attitude determination," *International Journal of Navigation and Observation*, 15 pages, doi: <http://dx.doi.org/10.1155/2009/592073>

O'Keefe, K., M. Petovello, G. Lachapelle, and M. E. Cannon (2006) "Assessing Probability of Correct Ambiguity Resolution in the Presence of Time-Correlated Errors," *Navigation, Journal of the Institute of Navigation*, vol 53 no 4, December, John Wiley & Sons Inc., New York, NY, pp. 269-282. doi: 0.1002/j.2161-4296.2006.tb00389.x

Olynik, M., M. Petovello, M. E. Cannon, and G. Lachapelle (2002) "Temporal impact of selected GPS errors on point positioning," *GPS Solutions*, vol 6, no 1-2, November, pp. 47–57. doi: 10.1007/s10291-002-0011-9

Ong, R. (2010) *Reliability of combined GPS/GLONASS ambiguity resolution*, MSc. Thesis, Department of Geomatics Engineering, University of Calgary, Canada, 185 pages (Available at <http://www.geomatics.ucalgary.ca/research/publications>)

Ong, R. B., M. Petovello, and G. Lachapelle (2009) "Assessment of GPS/GLONASS RTK under various operational conditions," in *Proceedings of the ION GNSS*, 22-25 September, Savannah, GA, pp. 3297–3308, U.S. The Institute of Navigation, Fairfax VA

Parkinson, B. W., P. Enge, P. Axelrad, J. J. and Spilker Jr. (1996a) *Global Positioning System: Theory and Applications Volume I*, American Institute of Aeronautics and Astronautics, Washington, DC

Parkinson, B. W., J. J. Spilker Jr., P. Axelrad, and P. Enge (1996b) *Global Positioning System: Theory and Applications, Volume II*, American Institute of Aeronautics and Astronautics, Washington, DC

Pesyna, K. M., T. E. Humphreys, R. W. Heath, T. D. Novlan, and J. C. Zhang (2017) "Exploiting antenna motion for faster initialization of centimeter-accurate GNSS positioning with low-cost antennas," *IEEE Transactions on Aerospace and Electronic Systems*, vol PP, no 99, 14 pages, doi:10.1109/TAES.2017.2665221

Petovello, M. G., C. O'Driscoll, G. Lachapelle G, D. Borio, and H. Murtaza (2008) "Architecture and benefits of an advanced GNSS software receiver," *Journal of Global Positioning Systems*, vol 7, no 2, November, pp. 156–168

Petovello, M. G., K. O'Keefe, G. Lachapelle, and M. E. Cannon (2009) "Consideration of time-correlated errors in a Kalman filter applicable to GNSS," *Journal of Geodesy*, vol 83, no 1, January, pp. 51–56, doi: 10.1007/s00190-008-0231-z

Petovello, M. G., K. O'Keefe, G. Lachapelle, and M. E. Cannon (2005) "Quantifying ambiguity resolution performance in the presence of time-correlated measurement errors using geometric-based techniques," in *Proceedings of the 61st Institute of Navigation Annual Meeting*, 27-29 June, Cambridge, MA, pp 1073–1085

QZSS ICD (2016) *Quasi-Zenith Satellite System Navigation Service, Interface Specification for QZSS (IS-QZSS) Version 1.8.*

Rao, V. (2013) *Proposed LOS fast TTFF signal design for IRNSS*, Ph.D. Thesis, Department of Geomatics Engineering, University of Calgary, Canada, 271 pages (Available at <http://www.geomatics.ucalgary.ca/research/publications>)

Ray, J. K. (2000) *Mitigation of GPS code and carrier phase multipath effects using a multi-antenna system*. Ph.D. Thesis, Department of Geomatics Engineering, University of Calgary, Canada, 285 pages (Available at <http://www.geomatics.ucalgary.ca/research/publications>)

Ray, J. K., M. E. Cannon, and P. C. Fenton (1999) "Mitigation of Static Carrier-Phase Multipath Effects Using Multiple Closely Spaced Antennas," *Navigation, Journal of the Institute of Navigation*, vol 46 no 3, December, John Wiley & Sons Inc., New York, NY, pp. 193–201. doi: 10.1002/j.2161-4296.1999.tb02406.x

Remondi, B. W. (1985) "Global positioning system carrier phase: Description and use," *Journal of Geodesy*, vol 59, no 4, January, pp. 361–377 doi: 10.1007/BF02521069

Reussner, N. and L. Wanninger (2011) "GLONASS inter-frequency biases and their effects on RTK and PPP carrier-phase ambiguity resolution," in *Proceedings of ION GNSS*, 20-23 September, Portland, OR, pp. 712–716, U.S. The Institute of Navigation, Fairfax VA

Rosbach, U. (2000) "GLONASS double difference ambiguity resolution in real-time," in *Proceedings of ION GPS*, 19-22 September, Salt Lake City, UT, pp 163–171, U.S. The Institute of Navigation, Fairfax VA

Saastamoinen, J. (1972) "Atmospheric correction for the troposphere and stratosphere in radio ranging satellites," *The Use of Artificial Satellites for Geodesy*, American Geophysical Union, Washington, D. C., pp. 247–251 doi: 10.1029/GM015p0247

Schempp, T., J. Burke, and A. Rubin (2008) "WAAS Benefits of GEO Ranging," in *Proceedings of ION GNSS*, 16-19 Savannah, GA, pp 1903–1910, U.S. The Institute of Navigation, Fairfax VA

Shi, C., Q. Zhao, Z. Hu, Liu J (2013) "Precise relative positioning using real tracking data from COMPASS GEO and IGSO satellites," *GPS Solutions*, vol 17, no 1, May, pp. 103–119

- Spilker Jr., J. J. (1996) "GPS Signal Structure and Theoretical Performance," [Chapter-3] in *Global Positioning System: Theory and Applications Volume I*, American Institute of Aeronautics and Astronautics, Washington, DC, pp. 57-120
- Takac, F. (2009) "GLONASS inter-frequency biases and ambiguity resolution," *Inside GNSS*, vol 4, no 2, Gibbons Media & Research LLC, New Jersey, USA, pages 24-28
- Talbot, N. C. (1993) "Centimeters in the Field, a Users Perspective of Real-Time Kinematic Positioning in a Production Environment," in *Proceedings of ION GPS 1993*, 22-24 September, Salt Lake City, UT, pp 1049–1057, U.S. The Institute of Navigation, Fairfax VA
- Teunissen, P. J. G. (1993) *Least-squares estimation of the integer GPS ambiguities* Invited lecture, section IV theory and methodology, IAG general meeting, Beijing, China, 16 pages
- Teunissen, P. J. G. (1995) "The least-squares ambiguity decorrelation adjustment: a method for fast GPS integer ambiguity estimation," *Journal of Geodesy*, vol 70, no 1-2, November, pp. 65–82. doi: 10.1007/BF00863419
- Teunissen, P. J. G. (1998) "Success probability of integer GPS ambiguity rounding and bootstrapping," *Journal of Geodesy*, vol 72, no 10, October, pp. 606–612
- Teunissen, P. J. G. (1999) "An optimality property of the integer least-squares estimator," *Journal of Geodesy*, vol 73, no 11, December, pp.587–593
- Teunissen, P. J. G., D. Odijk (1999) "The reliability of GPS ambiguity resolution," *GPS Solutions*, vol 2, no 3, January, pp. 63–69, doi: 10.1007/PL00012758
- Teunissen, P. J. G. (2000) "The success rate and precision of GPS ambiguities," *Journal of Geodesy*, vol 74, no 3-4, May, pp. 321–326
- Teunissen, P. J. G. (2001a) "Integer estimation in the presence of biases," *Journal of Geodesy*, vol 75, no 7-8, September, pp. 399–407, doi: 10.1007/s001900100191
- Teunissen, P. J. G. (2001b) "Statistical GNSS carrier phase ambiguity resolution: a review," in *Statistical Signal Processing 2001, Proceedings of the 11th IEEE Signal Processing Workshop on. IEEE*, pp 4–12
- Teunissen, P. J. G, R. Odolinski, D. Odijk (2014) "Instantaneous BeiDou+GPS RTK positioning with high cut-off elevation angles," *Journal of Geodesy*, vol 88, no 4, April pp. 335–350, doi: 10.1007/s00190-013-0686-4
- Thoelert, S., O. Montenbruck, M. Meurer (2014) "IRNSS-1A: signal and clock characterization of the Indian regional navigation system," *GPS Solutions*, vol 18, no 1, January, pp. 147–152, doi: 10.1007/s10291-013-0351-7

Tiberius, C., T. Pany, B. Eissfeller, P. Joosten, and S. Verhagen (2002) "0.99999999 confidence ambiguity resolution with GPS and Galileo," *GPS Solutions*, vol 6, no 1-2, November, pp. 96–99, doi: 10.1007/s10291-002-0022-6

Townsend, B., P. Fenton (1994) "A practical approach to the reduction of pseudorange multipath errors in a L1 GPS receiver," in *Proceedings of ION GPS*, 20-23 September, Salt Lake City, UT, pp. 143-148, U.S. The Institute of Navigation, Fairfax VA

Van Dierendonck, A. J., P. Fenton, T. Ford (1992) "Theory and Performance of Narrow Correlator Spacing in a GPS Receiver," *Navigation, Journal of the Institute of Navigation*, vol 39 no 3, September, John Wiley & Sons Inc., New York, NY, pp. 23-33, doi: 10.1002/j.2161-4296.1992.tb02276.x

Van Dierendonck, A. J., G. A. McGraw, R. J. Erlandson, R. Coker (1999) "Cross-correlation of C/A codes in GPS/WAAS Receivers," in *Proceedings of ION GPS*, 14-17 September, Nashville, TN, pp 581–590, U.S. The Institute of Navigation, Fairfax VA

Verhagen, S. (2005a) "On the Reliability of Integer Ambiguity Resolution," *Navigation, Journal of the Institute of Navigation*, vol 52 no 2, June, John Wiley & Sons Inc., New York, NY, pp. 99–110. doi: 10.1002/j.2161-4296.2005.tb01736.x

Verhagen, S. (2005b) *The GNSS integer ambiguities: estimation and validation*, Ph.D. Thesis, Delft University of Technology, Delft, Netherlands, 196 pages (Available at [uuid:07c6f2be-3a70-42aa-97b3-894a5770454d](https://doi.org/10.1002/j.2161-4296.2005.tb01736.x))

Verhagen, S., D. Odijk, P. J. G. Teunissen, and L. Huisman (2010) "Performance improvement with low-cost multi-GNSS receivers," in *Satellite Navigation Technologies and European Workshop on GNSS Signals and Signal Processing (NAVITEC), 2010 5th ESA Workshop on*. IEEE, pp 1–8

Vollath, U., S. Birnbach, L. Landau, J. M. Fraile-Ordonez, and M. Marti-Neira, (1999) "Analysis of Three-Carrier Ambiguity Resolution Technique for Precise Relative Positioning in GNSS-2," *Navigation, Journal of the Institute of Navigation*, vol 46 no 1, March, John Wiley & Sons Inc., New York, NY, pp. 13-23, doi: 10.1002/j.2161-4296.1999.tb02392.x

Wang, G., K. de Jong, Q. Zhao, Z. Hu, and J. Guo (2015) "Multipath analysis of code measurements for BeiDou geostationary satellites," *GPS Solutions*, vol 19 no 1, January, pp. 129–139. doi: 10.1007/s10291-014-0374-8

Wanninger, L. (2008) "The Future is Now GPS + GLONASS + SBAS = GNSS," *GPS World*, vol 19 no 7, A Questex Publication, NewTon, MA, pp. 42-48

Zaminpardaz, S., P. J. G. Teunissen, and N. Nadarajah (2016a) "IRNSS stand-alone positioning: first results in Australia," *Journal of Spatial Science*, vol 61, no 1, April, pp. 5–27, doi: 10.1080/14498596.2016.1142398

Zaminpardaz, S., P. J. G. Teunissen, and N. Nadarajah (2016b) "IRNSS/NavIC Single-Point Positioning: A Service Area Precision Analysis," *Marine Geodesy*, July, doi: 10.1080/01490419.2016.1269034

Zhang, W., M. E. Cannon, O. Julien, and P. Alves (2003) "Investigation of combined GPS/GALILEO cascading ambiguity resolution schemes," in Proceedings of ION GPS/GNSS, September 9-12, Portland, OR, pp 2599–2610, U.S. The Institute of Navigation, Fairfax VA

APPENDIX A: BEIDOU B1I CROSS-CORRELATION DISTRIBUTION

Table 3-2 provides the distribution of cross-correlation values of BeiDou B1I. To obtain the distribution, the B1I ranging code between two satellites is convoluted over entire length of the code. Figure A-1 provides an example of cross-correlation values between two BeiDou satellites PRN1 and PRN2. Also, it provides the distribution of cross-correlation peaks.

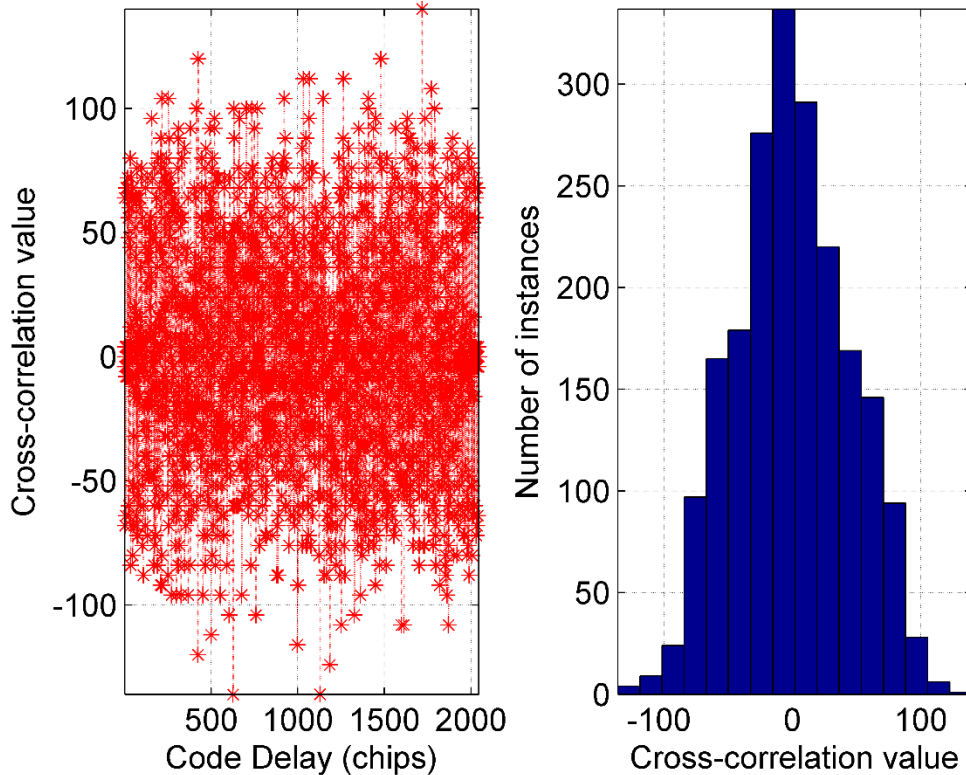


Figure A-1 Plot of cross-correlation values between BDS PRN1 and PRN2 and its distribution

Table A-1 provides the probability of the distribution of cross-correlation peaks for the given example. The actual values are similar to the theoretical values given in Table 3-2.

Table A-1 Probability of the distribution of the cross-correlation values between BDS PRN1 and PRN2

Distribution of levels	Probability of distribution
Level > 96	1.07 %
Level > 64	8.65 %
Level > 32	24.30 %
Level < -32	25.41 %
Level < -64	7.48 %
Level < -96	0.78 %

The probability distribution shows that the magnitude of cross-correlation peaks varies between different levels and the probability of the highest magnitude peak is very small.

APPENDIX B: CROSS-CORRELATION MEASUREMENT ERROR

Ray (2000) describes multipath cross-correlation peak in detail and enlist methods to compute the magnitude of multipath error envelope. The Doppler collision error is similar to multipath and follows the same error envelope, albeit, the cross-correlation peak could be present on either side of the primary peak. The C/A code error envelope (in chips) is given as

$$\begin{aligned} \tau_{error} &= \pm \frac{\alpha \tau_d}{1 + \alpha}, \text{ in the range of } 0 \leq \tau_d < (1 + \alpha)T_d \\ \tau_{error} &= \pm \alpha T_d, \text{ in the range of } (1 \pm \alpha)T_d \leq \tau_d < T_c - (1 \mp \alpha)T_d \\ \tau_{error} &= \pm \frac{\alpha(T_c + T_d - \tau_d)}{(2 \mp \alpha)}, \text{ in the range of } T_c - (1 \mp \alpha)T_d \leq \tau_d < T_c + T_d \end{aligned} \quad \text{B.1}$$

where α is the ratio of the cross-correlation peak to primary peak, τ_d is the code delay of cross-correlation peak, T_d is the chip spacing, and T_c is the code length.

A code delay τ_d can be obtained for given code phases of two GPS or WAAS satellites. The value α is determined using relative signal strength between two satellites. The code error due to cross-correlation peak can be computed using Equation B.1. Section 3.2.1 computes the error due to Doppler collision using this method and plots it as an error envelope along with code-minus-carrier measurement.

APPENDIX C: DOPPLER COLLISION ERROR ENVELOPE

Doppler collision error is determined by the cross-correlation function and the relative code phase. The error follows a bound similarly to a multipath error envelope (Spilker et al. 1996; Cox et al. 1999). In order to obtain Doppler collision error, code phases of the primary peak and the cross-correlation peak are obtained using true ranges. The relative code phase will determine the overlapping geographical area and the magnitude of Doppler collision.

If the user position is not known, the true ranges cannot be determined. In such cases, pseudorange code phases can be used to generate the error envelope. However, the pseudorange code phases are affected by the presence of multiple GEO satellites. Consider a case of only two WAAS satellites in view. The observed code phases of the two satellites are given by

$$\tau_{eff1} = \tau_1 \pm \Delta\tau_{DC} \quad \text{C.1}$$

$$\tau_{eff2} = \tau_2 \mp \Delta\tau_{DC} \quad \text{C.2}$$

where τ_1 and τ_2 are pseudorange code phases for the first and the second satellite respectively, with no Doppler collision conditions, and $\Delta\tau_{DC}$ is the code phase error due to Doppler collision. The effect of Doppler collision on desired satellite is exactly equal but opposite in magnitude on the second satellite. The Doppler collision error follows a multipath envelope and thus the code measurement errors (in chips) are given in Equation B.1 (Ray 2000).

If the observed code phase is used, the relative delay will be affected by two times $\Delta\tau_{DC}$ and the code delay of the cross-correlation peak during Doppler collision is

$$\tau_d^{DC} = \tau_d \pm 2\Delta\tau_{DC} \quad \text{C.3}$$

Thus the offset in code measurement error is given as

$$\begin{aligned} \Delta\tau_{error} &= \mp \frac{\alpha}{1+\alpha} 2\Delta\tau_{DC}, \text{ in the range of } 0 \leq \tau_d < (1+\alpha)T_d \\ \Delta\tau_{error} &= 0, \text{ in the range of } (1\pm\alpha)T_d \leq \tau_d < T_c - (1\mp\alpha)T_d \\ \Delta\tau_{error} &= \pm \frac{\alpha(T_c + T_d \mp 2\Delta\tau_{DC})}{(2\mp\alpha)}, \text{ in the range of } T_c - (1\mp\alpha)T_d \leq \tau_d < T_c + T_d \end{aligned} \quad \text{C.4}$$

If the relative signal strength of the WAAS satellites is zero, $\alpha = 0.0616$. For a standard correlator $T_d = 1$ and the maximum error due to Doppler collision is $\Delta\tau_{DC} = 0.0304$ chip (~ 9 m). Thus the maximum offset in Doppler collision error caused by approximating the true range code phases with pseudorange code phases is given by

$$\begin{aligned} \Delta\tau_{error} &= 0.0035 \text{ chip} \cong 1.03 \text{ m}, \text{ in the range of } 0 \leq \tau_d < (1+\alpha)T_d \\ \Delta\tau_{error} &= 0.0 \text{ chip}, \text{ in the range of } (1\pm\alpha)T_d \leq \tau_d < T_c - (1\mp\alpha)T_d \\ \Delta\tau_{error} &= 0.0018 \text{ chip} \cong 0.53 \text{ m}, \text{ in the range of } T_c - (1\mp\alpha)T_d \leq \tau_d < T_c + T_d \end{aligned} \quad \text{C.5}$$

Considering that the error envelope varies up to 9 m, an offset less than one meter is acceptable. The error envelope computed using pseudorange code phases for Rx1, the receiver used in Section 3.4.1 is shown in Figure C-2. The pseudorange based error

envelope is compared against the error envelope obtained using the true geometric ranges. The difference between the envelopes never exceeds 1.1 m and has a standard deviation of 0.24 m. The variation is large during the rise and fall of the error envelope.

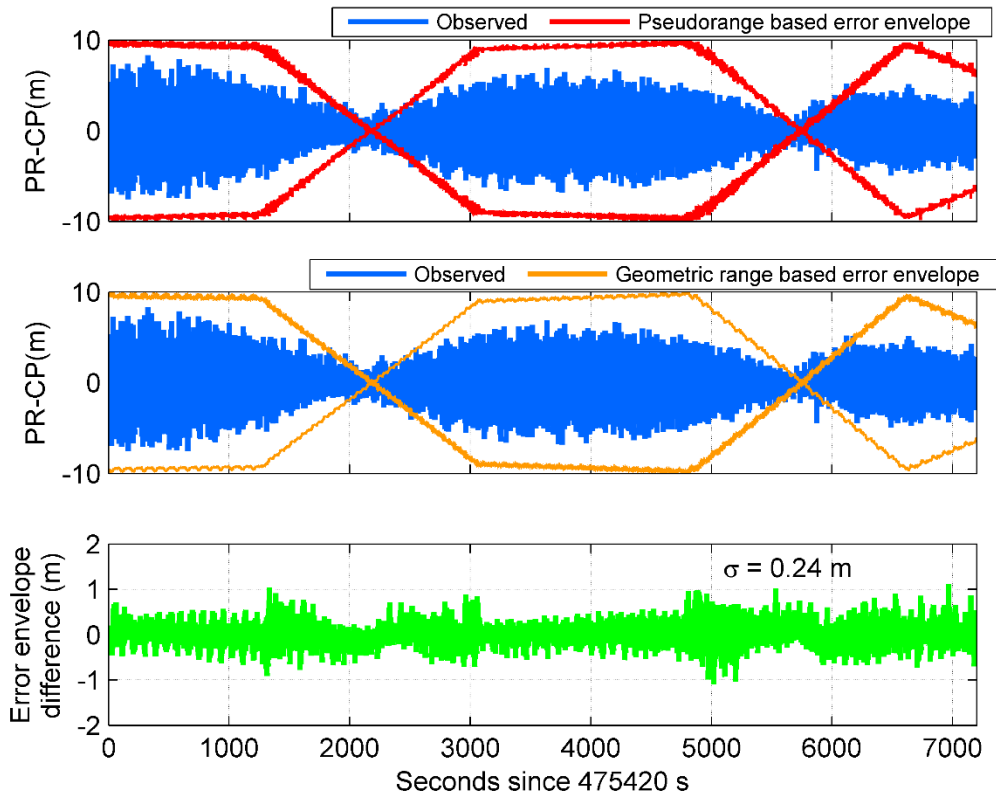


Figure C-2 Doppler collision error envelope using code phase from pseudorange and geometric range

The theoretical error envelope is derived on a set of assumptions given below.

1. Infinite receiver bandwidth: In order to obtain C/A code error envelope given in the equation B.1, the basic assumption is that the receiver bandwidth is infinite. However, in practical conditions, the receiver bandwidth is always limited and the correlation is never sharp (Braasch and Dierendonck 1999; Ray 2000). Instead,

the peak is smooth and affects the measurement accuracy. The correlator triangle peak would become sharper if the IF sampling rate is increased, which would also provide smaller chip spacing. There is always a limitation to receiver bandwidth and is determined by factors such as signal bandwidth, signal-to-noise ratio and receiver cost.

2. Choice of discriminator: In order to compute error envelope, it is assumed that the code lock loop discriminator is operating in a linear region. For example, in case of E-L discriminator, the linear region is ± 0.5 chip. If the correlator arms go beyond this range, the discriminator output is constant and does not match the actual value (Kaplan and Hegarty 2005). The choice of discriminator is an important factor in determining error envelope.
3. No receiver noise or multipath: An important assumption to derive theoretical error envelope is the absence of receiver noise and multipath error. If receiver noise is present, the error envelope will not be smooth. In the above example, the error envelope has variations because the code phases are derived from actual measurements. Additionally, if there were a multipath on the incoming signal, it would be difficult to isolate it from Doppler collision effect because both effects have similar impact on the measurement error.
4. Proper choice of DLL Bandwidth: In Figure C-2, the maximum observed error hardly reached the theoretical error envelope mainly because the data was processed using a DLL bandwidth of 0.5 Hz. As explained in section 4.3.4, if the DLL bandwidth is increased to 1 Hz, the observed error envelope closely matches the theoretical error envelope.

APPENDIX D: SOFTWARE DEVELOPMENT

The analysis of Doppler collision and its impact on an RTK solution is done using two important software packages. The details of the software development undertaken to achieve the research goals are listed below.

1. Software defined receiver - GSNRx™

In order to process IF data, a software defined receiver is required. Figure D-3 shows a block diagram of a generic software receiver (Kaplan and Hegarty 2005).

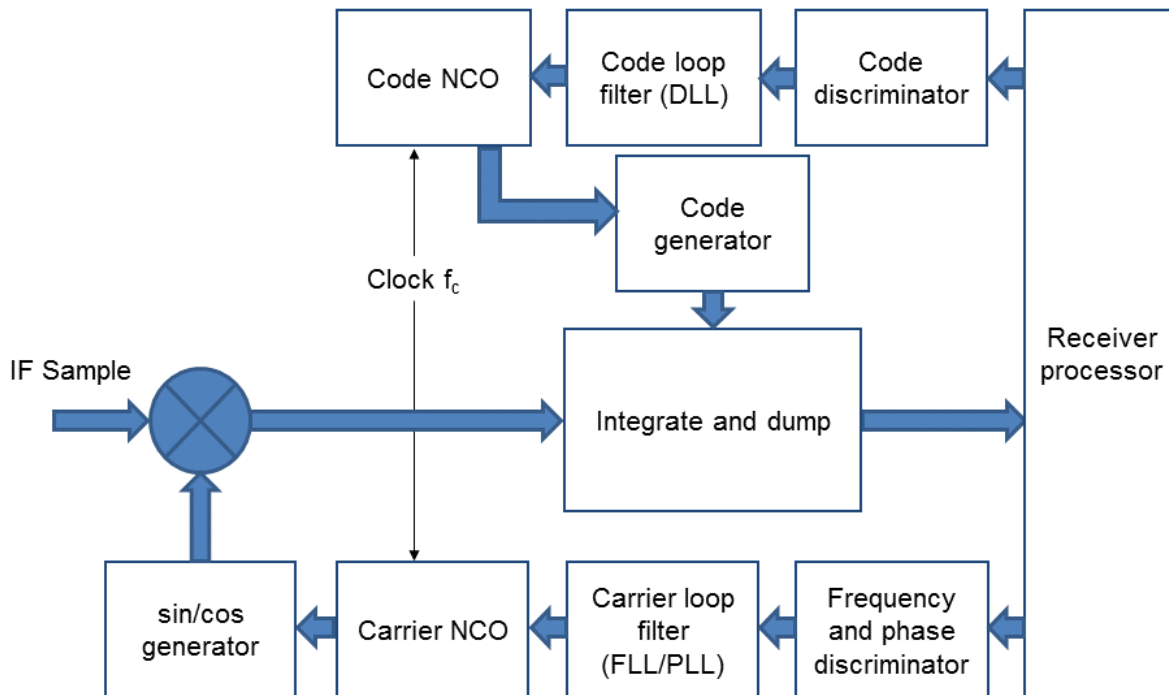


Figure D-3 Development of the modified software defined receiver

GSNRx™, a highly configurable software defined GNSS receiver developed at the University of Calgary (Petovello et al. 2008) is used to obtain GPS measurements which include code, carrier phase, and Doppler observations. However, GSNRx™ does not have WAAS capability and cannot provide WAAS measurements. A software development was undertaken, and a modified version of GSNRx™ was realized which can acquire and track WAAS satellites. Figure D-4 shows the modules implemented in GSNRx™.

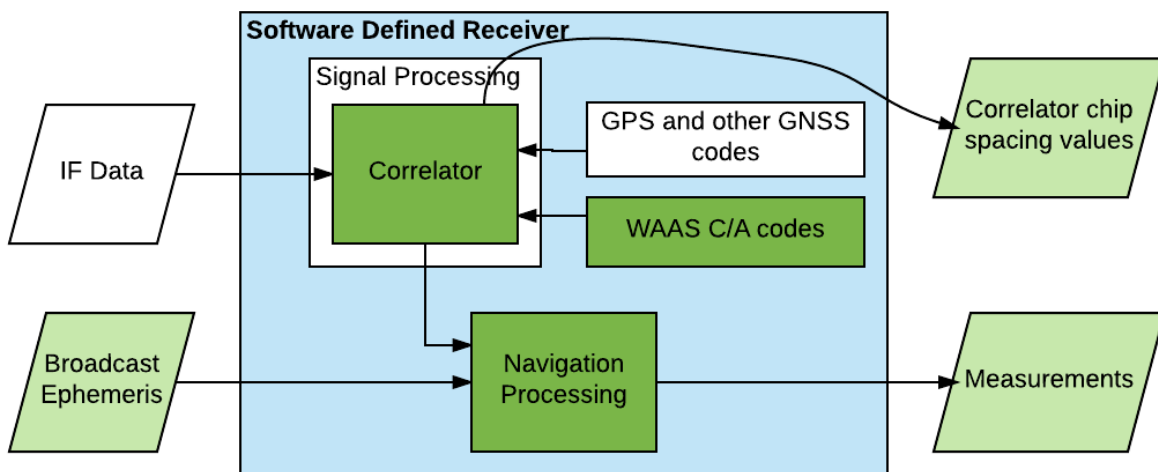


Figure D-4 Development of the modified software defined receiver

Since WAAS navigation messages are different and extensive, no navigation message decoder was implemented and instead, only code phase measurements were generated. The full pseudorange was generated using Broadcast Ephemeris (Montenbruck et al.

2014, 2017). Multiple tests were conducted to validate the WAAS measurements using hardware-simulator and live data.

Table D-2 provides the list of parameters used in processing all GPS and WAAS IF data in this thesis. If a parameter is changed for a specific condition, it is clearly mentioned in relevant sections.

Table D-2 Parameters of modified GSNRx™

Discriminators	DLL	Early – Late (E-L) discriminator		
	PLL	A mix of discriminators (Kaplan and Hegarty 2005)		
Details	PLL Order	PLL Bandwidth (Hz)	DLL Order	DLL Bandwidth (Hz)
PLL DLL Tracker (Code Rate aided with carrier)	3	5.0	1	0.5
Coherent Integration	1 ms for GPS and WAAS			

2. RTK software solution - PLANSoft™

Once the measurements are obtained, an RTK solution is obtained using PLANSoft™, a C++ based RTK solution software developed by the PLAN Group (Ong et al. 2009; Bhandari et al. 2013). However, the RTK software solution could process only GPS and GLONASS observations and has no capability to process Galileo, BeiDou, QZSS, WAAS

or IRNSS measurements. A software development was conducted to add processing modules for all remaining constellations. The development process involved realization of decoders to utilize Broadcast Ephemeris for IRNSS and WAAS satellites. Figure D-5 shows the development of RTK software. The six constellations + SBAS RTK software is one of the benefits of this research.

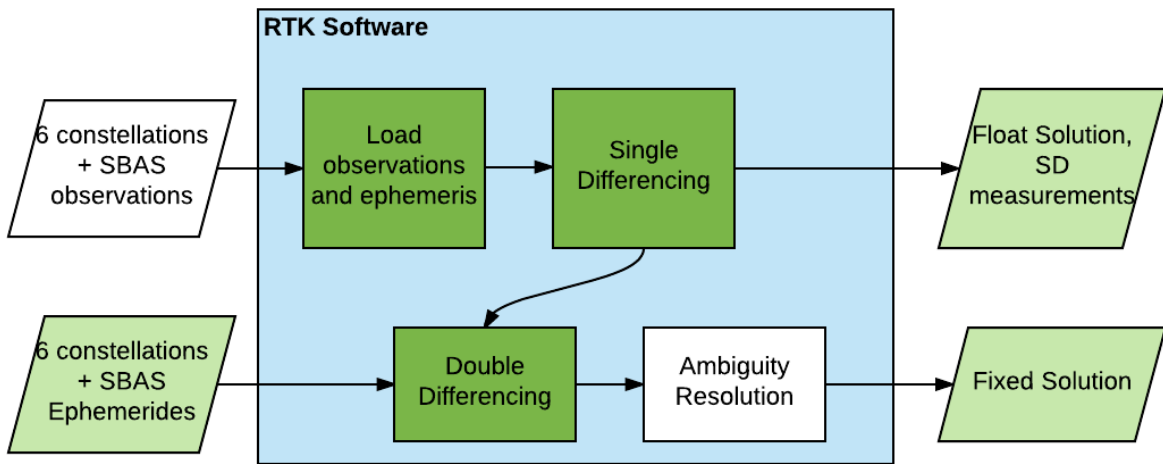


Figure D-5 Development of the six constellations + WAAS RTK software